THE COMPLEX PHASE TRANSFORMATION OF AUSTENITE IN HIGH STRENGTH LINEPIPE STEELS AND ITS INFLUENCE ON THE MECHANICAL PROPERTIES

by

Xiaojun Liang

B.S. in Materials Science & Engineering, Anhui University of Technology, China, 2000

M.S. in Materials Processing Engineering, Southeast University, China, 2004

Submitted to the Graduate Faculty of

Swanson School of Engineering in partial fulfillment

of the requirements for the degree of

Doctor of Philosophy

University of Pittsburgh

2012

UNIVERSITY OF PITTSBURGH

SWANSON SCHOOL OF ENGINEERING

This dissertation was presented

by

Xiaojun Liang

It was defended on

June 26, 2012

and approved by

John A. Barnard, PhD, Professor,
Department of Mechanical Engineering and Materials Science

Luis E. Vallejo, PhD, Professor,
Department of Civil and Environmental Engineering

Dissertation Director:
Anthony J. DeArdo, PhD, Professor,
Department of Mechanical Engineering and Materials Science

Dissertation Co-Director:
Calixto I. Garcia, PhD, Research Professor,
Department of Mechanical Engineering and Materials Science

THE COMPLEX PHASE TRANSFORMATION OF AUSTENITE IN HIGH STRENGTH LINEPIPE STEELS AND ITS INFLUENCE ON THE MECHANICAL PROPERTIES

Xiaojun Liang, PhD

University of Pittsburgh, 2012

During processing of low carbon high strength linepipe steels, complex microstructures are usually obtained. Toughness of the steels is found to be strongly dependent on the complex microstructures. Since the microstructural and chemical condition of austenite is very important for the subsequent microstructures, austenite grain coarsening and recrystallization temperatures were determined. The results showed addition of 0.3wt% more chromium can reduce about 100 ℃ of the grain coarsening temperature. Thus, the alloy design should be considered together with thermomechanical processing to avoid the mixture of austenite grain size. It was found that Bs temperatures of steel have a wide range from 400 ℃ to 580 ℃, depending on cooling rates. The formation of martensite-austenite (MA) constituents and bainitic transformation were investigated in isothermal treatment and continuous cooling conditions. The carbon diffusion was discussed from the view point of thermodynamics and kinetics to explain the formation of MA during bainitic transformation. It was found that controlling carbon diffusion is most important point for the formation of MA. Some experiments were designed and the results confirmed the thermodynamics analysis. In addition, the crystallographic orientations of bainite formed at different bainite transformation temperatures were also determined by EBSD analysis. The orientations of bainite are irrational, but two typical orientations were found. The orientation is near <113> at a higher transformation temperature and the orientation is near <331> at a lower

transformation temperature. The crystallographic packet size of bainite is large when the orientation is near <113>. Coincident Site Lattice (CSL) grain boundaries were introduced to explain its relationship to toughness. As proposed in this thesis, the size and volume fraction of MA, crystallographic packet size and CSL grain boundaries are the three predominant factors affecting the impact toughness of steels. Thus, some methods were proposed for impact toughness improvement. In this regard, a schematic CCT diagram was developed based on the classification of bainite and the distribution of MA within each classification. These results could provide some guidance for improved understanding of the complex microstructures of these steels.

TABLE OF CONTENTS

LIST OF TABLES

LIST OF FIGURES

ACKNOWLEDGEMENTS

I should like to express my sincere gratitude to my advisors, Dr. A. J. DeArdo and Dr. C.I. Garcia for their thoroughly guidance, encouragement and support.

Special appreciation is to Dr. K. Goldman for his generous help improving my English and my thesis writing. I would also like to express my special gratitude to Dr. S.H. Jiao for his invaluable help and encouragement. I am also indebted to Drs. M.J. Hua, K.G. Cho and Chao Fang for their invaluable discussions and help.

Additionally, I should like to thank Mr. Albert Steward and other BAMPRI members: Bob Giles, Victoria Wang, Ryan, David, Rita and Dr. Raymundo Ordonez, for their kind help in materials characterization or my research.

Special acknowledgement is extended to Dr. Xiahan Sang and Xiaodan Wu, Zhuoqun Li for many insightful discussions for some experimental or thesis work. I am also appreciative of the following persons for their kinds of help during my study in Pittsburgh: Maohan Zhang, Hongfu Shu, Jiazhao Cai & Dr. Junhang Luo, Tao An, Kaizhong Wang, Dr. Qin Zhang, Bo Ding, Can Liu, Lina Xu, Wenchen Zhao, Xu Liu, Yihong Kang, Zhongfan Zhang, Dr. Mengjin Yang & Dr. Wei Zhao.

My Ph.D committee consisted of Drs. Barnard, Vallejo, Garcia and DeArdo. I appreciate their performing this task collectively and the helpful suggestions for different aspects of this research.

Finally, I should like to thank my family for their concern and love. In particular, sincere appreciation is extended to my parents for their always unselfish and unrequited support and to my brothers for their encouragement. Special gratitude is extended to my parents-in-law for their understanding and help during my study in the USA. Last but not the least, I want to express my thanks to my wife, Xiaoli, and my daughter, Yawei, for their encouragement and expectations which always inspire me to face and overcome any difficulties. This work is dedicated to them.

1.0 INTRODUCTION

The last fifty years have witnessed an increase of yield strength from 400 MPa to 800 MPa for microalloyed steels. Until 1980, the yield strength available in hot rolled strip and plate was about 420 MPa. However, around 1980, both the linepipe and the automotive industries desired strengths in excess of the 420 MPa that could be readily supplied with fine grained ferrite-pearlite steels[1]. And in these several decades, the grade of linepipe steel was extended from API X52 to X100 or X120[2-5]. In the API Standards, for examples, X52 represents that the yield strength of steel is 52ksi.

Linepipe steel is commonly used for oil or gas transportation over large distances, which range from several miles to thousands of miles. To make transportation more efficient, larger diameters of pipes and higher pressure are preferred. According to the mechanics of materials, a pipe mainly sustains two stresses, σ_1(tangential), σ_2(axial), as shown in Figure 1.1.

$$\sigma_1 = \frac{PD}{2t}, \sigma_2 = \frac{PD}{4t}, \ \sigma_3 = 0 \ \text{(due to plane stress).} \tag{1.1}$$

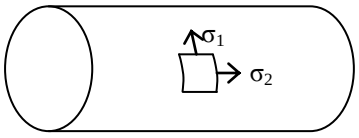

Figure 1.1 Schematical diagram of plane stresses for pipeline

In Equation (1.1), P is the inner pressure, D is the inner diameter of the line pipe, and t is the wall thickness. Using the Von Mises criterion, the following equation can be obtained[6]:

$$\sigma_0 = \sqrt{2}(\sigma_1^2 - \sigma_1\sigma_2 + \sigma_2^2)^{\frac{1}{2}} \tag{1.2}$$

where σ_0 is the yield strength of the material.

Substitute (1.1) into (1.2), and the following equation (1.3) is obtained.

$$\sigma_0 = \sqrt{6}/4\,\frac{PD}{t} \quad \text{or} \quad PD = 4\,\frac{\sigma_0 t}{\sqrt{6}} \tag{1.3}$$

The oil and gas industry demands higher efficiency transportation, since inner pressure, P, and diameter, D, of linepipe steel should be higher to achieve these demands, the wall thickness, t, of the pipe is expected to be thinner to minimize the cost per mile; therefore, increasing yield strength, σ_0, seems to be the only practical solution to this problem.

Compared to X52 linepipe steels, the use of grade X80 linepipe steel has already been shown to result in substantial cost savings. The results summarized in Figure 1.2 show the effect of varying material grade or yield strength level on the Net Present Cost (NPC) of the optimized pipeline system using the base case parameters and clearly indicates potential cost savings from the use of higher strength line pipe for large diameter gas pipelines[2]. The economic transport of gas over very long distances requires additional cost cuts[2, 7]. Then the use of grade X100 and/or X120 could be a solution. Therefore, research of X100 or X120 has been conducted by many researchers in the world in the past ten years[3, 4, 8-11].

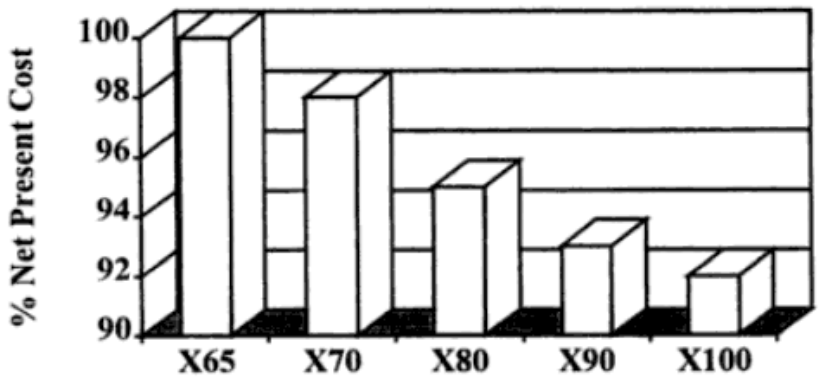

Figure 1.2 Effect of varying material grade on net present cost

However, nearly all strengthening approaches lead to a deterioration of cleavage fracture resistance with the exception of grain size refinement. The following modified Hall-Petch and Cottrell-Petch relationships show the yield strength (Equation 1.4) and Charpy-V-Notch (CVN) Ductile Brittle Transition Temperature (DBTT), or V_{Trs} (Equation 1.5), as a function of common strengthening approaches in structural steels[12].

$$\sigma = \sigma_0 + \sigma_s + \sigma_D + \sigma_P + k_y D^{-1/2} \tag{1.4}$$

$$V_{Trs} = F(\sigma_0 + \sigma_s + \sigma_D + \sigma_P) - k_y D^{-1/2} \tag{1.5}$$

where

σ_0: Lattice friction strengthening

σ_s: Solid solution strengthening

σ_D: Dislocation strengthening

σ_P: Precipitation strengthening

D is the effective grain size or facet size for cleavage.

As shown in Equation (1.5), V_{Trs} goes up with increasing of $\sigma_0, \sigma_s, \sigma_D$ and σ_P, and only smaller grain size D can lower V_{Trs}, which is required.

Since linepipe steels are often used in cold areas, low temperature toughness is always a big problem which causes accidents for linepipe steels. Thus, the level of toughness is a very strict acceptance criterion for linepipe steels.

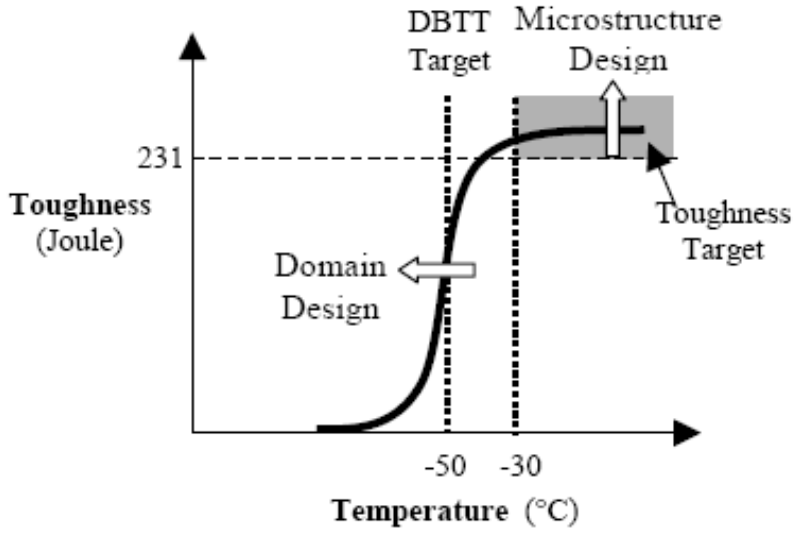

Figure 1.3 X120 Design guideline for toughness

To produce the low DBTT and high upper shelf energy at high strength, the design idea is schematically illustrated in Figure 1.3. A key component of the design guidelines shown in Figure 1.3 is to minimize the solid solution strengthening from interstitial alloying. That is, by reducing carbon concentration, the beneficial effects in terms of impact toughness and weldability are obtained. In order to compensate for the loss of strength due to low C content, the

alloy design philosophy is based on the advanced use of cost effective microalloying elements (MAE), such as niobium, vanadium, titanium and boron in conjunction with moderate levels of other alloying elements, manganese, chromium, nickel, copper and so on. To fulfill the target of strength and toughness, different microstructure design criteria have been expected.

Before the 1980s, ferrite and pearlite steels were designed for linepipe steel X52 and X60. The most obvious contributor to strength was grain refinement, as was clearly shown by quantitative optical microscopy[1]. Between the 80s and 90s, non-polygonal or acicular ferrite, and a small fraction of bainite were designed for X70 or X80. However, for X120 steels, the microstructure of bainite or the mixture of bainite and martensite is required for strength, as shown in Figure 1.4[13] and Figure 1.5[14]. With the increase of strength of steel, toughness becomes a main issue for X120 steels. Reports on X100/X120 microstructure and mechanical processing are plentiful in the literature [10, 12, 15-17]. However, a clear understanding of the role of microstructure in low carbon bainitic steel or low carbon bainitic and martensitic steel[18, 19], and the effect of microstructure factors on the toughness response is of high interest. Furthermore, understanding the mechanism for improving toughness of this type of high strength steel is essential.

The martensite austenite (MA) constituents commonly appear in steel due to carbon partitioning. During the formation of ferritic microstructure, the carbon is rejected to the remaining untransformed austenite. When the carbon enrichment is low, the result is martensite. But, when enrichment is high, the result can be retained austenite. MA constituents can be formed during transformation. These constituents are hard second phase distributed in the matrix. And stress concentration occurs at the surface between the hard MA constituents (>500VHN) and the softer matrix (200~400VHN). The crack tendency varies according to the different

morphologies and hardness of the MA constituents, which could deteriorate the toughness to different extents.

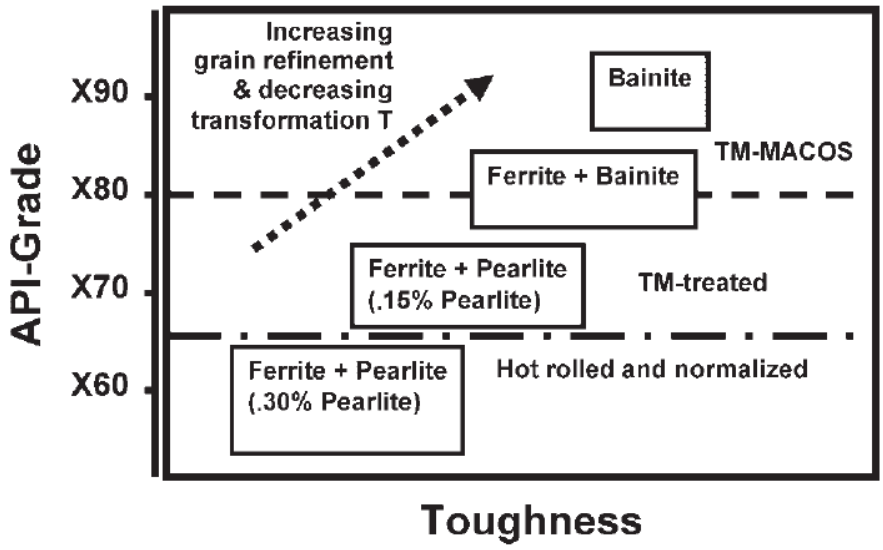

Figure 1.4 Evolution of plate steel for large diameter linepipe: microstructure and mechanical properties (API – American Petroleum Institute; MACOS – accelerated cooling with Mannesmann Cooling System)

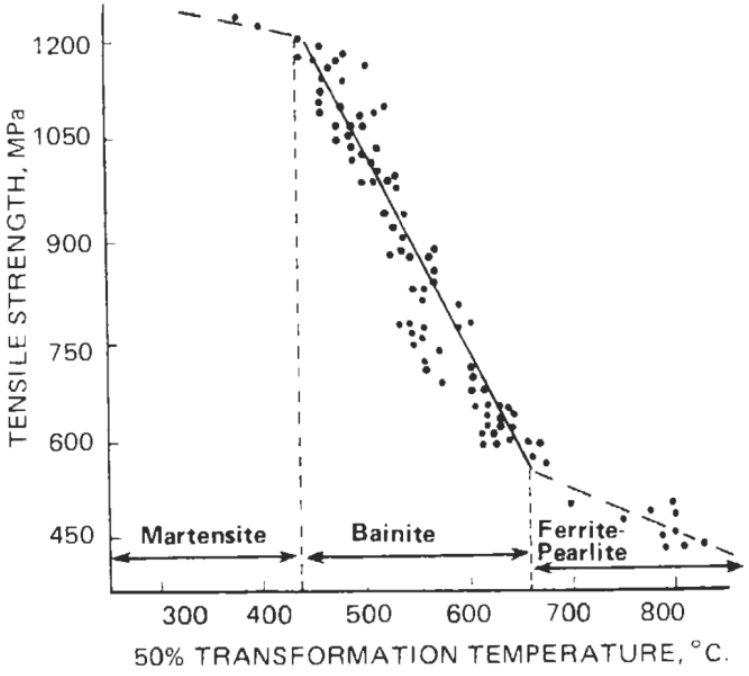

Figure 1.5 Effect of 50% transformation temperature on tensile strength of bainitic steels

2.0 BACKGROUND

2.1 DEVELOPMENT AND MARKET DEMANDS OF LINEPIPE STEELS

Linepipe steels are generally produced using two approaches: seamless pipe steels and welded linepipe steels by Double Submerged Arc Welded (DSAW). Seamless pipe steels are made by hot piercing and then by hot rolling or extrusion. The latter type of pipes is bent on a UOE process and welded from hot rolled plates. The cost of seamless steels is high and the diameter of pipes is commonly small, thus, it is preferably used for transporting high pressure, high temperature, inflammable, or toxic fluids. Then, seamed, or welded linepipe steels are the primary choice for long, large diameter pipes.

2.2 MECHANICAL PROPERTIES REQUIREMENTS OF HIGH STRENGTH X-100 AND X-120 LINEPIPE STEELS

The target mechanical properties established at the beginning of the development of X100 and X120 linepipe are summarized in Table 2.1[20] and Table 2.2[4]. Other than the target strength for linepipe steels, the parameters of toughness, such as Charpy upper shelf energy, impact transition temperatures and DWTT shear area, are also very strict as described in the following tables. The target upper shelf energy is expected as high as 231J shown in Table 2.2. With respect to seamed linepipe steels, the X120 pipe should also exhibit good HAZ cracking resistance. The target mechanical properties for welded joints are listed in Table 2.3.

Table 2.1 Target mechanical properties of X100 linepipe[20]

Yield strength Rt0.5 (MPa)	Tensile strength Rm (MPa)	Y/T ratio	Charpy V upper shelf energy (J)	DWTT 85% shear area (℃)
≥690	≥770	≤0.93	>150	≤-20

Table 2.2 Target mechanical properties of X120 linepipe[4]

Tensile property		Charpy impact property		DWTT
YS(MPa)	TS (MPa)	$vE_{-30℃}$	vTrs	shear $area_{-20℃}$
827	931	231J	-50℃	75%

Table 2.3 Target mechanical properties of X120 linepipe (welded joint) [4]

Tensile property	Charpy impact property		DWTT	DWTT
Welded joint	HAZ	WM	HAZ	WM
TS (MPa)	$vE_{-30℃}$	$vE_{-30℃}$	$CTOD_{-20℃}$	$CTOD_{-20℃}$
931	84J	84J	0.08 mm	0.08 mm

Since the DSAW linepipe steels are studied in this research, the design of the chemical composition should fulfill the requirement of weldability. The Graville Weldability Diagram[21] is illustrated in Figure 2.1; it is classified into three categories, namely, easy to weld, weldable with good control, and difficult to weld, based on the steel's carbon content and carbon

equivalent (CE, or Pcm), as shown in Equations 2.1 & 2.2. In the figure, a low carbon steel (<0.13%) with low CE (0.45) falls under zone I and ensures the highest safety to cracking under all welding conditions. Two types of equations of carbon equivalent can be seen in Equations 2.1[22] and 2.2[23].

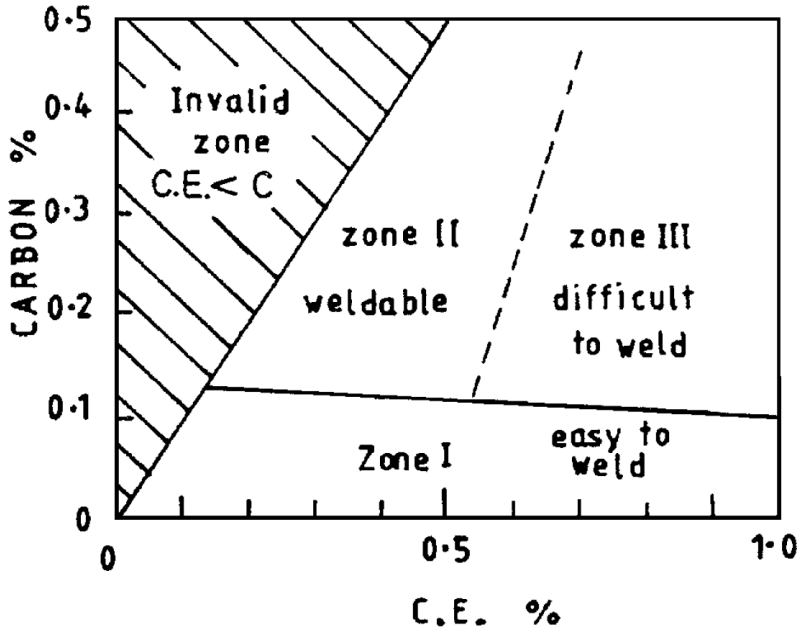

Figure 2.1 Graville Wedability Diagram

$$Ceq=C+(Mn/6)+\{(Cu+Ni)/15+(Cr+Mo+V)/5\ ^{[22]} \quad (2.1)$$

$$Pcm=C+Si/30+(Mn+Cu+Cr)/20+Ni/60+Mo/15+V/10+5B^{[23]} \quad (2.2)$$

2.3 STRENGTHENING MECHANISMS

For linepipe steels, several strengthening mechanisms can be used, which include: solid solution strengthening, grain boundary strengthening, dislocation strengthening, and precipitation strengthening.

2.3.1 **Solid solution strengthening**

The solid solution strengthening includes two categories: by interstitials and by substitutional atoms. Carbon and nitrogen are two of the most important interstitial elements in steels, which have a disproportionate influence on the strength of ferritic iron. Solid solution strengthening occurs when the strain fields around misfitting solutes interfere with the motion of dislocations. Atoms which substitute for iron cause local expansions or contractions; these strains are isotropic and therefore can only interact with the hydrostatic components of the strain fields of the edge dislocations. In contrast, an interstitial atom located in the irregular octahedron interstice in ferrite causes a tetragonal distortion (Figure 2.2) which has a powerful interaction with the shear that is the dominant component of a dislocation strain field[24].

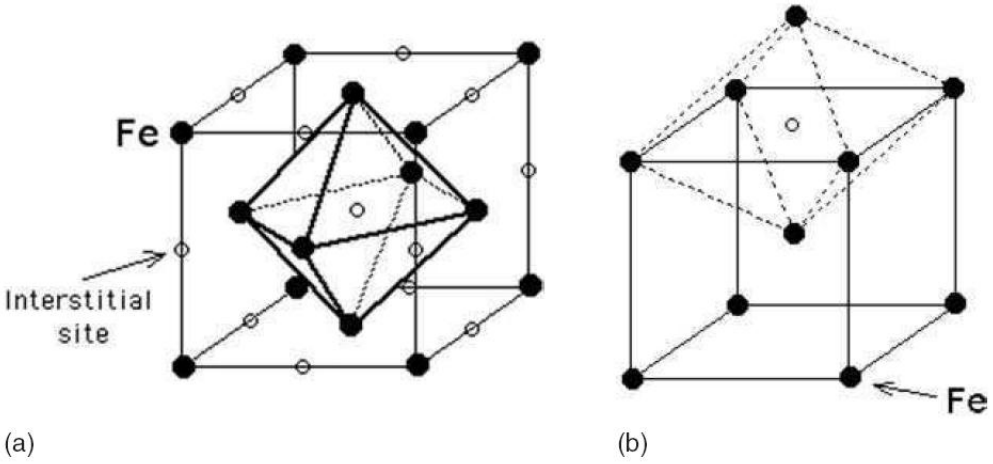

Figure 2.2 (a) The regular octahedron interstice in austenite. (b) Octahedral interstice in ferrite-notice that two of the axes are longer than the third (vertical axis). This leads to a tetragonal distortion when the site is occupied by carbon.

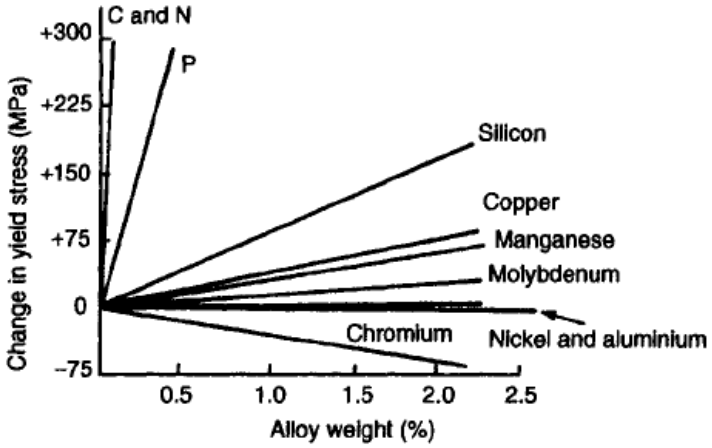

Figure 2.3 Solid solution strengthening effects in ferrite-pearlite high-strength low-alloy steels[14]

In general, the strengthening achieved by substitutional solute atoms is greater the larger the difference in atomic size of the solute from that of iron, applying the Hume-Rothery size effect[25]. However, from the work of Fleischer and Takeuchi it is apparent that differences in the elastic behavior of solute and solvent atoms are also important in determining the overall strengthening achieved. In industrial steels, solid solution strengthening is an important factor in the overall strength, where it is achieved by a number of familiar alloying elements, such as manganese, silicon, nickel, molybdenum. The solid solution strengthening effects of the common alloying elements in high strength low alloy steels are illustrated in Figure 2.3[14]. Work by Pickering and Gladman has provided the strengthening coeffients shown in Table 2.4. [26][26]The data show that carbon and nitrogen have powerful strengthening effects on yield strength. However, it should be remembered that carbon and nitrogen, such interstitial atoms, have a severely detrimental effect on toughness and to a large extent, weldability is dependent on carbon contents and, therefore, these elements should be reduced to a limited number for the design of linepipe steels.

Table 2.4 The change in yield stress per weight percent of the varying alloying elements[26]

Element	MPa per 1wt%
C and N	5544
Si	83
Cu	39
Mn	32
Mo	11
Cr	-31

2.3.2 **Dislocation strengthening**

Steels with heavy deformation in the austenite non recrystallizaion zone and with transformation of bainite or martensite have a high density of dislocations, which can increase the yield strength up to 250MPa, as illustrated in Figure 2.4[27]. However, this strengthening mechanism has a disadvantage that dislocation density will decrease rapidly due to recovery when steel suffers an elevated working temperature. The equations of yield strength vs. dislocation density can be expressed as (2.3)[28]:

$$\sigma_D = \mu b \rho^{1/2} \tag{2.3}$$

where σ_D is the incremental yield strength by dislocation density; μ is the shear modules; b is the Burgers vector; ρ is dislocation density.

2.3.3 **Precipitation strengthening**

Precipitation strengthening is one of the important strengthening mechanisms for microalloyed linepipe steels. In linepipe steels, most of precipitates form according to the Orowan strengthening mechanism; the effect of strengthening mechanism can be described by Orowan - Ashby model[29]:

$$\Delta\sigma_p = \frac{0.538Gb}{X} f^{1/2} ln\left(\frac{X}{2b}\right) \tag{2.4}$$

where, $\Delta\sigma_p$ is the yield strength increment by precipitation; G is the shear modules; b is the Burgers vector; X is the real diameter of the particles; f is the volume fraction of precipitates.

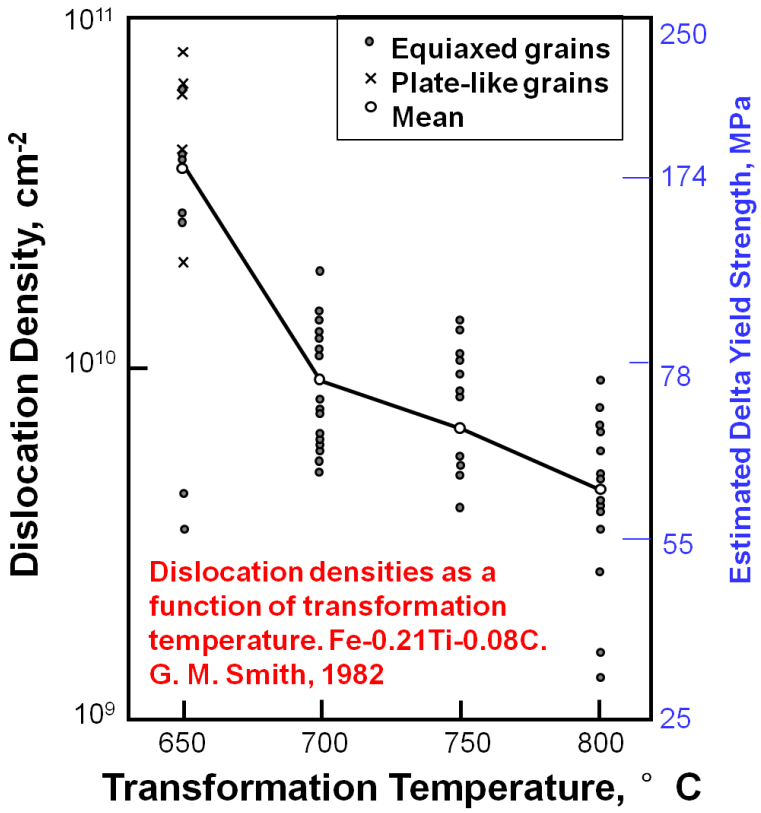

Figure 2.4 Changes of dislocation density with transformation temperatures in Fe-0.21Ti-0.08C steel

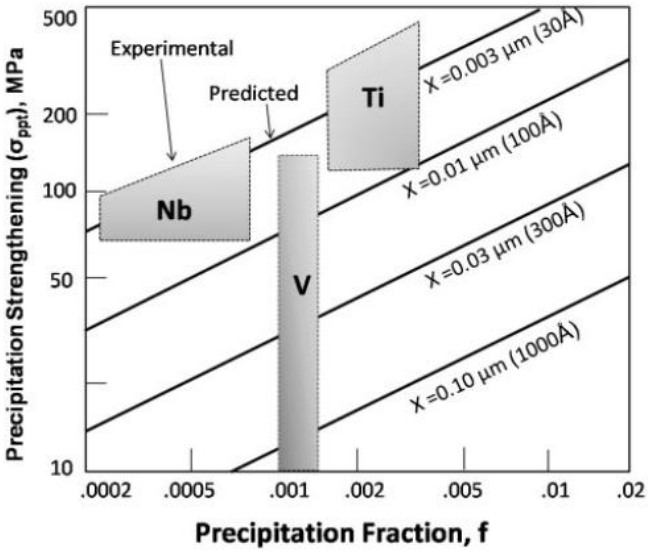

Figure 2.5 Dependence of precipitation strengthening on precipitate size X and fraction according to Orowan - Ashby model, compared with experimental observations for given microalloying additions.

The effect of microalloying elements, Nb, V and Ti on precipitation strengthening is shown in Figure 2.5[30]. The strength increment coming from precipitation strengthening can have a range from several MPa to 150Mpa.

2.3.4 **Grain boundary strengthening**

Grain boundaries are one of the largest obstacles for dislocation motion. Thus, refining grain size can obviously increase grain boundary area per unit volume, and then the yield strength increment can be described by the simple Hall-Petch relationship[14, 31] as shown in Equation (2.5):

$$\sigma = \sigma_0 + kD^{-1/2} \tag{2.5}$$

and the overall contribution to strength by all other strengthening mechanisms can be expressed in a linear form of the extended Hall-Petch equation (2.6):

$$\sigma = \sigma_0 + \sigma_s + \sigma_D + \sigma_P + k_y D^{-1/2} \quad (2.6)$$

This type of relationship holds for a wide variety of irons and steels as well as many non-ferrous metals and alloys. For linepipe steels, the ferrite grain size can be controlled as small as 3-5μm. However, further refinement of the ferrite grain size is no longer easy to obtain by thermomechanical processing. Thus, in the higher strength steels, the microstructure needs to be changed from ferrite into bainite or martensite. Then, D in the above relationship should be an effective size, which may be the subgrain of bainite or martensite.

2.4 TOUGHNESS MECHANISMS

Fracture frequently occurs for linepipe steels at low temperatures even with a low stress. Many accidents made researchers realize that toughness (fracture resistance) is a very important factor for mechanical properties. For the new grade of linepipe steels, the principal goal is to get expected high strength with excellent toughness.

Many ways are used to define toughness; however, current methods of assessing toughness are closely linked to the engineering applications, in which components are exposed to certain stresses, constraints and environments. The Charpy V-Notch impact test is commonly applied to steels to assess the impact toughness.

In engineering applications, however, there are two aspects of the toughness problems, when considering steels. One is the energy absorption when fracture occurs by the ductile-failure mode, and the other is the ductile-brittle transition behavior[31]. These can be described as:

a) The ductile upper shelf energy (USE). This energy is controlled by the metallurgical features that control the extent of energy absorption when an impact test specimen fails in a ductile

mode. Very high USE means the steel has good resistance to ductile tearing and good crack arresting capacity.

b) The ductile to brittle transition temperature (DBTT). Body centered cubic metals, such as iron, show a transition from ductile fracture behavior (void initiation, growth and coalescence) at above room temperature to a brittle failure mechanism by cleavage at low temperatures.

Effects of microstructural and compositional variables are complex, in that some compositional variables also have effects on microstructure. Results have been published by Pickering and Gladman[31], giving a relationship for the Charpy V-Notch impact transition temperature as

$$V_{Trs}(°C) = 19 + 44(\%Si) + 700(N_f)^{\frac{1}{2}} + 2.2(\%Pearlite) - 11.5d^{-1/2} \qquad (2.7)$$

where N_f is the 'free' nitrogen content (wt%) and d is the mean linear intercept ferrite grain size.

However, Equation (2.7) is supposed to be only applicable for ferrite-pearlite steels. For modern high strength steels, polygonal ferrite and pearlite are not the main microstructures, while lower bainite or low carbon martensite is expected to be the principal microstructure. Thus, the above equation is not applicable for high strength steels, such as X120 linepipe steels. But, in general, the effect of alloying elements on toughness is still similar. Grain refinement is still a very useful factor since it increases strength and improves toughness, simultaneously. However, we should know here, that the grain size is not ferrite grain size any more. This new grain size needs a different definition.

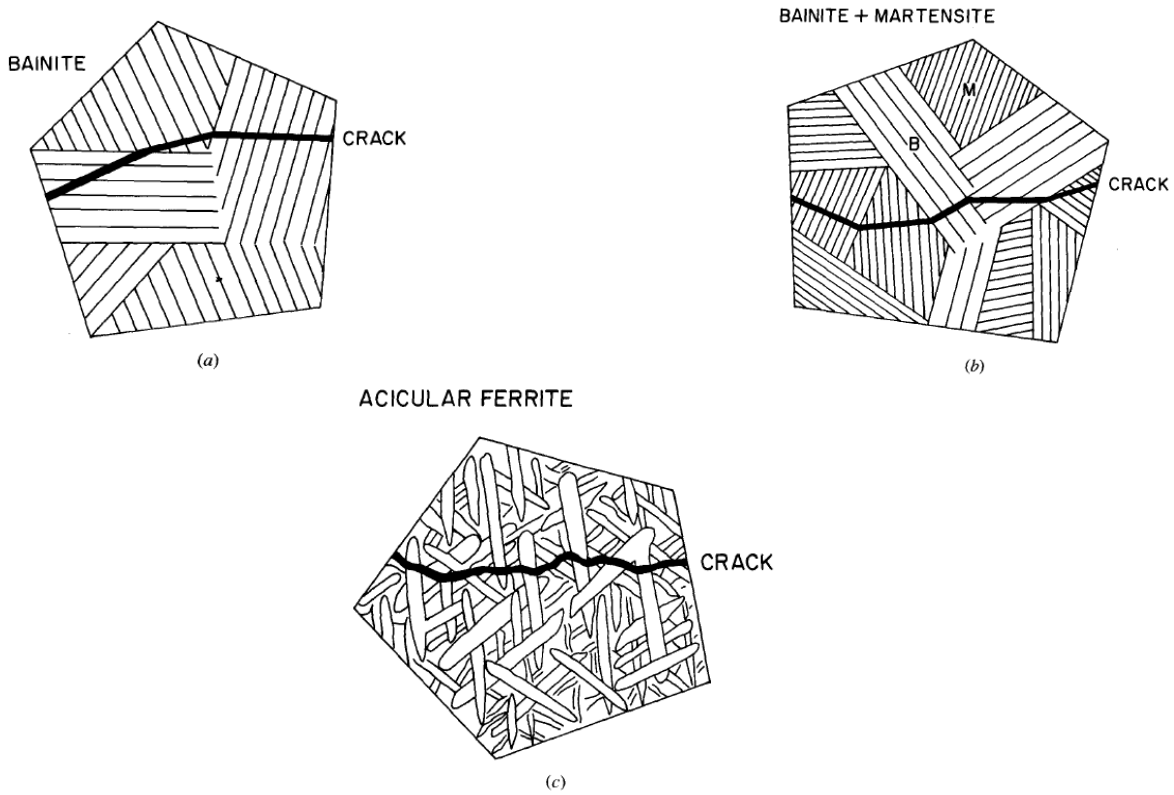

Figure 2.6 Schematic diagrams: (a) cleavage crack deflection at colony (or packet) boundaries; (b) austenite grains subdivided by bainite; and (c) cleavage crack deflection at lath boundaries.

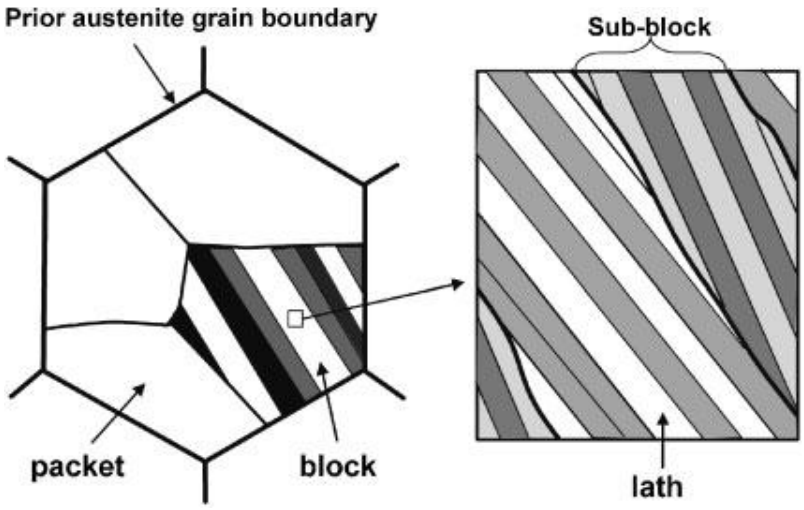

Figure 2.7 Schematic illustration of the definitions of packet, block and sub-block.

Most studies for low carbon steels agree that the important structural unit is the cleavage facet size; thus the relationship between this and the microstructure is important. It is found that the cleavage size is the polygonal ferrite grain size for ferrite-pearlite steels; however, the facet size is different for different steel microstructures. A large body of research showed that the toughness of bainitic steel is relevant to the packet size of bainite[32-34]. The schematic diagrams are shown in Figure 2.6[34]. A more detailed schematic illustration of packet, block and sub-block in lath martensite or bainite is shown in Figure 2.7[35]. For bainitic steels, the cleavage crack is deflected at the colony or packet boundaries, as indicated in Figure 2.6 (a). For mixed bainite/martensite microstructures, similar relationships have been noted, but a finer facet size results from the martensite packets forming in austenite grains subdivided by the bainitic laths, as shown in Figure 2.6 (b). However, for acicular ferrite, the limiting structural unit for cleavage can be the lath size, as illustrated in Figure 2.6 (c). Thus, for low carbon bainitic steels, smaller

subgrains are expected to be subdivided which provides resistance to fracture. Naylor and Krahe did research on the effect of the bainite packet size on toughness[33]. They found the relative improvement of the impact properties is related to the average size which seems to be the effective grain size in upper bainitic structures, as shown in Figure 2.8 and Table 2.5. It shows the decrease of bainite packet size improves both strength and toughness apparently.

However, if the size of the carbides precipitated from bainite or martensite is too big, they may become the source of crack initiation, and then the toughness decreases rapidly. Microstructure designed for high grade linepipe steels should be bainite or a mixture of bainite and low carbon lath martensite since bainite and martensite have low transformation temperatures, and therefore, the strength is higher for those types of microstructures.

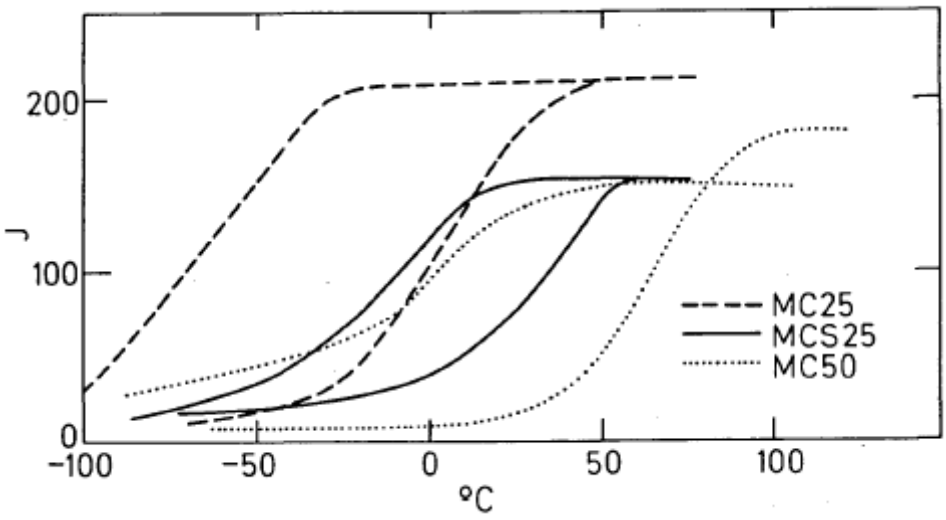

Figure 2.8 Effect of bainitic packet refinement on Charpy-V transition curves for three steels. Three sets of curves refer to packet sizes respectively given in Table 2.5[33].

Table 2.5 Results of variable-temperature mechanical tests

Material	Slow bending tests			Charpy tests		Uniaxial tensile test (room temperature)
	$d_B^{-1/2}$, $mm^{-1/2}$	σ_{cf}, MPa	NDT, °C	$d_B^{-1/2}$, $mm^{-1/2}$	FATT, °C	$\sigma_{0.2}$, MPa
MC25	9·2	1850	−166	8·9	15	550
	11·2	2370	−198	12·4	−50	620
MCS25	9·1	1690	−140	9·1	40	550
	12·9	2410	−205	12·1	− 5	580
MC50	10	1850	− 60	9·1	75	700
	14·4	2680	−196	16·9	0	750
MCS50	11·2	2240	−170	—	—	—
	14·4	2670	−190	—	—	—

2.5 RECRYSTALLIZATION AND GRAIN COARSENING

At higher temperatures, steel with deformed microstructure will undergo a discontinuous change in grain structure, which is often called primary recrystallization. After recrystallization, grain growth may always appear simultaneously. Grain growth may be divided into two types, normal grain growth and abnormal grain growth. Normal grain growth coarsens uniformly and is classified as a continuous process. Abnormal grain growth is a discontinuous process. Only a few grains grow and consume the matrix of smaller grains and a bimodal grain size distribution develops[36, 37], as shown in Figure 2.9. Abnormal grain growth is sometimes called secondary recrystallization. The driving force for the primary recrystallization is the stored energy of cold work, while the driving force for the growth of grains is the driving pressure of grain boundaries. The driving force for grain growth is about two orders of magnitude less than that for primary recrystallization. Therefore, the grain boundary velocities are much slower than that in primary

recrystallization. Moreover, boundary migration is more affected by the pinning effects of solute and second phase particles[36, 38].

In the thermomechanical processing of steels, the reheating temperatures and time may affect the grain growth of steels. The abnormal grain growth will produce the bimodal grain size distribution, thus causing the mixture of grain sizes or microstructures in steel. The mixture usually brings some bad effects in steels, such as low strength and high cracking susceptibility[39].

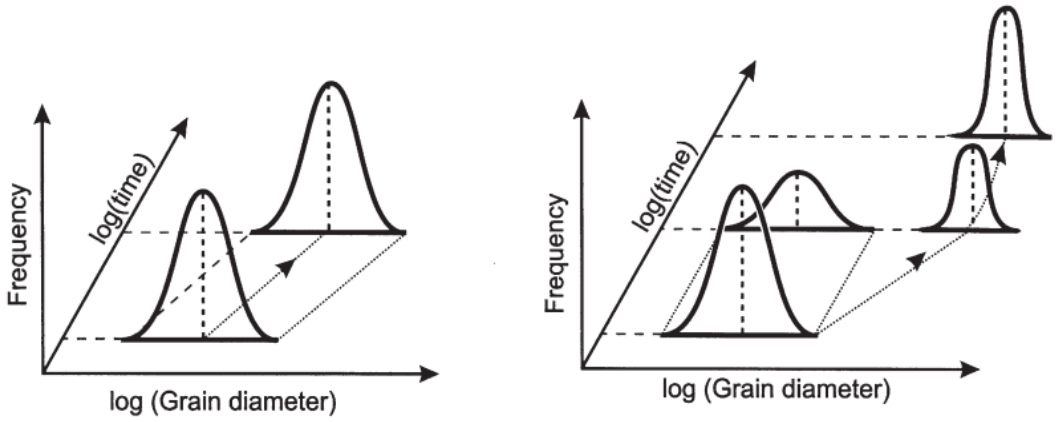

(a) (b)

Figure 2.9 Schematic representation of the change in grain size distribution during (a) Normal grain growth and (b) Abnormal grain growth.

2.6 BAINITIC TRANSFORMATION

Bainite was first discovered by Bain and his colleagues during the late 1920s and was described as a microstructure consisting of an 'acicular, dark etching aggregate' which was quite unlike the pearlite or martensite observed in the same steel[40]. The pearlite reaction is essentially a high temperature one occurring between 550℃ and 720℃, and it is diffusion controlled. And bainite is formed at lower temperature, which is generally accepted to be called displacive transformation, which they are the formation of the bainite or martensite is a medium or low-temperature reaction. Bainite was first found in the studies of the isothermal decomposition of austenite. However, bainite also occurs during athermal treatments at cooling rates too fast for pearlite to form, yet not rapid enough or low enough transformation to produce martensite.

2.6.1 **Definitions of bainite**

Bainite changes as the transformation temperature decreases. Generally, bainite can be divided into two main forms: upper bainite and lower bainite.

Upper bainite: The upper bainite's transformation temperature ranges from about 550℃ to 400℃. The microstructure of upper bainite consists of fine plates of ferrite, each of which is about 0.2μm thick and about 10μm long. The plates grow in clusters are called sheaves. Within each sheaf the plates are parallel and of identical crystallographic orientation, each with a well-defined crystallographic habit[24].

The growth of each plate is accompanied by a change in shape of the transformed region. Thus, the change can be described precisely as an invariant-plane strain (IPS) with a large shear component.

It is well recognized that upper bainite forms in two distinct stages, the first involving the formation of bainitic ferrite which has a very low solubility for carbon (0.02wt%). Then the remaining austenite is carbon enriched during the growth of the ferrite. Eventually, the layer of retained austenite or cementite precipitate exists in between the ferrite sub-units (Figure 2.10[24]).

Lower Bainite: Lower bainite forms in the temperature range of 400-250℃. Lower bainite has similar microstructure and crystallographic features as that of upper bainite. The main distinction between them is the form of the cementite particles in the microstructure. The carbide particles precipitate inside the plates of ferrite in lower bainite, as shown in Figure 2.11[24]. And the carbides in lower bainite frequently precipitate in just one variant of the orientation relationship, such that they form parallel arrays at about 60 °to the axis of the bainite plate.

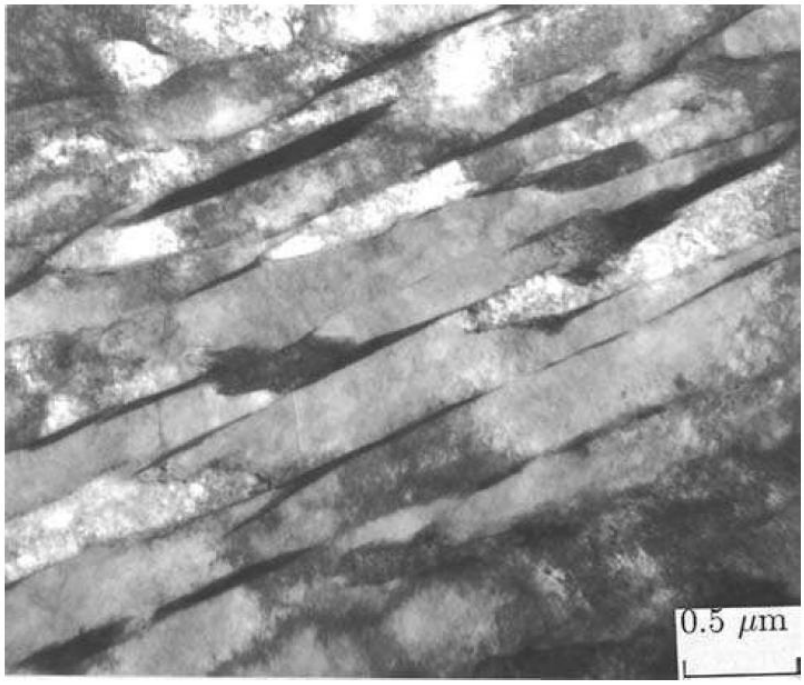

Figure 2.10 Upper bainite in Fe-0.095C-1.63Si-2Mn-2Cr wt% steel transformed isothermally at 400℃. The cementite has been suppressed to leave austenite films between the bainite ferrite plates.

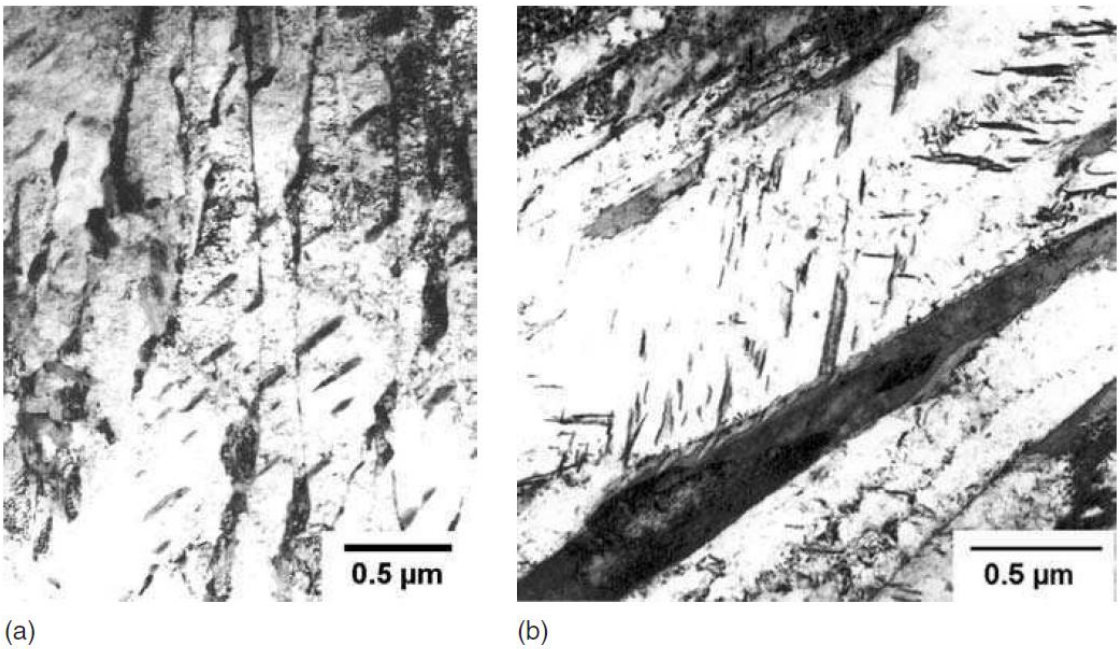

Figure 2.11 (a) Single variant of cementite in lower bainite, Fe-0.3c-4Cr wt%, transformed isothermally at 435℃. (b) Multiple variants of cementite in lower bainite, Fe-0.4C-2Si-3Mn wt%, transformed isothermally at 300℃

Although upper bainite and lower bainite are two general forms of bainite often found in most engineering steels, several other types of bainite are observed according to its morphologies. The mechanical properties vary depending on the bainite morphologies. Since bainite microstructures are complex, several definitions describing bainite microstructure are used. Thus, a short review of these definitions is necessary. Several morphologies of bainite are described as Figure 2.12[41]. These are nodular bainite (a), columnar bainite (b), upper bainite (c), lower bainite (d), grain boundary allotromorphic bainite (e), inverse bainite (f). Although these definitions seem clear, however, they are not used very often in steels. One reason may be

the microstructures (a), (b), (e) and (f) are not common. The other reason is that in the engineering steels, microstructures are complicated and mostly are composed of several constituents, and the differences between them are not as large as the sketch for definition indicates. These definitions were first developed for medium carbon steels where precipitates of Fe_3C are part of the definition. Thus, for low carbon steels, where little Fe_3C is found, the morphologies are not the same as those in medium carbon steels.

Another way for classifying bainite is based on the form of carbon in the second phases and the distribution of the second phases. Not all bainite is composed of ferrite with carbides. Some bainite was recognized as a kind of carbide free bainite which is composed of ferrite and retained austenite. Ohmori[42] et al., classified bainite in low carbon steels as three types: BI consists of carbide-free ferrite with austenite retained between the ferrite lath, BII is a kind of bainite with carbides in between ferrite lath, and in BIII, carbides distributed within ferrite laths.

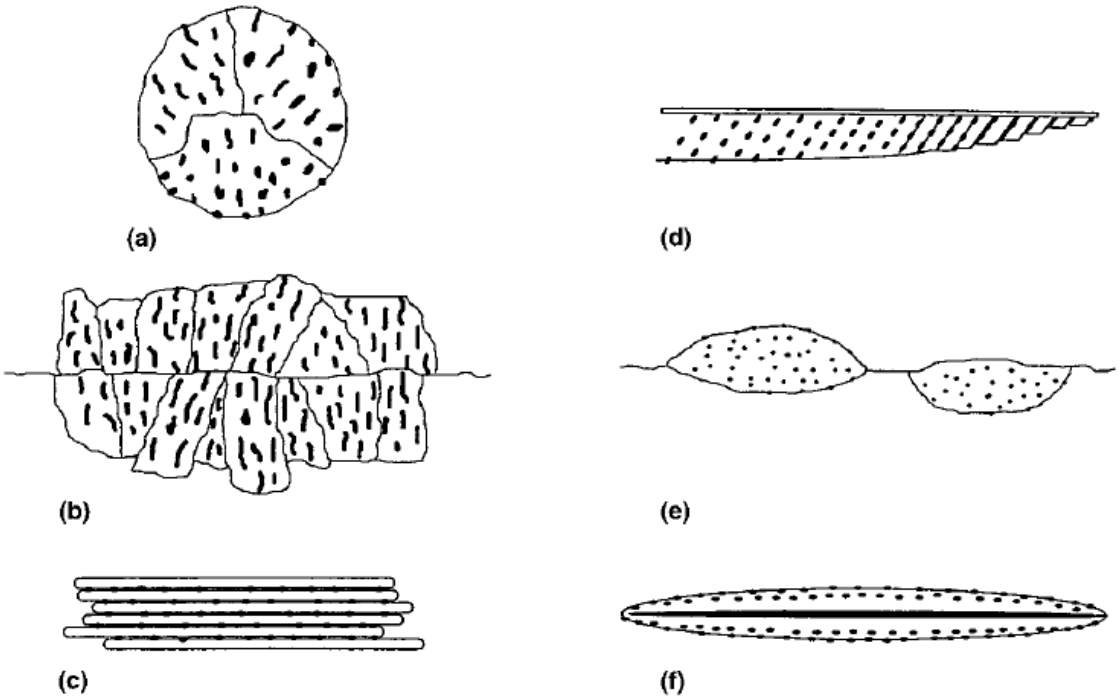

Figure 2.12 Schematic illustrations of various ferrite (white)-cementite (black) microstructures defined as bainite. (a) Nodular bainite; (b) Columnar bainite; (c) Upper bainite; (d) Lower bainite; (e) Grain boundary allotromorphic bainite; (f) Inverse bainite

Zajac et al., classified bainite in a different way[43]. Bainite is defined based on the morphologies of ferrite and the type of second phase in the microstructure. According to this definition: five types of bainite were named: granular bainite, upper bainite, degenerate upper bainite, lower bainite and degenerate lower bainite, as shown in Figure 2.13[43].

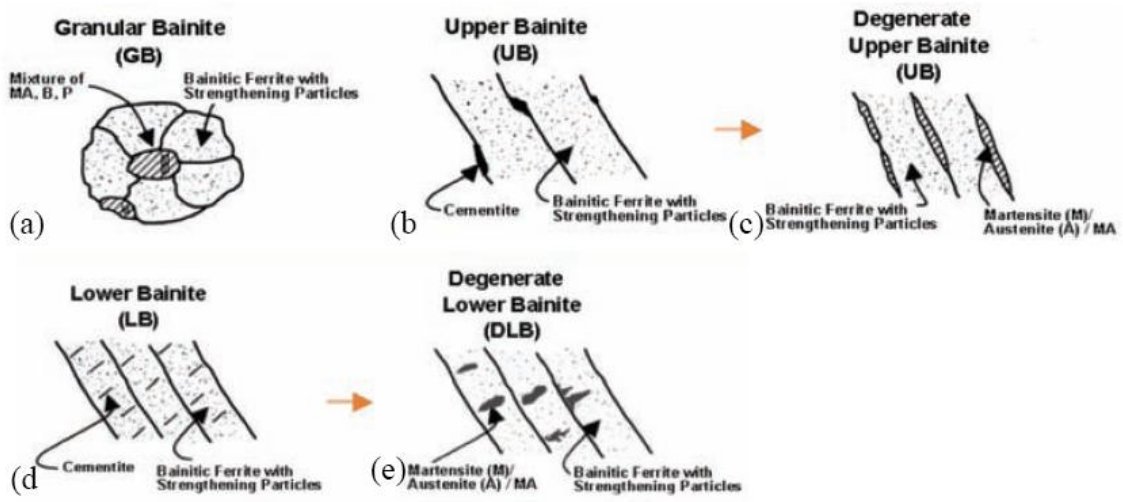

Figure 2.13 A schematic illustration of bainite morphologies in low carbon steel showing granular bainite (a) upper bainite; (b) degenerate upper bainite; (c) lower bainite; (d) and degenerate lower bainite (e).

The following is a brief description of the Zajac bainite classification system.

Granular bainite: A characteristic (though not unique) feature of granular bainite is the lack of carbides in the microstructure. The carbon that is partitioned from the bainitic ferrite stabilizes the residual austenite, so that the final microstructure contains both retained austenite and some high-carbon martensite along with the bainitic ferrite.

Upper bainite: ferritic laths with some carbides in between.

Degenerate upper bainite: In some steels, the cementite formation is prevented, and the microstructure is composed of ferritic lath with thin layers of retained austenite or martensite in between laths.

Lower bainite: carbides precipitate inside ferrite.

Degenerate lower bainite: carbides are prevented to form, and the retained austenite instead of carbides precipitate inside the ferrite.

Compared to ferrite, pearlite, and martensite, bainite is more complicated to recognize. Thus, the above definitions are often used by many researchers for different steels. But in low carbon high strength steels, for the consideration of toughness of steels, Zajac's definition is more useful to classify the types of bainite since MA (martensite-austenite constituent) is a sensitive factor for the toughness of low carbon high strength steels.

2.6.2 **The transformation from austenite to bainite**

In this section, thermodynamics and kinetics of bainite transformation are introduced. Zener[44] assumed the bainite growth for iron or other substitutional atoms is diffusionless. Carbon supersaturation in bainitic ferrite will be relieved by partitioning into residual austenite. However, unlike martensite, no strain energy exists during the growth of bainite. And bainite should form at a temperature just below T_0, where the austenite and ferrite have identical free energies, as shown in Figure 2.14[40]. The Ae3 is the temperature separating the $\alpha + \gamma$ and γ phase fields for a specific alloy. The Ae1 is the temperature separating the $\alpha + \gamma$ and α phase fields for a specific alloy. As shown in this figure, if the ferrite with some strain, the Gibbs free energy increases, and then, the corresponding T_0 will be changed to T_0'.

The results of atom probe experiments showed that there is no redistribution of substitutional solutes during the bainite transformation. For the martensitic transformation, it is simple to prove the martensitic transformation is diffusionless by measuring the chemical compositions before and after transformation. In bainite, it was found that interstitial atoms, especially the carbon atoms, still diffuse between bainitic ferrite and the remaining austenite.

Diffusionless growth requires that transformation occurs at a temperature below T0, when the free energy of bainite becomes less than that of austenite of the same composition. Growth without diffusion can only occur when carbon concentration of the austenite lies to the left of T0 curve, depicted in Figure 2.15.

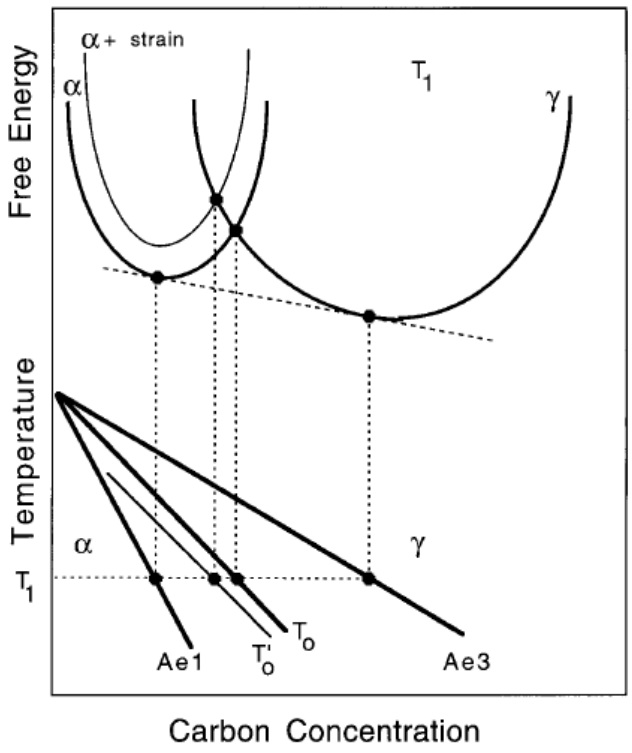

Figure 2.14 Schematic illustration of T_0 curve on the phase diagram[40]. T_0' curve incorporates a strain energy for the ferrite

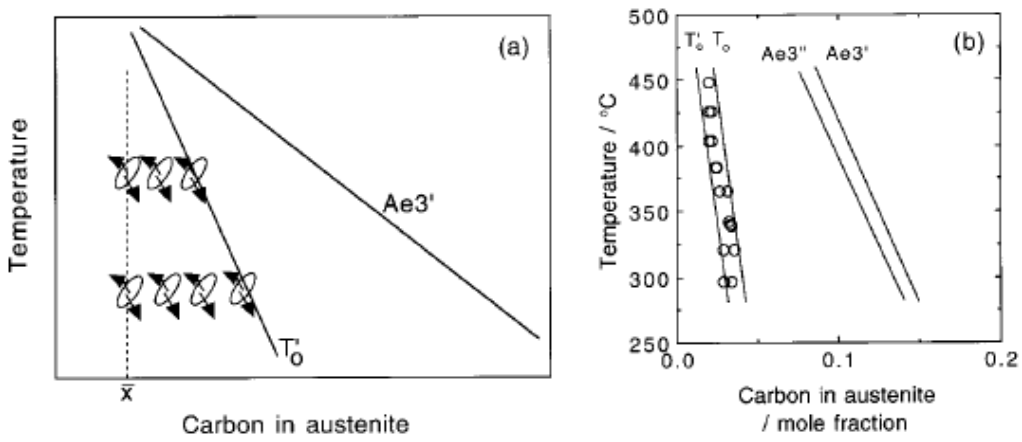

Figure 2.15 The incomplete reaction phenomenon[40] (a) A plate of bainite grows without diffusion, then partitions its excess carbon into the residual austenite. (b) Experimental data on the incomplete reaction phenomenon. Ae3' refers to the equilibrium (γ+α)/γ phase boundary and Ae3" refers to the same as Ae3' with accounting strain energy of α[45].

When the bainite forms without any diffusion of substitutional atoms, the supersaturated carbon will be rejected into residual austenite quickly. As shown in Figure 2.15[45], the next formation of bainite will be from carbon enriched austenite. When austenite concentration reaches the T0 curve, the bainite formation must cease. Thus, the bainite reaction is always incomplete. Experimental results provided evidence that the transformation to bainite does stop at the T0 boundary as indicated in Figure 2.15(b). The figure shows that austenite can accommodate more carbon at lower temperatures. In other words, the bainite reaction can proceed even if the residual austenite has more carbon.

Carbon plays a very important role in the bainitic reaction. Usually, T_0 is more important than Ae3 in bainitic steel design.

2.6.3 **The thermodynamics and kinetics in bainitic transformation**

In Figure 2.16, $x^{\alpha\gamma}$and $x^{\gamma\alpha}$ are the equilibrium compositions of ferrite and austenite respectively, by using the common tangent construction[40]. Suppose the austenite composition is $\bar{x}$ when it decomposes into the equilibrium mixture of ferrite and carbon enriched austenite (γ'), the change of Gibbs free energy is $\Delta G^{\gamma\rightarrow\alpha+\gamma'}$.

The equilibrium fraction of ferrite is $(x^{\gamma\alpha}-\bar{x})/(x^{\gamma\alpha}-x^{\alpha\gamma})$. According to Figure 2.16(a), the free energy change per mole of ferrite is

$$\Delta G_2 = \Delta G^{\gamma\rightarrow\alpha+\gamma'} \times \frac{x^{\gamma\alpha}-x^{\alpha\gamma}}{x^{\gamma\alpha}-\bar{x}} \tag{2.8}$$

The significant change of chemical composition of the austenite exists when it changes into ferrite and austenite. The calculation of the free energy change associated with nucleation must take into account a small amount of ferrite that is formed since it does not affect the composition of the remaining austenite. Consider the change ΔG_2 as austenite decomposes to a mixture of ferrite and enriched austenite of composition $x^{\gamma} = x^{\gamma\alpha}$. As the fraction of ferrite is reduced, x^{γ} and $\bar{x}$ move towards each other causing the line AB to tilt upwards. In the limit that $x^{\gamma}=\bar{x}$, AB becomes tangential to the curve at $\bar{x}$, as shown in Figure 2.16(b). The free energy change for the formation of ferrite nuclei of composition x^{α} is ΔG_3.

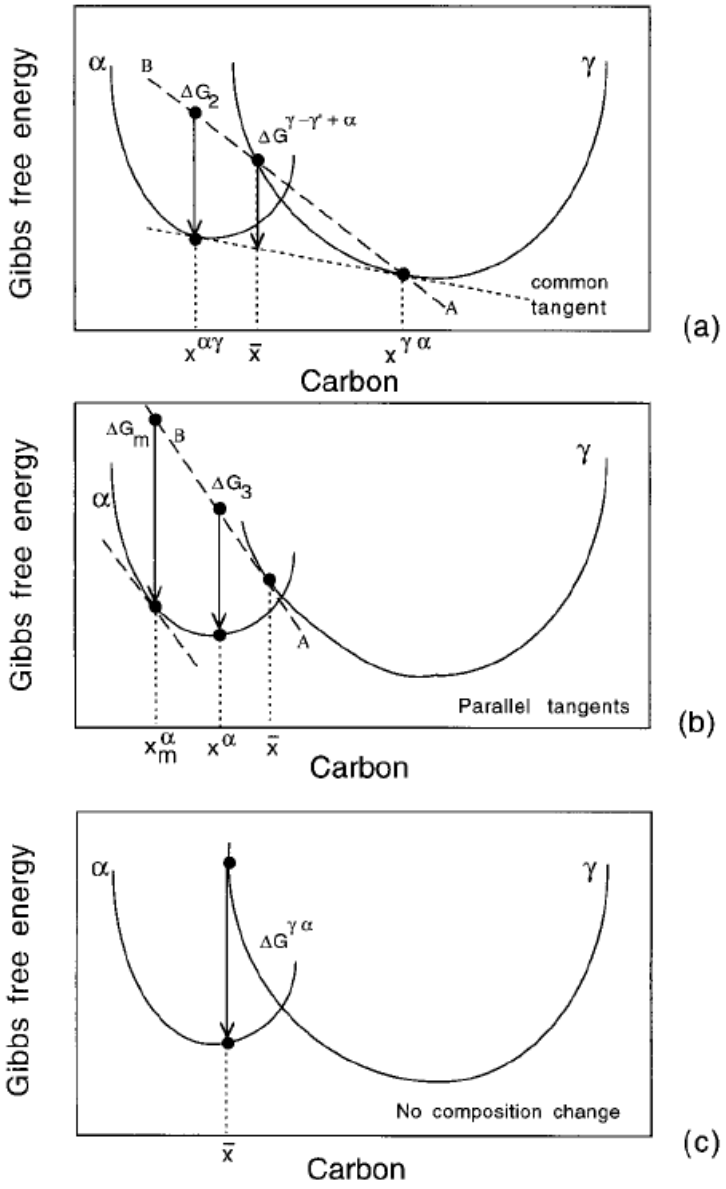

Figure 2.16 Schematic free energy diagram during the nucleation and growth of ferrite from austenite of composition $\bar{x}$

The greatest reduction in free energy during nucleation is obtained if the composition of the ferrite nucleus is set to a value x_m, given by a tangent to the ferrite free energy curve which is parallel to the tangent to the austenite free energy curve at $\bar{x}$. This maximum possible free energy change for nucleation is designated as ΔG_m.

A simplification is used when the transformation occurs without composition change, as shown in Figure 2.16(c). The change, $\Delta G^{\gamma \rightarrow \alpha}$, is the vertical distance between the austenite and ferrite free energy curves at the composition of interest.

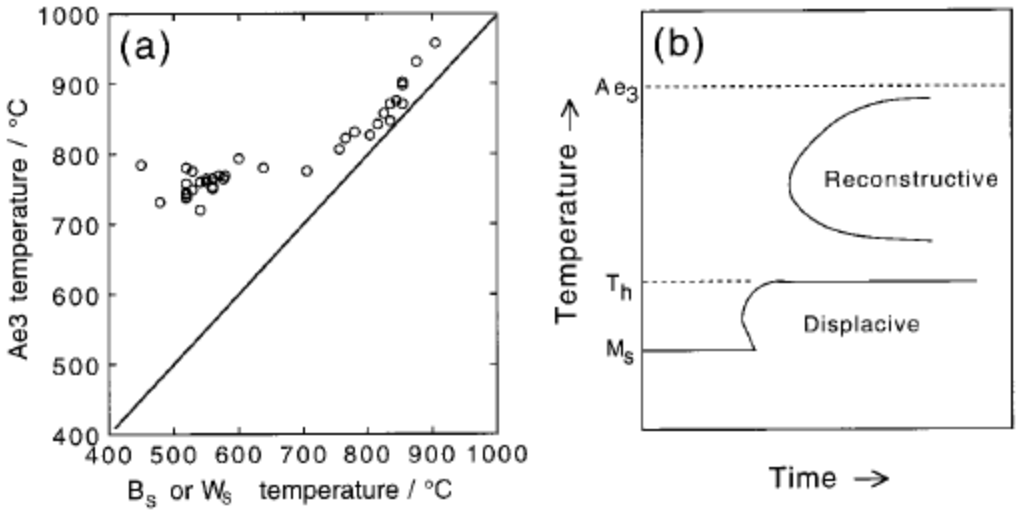

Figure 2.17 (a) Diagram illustrating the variation of the Widmanstätten ferrite start and bainite start temperatures as a function of the Ae3 temperature of the steel concerned[46]. (b) Schematic TTT diagram illustrating the two C curves and the T_h temperature.

Widmanstätten ferrite usually nucleates at austenite grain boundaries and grows as Widmanstätten side plates into austenite interior. It is accompanied by atoms reconstructive mode, thus it is considered a kind of ferrite morphology. Bainite have the identical nucleus. They are more sensitive to the steel composition than the Ae3 temperatures. That means the influence of solutes on the nucleation of Widmanstätten ferrite and bainite is more than just thermodynamic (Figure 2.17 (a)).

Figure 2.17 (b) illustrates the time-temperature-transformation diagrams, which consist essentially of two C-curves. The lower C-curve has a characteristic flat top at a temperature, T_h, which is the highest temperature at which ferrite can form by displacive transformation. The transformation product at T_h may be Widmanstätten ferrite or bainite. The driving force, ΔG_m, for nucleation at T_h is plotted in Figure 2.18(a). Each point came from a different steel. This analysis proves that carbon must partition during the nucleation stage in order to obtain a reduction in free energy. Figure 2.18(a) represents the free energy change, ΔG_m, at the temperature T_h where the displacive transformation first occurs. One equation calculated by Ali and Bhadeshia for G_N(which is regarded as the universal nucleation function) is given in the following equation[46]:

$$G_N = C_1(T - 273.18) - -C_2 \quad J\,mol^{-1} \tag{2.9}$$

where the fitting constants are found to be C_1=3.637 ±0.2 J mol-1K-1 and C_2 = 2540 ± 120 J mol-1 for the temperature range 670-920K. The definition of G_N is because the minimum driving force is necessary to achieve a perceptible nucleation rate for Widmanstätten ferrite or bainite in any steel.

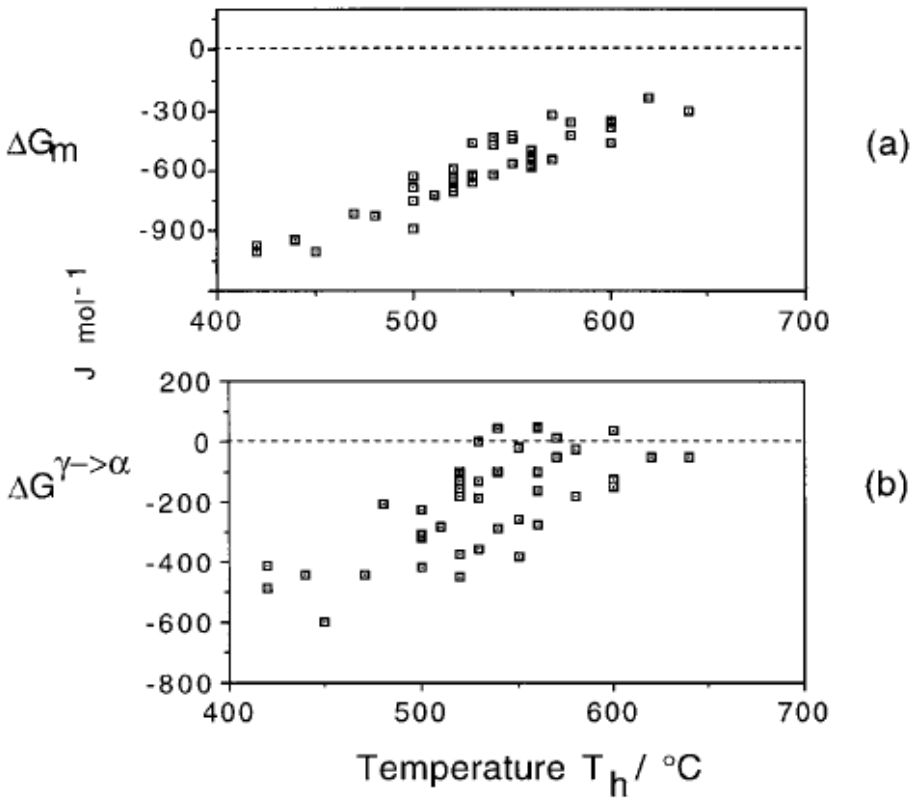

Figure 2.18 (a) The free energy change calculated assuming the partitioning of carbon occurs during the nucleation of ferrite. (b) The free energy change calculated assuming that the ferrite nucleus inherits the composition of the parent austenite.

The way to determine whether the nucleus evolves into bainite or Widmanstätten ferrite is straightforward. If diffusionless growth cannot be sustained at T_h then the nucleus develops into Widmanstätten ferrite. A larger undercooling is necessary before bainite can be stimulated. If the driving force at T_h is sufficient to account for diffusionless growth, Widmanstätten ferrite does not form at all.

Widmanstätten ferrite forms below the Ae3 temperature when:

$$\Delta G^{\gamma \rightarrow \gamma' + \alpha} < -G_{SW} \tag{2.10}$$

$$\Delta G_m < G_N \quad (2.11)$$

where G_{SW} is the stored energy of Widmanstätten ferrite (about 50 J mol^{-1}). The first of these conditions ensures that the chemical free energy change exceeds the stored energy of the Widmanstätten ferrite, and the second that there is a detectable nucleation rate[40].

Bainite is expected below the T_0' temperature when

$$\Delta G^{\gamma \rightarrow \gamma' + \alpha} < -G_{SW} \quad (2.12)$$

$$\Delta G_m < G_N \quad (2.13)$$

where G_{SB} is the stored energy of bainite (about 400 J mol^{-1}). The universal function, when used with these conditions, allows the calculation of the Widmanstätten ferrite and the bainite start temperatures from knowledge of thermodynamics alone.

In some steels, all three transformations can be found, but for other steels, only bainite and martensite, or only martensite is found. If bainite has a kinetic advantage, then Widmanstätten ferrite does not form. Further alloying increases the stability of the austenite, so the nucleation of Widmanstätten ferrite and bainite is suppressed to temperatures below the Ms, thus, only martensite can form.

2.7 INFLUENCE OF THE MA CONSTITUENT ON TOUGHNESS

The metallurgical factors for improvement of toughness are classified as follows: (1) refinement of effective grain size, (2) decrease in MA microconstituents and (3) reduction of impurities. The MA was first studied in heat affected zones (HAZ) in welding since people realized early that MA has a substantial effect on toughness of HAZ. Matsuda[47, 48] et al. showed that the Charpy transition temperature (DBTT) and Crack Tip Opening Displacement (CTOD) property are

linear functions of the fraction of MA constituent[48]. The deterioration of toughness by MA constituents occurs in any grade of steel, and both Charpy DBTT and critical CTOD property are reduced with increasing fractions of MA constituent. A few researchers reported that MA was insignificant to toughness in the fine structure [48].

2.7.1 **Mechanism of MA formation**

An accepted explanation of its formation [49] is that, on cooling from the austenitic state, carbon-free bainitic ferrite is formed and the remaining austenite is enriched in carbon and becomes stable. This enrichment is completed at about 350-400 ℃, with the carbon content of the remaining austenite reaching 0.5%-4.8%. On further cooling, part of this austenite decomposes into ferrite and carbide in the 300-350 ℃ temperature range. If the cooling is rapid enough, this decomposition does not happen. The undecomposed high carbon austenite transforms into lath and twin martensite at lower temperatures and a small amount of austenite is retained. This is the so-called MA constituent[50, 51].

The MA constituent is a harder second phase compared to the matrix. And the interface between the MA constituent and matrix is a source of cracks since stress concentration easily takes place in these areas. The MA constituent is formed preferentially at the grain boundary, and stress is more likely to be concentrated at the grain boundary region than at the intragranular region by dislocation pile up.

Moreover, the morphologies or sizes of MA are very important in that they have large differences for crack initiation and growth. When the MA constituent with an aspect ratio greater than four was defined as slender MA constituent, the slender MA constituent influenced the HAZ toughness more seriously than the total content of MA constituent as shown in Figure

2.19[48]. On the other hand, it has been proposed that the maximum size of the MA constituent is not a unique metallurgical factor which reduces the toughness. Mean free path and the statistical distribution of the MA constituents may have also a great influence on cleavage fracture toughness.

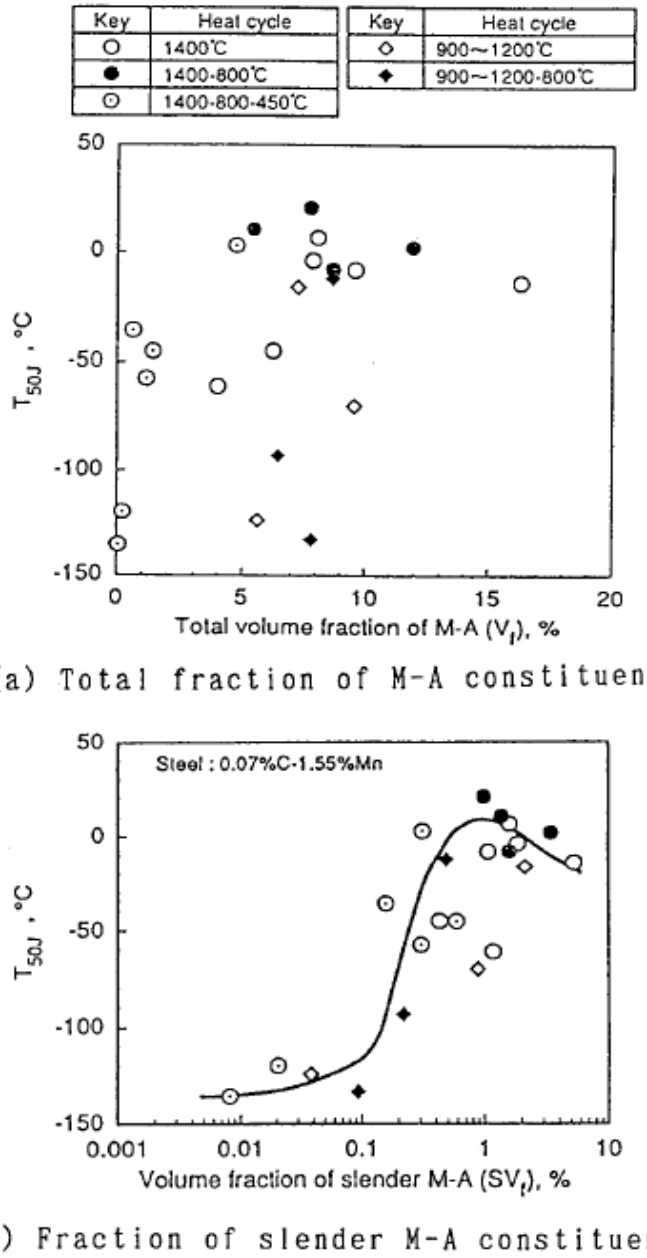

Figure 2.19 Effect of volume fraction of M-A constituent on LBZ toughness: (a) total fraction of M-A constituent and (b) fraction of slender M-A constituent[52].

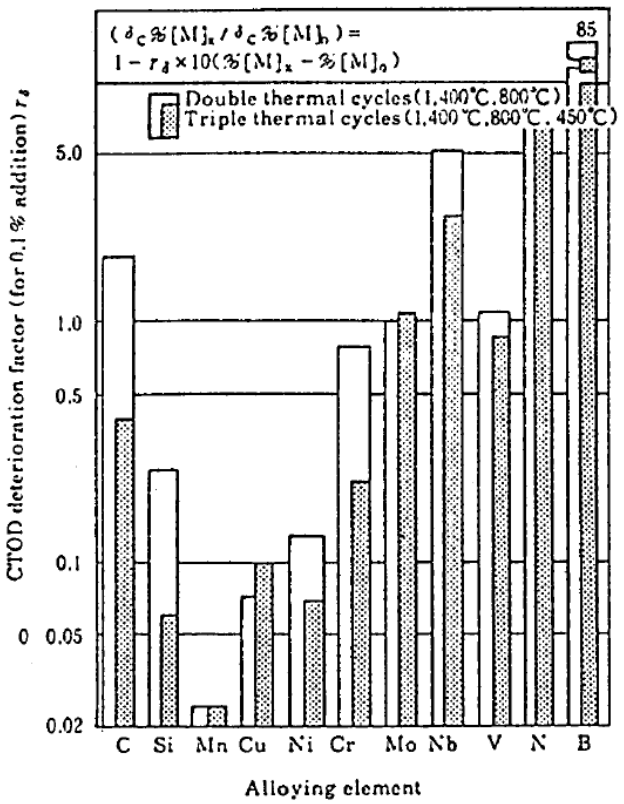

Figure 2.20 Comparison of alloying elements in terms of effect on CTOD[53]

2.7.2 **Effect of alloying elements on the MA formation**

In order to reduce the MA constituent, it is important to reduce the alloying elements which tend to form the MA constituent. The effect of elements on the MA constituent in the HAZ is shown in Figure 2.20. The MA constituent is formed more easily by adding B, N,C and carbide forming elements such as Mo, Nb and V, because carbide forming elements retard the diffusion of carbon during transformation from austenite to ferrite and, hence, retard the decomposition of the MA constituent. Moreover, it has been reported that these elements are easily segregated, which

leads to the formation of MA constituents. Segregation is classified into two categories: the first occurs during solidification for elements such as Mn, Ni, P and S. The second occurs during transformation from austenite to ferrite, and applies to elements such as C, N and B.

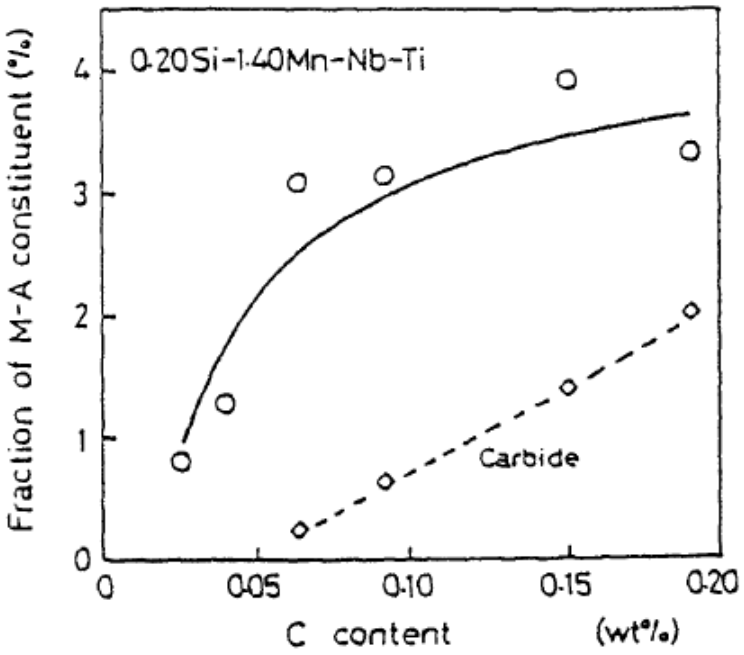

Figure 2.21 Effect of C content on fraction of M-A constituent

The effect of carbon content on the formation of the MA constituent has been reported in many papers[47, 48]. The carbon content in the MA constituent is almost independent of the carbon content of the matrix material. The estimated carbon content in the MA constituent is around 0.5-1.5mass%[48]. The carbon content greatly affects the volume fraction of both the MA constituents

and carbides. The volume fraction of the MA constituents and fine carbides both increase with carbon content, especially for low carbon steel, as shown in Figure 2.21[48].

Silicon is known to increase the MA constituent due to its ability to hinder carbide precipitation and, therefore, stabilize the MA phase against decomposition. In a similar fashion, aluminum is also reported to increase the MA constituent.

An increase in chemical compositions enhances the formation of the MA constituent in most cases. Since X120 steel is a high strength steel, with higher levels of manganese and other alloy elements needed to reach the expected strength, problems associated with MA cannot be unexpected.

2.7.3 **Effect of cooling rate on the MA formation**

Okada et al[48]., investigated the effect of cooling rate on the shape of the MA constituent in the HAZ of welds. The MA constituent is classified morphologically into two types: massive MA constituent and elongated MA constituent, as shown in Figure 2.22. The type of MA constituent changes with an increase in cooling time, as follows: elongated MA constituent, elongated MA constituent + massive MA constituent, elongated MA constituent + massive MA constituent + carbide.

Figure 2.23 shows the effect of cooling time on Charpy absorbed energy (vE) and area fraction of the MA constituent in the HAZ in an HT-80 steel. The toughness deteriorates for cooling times more than 50s, according to the formation of the MA constituent as the microstructure changes from martensite and lower bainite structure to upper bainite structure. But the authors also thought that the toughness of higher strength steel does not deteriorate with

increase in cooling time, because the upper bainite structure with the MA constituent does not form on account of high hardenability of steels.

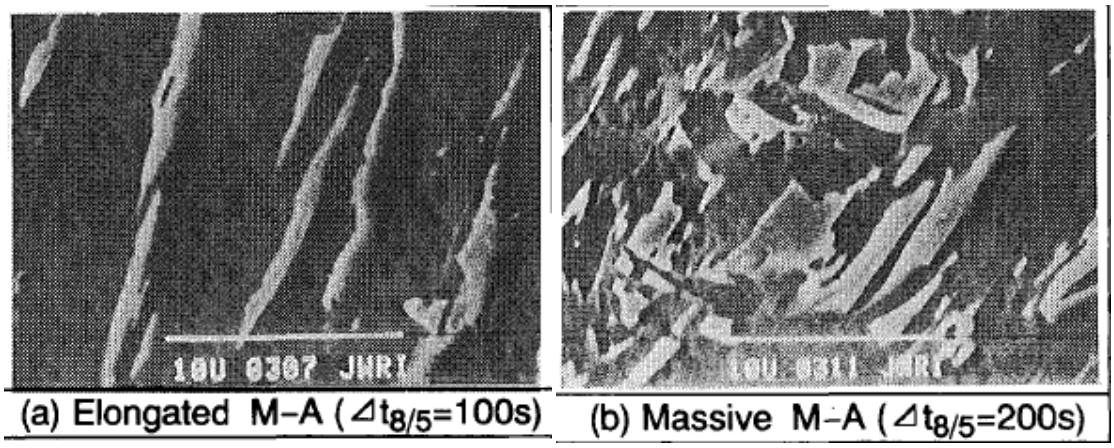

Figure 2.22 Examples of morphology of elongated M-A constituent and massive M-A constituent

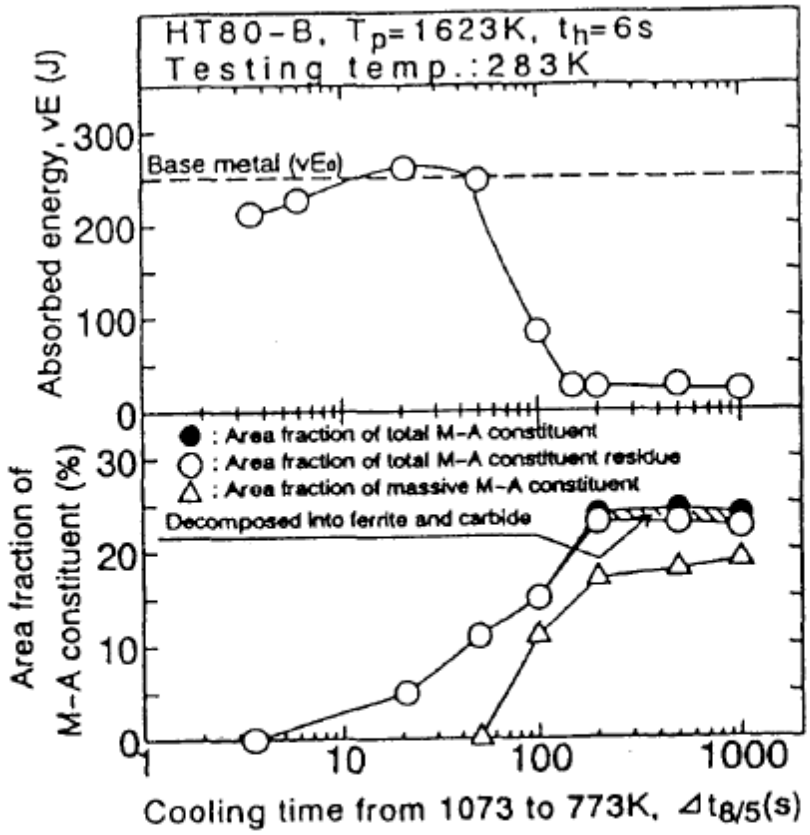

Figure 2.23 Relations between vE and $\Delta t_{8/5}$ and between fraction of M-A constituent and $\Delta t_{8/5}$ for HT-80 steel, HAZ

2.7.4 **Effect of thermomechanical processing on the formation of the MA constituent**

I.A. Yakubtsov et al.[54], did research on the effect of TMP on bainite transformation during continuous cooling of low carbon microalloyed steel. They studied a low carbon Nb-Ti microalloyed plate steel during a simulation of thermomechanical processing for hot rolling following by accelerated cooling. The deformation below the non-recrstallization temperature,

cooling rate, and interrupt temperature on the formation of different microstructures were determined. The results showed the evolution of conventional bainite, acicular ferrite and the MA constituent. However, the investigation of the MA was very minor. Thus, it is of interest to understand how TMP has an effect on the formation of MA in a low carbon high strength steel.

2.7.5 **Effect of finishing cooling temperatures on the formation of the MA constituents**

Cota and Santos studied the microstructure of HSLA low carbon steels. Figure 2.24 illustrated the formation of the MA constituents with different cooling rates and finishing cooling temperatures [55]. It shows that the increase in cooling rate or decrease in finish cooling temperature implies a decrease in the volume fraction and the average size of the MA islands.

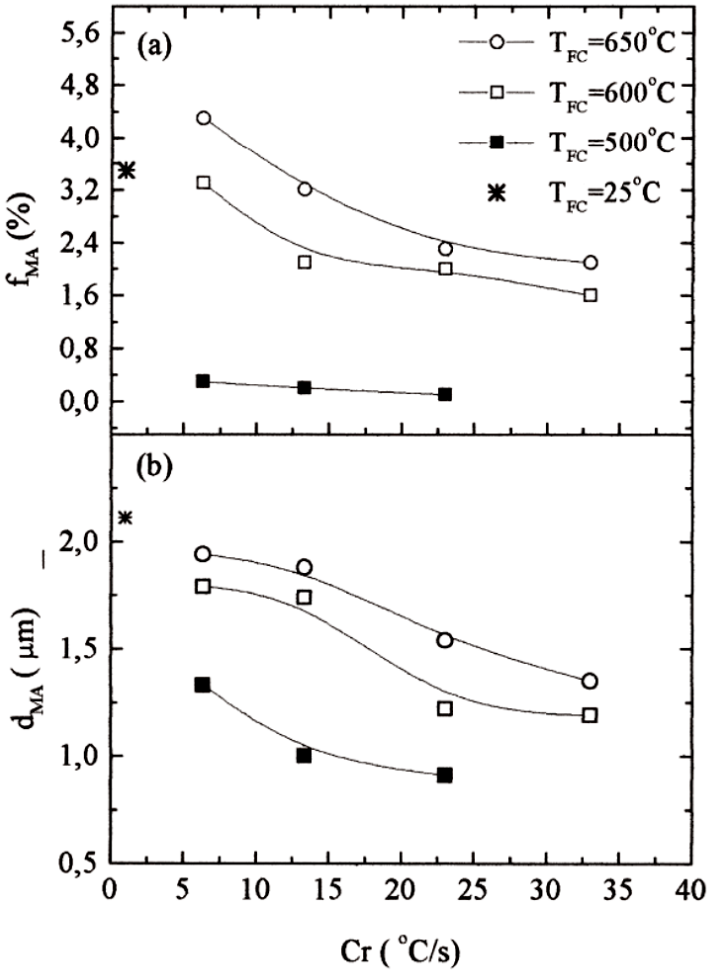

Figure 2.24 Influence of cooling rate on: (a) the volume fraction of the MA islands (f_{MA}); (b) the average size of the MA islands (d_{MA})

2.8 EFFECT OF PROCESSING ON TRANSFORMATION OF AUSTENITE TO FERRITE AND DEFORMATION INDUCED FERRITE TRANSFORMATION (DIFT)

The transformation temperature from austenite to ferrite, Ar3 is very relevant to processing. Isao Kozasu et al.[56], studied the effect of reductions on transformation temperatures of austenite to ferrite at different rolling temperatures, as shown in Figure 2.25. It shows that the different reductions below recrystallization temperature could have a range of 0 to 100℃ in increasing the Ar3. Manohar and Chandra investigated the change of Ar3 temperatures between deformed and undeformed steels containing manganese and silicon, and the change with different cooling rates, as shown in Figure 2.26[57]. The figure showed that deformation increased Ar3 temperature but faster cooling rate caused the decrease of Ar3. Some relevant work was conducted according to the processing, which is called Deformation Induced Ferrite Transformation (DIFT)[58-60]. A prominent feature of DIFT distinguished from static transformation without deformation is the addition of deformation stored energy into the transformation driving force, which leads to an increase in the Ae_3 and Ar_3.

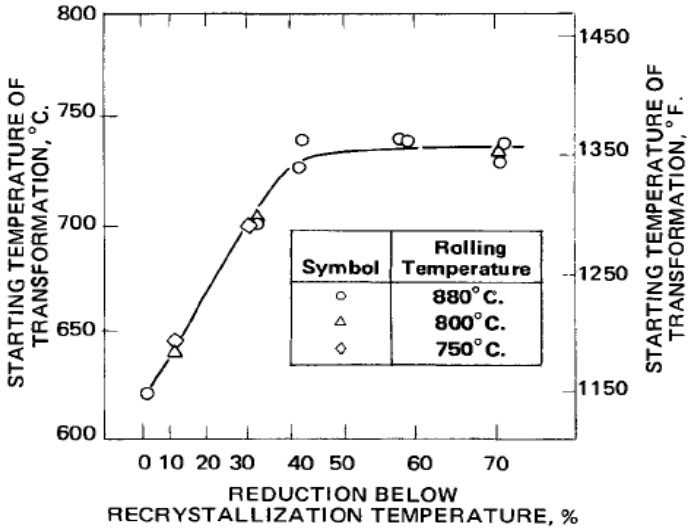

Figure 2.25 Variation of the austenite-to-ferrite transformation temperature of 0.03% Nb steel with the deformation below the austenitic-recrystallization temperature.

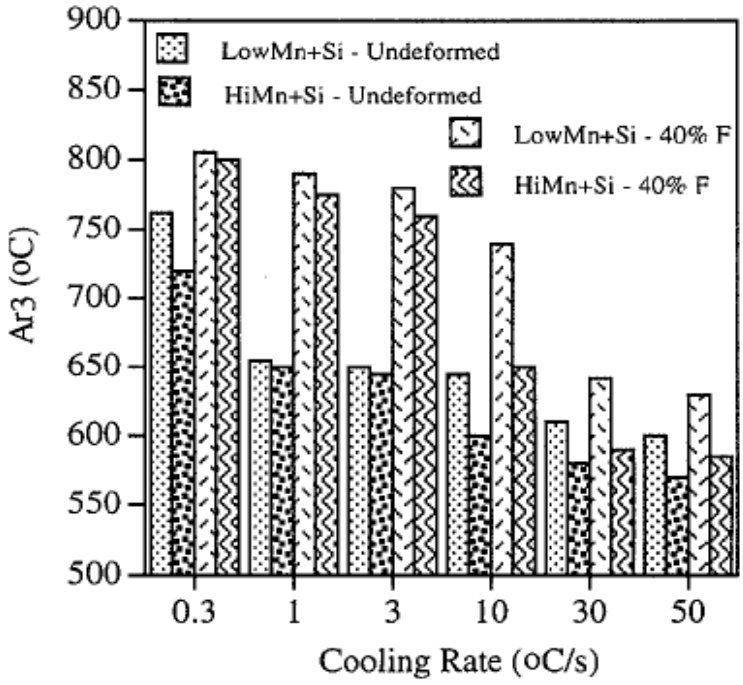

Figure 2.26 Effect of composition (Mn+Si) contents on Ar_3 temperature

The dynamic γ→α transformation has been extensively studied since 1990s. Although different names are used, such as "Strain-induced Transformation to Ferrite", "Deformation Induced Transformation", "Strain induced transformation", and "Strain induced dynamic transformation" and "Deformation Induced Ferrite Transformation", all these concepts have two common characteristics. First, the γ→α transformation occurs during deformation rather than during cooling after deformation. Second, ultrafine ferrite grains could be obtained through the transformation. The mechanism for DIFT is still not very clear. Han Dong et al. [58] summarized it as follows. Two typical opinions exist regarding the DIFT mechanism. One is a massive transformation mechanism proposed by H. Yada et al[61-63]. This mechanism does not involve long distance diffusion within austenite. The second opinion is the long range diffusion controlled transformation mechanism proposed by some researchers [64-66] (Qi, 2002; Du, 2002; Hurleg, 2001). This mechanism is essentially the same as that of pro-eutectoid ferrite transformation. Some experimental facts that support the transformation observation are discussed below:

1. The effect of alloying elements such as carbon and manganese on DIFT is the same as that on pro-eutectoid ferrite transformation, that is, the increase in the contents of C, Mn and Nb in solution can retard the transformation.
2. Carbides formed during DIFT are mainly distributed at austentite grain boundaries, which means the carbides precipitate from the remaining austenite which has been enriched in carbon during the transformation[64].
3. The hardenability of retained austenite after DIFT is increased compared with that of the initial austenite. This indicates that retained austenite is enriched in alloying elements, especially the carbon in steel[66].

4. A transition zone existing within the austenite in front of the γ/α boundary is observed by SEM. This zone is thought to be due to the enrichment of carbon in front of the γ/α boundary[65].

The processing changes the stored energy of steel, and thus the diffusion rate of alloy elements will be different, which results in deformation induced ferrite transformation (DIFT). In our present study, the DIFT is not of our interest; however, the diffusion of interstitial elements such as carbon, nitrogen and boron is interesting. The evidence of DIFT is introduced to prove that the deformation and the holding time after deformation may affect the carbon partitioning and the enrichment of carbon in the remaining austenite. Thus, the volume fraction, the size and the morphology of MA constituents may be affected. And also different types of bainite may be obtained after transformation. The model of carbon partitioning during transformation is presented.

2.9 PARTITIONING OF CARBON AND OTHER ALLOYING ELEMENTS DURING THE AUSTENITE DECOMPOSITION IN STEELS [24]

Due to the different solubility of alloying elements in austenite and ferrite, elements often have partitioning phenomena during transformation from austenite to ferrite. The extent of elements partitioning mainly depends on the diffusion rate of elements. The solubility ($C^{\alpha\gamma}$) for carbon in ferrite is lower than that in austenite ($C^{\gamma\alpha}$), so carbon is partitioned into the latter. As the ferrite grows, so does the extent of its diffusion field in the austenite. This retards growth because the solute then has to diffuse over larger distances. Bhadeshia and Honeycombe[24] described the models as follows.

For isothermal transformation in a plain carbon steel, the concentrations at the interface are given by a tie-line of the phase diagram, as shown in Figure 2.27. The diffusion flux of solute from the interface must equal the rate at which solute is incorporated in the ferrite so that:

$$(c^{\alpha\gamma} - c^{\gamma\alpha})\frac{\partial z^*}{\partial t} = -D_C^{\gamma}\frac{\partial c}{\partial z} \approx D_C^{\gamma}\frac{\bar{c}-c^{\gamma\alpha}}{\Delta z} \tag{2.14}$$

The left side of equation is the rate solute partitioned, and the middle one is the diffusion flux from interface. Following Zener, it is assumed in the derivation that the concentration gradient in the matrix is constant, and the far-field concentration, $\bar{C}$, never changes. z is a coordinate normal to the interface with a value z* at the position of the interface.

A second equation can be derived by considering the overall conservation of mass:

$$(c^{\alpha\gamma} - \bar{c})z^* = \frac{1}{2}(\bar{c} - c^{\gamma\alpha})\Delta z \tag{2.15}$$

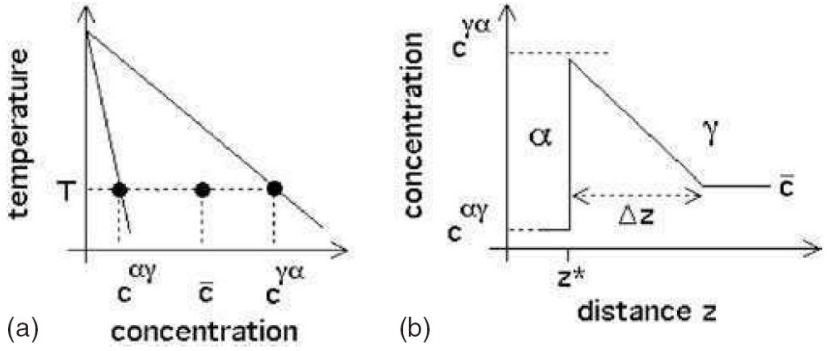

Figure 2.27 Phase diagram and its relationship to the concentration profile at the ferrite/austenite interface during diffusion-controlled growth

On combining these expressions to eliminate Δz, we get:

$$\frac{\partial z^*}{\partial t} = \frac{D_C^\gamma (\bar{c} - c^{\gamma\alpha})^2}{2z^*(c^{\alpha\gamma} - c^{\gamma\alpha})(c^{\alpha\gamma} - \bar{c})} \tag{2.16}$$

It follows that:

$$z^* = \frac{(\bar{c} - c^{\gamma\alpha})}{[2(c^{\alpha\gamma} - c^{\gamma\alpha})(c^{\alpha\gamma} - \bar{c})]^{1/2}} \times \sqrt{D_C^\gamma t} \tag{2.17}$$

Consider Fe-Mn-C ternary steel; it would be necessary to satisfy two equations of the form of Equation 2.14, simultaneously, for each of the solutes:

$$\left(c_{\mathrm{C}}^{\gamma\alpha} - c_{\mathrm{C}}^{\alpha\gamma}\right)v = -D_{\mathrm{C}}^{\gamma} \nabla c_{\mathrm{C}} \tag{2.18}$$

$$\left(c_{\mathrm{Mn}}^{\gamma\alpha} - c_{\mathrm{Mn}}^{\alpha\gamma}\right)v = -D_{\mathrm{Mn}}^{\gamma} \nabla c_{\mathrm{Mn}} \tag{2.19}$$

Since $D_C^\gamma \gg D_{Mn}^\gamma$, these equations cannot be simultaneously satisfied for the tie-line passing through the alloy composition $\bar{c}_C, \bar{c}_{Mn}$. If the tie-line is such that $c^{\gamma\alpha} = \bar{c}_C$ (e.g. line *cd* for alloy A of (a)), then ∇c_C will become very small, the driving force for carbon diffusion in effect being reduced, so that the flux of carbon atoms is forced to slow down to a rate consistent with the diffusion of manganese. This mechanism is called "Partitioning, Local Equilibrium" (or PLE) mechanism. However, ${c_{Mn}}^{\alpha\gamma}$ can differ significantly from $\bar{c}_{Mn}$, giving considerable partitioning and long-range diffusion of manganese into the austenite.

Another mechanism is called a "Negligible Partitioning, Local Equilibrium" (or NPLE). It is shown in Figure 2.28(b). The tie-line cd allows ${c_{Mn}}^{\alpha\gamma} \rightarrow \bar{c}_{Mn}$, so that ∇c_{Mn} is drastically increased since only very small amounts of Mn are partitioned into the austenite. The flux of manganese atoms at the interface correspondingly increases and manganese diffusion can then keep pace with that of carbon, satisfying the mass conservation conditions of Equations 2.18&2.19.

So during transformation from austenite to ferrite, ferrite can grow by two mechanisms: low supersaturation mode, the PLE mode, and high supersaturation mode, the NPLE mode.

Para-equilibrium is a constrained equilibrium. It occurs at temperatures where the diffusion of substitutional solutes is not possible within the time scale of the experiment. Nevertheless, interstitials may remain highly mobile. Thus, in steel, manganese does not partition between the ferrite and austenite, but is subject to that constraint. The carbon redistributes until it has the same chemical potential in both phases. Thus, the tie lines are horizontal because Mn does not partition between ferrite and austenite (Figure 2.29).

Since steel transformation during or after hot rolling is mostly para-equilibrium or non-equilibrium, then partitioning of carbon is very important for transformation and mechanical properties of steels.

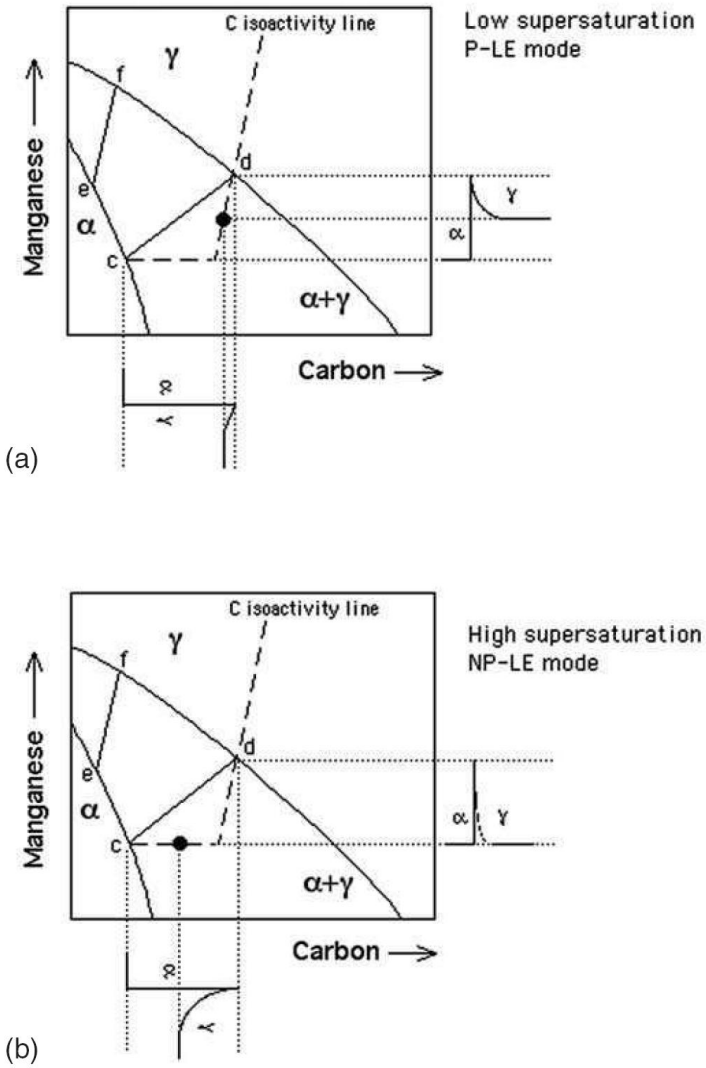

Figure 2.28 Schematic isothermal sections of the Fe-Mn-C system, illustrating ferrite growth occurring with local equilibrium at the α/γ interface. (a) Growth at low supersaturations(PLE) with bulk redistribution of manganese, (b) growth at high supersaturations (NPLE) with negiligible partitioning of manganese during transformation. The bulk alloy compositions are designated by the symbol • in each case.

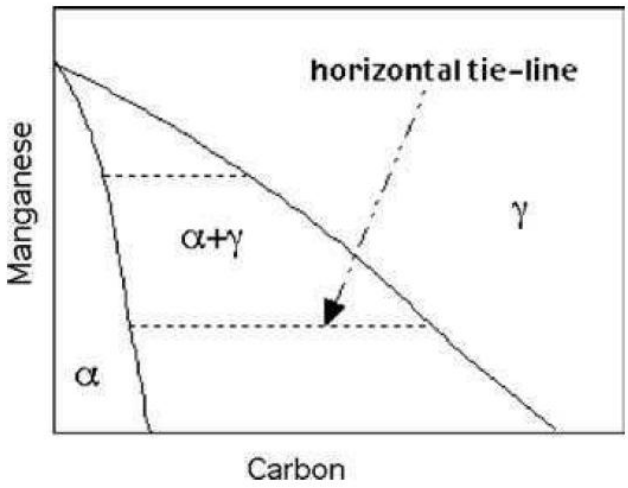

Figure 2.29 A para-equilibrium phase diagram

2.10 EFFECT OF ALLOYING ELEMENTS ON THE DESIGN OF HIGH GRADE LINEPIPE STEELS

2.10.1 **Carbon**

In an earlier time, carbon was a preferred element for improving strength. But later, substantial research showed that high carbon contents brought some severe problems for steels, that is, toughness of steels and the weldability. Since for high grade linepipe steels, toughness and weldability are two important factors, carbon is expected to be as low as possible. In another aspect, however, some carbon content should be guaranteed for two reasons: (1) solid solution strengthening in steels; (2) a part of carbon atoms combine with microalloyed elements, which can retard recrystallization at high temperatures and form precipitates at lower temperatures.

Low carbon is easier for solution of vanadium, niobium during reheating, but carbon needs to strengthen bainite and martensite in steel. Thus, carbon between 0.01~0.06wt% is the preferred range for linepipe steel, because it has been shown in many results that this type of steel will not discompose into ferrite and cementite during cooling after hot rolling. Supercooled austenite will form directly to different morphological ferrite and some martensite-austenite constituent. Due to carbon reduction in steel, the weldability of steel is much improved. It is well established that decrease of C content results in reduction of volume fraction of MA constituents, which improves the toughness.

2.10.2 **Manganese**

Manganese is a commonly used element in steels. Manganese in solid solution increases strength. In addition to solid solution strengthening, manganese is also a strong austenite stabilizer, thus it lowers the Ar3 temperatures, which may hinder high temperature transformations such as ferrite. Then it increases the hardenability of steels. Some studies have shown that Mn can also lower the bainite start transformation temperature. Thus, it is more possible to form lower bainite, the type of bainite which has better toughness.

However, manganese segregation is usually a problem for transformation since manganese segregation happens during solidification of steel. Thus, a banded structure is usually seen in steels after hot rolling. Then, this kind of banded structure may deteriorate the toughness of steel.

2.10.3 **Mo, Cr and V**

The effect of Mo, Cr, V on strength and toughness were studied by S.Y. Han et al [49] in X80 linepipe steel. The results showed that Cr, Mo, and V increase the pearlite start temperature (Ps) and decrease the bainite start temperature (Bs); Mo is an element for enhanced hardenability, interrupting the carbon diffusion by raising the diffusion activation energy of carbon. The Mo addition prevents the formation of upper bainite and coarse granular bainite (GB), promotes acicular ferrite and small GB formation, and makes the microstructures dense and the grains fine by reducing the Bs.

The addition of chromium (0.3wt%) increases tensile strength and decreases upper shelf energy, because it has the ability to increase the volume fraction of second phases such as MA constituents. The authors compared the steel containing Cr and without Cr, higher volume fraction of GB and MA were found in the Cr containing steel[49].

Therefore, for enhanced low-temperature toughness, it is required to refine grains by adding Mo and V, and to reduce the volume fraction of GB and secondary phases by lowering the Cr content, and to reduce the effective grain size by preventing the formation of coarse GB.[49]

2.10.4 **Ti and Nb**

Titanium and niobium are two important microalloying elements in thermomechanical processing of steels. Titanium is an element, which exhibits a strong tendency to form oxides and sulfides as well as nitrides and carbides. Even titanium nitride, considering most typical nitrogen levels in steel, will be formed before or during solidification. Such particles, already formed in

the liquid steel, can be separated into the slag and have no effect on the properties of the steel. If not, they are relatively large as a result of their high formation temperature and must be considered as inclusions, having a ductility-impairing effect on the steel properties.

The lower is the content of oxygen, nitrogen or titanium, , the lower will be the temperature for TiN formation, resulting in a finer size of precipitates. Finely distributed and stable particles are able to control the austenite grain size during reheating and this effect is used during hot rolling. The presence of fine TiN refines the grain coarsened heat affected zone during welding. Only about 0.01wt% titanium can effectively retard austenite grain coarsening to 1250℃ or higher[67].

During rolling, niobium retards the recovery and recrystallization processes which form the basis for thermomechanical treatments, and its effectiveness in small amounts distinguishes it from other microalloying elements[68]. The solute drag effect of niobium and precipitates of niobium carbides retards recrystallization of austenite. Thus, it increases recrystallization temperatures, and, since the non-recrystalliztion region is large, the deformation can be easily conducted in this region which obtains pancaked austenite grain.

2.10.5 **Boron**

Boron is a very effective element for hardenability. Only 10-15ppm boron (solute) can increase hardenability significantly. Boron not only increases hardenability of steels, but also lowers the transformation temperatures for bainite [10, 69]. As shown in Figure 2.30[10], the Bs temperature was reduced about 100℃ with a 9ppm boron addition. Therefore, this may be beneficial to the formation of lower bainite. Figure 2.31 shows the toughness of HAZ in boron added and boron free steels. Boron is a very effective element to control lower bainite and upper bainite.

However, boron has a strong tendency to form carbides together with iron. The big carbides precipitate on austenite grain boundaries, which deteriorate toughness significantly in steel. Thus, it is of importance to control the concentration of carbon and boron in steel.

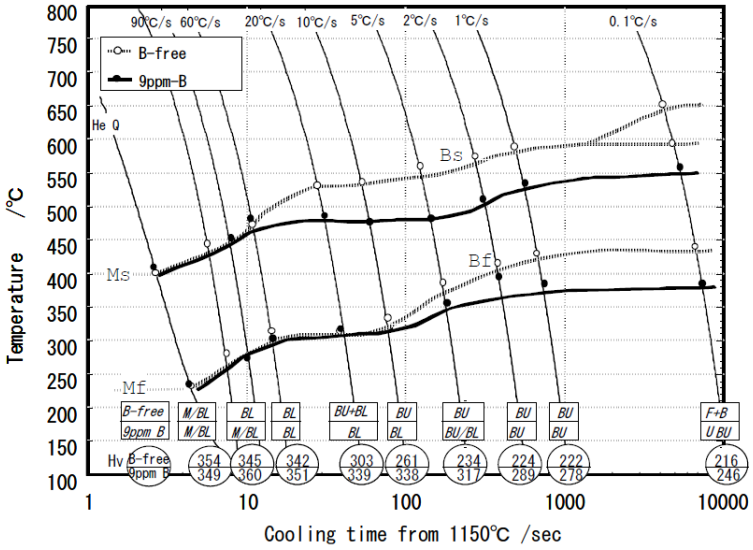

Figure 2.30 Continuous cooling transformation diagram of B steel and B-free steel

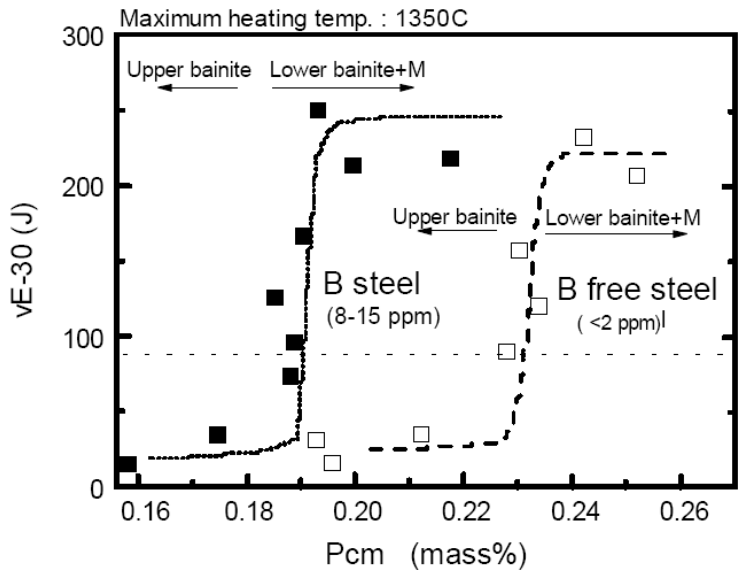

Figure 2.31 Effect of Pcm value on toughness of synthetic HAZ in boron added and boron free steels

2.11 GRAIN BOUNDARY CHARACTER DISTRIBUTION

Many properties are well known to be affected by microstructures. Especially, properties such as fracture, corrosion and oxidation preferentially occur along grain boundaries. Since the 1950s, grain boundary properties have been found to depend strongly on the grain boundary character and structure. Watanabe proposed the concept of grain boundary design in 1980 and introduced the parameter called the "grain boundary character distribution" (GBCD) as a ranking parameter of grain boundary engineering[70]. Recently, coincident site lattice (CSL) boundaries have been studied and found to play important role in texture, fracture, corrosion, etc., in many types of alloys[70-73].

The concept of the coincident site lattice (CSL) was proposed by Kronberg and Wilson in 1949[74]. In the CSL description, two interpenetrating crystal lattices are considered. If the points

in the two lattices coincide, then these points form the coincident site lattice. Symbol Σ is used to describe the reciprocal of the ratio of CSL sites to lattice sites. The quantity of Σ is defined as:

$$\Sigma=\frac{\text{volume elemetary cell of CSL}}{\text{volume elementry cell of crystal lattice}}$$

As an example, for the rotation 36.9 °<100>, $\Sigma=\frac{a(a\sqrt{5})^2}{a^3}=5$, as shown in Figure 2.32[36].

In general, no simple orientation relationship exists between grains. Thus, Σ is usually large, and the grain boundaries have no special properties, which is often called random boundaries.

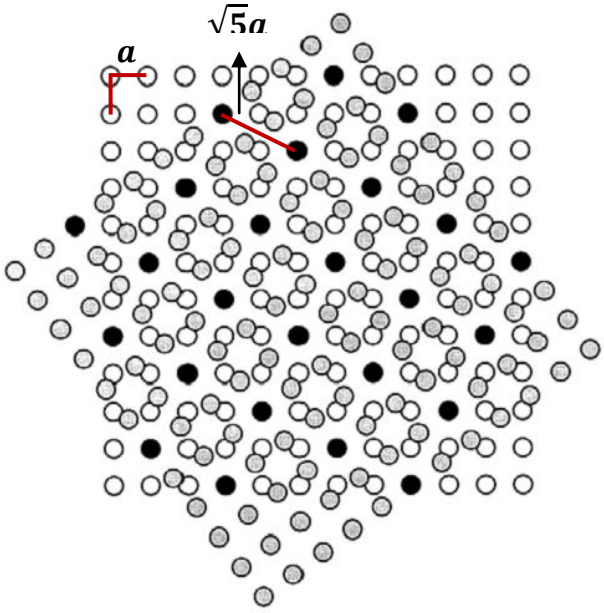

Figure 2.32 A coincident site lattice (Σ5) formed from two simple cubic lattices rotated by 36.9 ° about an <001> axis. Black solid circles are common sites of both lattices[36].

The CSL is a geometric relationship and any deviation from the exact coincidence relationship will destroy the CSL. But the special properties of a CSL boundary can still be maintained even if a little angle, $\Delta\theta$, deviates from the exact relationship. Therefore, it is important to define the angle $\Delta\theta$. This angular deviation limit is often taken as the Brandon criterion[75]

$$\Delta\theta \leq 15\Sigma^{-1/2} \tag{2.20}$$

Based on the Σ value, three different grain boundaries are classified. The first one is Σ1 grain boundaries. Σ1 means the low angle grain boundaries(<15°), is usually caused by dislocations. The second is the low Σ CSL grain boundaries, from Σ 3 up to Σ 29, which are called special CSL grain boundaries. In most papers and in the dissertation, CSL grain boundaries are specially denoted for these special CSL grain boundaries. Random grain boundaries are the third type with Σ value higher than Σ29.

On the consideration of the three types of grain boundaries, the energy of the boundaries is expected to be different. The energy of the boundary would be a minimum for an exact coincidence relationship. And the energy would increase when the orientation deviated from the perfect coincidence. Figure 2.33 shows the energy distribution with the variety of misorientations[76]. It can be seen that low energy are found for Σ3 and Σ11. However, the predicted low energy for Σ5 and Σ9 are not detected. While more recent measurements make it acceptable that the random grain boundaries have higher energy than low angle and CSL boundaries.

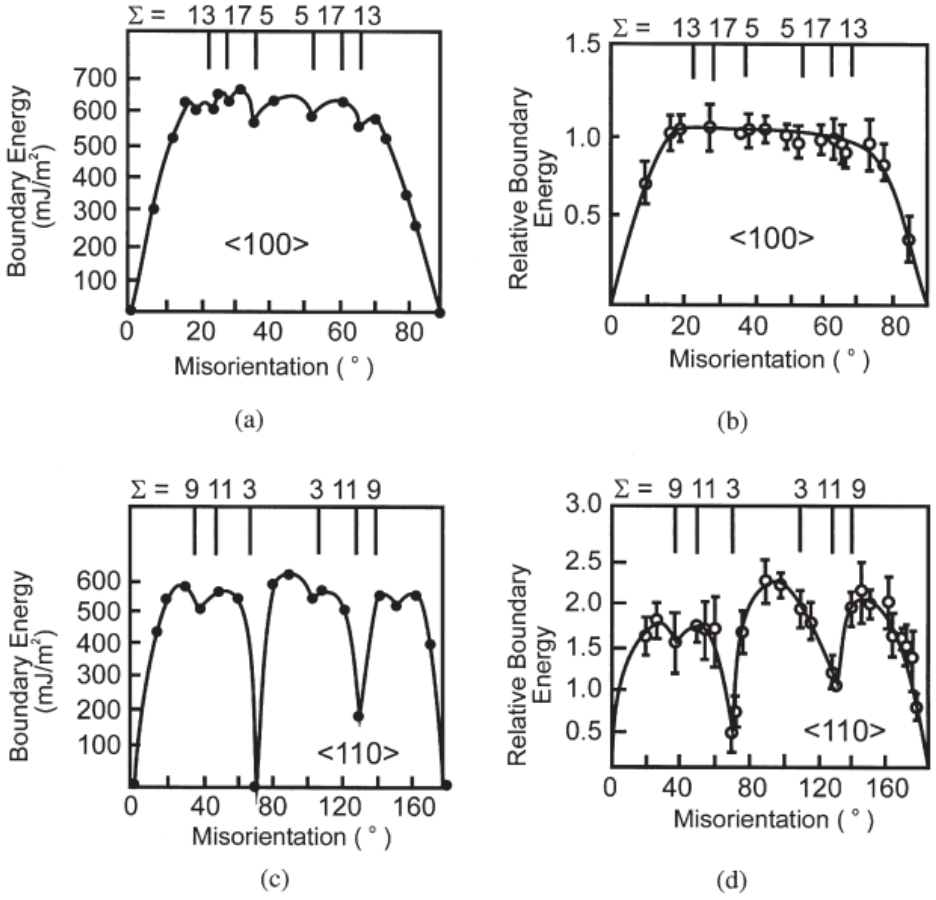

Figure 2.33 The computed (a) and (c) and measured (b) and (d) energies at 650C for symmetrical <100> and <110> tilt boundaries in aluminum[76].

3.0 STATEMENT OF OBJECTIVES

A substantial amount of research but most in CGHAZ not base plate has been conducted on the formation of MA constituents and their effect on toughness. Understanding the formation, size and volume fraction of MA constituents is especially important for controlling the toughness and the weldability or susceptibility to cold cracking of steels with high carbon contents or high carbon equivalent (CE) combinations. Recently, some studies have been conducted on the impact toughness (CVN and DWTT) of low carbon linepipe steels[77-81], especially for X70 and X80 steels. However, for the higher grade linepipe steel, such as API X100 and X120, MA constituents may be one of the very important factors for the toughness, as well as the effective grain size. There seems to be a lack of systematic information concerning the effect of MA in very low carbon steels. MA constituents might be the source of crack initiation sites, which reduces the toughness of high strength steels. Questions regarding the formation of MA constituent in very low carbon steel and how these microconstituents affect the toughness are still not very clear, especially for the very low carbon high strength steel with relatively high Mn contents.

The first objective of this study is to investigate the role of thermomechanical processing parameters such as the amount of strain prior to and after the $\gamma \rightarrow \alpha$ transformation temperature, the delay time and cooling rate on the onset of MA formation. . This part of the work will be conducted with the aid of the high temperature computer-controlled MTS deformation system.

The second part of this work will be directed to minimize the formation, the morphology and volume fraction of MA constituents. Due to the importance of austenite grain state, the factors that affect it, such as composition, microstructural state, i.e., fully recrystallized and/or unrecrystallized, and transformation behavior due to carbon partitioning will be central to the objective of this thesis.

The second objective of this thesis will be the systematic characterization of the bainite transformation and MA microconstituents by using Orientation Imaging Microscopy (OIM®) techniques (EBSD) and TEM.

4.0 EXPERIMENTAL PROCEDURE

4.1 CHEMICAL COMPOSITIONS AND THERMOMECHANICAL PROCESSING

Four different types of steel were used to study the austenite grain coarsening or the recrystallization temperatures. It is considered into two groups. The group 1 contains steel 1A and 1B. The group 2 contains steel 61A and 61C. The compositions are shown in Table 4.1.

Table 4.1 Chemical compositions of steels, wt%

	C	Si	Mn	P	S	Al	Ni	Cu	Mo	Nb	Ti	Cr	B	Ceq*	Pcm**
1A	0.056	0.30	1.96	0.01	0.002	0.025	0.25	0.251	0.25	0.04	0.01	0.30	0.0008	0.527	0.217
1B	0.058	0.30	1.91	0.01	0.002	0.027	0.25	0.155	0.15	0.04	-	0.50	-	0.535	0.211
61A	0.068	0.25	0.94	0.01	0.002	0.023	-	-	0.15	0.048	0.01	0.19	-	0.293	0.143
61C	0.089	0.25	0.94	0.01	0.002	0.024	-	-	0.15	0.049	0.01	0.51	-	0.377	0.180

Table 4.2 Chemical compositions of steels, wt%

	C	Mn	P	S	Si	Cu	Ni	Cr	Mo	Ti	Al	N	Nb	B
A	0.062	1.930	0.009	0.0016	0.300	0.243	0.244	0.298	0.149	<.001	0.030	0.0040	0.040	0.0004
B	0.062	1.892	0.009	0.0016	0.292	0.241	0.242	0.492	0.244	0.009	0.029	0.0046	0.039	0.0005
C	0.062	1.874	0.009	0.0016	0.291	0.242	0.450	0.490	0.380	0.009	0.032	0.0042	0.040	0.0063

Three main compositions were designed for hot rolling, as shown in Table 4.2. A 150kg split heat was melted in a vacuum induction furnace in the USS steel lab. The heat was split into three heats of 50kg each, respectively.

Thermomechanical processing was simulated in the MTS system. Figure 4.1 is a photo of a part of the MTS system. This system, Model MTS 458, contains a quartz filament furnace with 12*1200 watt halogen quartz infrared bulbs and parabolic reflectors. The entire system includes three parts: (a) heating system; (b) hydraulic system; (c) cooling system. The maximum heating rate of this furnace for standard compression specimens is about 10℃/s. The motion of the dies indicated by (b) in Figure 4.2 is controlled by a hydraulic system, which can provide 227 MN(million Newton) maximum load. And the range of the strain rate for the system is from $0.01s^{-1}$ to $60s^{-1}$. The work of the cooling system is schematically shown in Figure 4.2. Compressed air or helium is used for cooling the specimens after deformation. By using compressed air, the cooling rate can reach 10℃/s, and for helium, the cooling rate can reach 40℃/s.

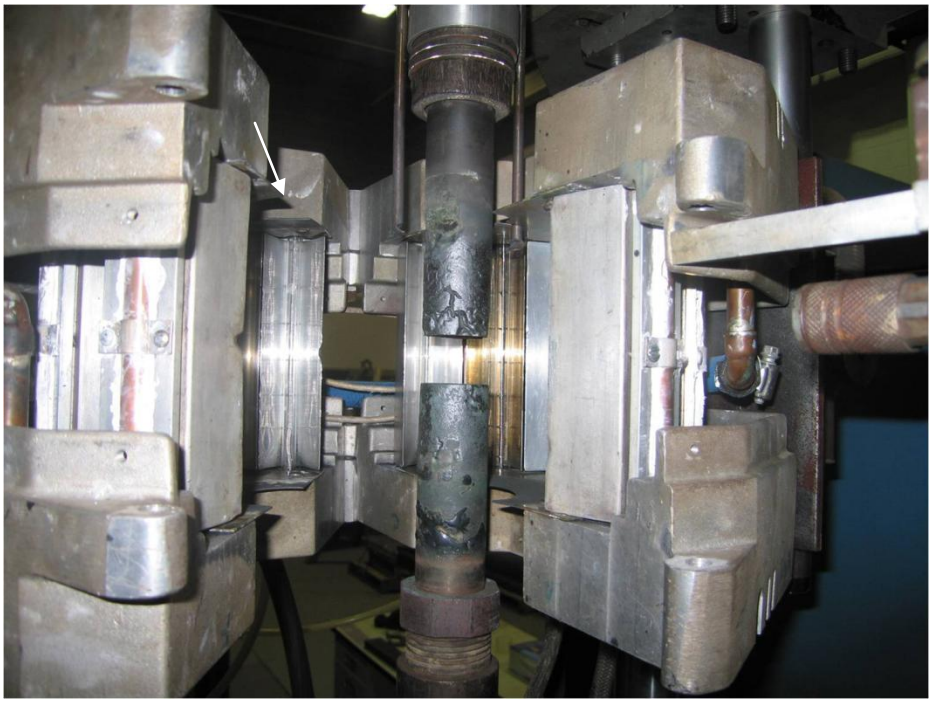

Figure 4.1 MTS system (a) heating system; (b) hydraulic system; (c) cooling system

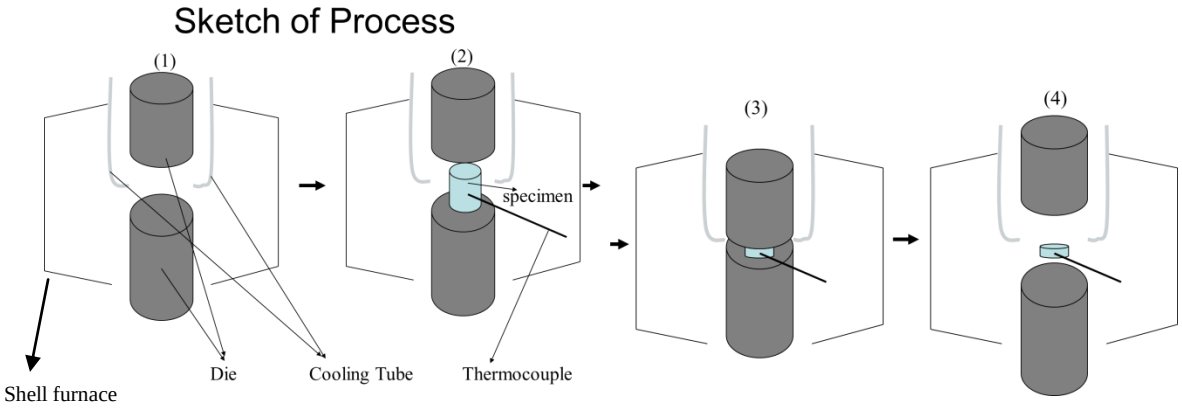

Figure 4.2 Schematical digrams of hot compresion tests

Specimens: the dimension of a standard compression specimen is 12.7mm in diameter and 19.1mm in height. An additional modification was made to the geometry of the cylinders in order to minimize die-specimen friction effects[82]. This is known as the modified Rastegaev's design[83], which prevents friction and barreling effects by addition of lubricant during deformation. The shape of the compression specimen is shown in Figure 4.3.

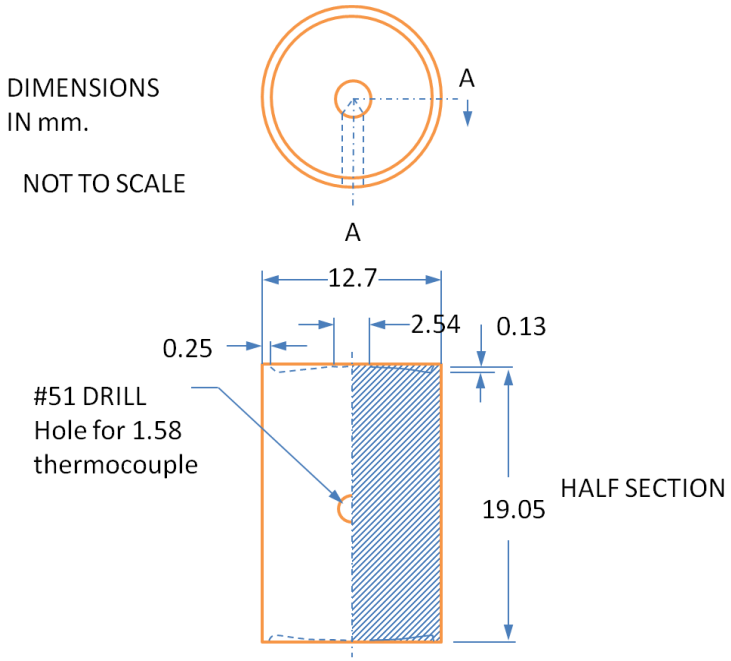

Figure 4.3 Shape of the modified Rastegaev's compression specimen design

Prior to deformation the specimens were encapsulated in a quartz tube and then were put in a furnace for heat treatment for an hour and then water quenched into ice brine water. After that, the specimens were nickel plated to prevent oxidation during reheating. To prevent shear stress caused by friction, one single glass based lubricant or a mixture of two types of glass based

lubricant called DeltaGlaze® were used based on hot deformation temperatures. Moreover, a special glass fiber was used to further reduce friction between the dies and specimen.

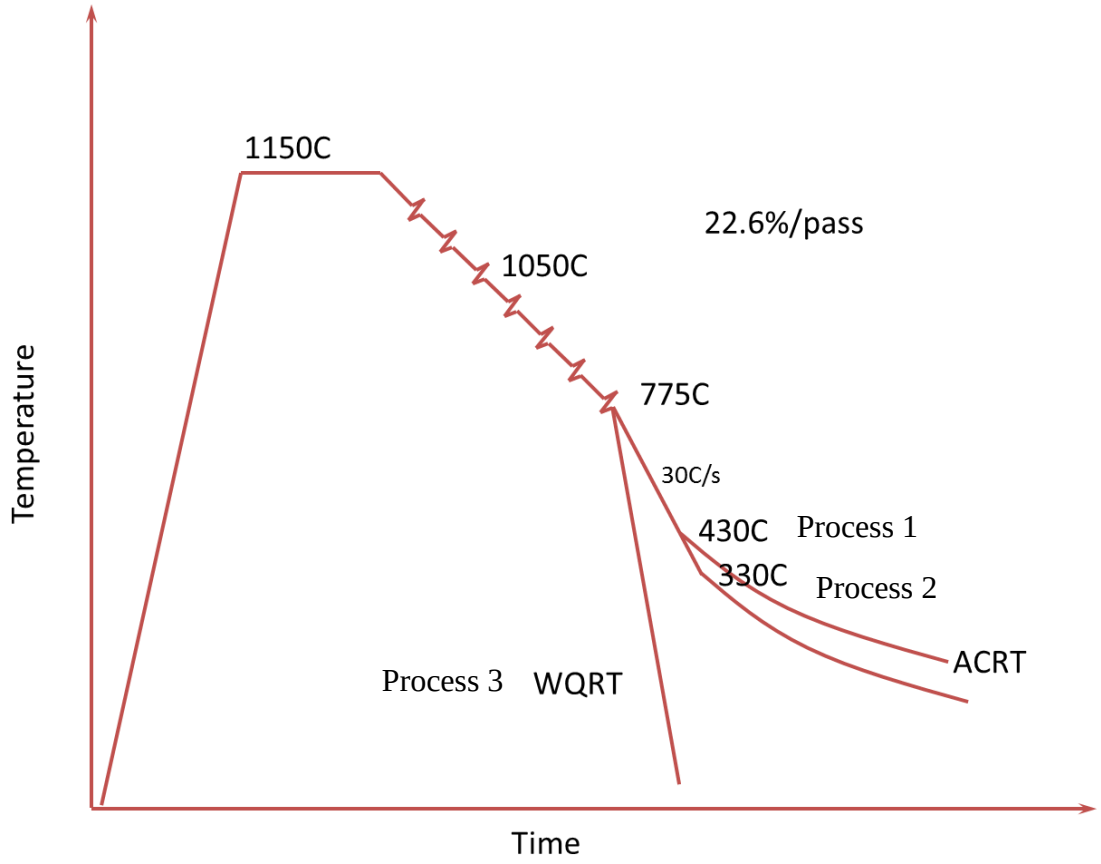

Figure 4.4 Sketch of hot rolling process in a pilot plant

Thermomechanical processing in a laboratory hot rolling mill: in the first round, ingots with dimensions 75mm thick x 100mm long x 114mm wide were hot rolled in a laboratory hot rolling mill. Three different processes were used for each type of steel. The detail is shown in a schematic diagram, Figure 4.4. Ingots were reheated at 1150℃ for four hours, and were hot

rolled using 7 passes, and the deformation is 22.6% per pass. The third pass was controlled at 1050℃ and the seventh pass was controlled at 775℃. After hot rolling, steels were fast cooled down to 430℃ for process 1, and to 330℃ for process 2; then the steels were air cooled to room temperature. For process 3, the steels were direct quenched to room temperature after hot rolling.

In the second round, based on the slab reheating results from the first round test, the soaking temperatures for these compositions should be in excess of 1150℃ for the steels examined. For the steels of Table 1, the ingots were reheated for hot rolling at 1218℃ for three hours, transferred immediately to the hot mill, where they were hot rolled from 100mm in thickness to 12.5 mm in five passes of approximately 34% reduction each. Since the 100mm square ingots are known to lose about 350-400℃ during the rolling process, the soaking temperature of 1218℃ was chosen to permit finishing temperatures of 800-850℃ to be achieved. The first pass was applied at approximately 1150℃ and two different finishing temperatures were used for each steel, 850℃ (for processes labeled 1,2 and 3) and 800℃ (for process labeled 4). The total reduction in the five passes expressed as true strain is -2.08 and the average pass true reduction strain is -0.415(-34% reduction per pass as linear strain). This means that the first two passes were applied above, and the last three passes took place below the T_5, the recrystallization-stop temperature.

4.2 MICROSTRUCTURAL ANALYSIS

4.2.1 **Optical microscopy**

The optical microscope is used at low magnifications since the preparation of samples is easy and identification of the different phases based on the etching of boundaries or different colors of phases is straightforward. Thus, different etchants can be used to identify different phases. The low magnification of microstructure such as 50 to 1000 magnifications is commonly used. Samples were cut from hot rolled plates or the simulated compression specimens and mounted in Bakelite. Then the specimens were ground with 180, 240, 320, 400, 600, 800 and 1200 grit silicon carbide abrasive papers. After grinding, specimens were polished with 0.05μm alumina powder. And then, specimens were etched by two possible types of etching solutions according to the requirements of phase identification. 2% Nital was used to reveal ferritic and bainitic microstructure. And the LePera etchant[84] was used to see the martensite-ferrite boundaries and the non-martensitic products (bainite and pearlite).

The quantitative analysis of microstructures such as grain size and volume fraction of microconstituents was conducted by Bioquant image analysis program which is a software system attached to an optical microscope.

4.2.2 **Scanning Electron Microscope (SEM) and EBSD**

A Philips XL-30 field emission scanning electron microscope was used to obtain higher magnifications of microstructure. More detailed identification of phases can be obtained because magnifications up to 100,000 can be reached. Samples used in the SEM should be mounted in conducting powder and/or conducting tapes to increase conductivity of specimens.

EBSD is an abbreviation for "Electron Backscattered Diffraction". This system is attached to a scanning electron microscope. The EBSD acquisition software collects diffraction patterns and saves the data in the computer. After analyzing the data, orientation maps can be obtained. Furthermore, based on the EBSD data, Wu et al[85]., developed a technique called "EBSD-IQ" to identify and calculate volume fraction of some complex phases in the steel. This is a powerful tool for those phases that are not easily distinguishable by OM or SEM, such as, different morphologies of ferrite, bainite and low carbon martensite. More orientations and misorientations can be analyzed by EBSD techniques[86-89].

Since the diffraction pattern of EBSD comes from the surface of the material, a properly prepared surface is always required. Two ways are used for the preparation of samples. One is mechanical polishing. When it is used, a specimen should be polished very gently by hand to avoid inducing some scratches and then the specimen is polished in a vibration machine. The second way is electro polishing. The solution is made up of 90% ethanol and 10% perchloric acid and the polishing was run at 40 V and 70-90 mA [90] for tens of seconds.

4.2.3 **TEM**

A 200kv JEOL 200CX TEM is used to obtain more detail than SEM can provide. Some microstructures such as lower bainite and low carbon martensite are not distinguishable by OM, or even SEM. The JEOL TEM can provide a linear resolution of 0.13nm. Thin foils are prepared for TEM samples[91].

Thin foils are prepared by cutting 1mm thick specimens from the selected locations with a Buehler diamond disk cut off machine. The samples are ground to ~250 μm, and reduced in

thickness to ~50 μm by chemical thinning. This solution consisted of 50 ml distilled water, 30 ml nitric acid, 15 ml hydrochloric acid and 7 ml hydrofluoric acid [87, 88, 90].

Discs of 3 mm in diameter are punched and then ground to ~30 μm on grit 600 sand paper. After that, the discs are electrochemically polished at room temperature on a Struers-Tunepol Jet polisher at room temperature and the final thickness of the disc at the center is of ~50-100 nm. The solution is made up of 90% ethanol and 10% perchloric acid and the polishing was run at 40 V and 70-90 mA [90]. The discs were thoroughly cleaned in ethyl alcohol before being taken to the TEM examination.

4.2.4 Special techniques to determine C-partitioning and the distribution of other elements

Carbon partitioning was an important factor for the present research. Nanoindentation is one of variety of indentation hardness tests applied to small volumes and it is used in many research areas[92, 93]. In high strength linepipe steels, the microstructures are complex and some microstructures are too small to be measured by common microhardness instruments. And in nanoindentation small loads and tip sizes are used, which makes the indentation area to be a few square micrometers or even nanometers. However, the contact area is not easily found. Thus, atomic force microscopy or scanning electron microscopy techniques may be utilized to image the indentation, but can be quite cumbersome. Instead, a record of the depth of penetration is made, and then the area of the indent is determined using the known geometry of the indentation tip. While indenting, various parameters, such as load and depth of penetration, can be measured.

A record of these values can be plotted on a graph to create a load-displacement curve. These curves can be used to extract mechanical properties of the material [92, 94].

4.3 MECHANICAL PROPERTIES

4.3.1 **Hardness**

Hardness of metal implies a resistance to permanent or plastic deformation, and it has the corresponding relationship to ultimate tensile testing. This test is also much more convenient to conduct than tensile testing; thus hardness is always used to estimate the approximated strength of the material.

4.3.2 **Tensile testing**

Tensile tests were conducted in the MTS 880 system. The sub-size tensile specimens, the gage length of which is 25mm, were machined for testing according to the ASTM standard E 8M-04. The specimens were cut from both the rolling direction and transverse direction.

4.3.3 **Standard CVN toughness testing**

A full size of Charpy V-notch specimens were machined and tested according to ASTM E23-02a. The dimension of a specimen is 55mm*10mm*10mm. The testing was conducted to evaluate the toughness of materials in the T-L direction.

4.3.4 **Nanoindentation**

The bainitic structure is very complex and many small microconstituents are not easily distinguishable even at high magnifications. Then nanoindentation was used to measure the hardness of the different microconstituents present. The Hysitron Tribo-Scope system was used to measure nanoindentation.

5.0 RESULTS

5.1 STUDY OF AUSTENITE RECRYSTALLIZATION AND GROWTH COARSENING

5.1.1 Austenite grain coarsening during reheating prior to thermomechanical processing

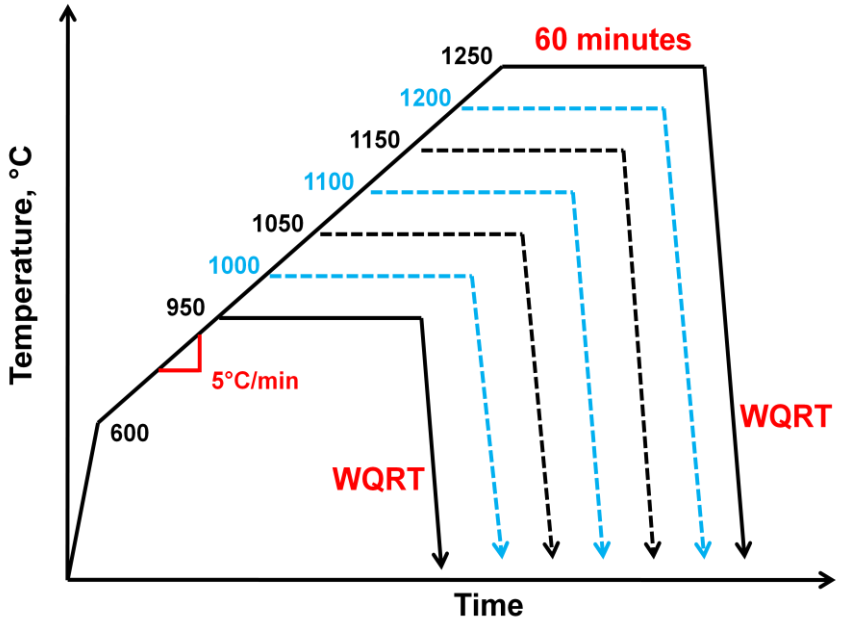

Figure 5.1 Heat treatments used for austenite grain coarsening study

Four steels, 1A, 1B, 61A & 61C, as shown in Table 4.1, were used in a grain coarsening study to approximate the behavior during the reheating of cold-charged, as-cast slabs. The heat treating procedure used is shown in Figure 5.1, where small pieces of the steels were heated to the desired temperature, held one hour, and then water quenched to room temperature (WQRT). The grain sizes were determined from these specimens.

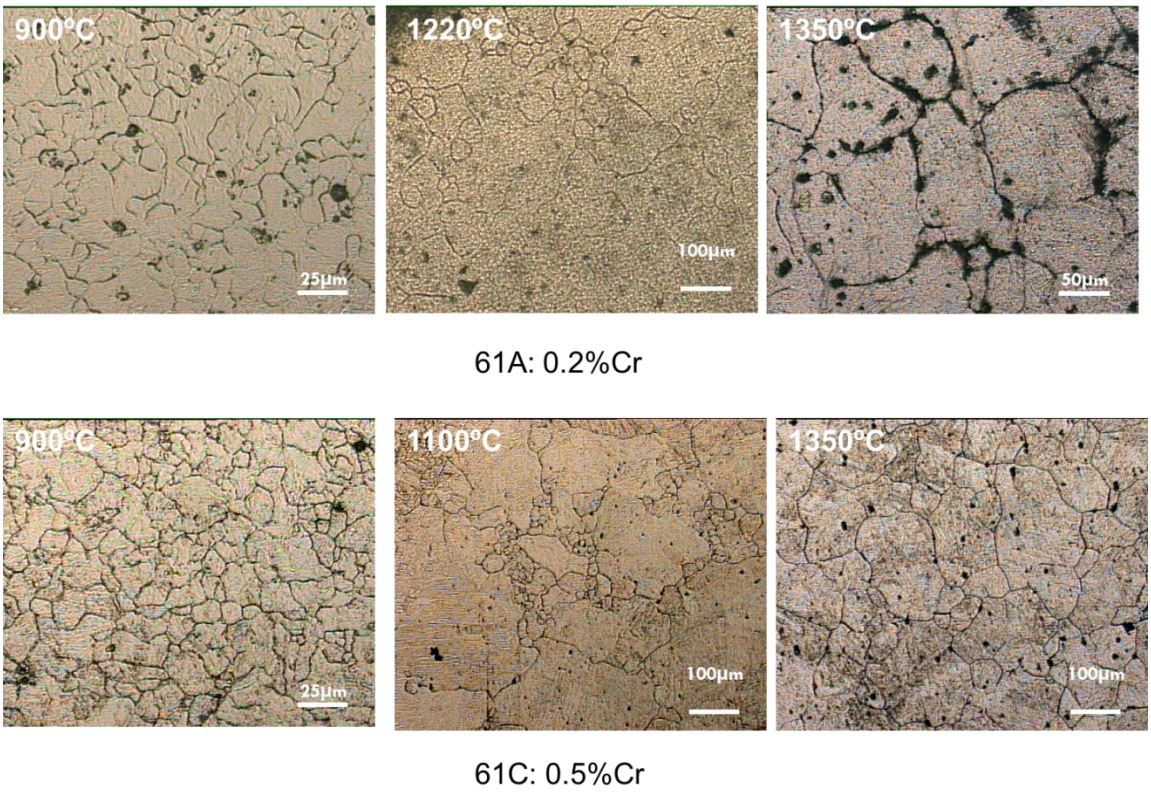

Figure 5.2 Austenite grain coarsening in steels 61A and 61C with different Cr

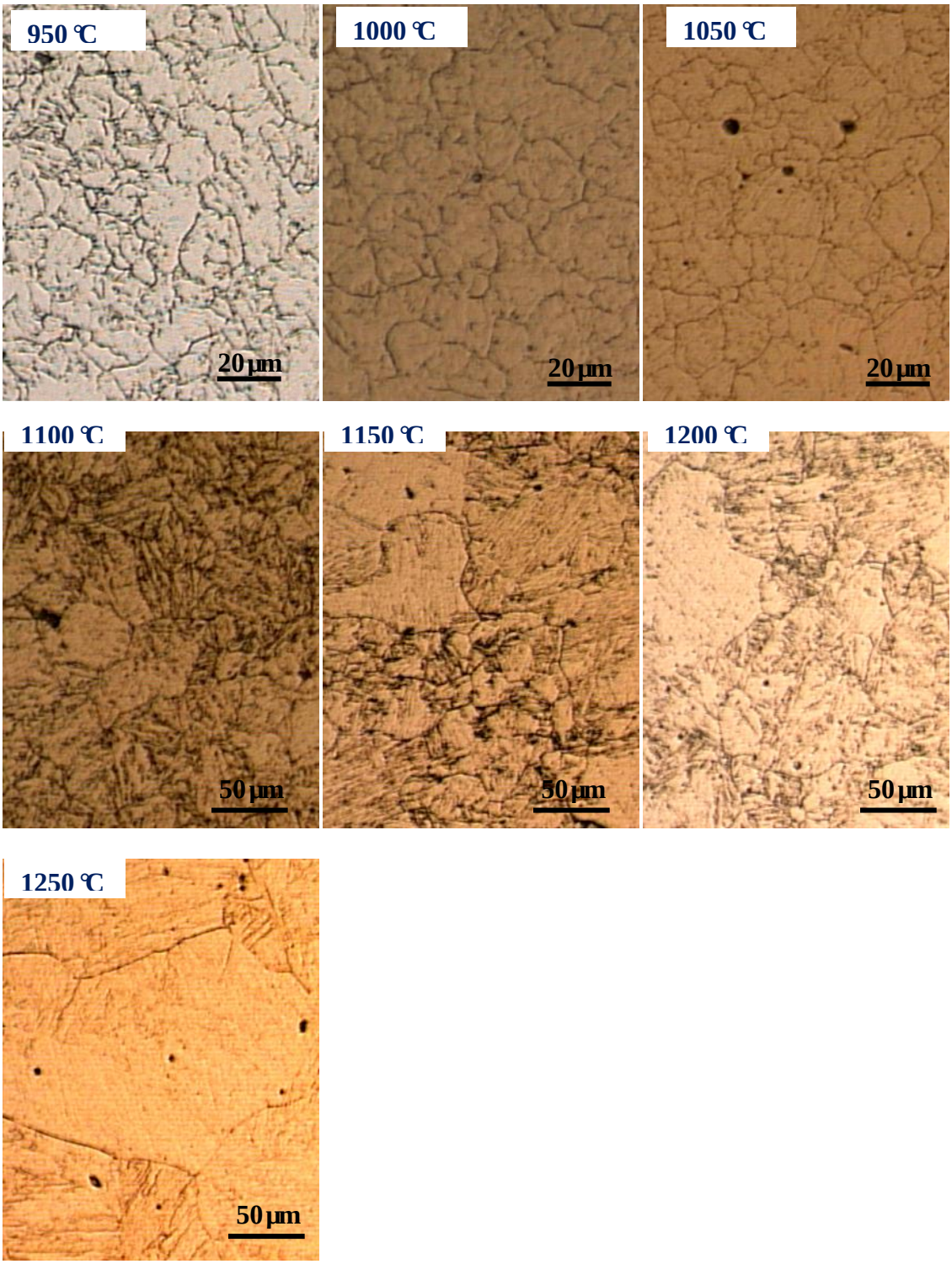

Figure 5.3 Austenite grain coarsening in steel 1A

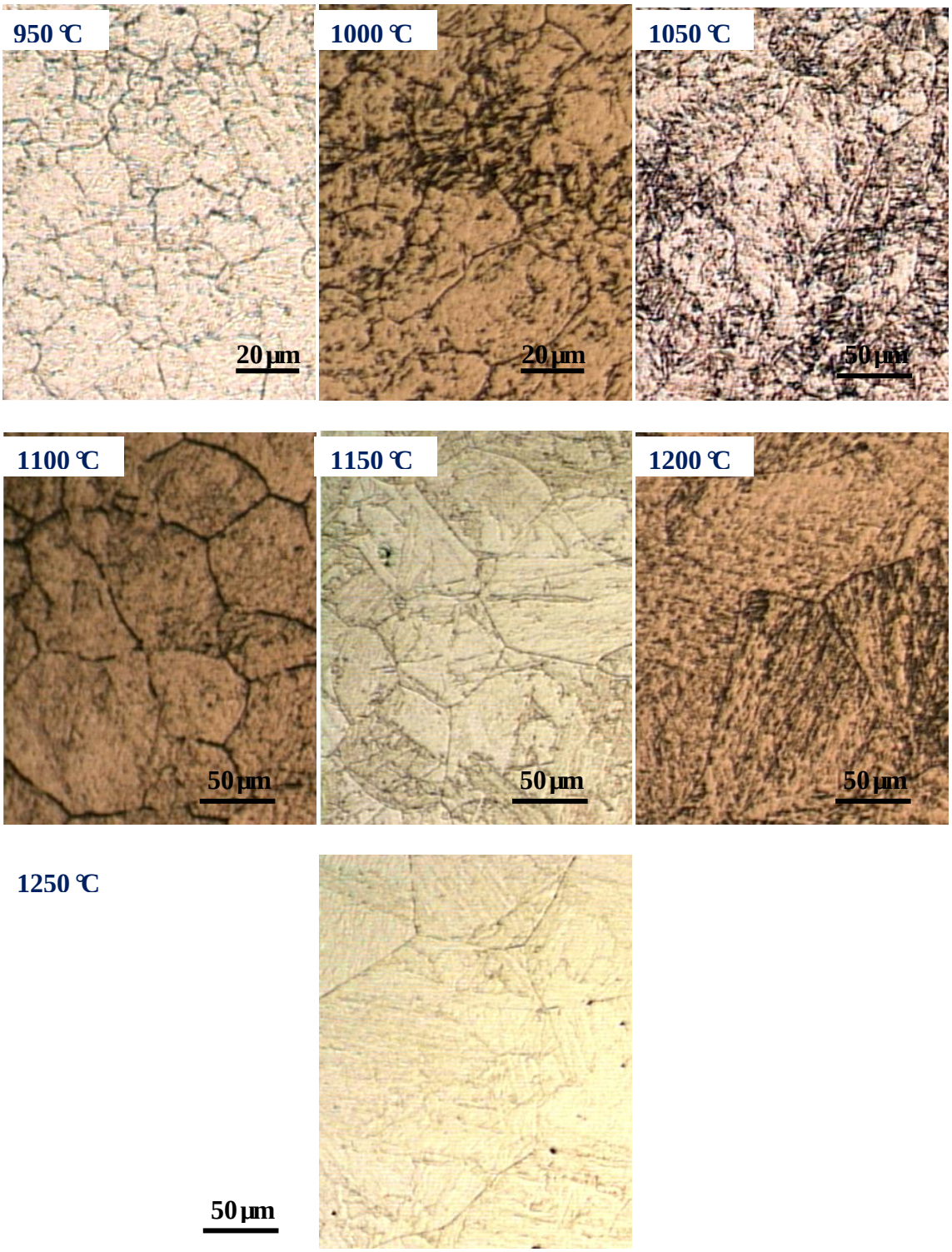

Figure 5.4 Austenite grain coarsening in steels 1B

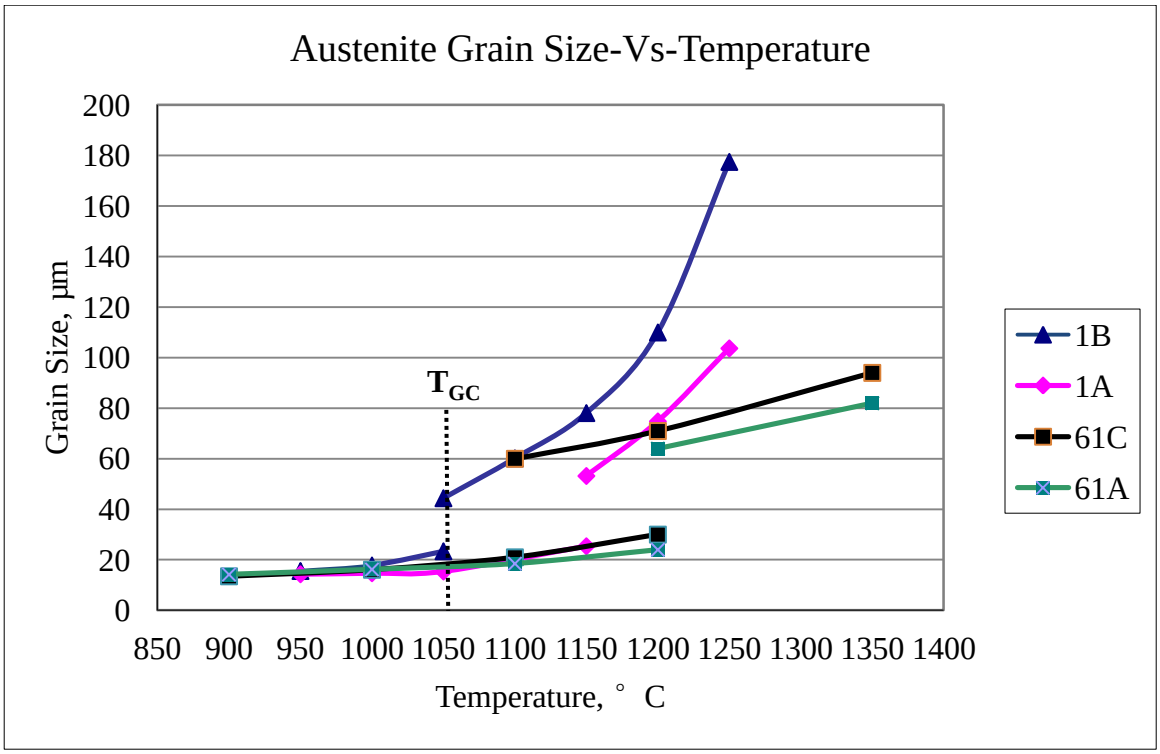

Figure 5.5 The austenite grain size of four steels. T_{GC}: grain coarsening temperature

The as-reheated prior-austenite grain growth data for steel 61A & 61C are shown in Figure 5.2 after reheating to some critical temperatures ranging from 950-1250 ℃. In a similar fashion, Figure 5.3 & Figure 5.4 illustrate the austenite grain coarsening for steel 1A and 1B after reheating to temperatures ranging from 950-1250 ℃. The measured prior-austenite grain sizes shown in Figure 5.5 illustrate the grain coarsening behavior of steels 1A and 1B, as well as steels 61A and 61C. The grain coarsening temperature[95, 96] T_{GC} (the beginning temperature of abnormal grain growth) is indicated for steel 1B in Figure 5.5. The figure shows that grain coarsening was retarded in 61A, 61C and steel 1A due to the effect of titanium on the resistance of austenite grain boundary mobility. Without titanium, the austenite grain size of steel 1B can

grow to around 200 μm at 1250 ℃; however, for other steels with titanium, it is around 100 μm even at higher reheating temperatures. The curves of 61A (0.2wt%Cr) and 61C (0.5wt%Cr) illustrate the effect of chromium on the grain coarsening. More chromium content in steel lowers the grain coarsening temperatures. Comparing these two curves, it shows that about 100 ℃ difference for grain coarsening was caused by 0.2 and 0.5wt% Cr in steel for the mixed grain size.

Based on this work, a reheating temperature of 1150 ℃ was chosen for further processing, resulting in a starting austenite grain size of 70 ±10μm.

5.1.2 **Hot deformation behavior**

In this portion of the research, the critical temperatures of the austenite were determined for steels 1A and 1B. The critical temperatures were T_{95} and T_5[97]. Rolling above T_{95} results in complete recrystallization of the austenite, often accompanied by grain refinement. Rolling below T_5 leads to pancaked austenite which is a desirable microstructure to have prior to final cooling. Rolling between T_{95} and T_5 can lead to mixed grain sizes and poor final microstructures and properties.

The thermomechanical processing schedule used in this study is shown in Figure 5.6. This schedule was programmed into the MTS system. In this schedule, the specimens were first reheated to 1250 ℃ to ensure that (i) all of the microalloying elements were in solution, (ii) that the as-cast structure was altered and the solute segregation was improved and (iii) that the final grain size distribution was achieved. After the 1250 ℃ treatment the samples were WQRT and reheated again to 1150 ℃ in preparation for the hot deformation studies.

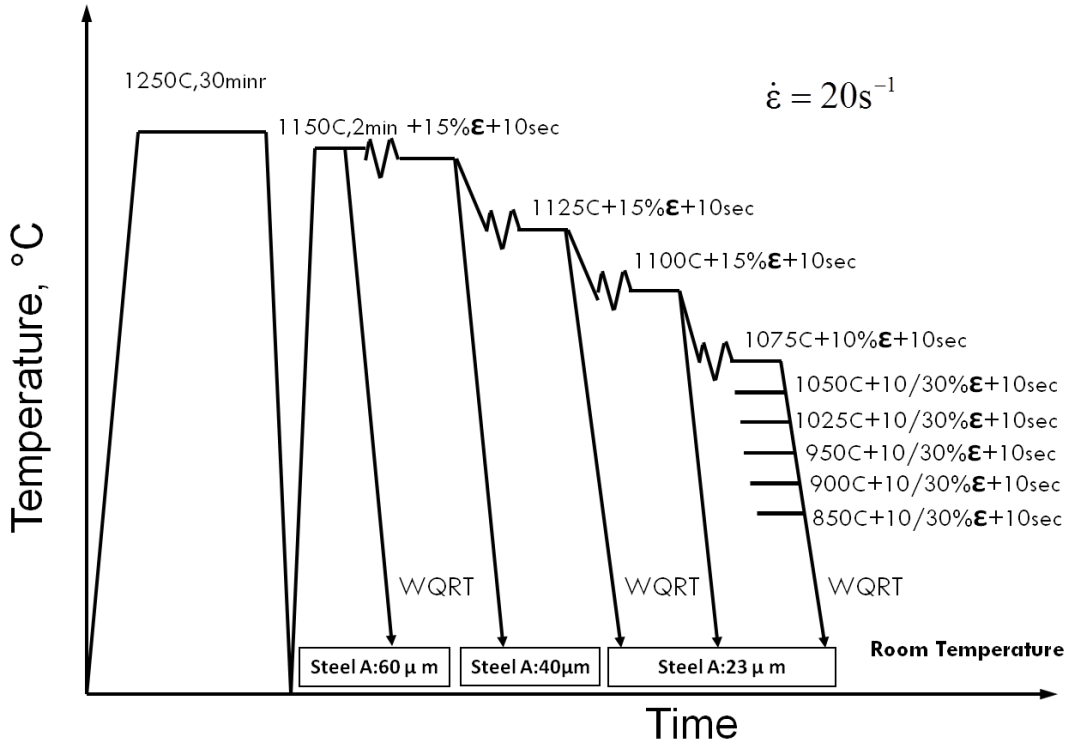

Figure 5.6 TMP schedule for determining T_{95} and T_5

The high temperature rough rolling passes were simulated by multiple deformations at a strain rate of 20 sec^{-1}, a reduction of 15% and an interpass time of 10 sec. The finishing passes were simulated by multiple deformations at a strain rate of 20 sec^{-1}, a reduction of 10 or 30% and an interpass time of 10 seconds. Specimens were WQRT from several stages of the processing simulation. The size and shape of the prior-austenite grains were determined from these as-quenched specimens.

The behavior of austenite during hot deformation is shown in Figure 5.7 and Figure 5.8 for Steel 1A with pass reductions of 10% and 30%, respectively. The results of Steel 1B are

illustrated in Figure 5.9 and Figure 5.10. The austenite grain size and microstructures are shown in Appendix A & B. The aspect ratio of 1.6 is used to describe that the grains are deformed but not recrystallized.

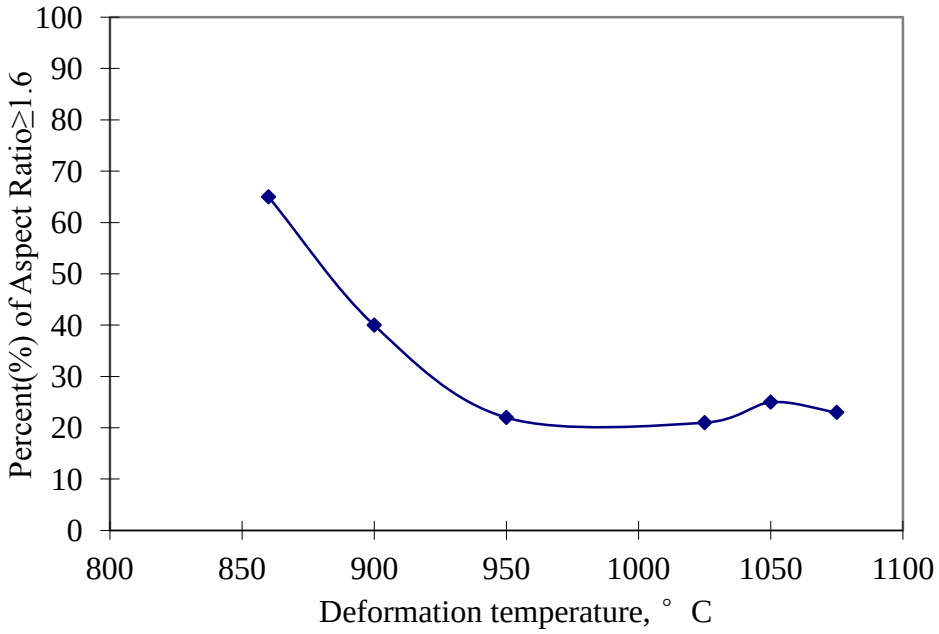

Figure 5.7 Percent of grains with aspect ratio ≥ 1.6 as a function of deformation temperature for Steel 1A, 10%ε.

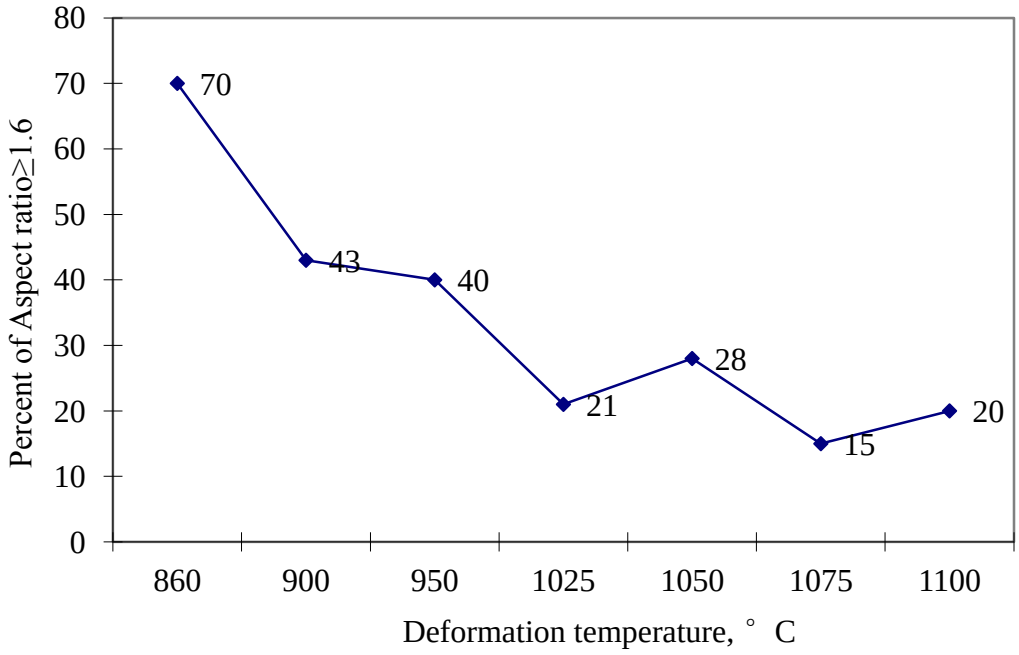

Figure 5.8 Percent of austenite grains with aspect ratio > 1.6 as a function of deformation

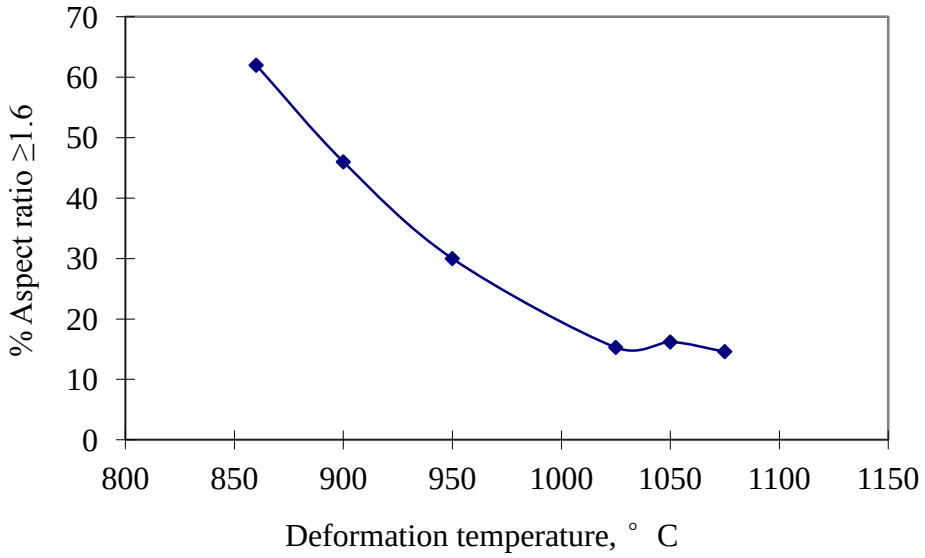

Figure 5.9 Percent of austenite grains with aspect ratio≥1.6 as a function of deformation temperature for Steel 1B, ε=10%

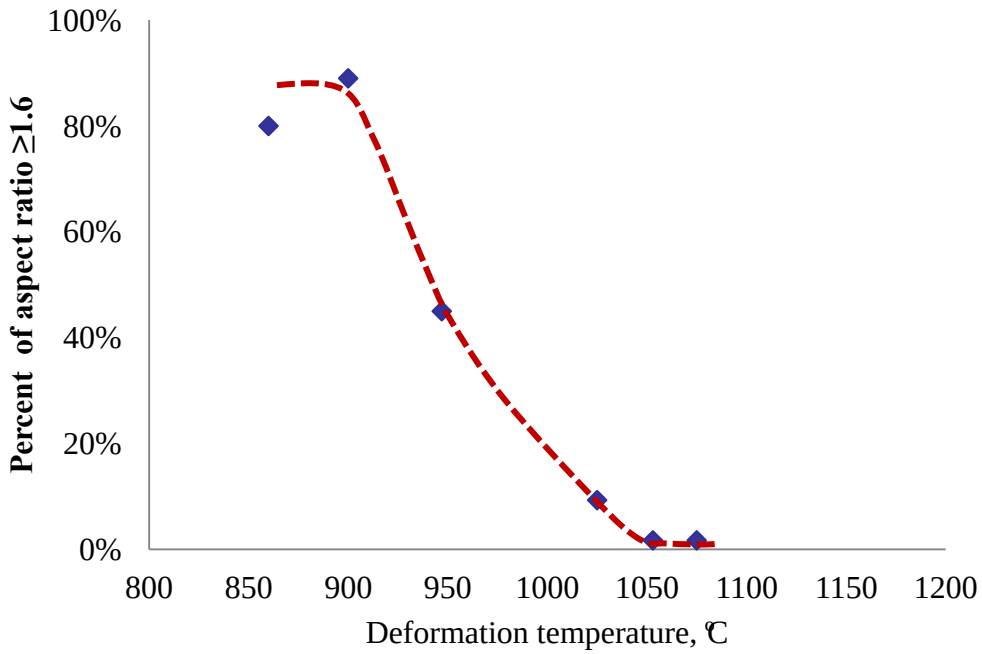

Figure 5.10 Percent of austenite grains with aspect ratio ≥ 1.6 as a function of deformation temperature for Steel 1B, ε=30%

5.1.3 **Austenite grain size after deformation**

The austenite recrystallized grain size after the rough rolling passes are shown in Table 5.1 and Figure 5.11 for both steels. Steel 1A with titanium has a much finer austenite grain size than steel 1B. The grain size in steel 1A, as shown in Figure 5.12, does not change much below 1025 ℃. Thus, according to the grain size and aspect ratio, the T_5 temperature for steel A appears to be in the range of 1025-950 ℃, while the T_{95} temperature is over 1075 ℃. Steel B should have similar results.

The pancaked austenite is always designed in HSLA steels[12, 15]. Sv is a parameter to describe the extent of pancaked austenite[56]. For elongated grain boundaries,

$$Sv,gb=0.429(NL)_{\parallel}+1.571(NL)_{\perp} \quad (5.1)$$

where $(NL)_{\parallel}$ and $(NL)_{\perp}$ are intercept numbers per unit length along rolling and thickness direction, respectively[56].

The austenite pancaked grain structure after the finishing passes was simulated by the TMP practice shown in Figure 5.14 and the resulting prior-austenite microstructure is shown in Figure 5.15. The pass strain used to simulate finish rolling was -0.916 (equivalent to a $t_0/t = 2.5$, t_0 is the initial thickness and t is the final thickness after deformation) and the resulting Sv was 111 mm^2/mm^3. Smaller austenite grain sizes and heavier pancaking strain, as to be expected in a real steel rolling mill, would have resulted in higher Sv values.

Table 5.1 Austenite grain size of Steels 1A & 1B after roughing passes

Steel 1A			Steel 1B		
Deformation Temperature	Average grain size (um)	Standard deviation	Deformation Temperature	Average grain size (um)	Standard deviation
11150 ℃(1)	42.0	14.2	1150 ℃	59.3	20.5
11125 ℃(2)	38.7	12.7	1125 ℃	51.1	11.3
11100 ℃(3)	22.8	8.5	1100 ℃	46.9	18.6

Please refer to Figure 5.6:
(1): 1150 ℃—15%
(2): 1150 ℃—15%, 1125 ℃—15%
(3): 1150 ℃—15%, 1125 ℃—15%, 1100 ℃ – 15%

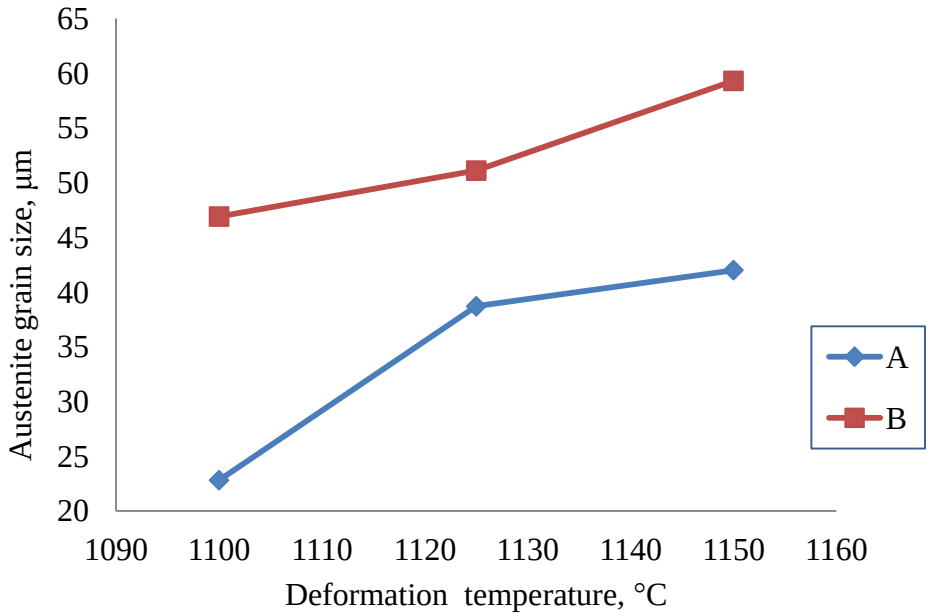

Figure 5.11 Austenite grain size after each deformation

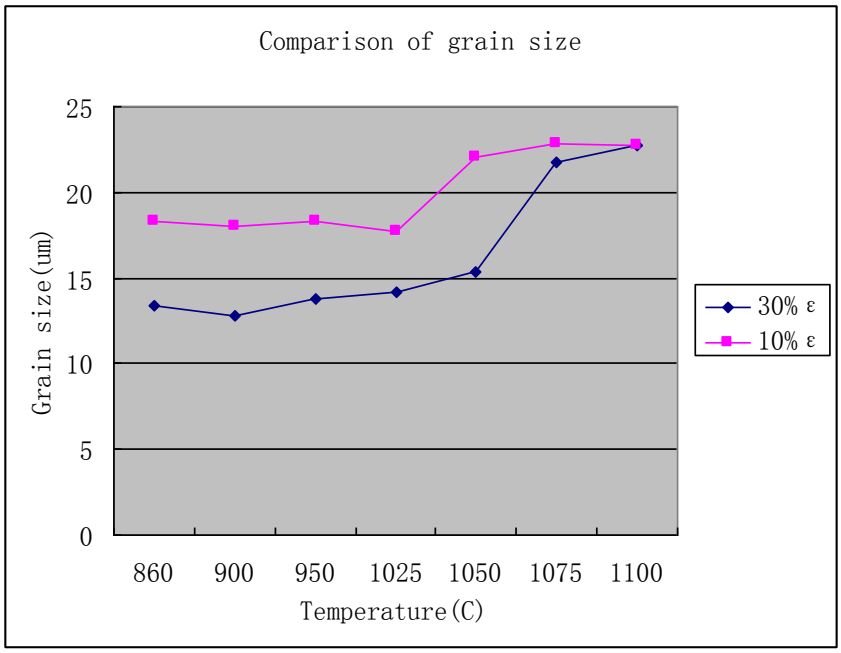

Figure 5.12 Grain size of Steel 1A with different amount of deformation

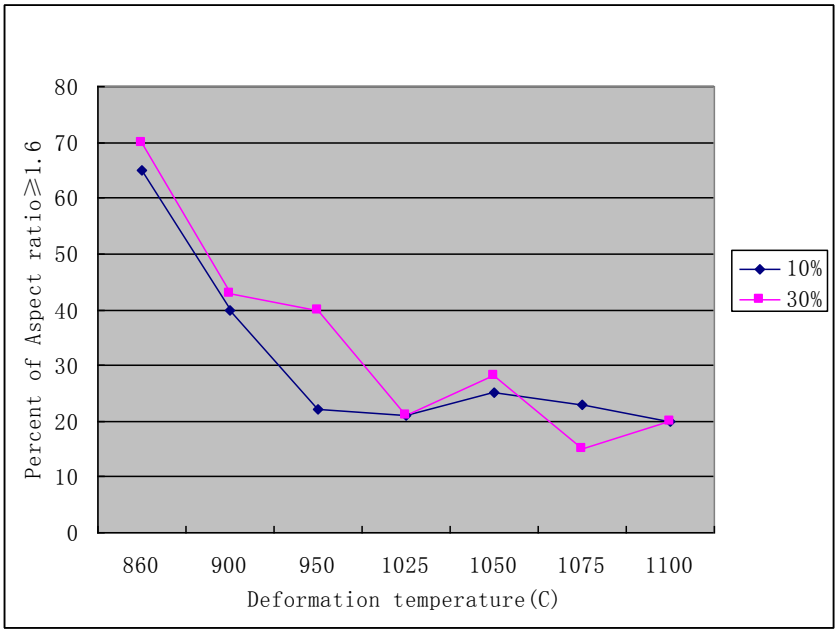

Figure 5.13 Aspect ratio of Steel 1A with different amount of deformation

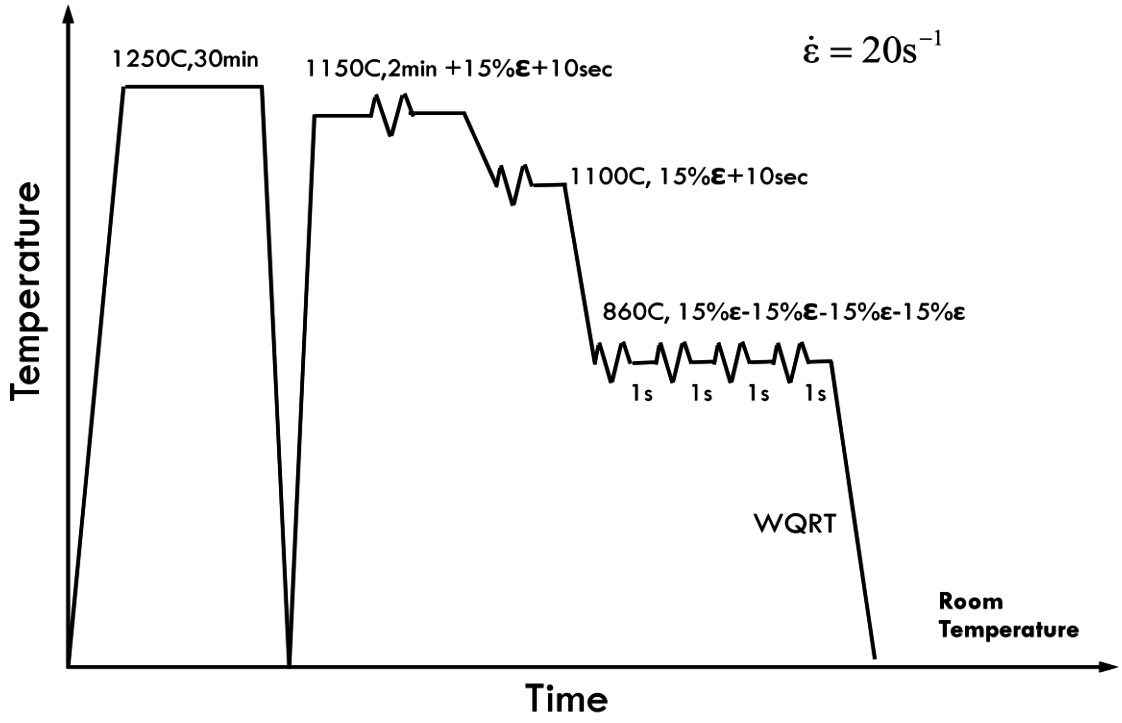

Figure 5.14 TMP schedule used to determine Sv for Steel 1A

Figure 5.15 Pancaked prior-austenite microstructure resulting from TMP of Figure 5.14.

5.2 BAINITE START TEMPERATURES CALCULATION AND MEASUREMENTS

Austenite is a transition state of microstructure in the high strength steels studied. The austenite state is important to affect the subsequent microstructures and thus causes the different mechanical properties. To obtain good mechanical properties, austenite grain size and shape should be controlled. However, it is not enough to guarantee good properties until the subsequent microstructures are also controlled. In high strength steel, bainite, martensite or the mixture of bainite and martensite is the predominant microstructure, as expected [12].

5.2.1 **Prediction of bainite start temperatures**

JMatPro is a cross-platform program which calculates a wide range of materials properties for alloys and is particularly aimed at multi-components alloys used in industrial practice[98]. By

using JMatPro software, a CCT diagram can be simulated in Figure 5.16 for steel 1A with a terminal austenite grain size of ASTM 8 (diameter 20 μm, Sv 100 mm^{-1}). Of interest in this diagram are the Ar3, B_S and M_S temperatures under equilibrium cooling and at cooling rates between 10 and 30 ℃/sec. The CCT diagram predicted for steel 1B is shown in Figure 5.17.

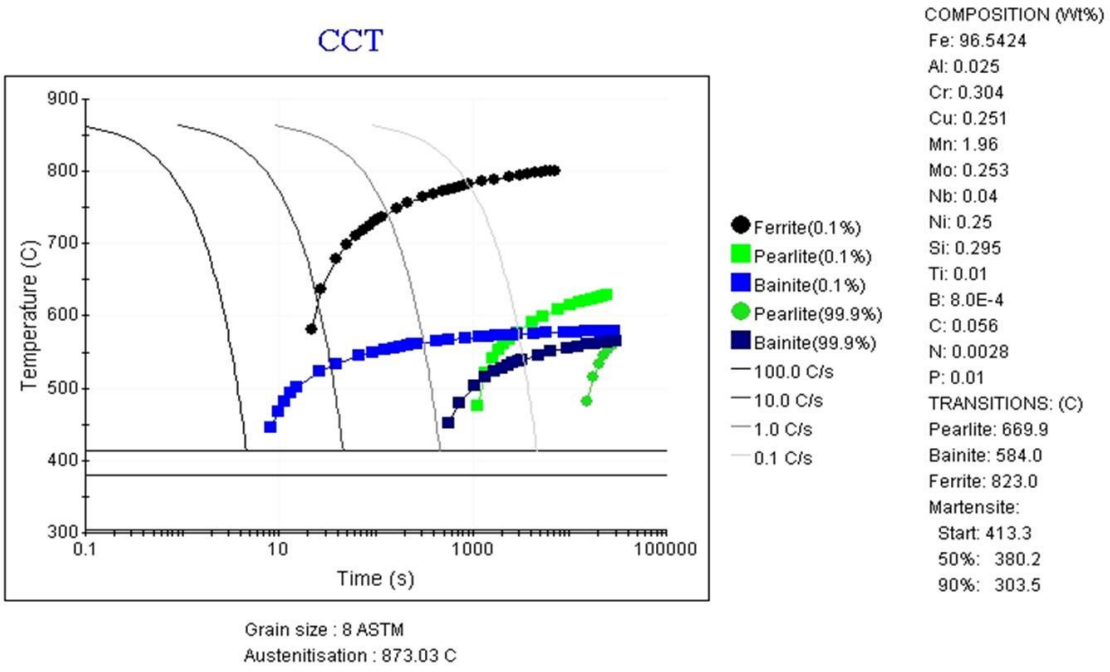

Figure 5.16 CCT Diagram of Steel 1A

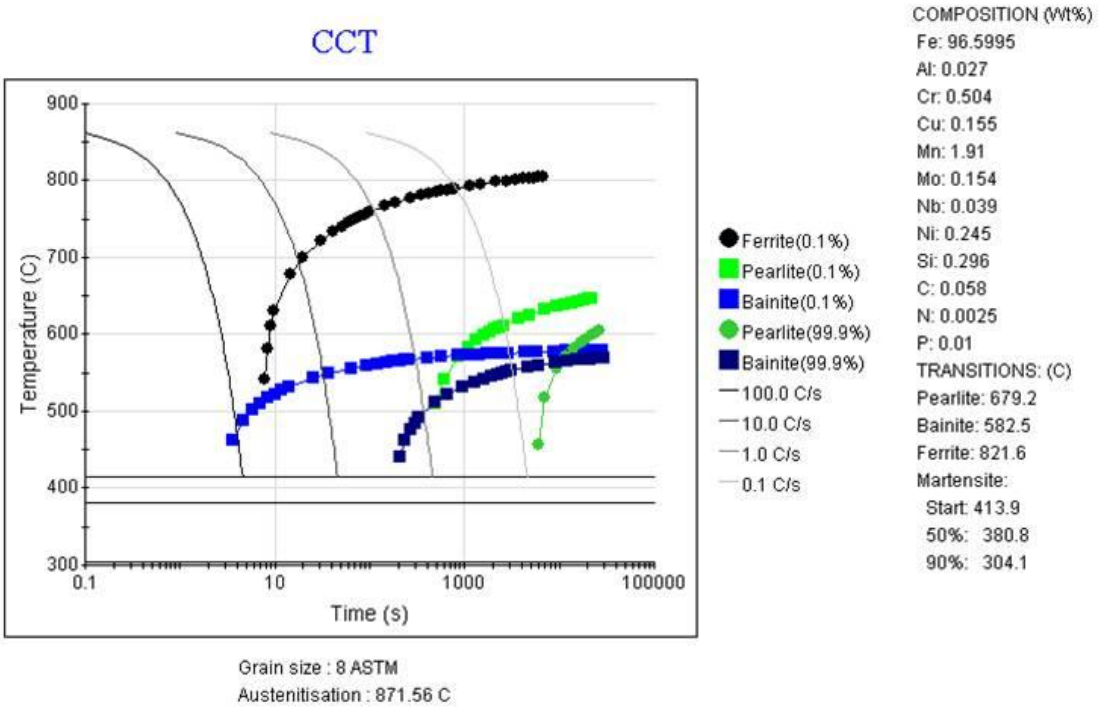

Figure 5.17 CCT Diagram for Steel 1B

5.2.2 **The measurement of Bs temperatures**

The cooling curves of steel 1A and 1B were recorded to investigate the Bs temperatures. The cooling curve of Steel 1A was measured after 30% deformation and constant helium flow was used to cool down the sample. Steel 1B was investigated to compare to steel 1A. Furthermore, the holding time: 0s, 40s, 100s and 400s between deformation and fast cooling were studied for their effect on the Bs temperatures.

One cooling curve of specimen of steel 1A with deformation was recorded as shown in Figure 5.18. As indicated in the figure, the Bs temperature of steel 1A is about 475℃.

Comparing the results calculated by JMatPro and the experimental data in Table 5.2, it is found about the actual Bs temperature is lower than the calculated one. The Bs temperatures of steel 1B with different holding temperatures and measured cooling rates are listed in Table 5.3. The results showed that longer holding time after deformation raised the Bs temperatures. The temperature rose from 506 ℃ to 529 ℃ when holding time was changed from 40 seconds to 100 seconds or 400 seconds. After 100 seconds holding, the change of Bs temperature is not apparent.

The measured Bs temperatures of steel 1B are very close to the calculated number in Table 5.2. After comparing steels 1A & 1B, boron appears to be the element which lowers the Bs temperature. According to the results in Table 5.2 & Table 5.3, the effect of 8~10 ppm boron on the bainite transformation temperature is given:

$$B_S(\text{with boron}) = B_S(\text{no boron}) - 45℃ \tag{5.2}$$

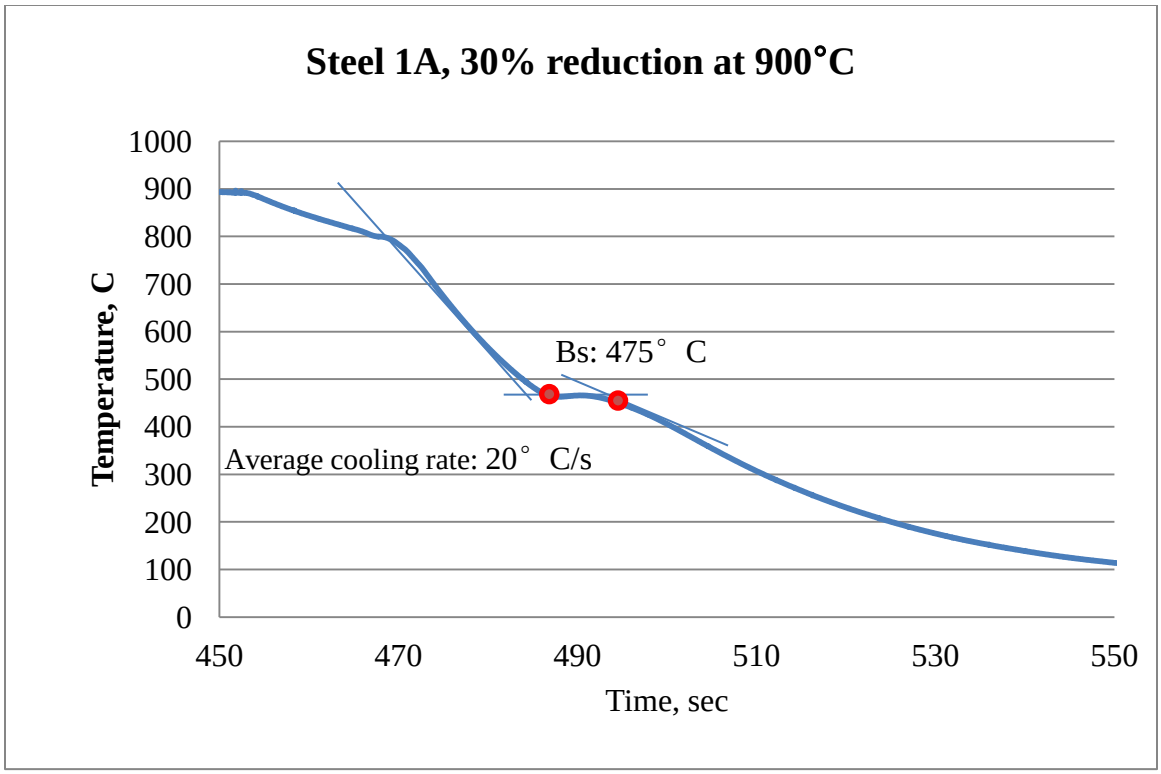

Figure 5.18 Measurement of B_s and M_s for Steel 1A, deformed at 900 ℃, ε= 30%

Table 5.2 Calculated and Measured Transformation Temperatures

	Steel	A_3, ℃	A1, ℃	Bs, ℃	Ms, ℃
JMatPro prediction Equilibrium	1A	825	641	584	413
	1B	825	655	582	413
JMatPro prediction CR 10 ℃/s	1A	625	-	520	413
	1B	690	-	518	413
Measured, CR 20 ℃/s	1A	690	-	475	406

Table 5.3 Measured Bs temperatures of steel 1B

Holding time,sec	Cooling rate, ℃/s	Bs temperatures, ℃
0	17	515
40	35	506
100	25	529
400	32	529

5.3 MICROSTRUCTURES AND MECHANICAL PROPERTIES OF HOT ROLLED PLATES

5.3.1 **First round hot rolling test**

5.3.1.1 **Thermomecanical processing of first round study**

The compositions of the experimental steels are shown earlier in Table 4.2. According to the investigation of grain coarsening and Bs temperatures, the ingots were cold charged into a reheating furnace and held at 1150 ℃ for three hours. Thermocouples were embedded in each ingot to record the temperature at the centerline during the entire rolling and cooling process. After reheating, each ingot was given the same rolling reductions consisting of three roughing passes(1100-1050 ℃) followed by four finishing passes(950-775 ℃). Each pass was a reduction of approximately 23%. These treatments are shown schematically in Figure 4.4.

The experimental cooling paths were designed based on the Bs and Ms temperatures of the austenite for the given compositions and cooling rates, as shown in Table 5.2 and Table 5.3. The aim WET temperatures are shown in Table 5.4.

Table 5.4 Predicted Ar3, Ar1, Bs, Ms & Mf, ℃ (JMatPro)

	Ar3	Ar1	Bs, ℃	Bs(30 ℃/s), ℃	Ms, ℃	Mf(90%), ℃
A	820	668	570	522	394	282
B	821	677	567	511	389	277
C	817	671	566	495	387	275

Within 20 seconds of leaving the final pass, the 12.5mm plates were either water sprayed to the water end temperature (WET) (Paths 1 or 2) or quenched into a water tank(Path 3). The three cooling conditions for each split are shown in Table 5.5.

Table 5.5 Requested cooling paths, 1, 2 & 3

	Three Cooling Conditions for each split	
1	30 ℃/sec cooling rate to 430 ℃, then air cool to room temperature	(A-1, B-1, C-1)
2	30 ℃/sec cooling rate to 330 ℃, then air cool to room temperature	(A-2, B-2, C-2)
3	Water Quench after last finishing pass	(A-3, B-3, C-3)

Three cooling paths were used for each steel. Path 1 was quenched to 430 ℃ which was well below the Bs temperature. Path 2 represented quenching to 330 ℃, which is well below the Ms temperature. Path 3 represented quenching into the water tank, causing rapid cooling to about 150 ℃. It should be noted that although Paths 1 and 2 were intended to be continuous, they in fact showed two-stage cooling with the cooling from 750-550 ℃ occurring at ~10 ℃ /sec and the remaining cooling from 550 to 150 ℃ occurring at ~30 ℃ /sec. Only steel C and Path 2 showed a continuous cooling path. The three steels all showed continuous cooling from 750-150 ℃ at 75 ℃ /sec when quenched into the water tank, Path 3.

5.3.1.2 **Microstructural characterization**

The microstructure of paths 1 & 2 conditions was characterized by optical microscopy and SEM using a nital etching. Each condition is identified by a letter and a number; the steel composition is given by the letter and the cooling path by the number.

The microstructures revealed by optical microscopy and nital etching are shown in Figure 5.19 to Figure 5.24. The SEM micrographs are shown in Figure 5.25 to Figure 5.30.

The optical micrographs taken after nital etching of Steels A-1 (Figure 5.19), A-2 (Figure 5.26), B-1 (Figure 5.21) and B-2 (Figure 5.22) revealed rather similar microstructures consisting of a mixture of granular bainite (GB) and degenerate upper bainite (DUB). The microstructures of C-1 and C-2 had a different appearance. Here the structure contained large amounts of lower bainite, with a lath-like ferrite morphology and some martensite. The prior austenite grain boundaries are clear, and the grain size is very large as shown in Figure 5.24.

The SEM micrographs revealed more detail concerning the microstructures. Steels A-1 and A-2 showed a granular bainite structure with MA on the ferrite grain boundaries. There was also an indication of non- or quasi-polygonal ferrite present, since the prior austenite boundaries were not visible. Importantly, the MA islands were at least one micron in length. Steels B-1 and B-2 had a similar appearance, but with smaller MA island size than the A steels. Overall, it appeared that B-1 had a better particle distribution of MA. Also, steel B-2 had a much finer microstructure than did B-1. Steel C-1 showed a very large amount of lath-like lower bainite with interlath MA along with some martensite, perhaps autotempered as evidenced by the presence of carbide particles. Steel C-2 had a similar appearance but with more martensite, beyond the MA.

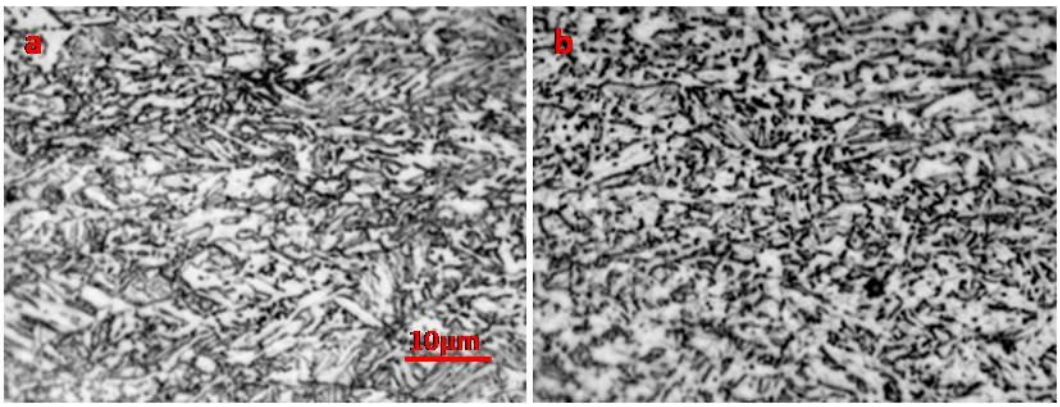

Figure 5.19 Optical microscopy of A-1, Nital. (a) longitudinal; (b) transverse

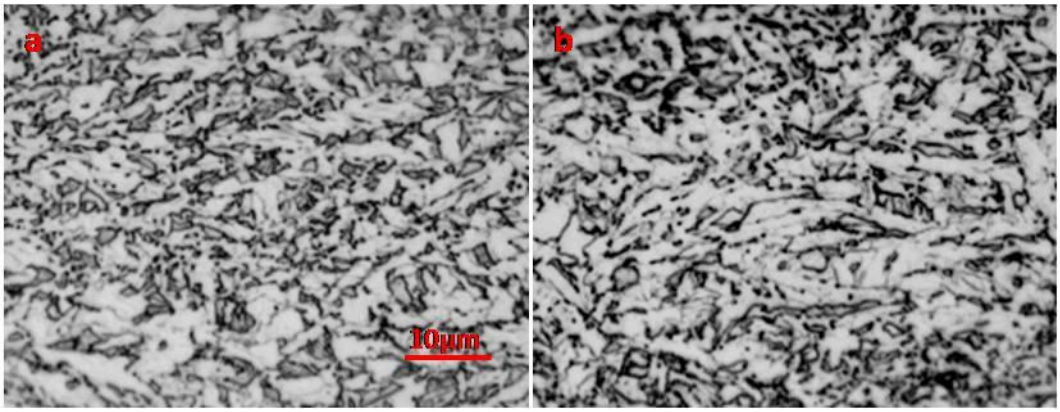

Figure 5.20 Optical microscopy of A-2, Nital. (a) longitudinal; (b) transverse

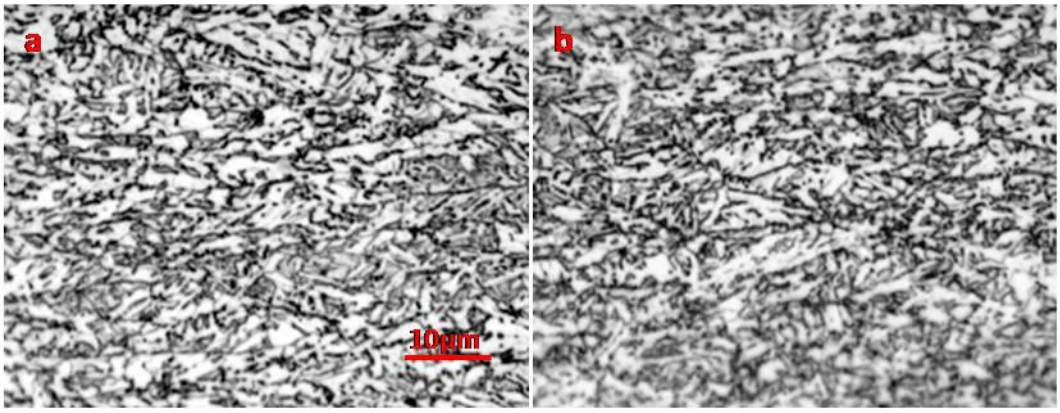

Figure 5.21 Optical microscopy of B-1, Nital. (a) longitudinal; (b) transverse

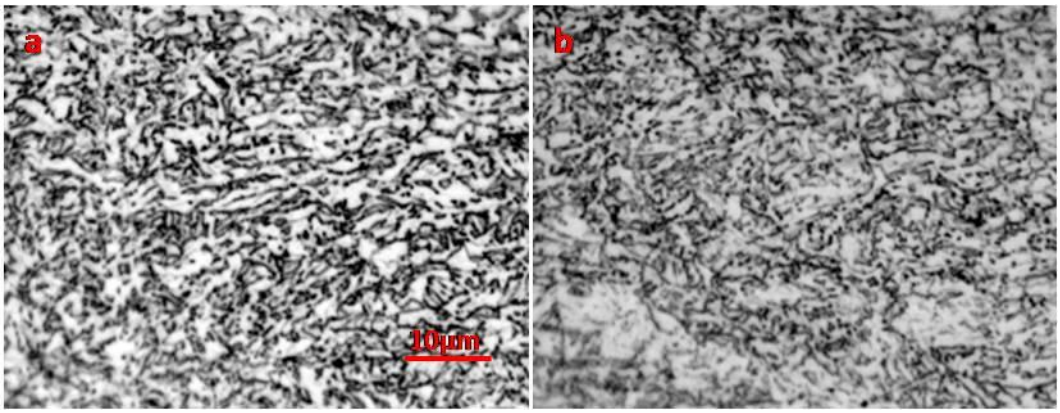

Figure 5.22 Optical microscopy of B-2, Nital. (a) longitudinal; (b) transverse

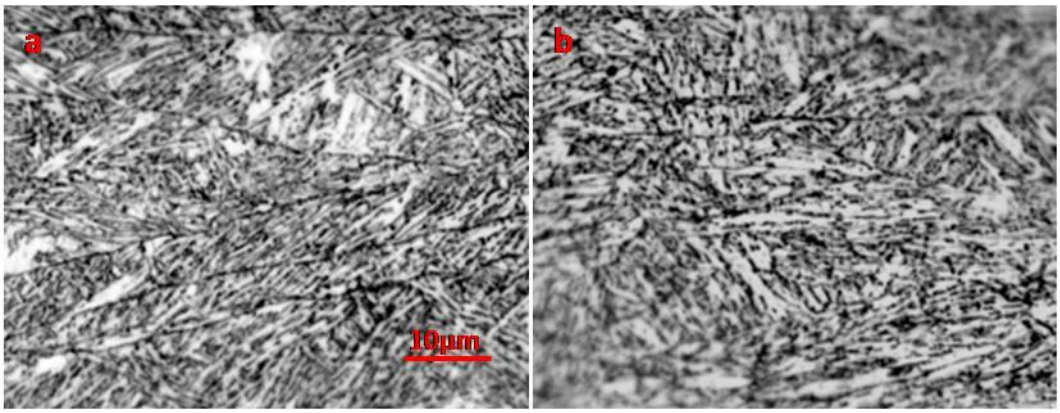

Figure 5.23 Optical microscopy of C-1, Nital. (a) longitudinal; (b) transverse

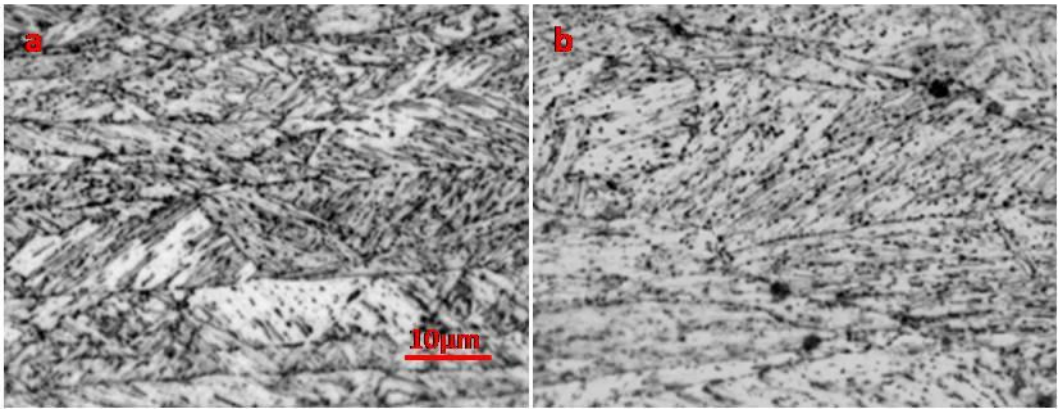

Figure 5.24 Optical microscopy of C-2, Nital. (a) longitudinal; (b) transverse

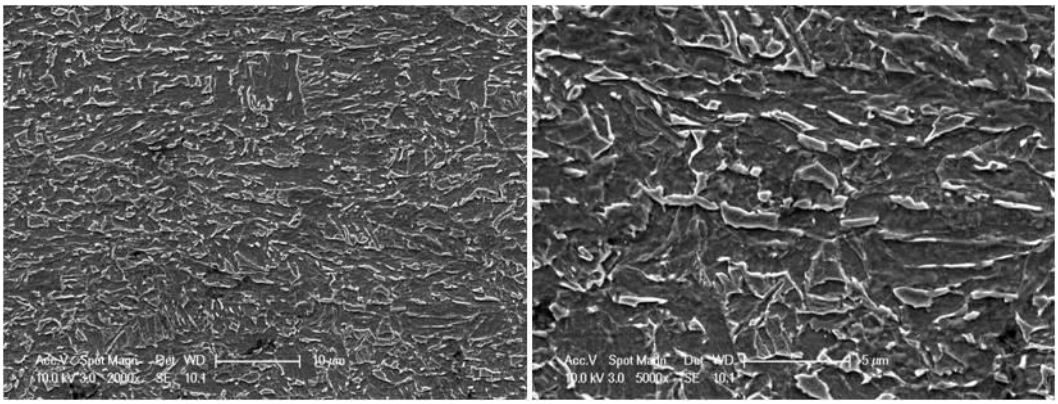

Figure 5.25 SEM micrographs of A-1 (transverse). Left:2000X; Right:5000X

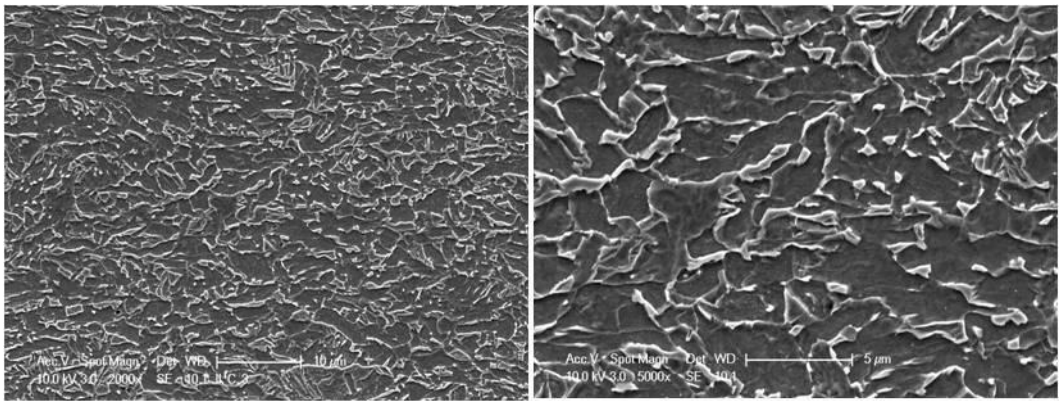

Figure 5.26 SEM micrographs of A-2 (transverse). Left:2000X; Right:5000X

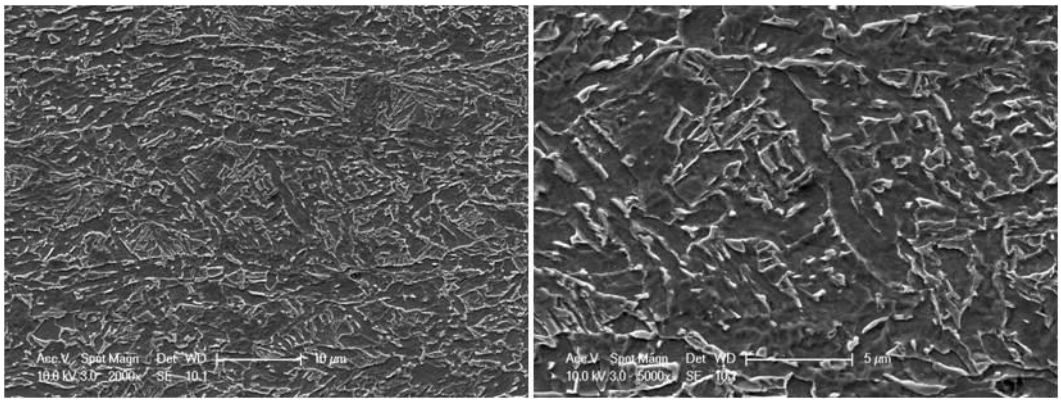

Figure 5.27 SEM micrographs of B-1 (transverse). Left:2000X; Right:5000X

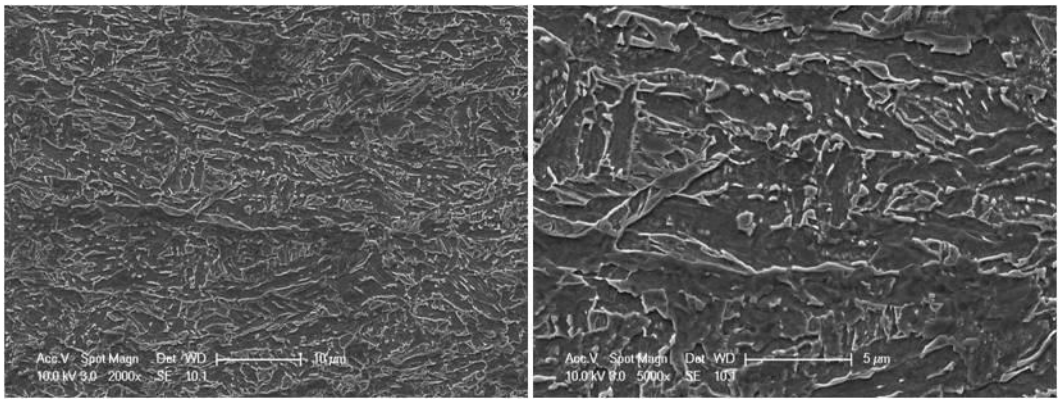

Figure 5.28 SEM micrographs of B-2 (transverse). Left:2000X; Right:5000X

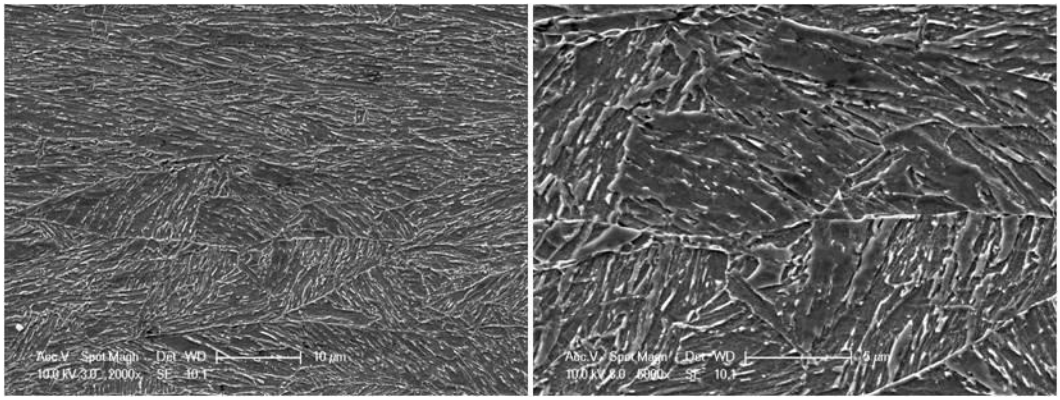

Figure 5.29 SEM micrographs of C-1 (transverse). Left:2000X; Right:5000X

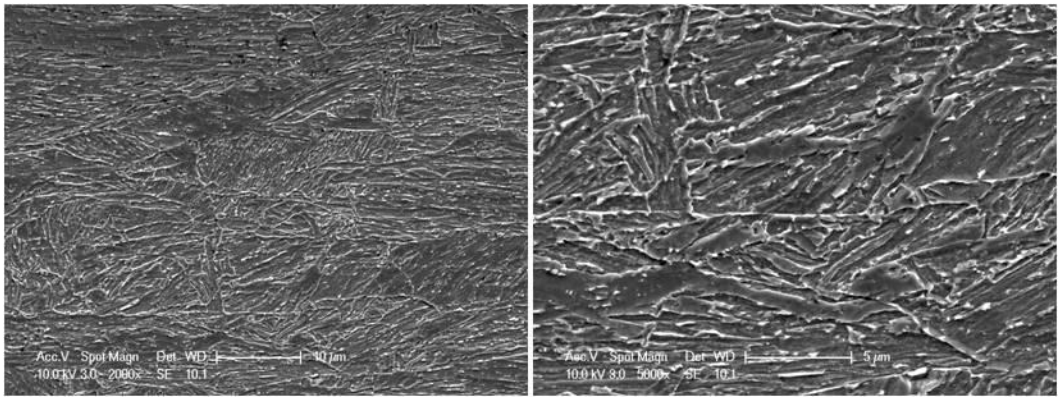

Figure 5.30 SEM micrographs of C-2 (transverse). Left:2000X; Right:5000X

5.3.1.3 **Mechanical properties**

The Vickers hardness of the final steels (VHN 500) is shown in Figure 5.31. For processes 1 and 2, the two A steels had hardness values near 280-300VHN, the two B steels near 320VHN and the two C steels near 400VHN. L and T represent longitudinal and transverse directions.

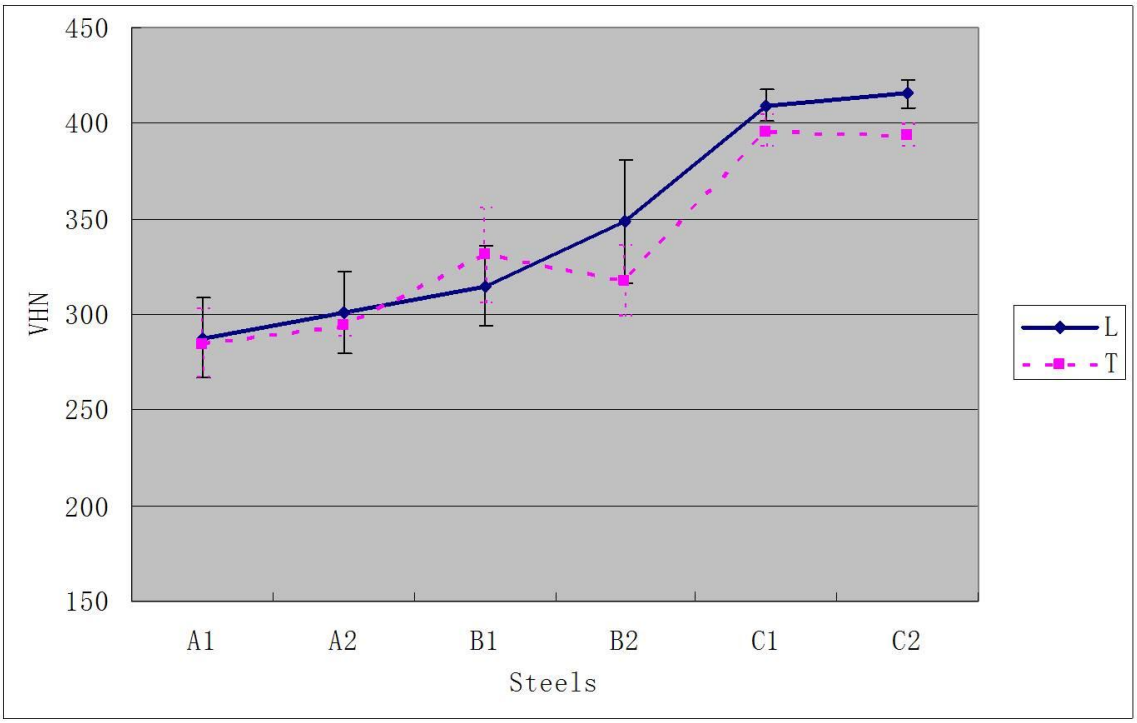

Figure 5.31 Vicker's hardness, load: 500g

The tensile properties of the steels can be predicted from the VHN hardness values. These predictions are shown in Table 5.6. The VHN of steel A-1 was about 285 and steel A-2 about 298. These hardness values would lead to predicted UTS levels near 135KSi or 930MPa and yield strengths of 121 KSi or 837MPa. The B steels with VHN levels over 315 would have

predicted UTS values over 145 KSi or 999 MPa. This would result in predicted yield strengths over 130 KSi or 899MPa.

The reheating and hot rolling behaviors of the steels were as expected. Unfortunately, the small thickness of the rolling block (75mm) meant that fairly small reductions could be applied during hot rolling, from 75 to 12.5mm. This caused the as-rolled austenite to be somewhat coarse with limited pancaking. The toughness of the steels might be limited by this rolling.

Table 5.6 Strength properties predicted from hardness values

	Transverse			**Longitudinal**		
	Hardness	Predicted UTS	YS=UTS*0.8	Hardness	Predicted UTS	YS=UTS*0.8
1	284.7	130.0	104.0	287.8	131.5	105.2
2	294.1	134.3	107.4	301.0	137.4	109.9
1	330.8	150.6	120.5	315.0	143.6	114.9
2	317.5	144.7	115.8	348.4	158.8	127.0
1	395.8	179.7	143.8	409.2	185.8	148.6
2	393.6	178.8	143.0	415.6	188.6	150.9

* converted from hardness data

The accelerated cooling data resulting from the laboratory rolling revealed that even with continuous water spray impingement, it is not likely to consistently have a uniform and constant cooling rate from the finish rolling temperature to the vicinity of 400 ℃. This will have a large and probably negative effect on final microstructure and properties. Clearly, the global literature

is very misleading in this area and more work must be done to better stabilize the cooling system and its effect.

5.3.2 **Second round hot rolling experiment**

The second hot rolling experiment was conducted to investigate the heavy deformation on the microstructure and mechanical properties. The chemical compositions of the steels used are listed in Table 5.7. The chemical compositions are very similar to those in Table 4.2. The steels were named A2, B2 and C2 to compare the corresponding steel in Table 4.2.

Table 5.7 Chemical compositions, wt%

	C	Mn	P	S	Si	Cr	Mo	Ti	Al	N	Nb	B	Cu	Ni	V	Ceq	Pcm
A-2	0.072	1.87	0.009	0.0015	0.30	0.30	0.15	0.001	0.03	0.0049	0.04	0.00011	0.25	0.25	0.003	0.51	0.22
B-2	0.071	1.86	0.009	0.0014	0.30	0.50	0.25	0.010	0.03	0.0048	0.04	0.00014	0.25	0.25	0.003	0.56	0.23
C-2	0.071	1.84	0.009	0.0014	0.30	0.49	0.39	0.010	0.03	0.004	0.04	0.00171	0.25	0.48	0.003	0.60	0.25

5.3.2.1 **Thermomechanical processing**

The ingots were reheated for hot rolling at 1218 ℃ for three hours, transferred immediately to the hot mill, where they were hot rolled from 100mm in thickness to 12.5 mm in five passes of approximately 34% reduction each. Since the 100mm square ingots are known to lose about 350-400 ℃ during the rolling process, the soaking temperature of 1218 ℃ was chosen to permit finishing temperatures of 800-850 ℃ to be achieved. The first pass was applied at approximately 1150 ℃ and two different finishing temperatures were used for each steel, 850 ℃(for processes labeled 1,2 and 3) and 800 ℃(for process labeled 4). The total reduction in the five passes

expressed as true strain is -2.08 and the average pass true reduction strain is -0.415(-34% reduction per pass as linear strain). It appears that the first two passes were applied above, and the last three passes took place below the T_5, the recrystallization-stop temperature. The choice of cooling rate depends on the CCT diagram after controlled rolling for the steel in question and the final microstructure required. There are numerous CCT diagrams in the literature for low and very low carbon steels of reasonable hardenability. An example is shown in Figure 5.32[99].

It is clear from Figure 5.32, that a cooling rate in excess of about 15 ℃/sec is required to maximize the amount of bainitic ferrite(BF) and quasi-polygonal ferrite(QF) and to minimize the amount of granular bainite(GB). This cooling rate agrees with the earlier work on X70-X120[3, 4, 12, 15, 100].

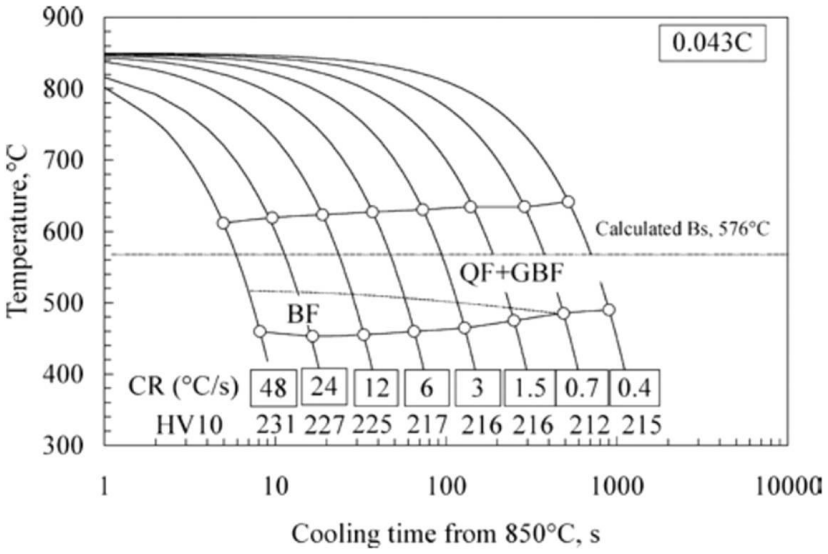

Figure 5.32 CCT Diagram from deformed austenite. Composition: 0.043C - 2Mn – 0.5Mo - 0.06Nb

In the production of high strength plate steels, and based on published information, the plates are interrupted direct-quenched immediately after hot rolling. The quenching rate was

selected as 30℃/sec, a high rate but certainly well within the capacity of modern, production cooling systems[101] , and high enough to avoid ferrite, pearlite and granular bainite in the final plate. Once the quench rate is set, the quench-end or water-end temperatures must be specified. This temperature is based on the Bs and Ms temperatures, and together with the cooling path, will determine the nature of the microstructure. With consideration of Bs and Ms temperatures in 5.2, the experimental plan requested for rolling (finishing temperatures), quench rate, and WET1 is shown in Table 5.8.

Table 5.8 Experimental Process Design (Aim Values)

Designation	T_{FIN}, ℃	Quench Rate, ℃/sec	WET, ℃
1	850	30	300
2	850	30	400
3	850	30	500
4	800	30	400

Cooling rates are believed to be very important from CCT diagram. The experimental cooling rates actually applied to the 12mm plates after hot rolling were determined in three ways: (i) Internal thermocouple(Chromel-Alumel) located at the mid-thickness of the plates, (ii) Ircon pyrometer, and (iii) Touch thermocouples. The touch thermocouples read temperatures at three different locations on the rolled plate during the last portion of the water cooling period. In this

[1] Water End Temperature: This definition is similar to finishing cooling temperature in other sections.

diagram of the location of the touch thermocouples, Figure 5.33, the plate was moving right-to-left.

The compositions and hot rolling parameters are very similar to the aimed results. Unfortunately, the post-rolling cooling practices were not as reliable as was expected. As described above, there can be up to five temperature readings made during water cooling/quenching: one from the internal thermocouple, one from the IRCON pyrometer, and three from the touch thermocouples. By way of an example, the cooling curves for steel B2-2 are given in Figure 5.34 as an example.

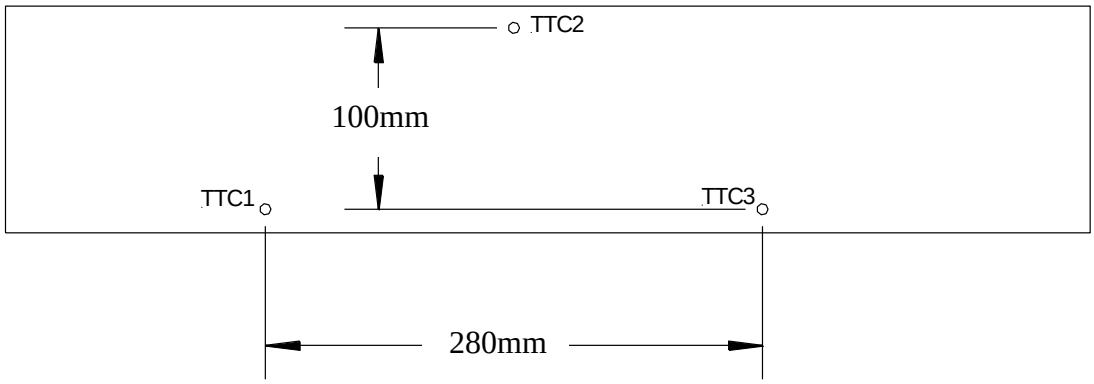

Figure 5.33 The location of the Touch Thermocouples TTC1, TTC2 and TTC3 in a hot rolled plate (dimensions in mm).

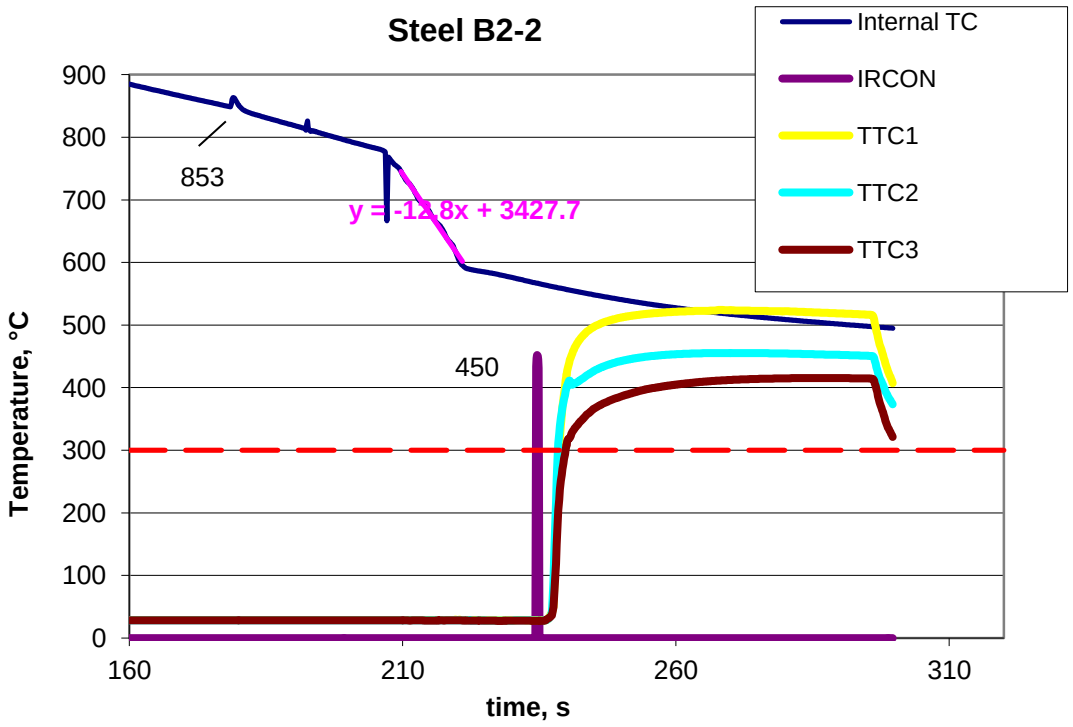

Figure 5.34 The cooling curve of steel B2-2(Steel B, High C. E. Melt Group 2, Cooling Path 2)

As noted above, five temperatures were recorded, respectively, by the internal thermocouple, the IRCON pyrometer, and the three touch thermocouples (TTC1, TTC2 and TTC3) on a plate surface.

From these curves, average cooling rates were determined, and these are shown in Table 5.9, along with the WETs. Again, both the aim and experimental values are shown in this table. Three ways were used to calculate cooling rates: 1. the first way is calculated from the average temperatures; 2 the second is from the IRCON temperatures; 3. the third one is calculated from internal temperatures, at least while they were fully functional. The WETs in the table are obtained from the average thermocouple data except the two temperatures denoted by bold font.

5.3.2.2 **Microstructural characterization**

The microstructures of the three steels with different processes are shown in Figure 5.35. The microstructures of Steel A2 and B2 are composed of granular bainite. However, the microstructures of steel C2 are lower bainite or martensite. The SEM micrographs in Figure 5.36 give further details of microstructures of the steels. The granular bainite comprises many MA constituents. The size of most of the MA is about 1-2 microns in steel A2 and B2. The microstructures of steel C2 are typical lower bainite and martensite, except C2-2 with granular bainite due to its very slow cooling rate.

Table 5.9 Average cooling rates and the water end temperatures

1*[2] AVG	A**[3] WET, ℃	B WET, ℃	C WET, ℃	A CR, ℃/s	B CR, ℃/s	C CR, ℃/s
1***[4]	**154**[5]	434	397	--	--	31.5
2***	526	495	**576**	6	6.7	2.8
3***	489	513	319	6	7.6	7.8
4***	555	509	343	4.9	5.6	6
2* IRCON	A WET, ℃	B WET, ℃	C WET, ℃	A CR, ℃/s	B CR, ℃/s	C CR, ℃/s
1***	--	468	454	--	9.4	9.6
2***	461	450		8.2	11.5	--
3***	450	425		12	--	--
4***	540	452		--	9.9	--
3* Internal	A WET, ℃	B WET, ℃	C WET, ℃	A CR, ℃/s	B CR, ℃/s	C CR, ℃/s
1***	154	399	340	66.3	32	31.5
2***	593	529	576	9	12.8	9
3***	517	572	400	12.8	10.4	12.4
4***	599	572		8	9.3	--

[2] 1-3* represent different averaging techniques. Here 1* represents the cooling from the start of cooling to the WET using all of the 5 data inputs, 2* from the start of cooling to the WET defined by the Ircon Pyrometer, and 3* from the start of cooling using only the embedded T/C(the slope of the cooling curve).

[3] A-C** represent the three steels.

[4] 1-4*** represent the cooling path identification and finish rolling temperature

[5] The WETs shown in bold font were determined without the center T/C.

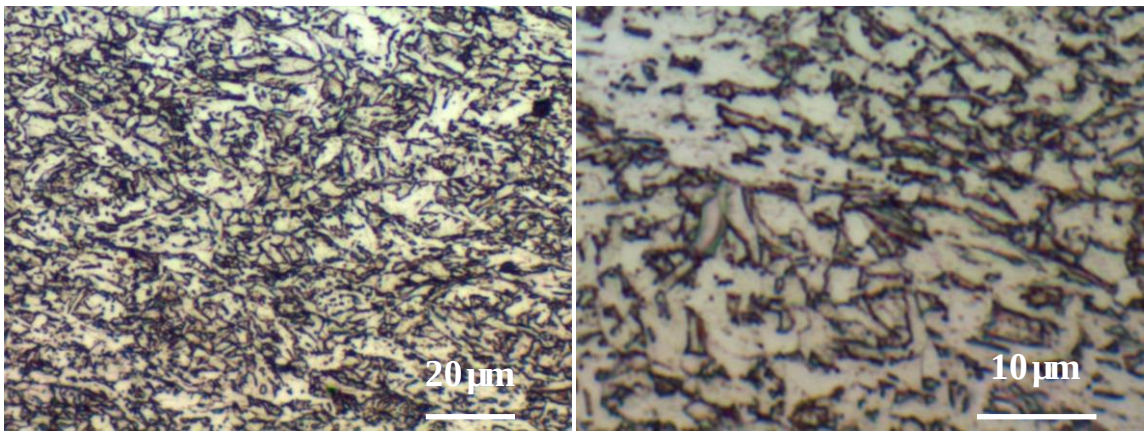

a A2-1T optical microstructure, Nital

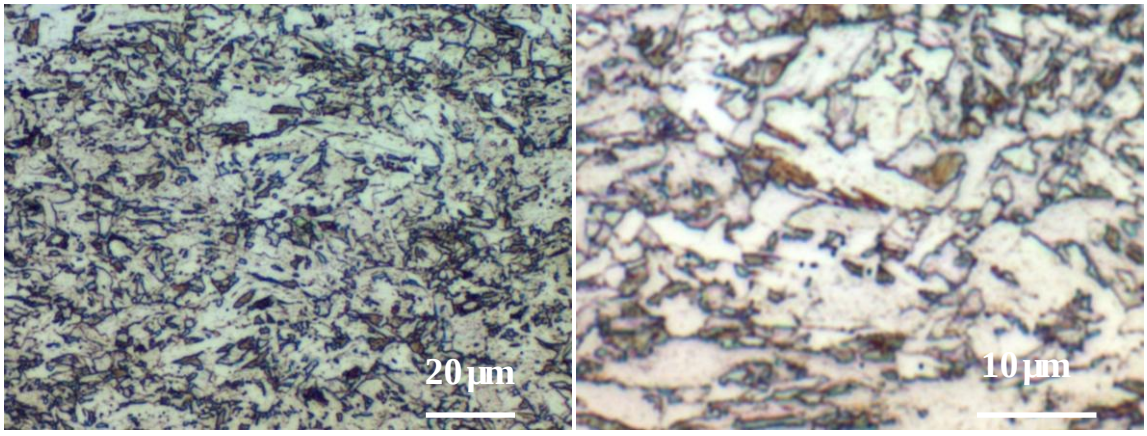

b A2-2T optical microstructure, Nital

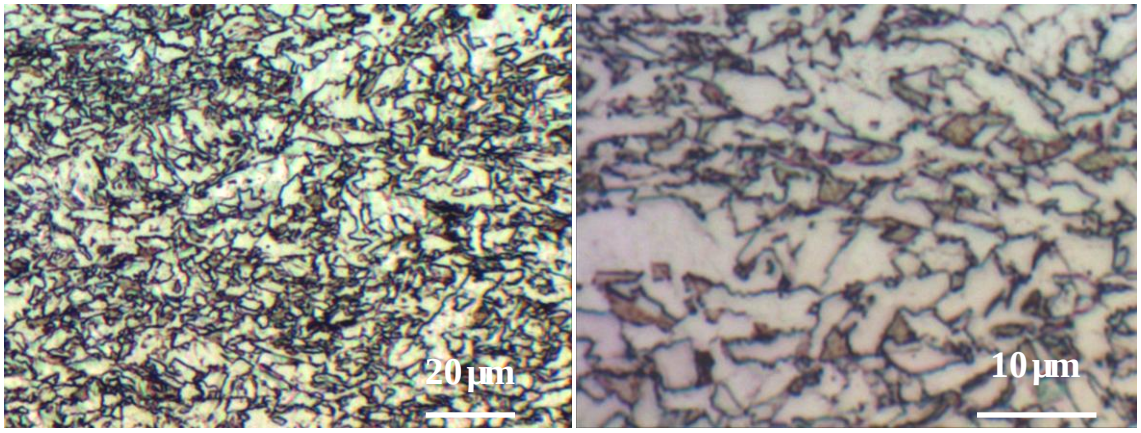

c A2-3T optical microstructure, Nital

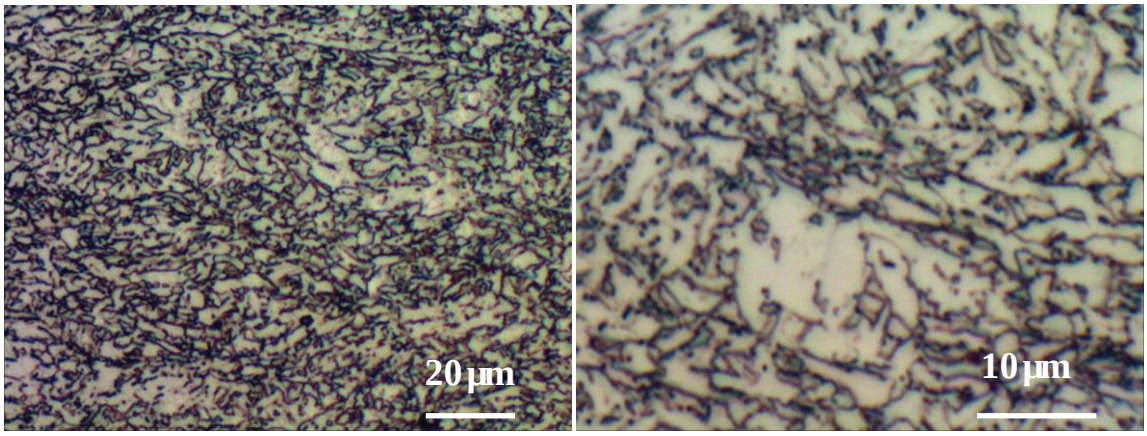

d A2-4T optical microstructure, Nital

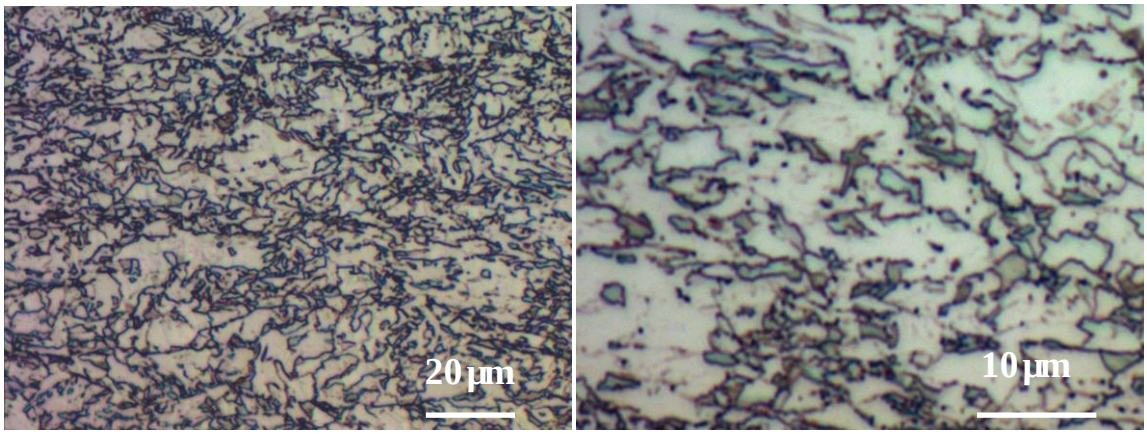

e B2-1T optical microstructure, Nital

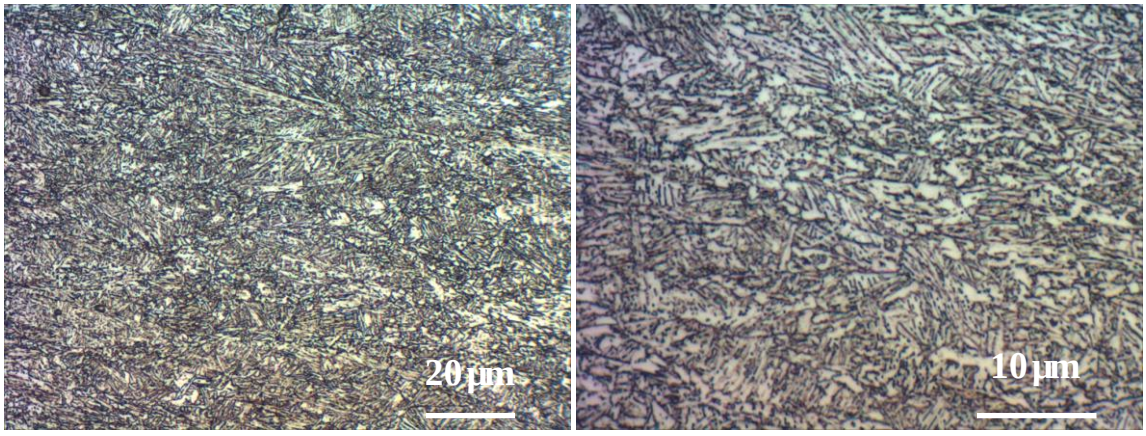

f B2-2T optical microstructure, Nital

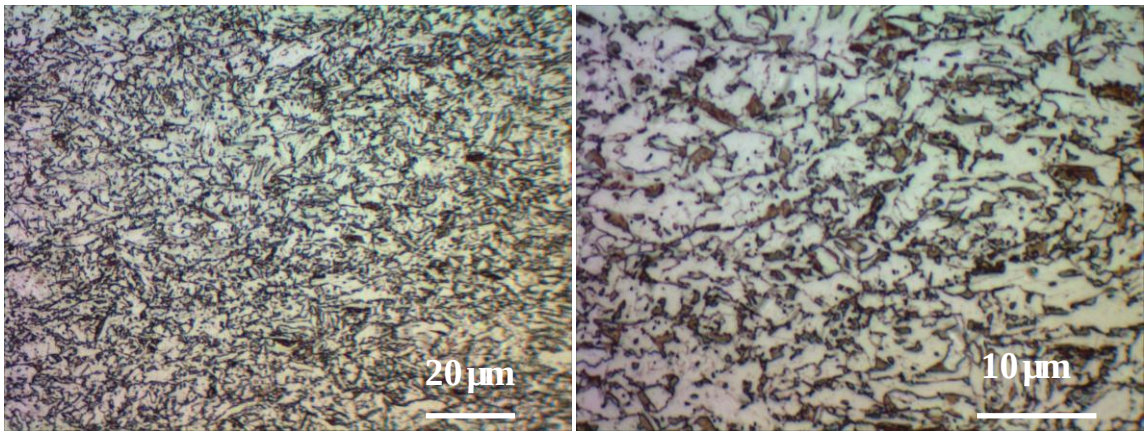

g B2-3T optical microstructure, Nital

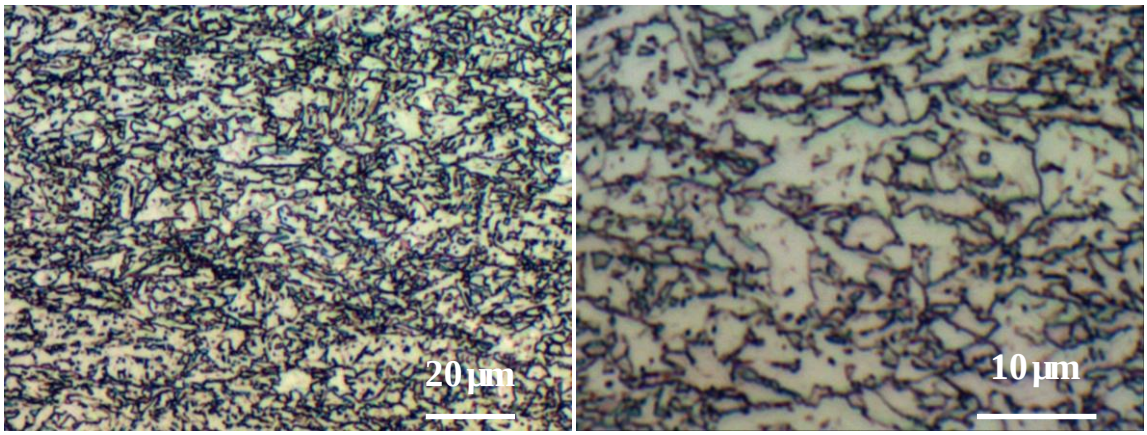

h B2-4T optical microstructure, Nital

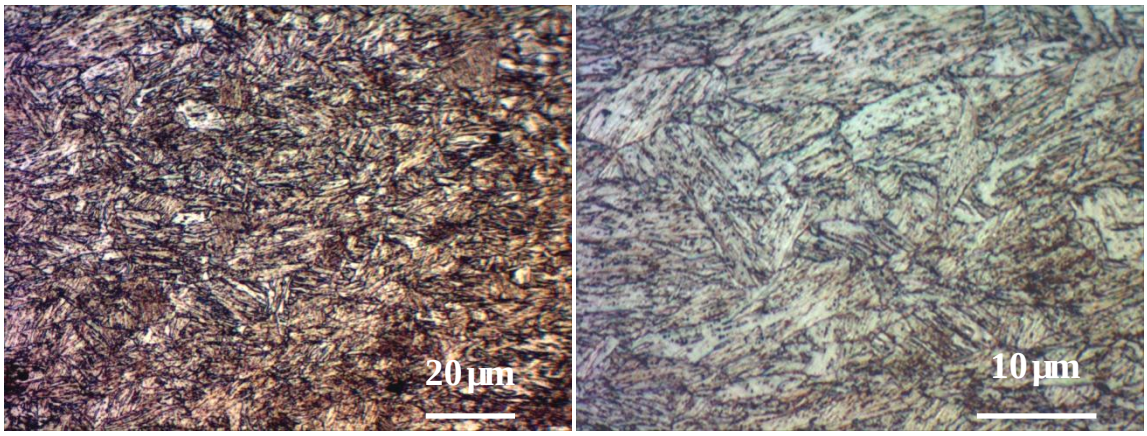

i C2-1T optical microstructure, Nital

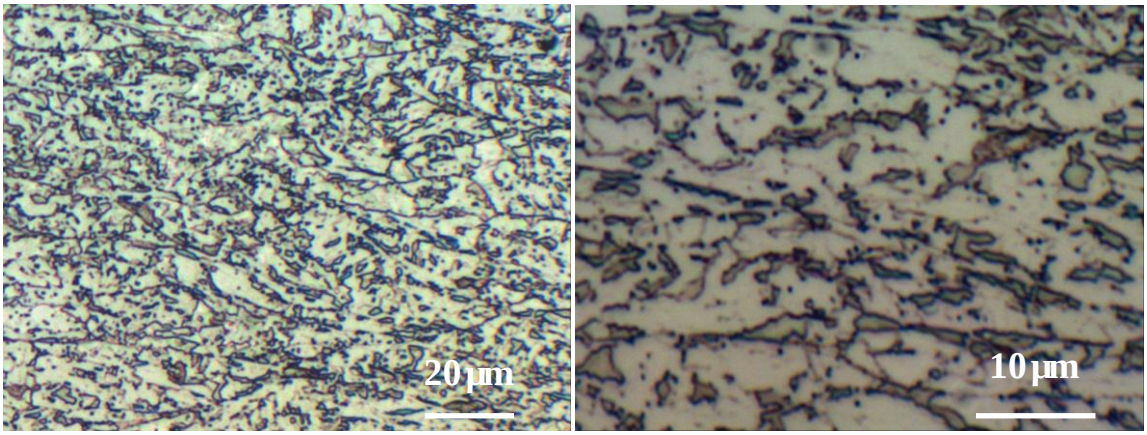

j C2-2T optical microstructure, Nital

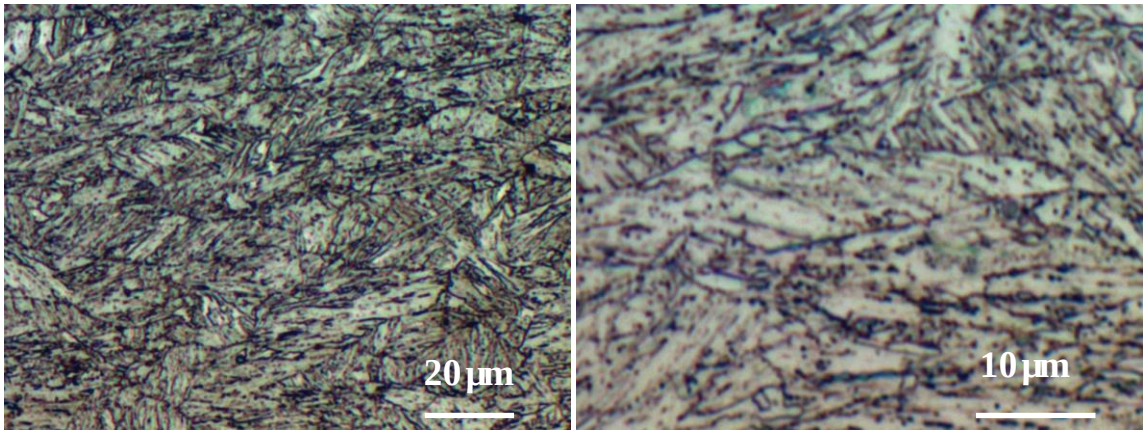

k C2-3T optical microstructure, Nital

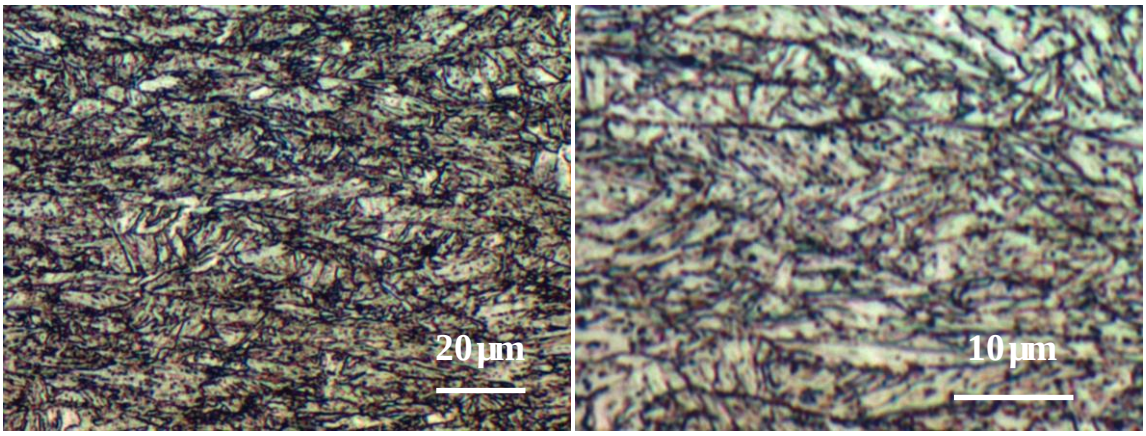

C2-4T optical microstructure, Nital

Figure 5.35 Optical microstructure of Steels A2，B2 & C2 in transverse direction

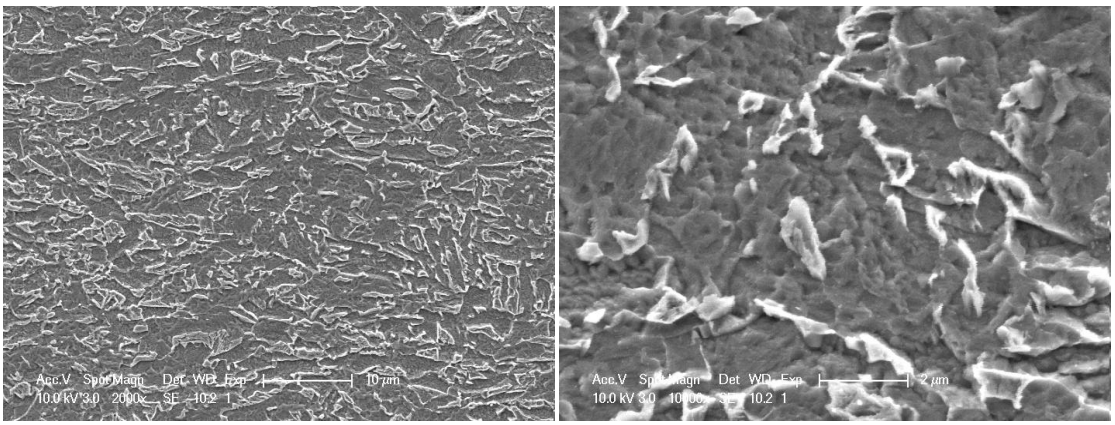

a A2-1T SEM, lower magnification(left), higher magnification(right), Nital

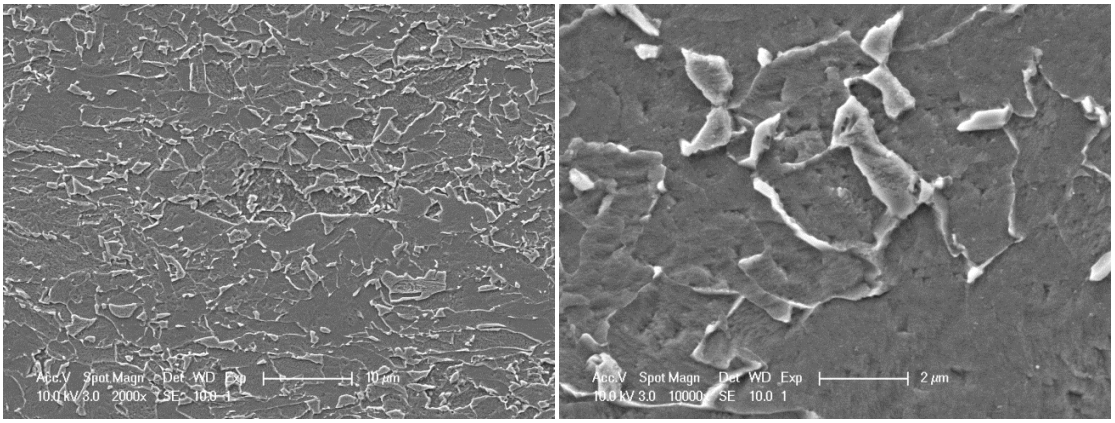

b A2-2T SEM, lower magnification(left), higher magnification(right), Nital

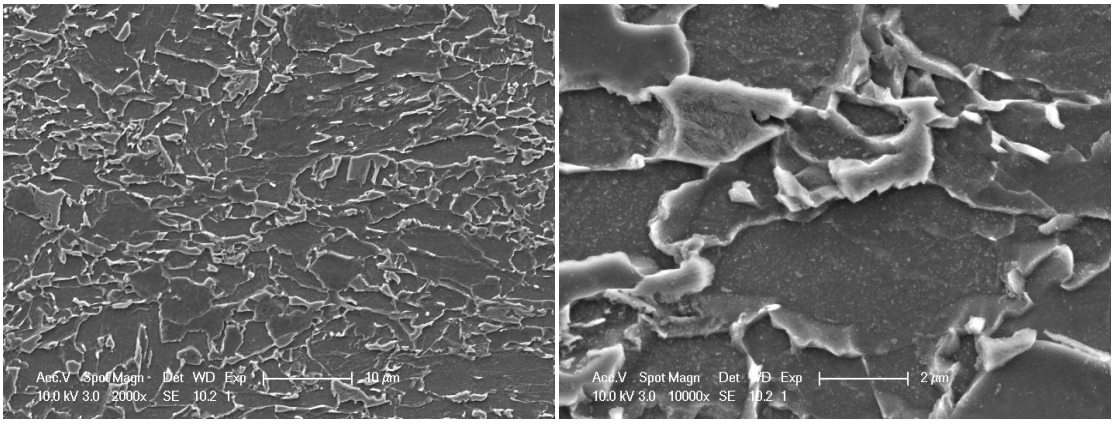

c A2-3T SEM, lower magnification(left), higher magnification(right), Nital

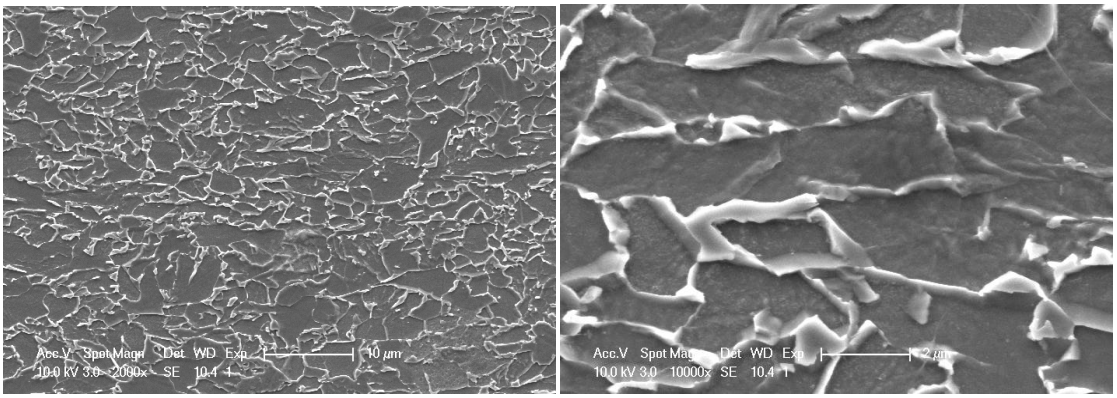

d A2-4T SEM, lower magnification(left), higher magnification(right), Nital

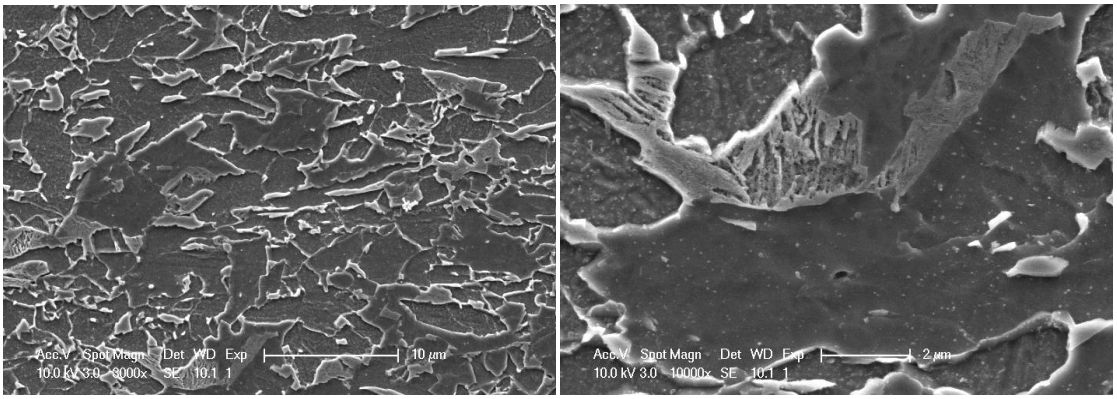

e B2-1T SEM, lower magnification(left), higher magnification(right), Nital

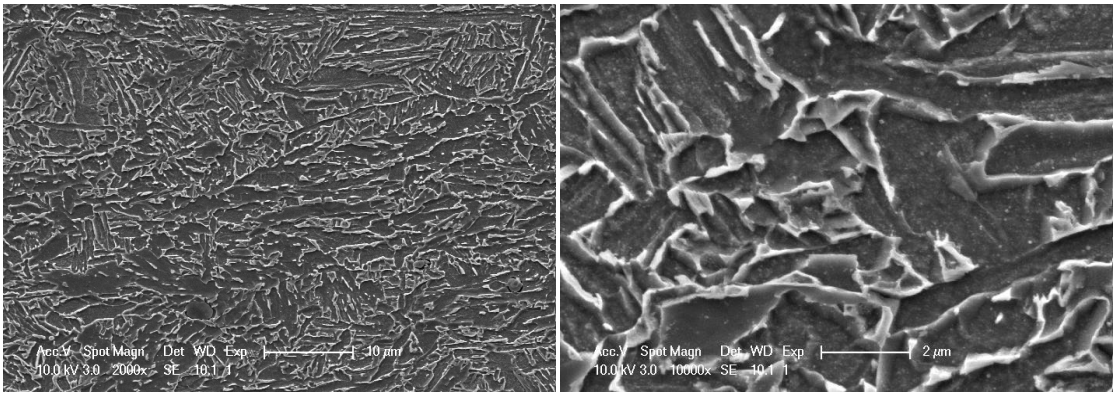

f B2-2T SEM, lower magnification(left), higher magnification(right), Nital

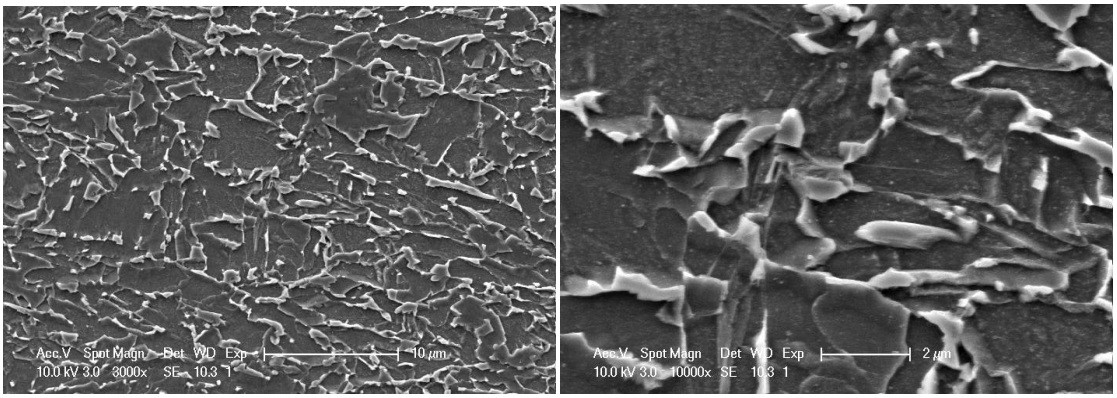

g B2-3T SEM, lower magnification(left), higher magnification(right), Nital

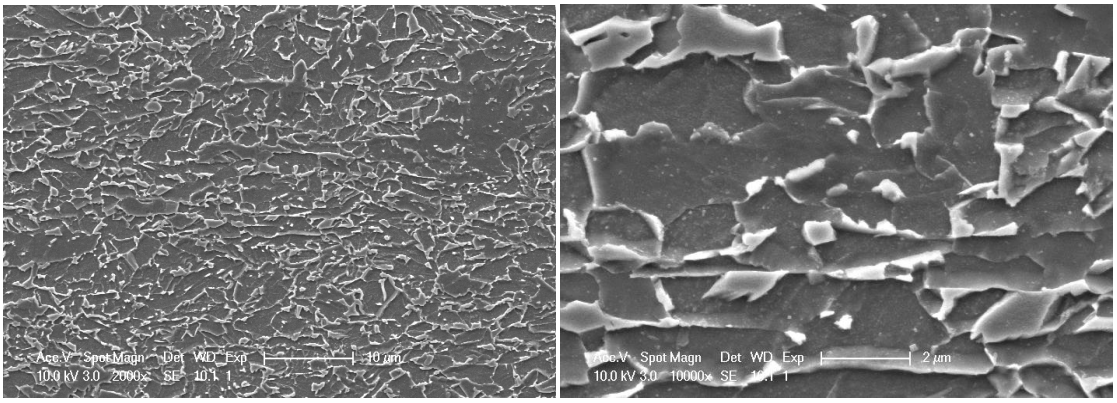

h B2-4T SEM, lower magnification(left), higher magnification(right), Nital

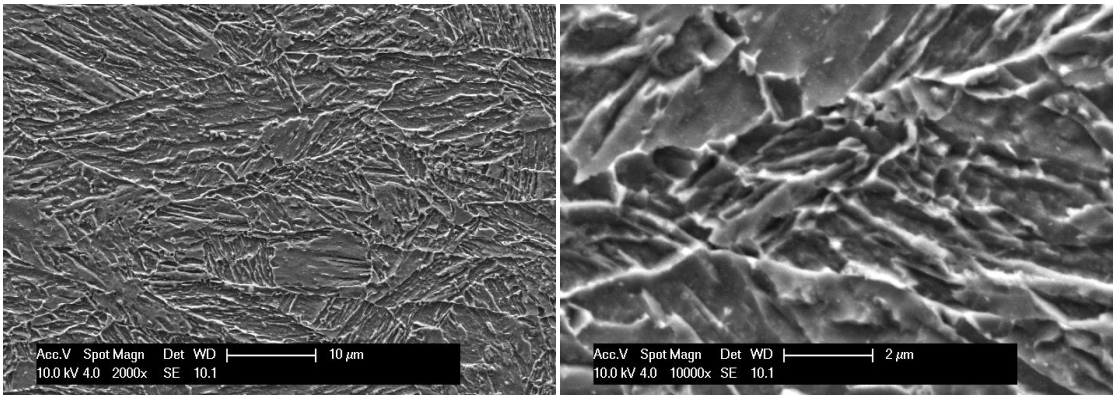

i C2-1T SEM, lower magnification(left), higher magnification(right), Nital

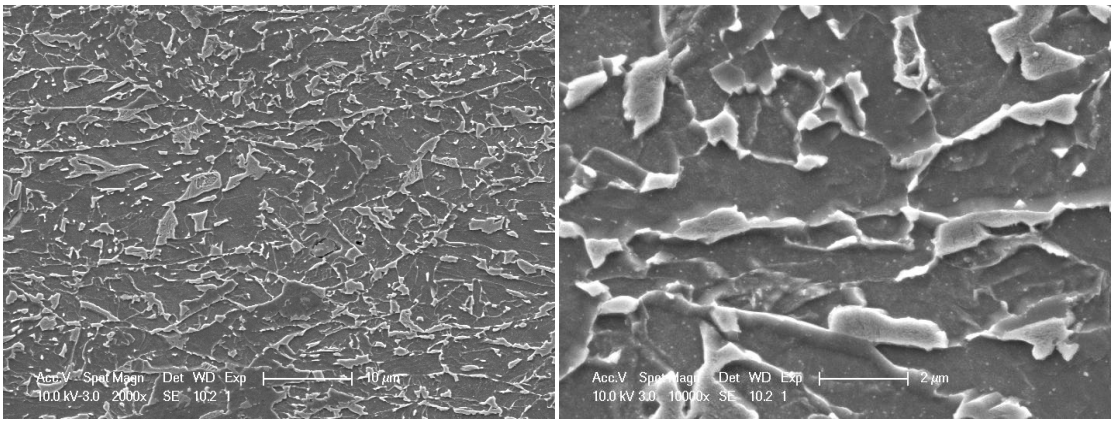

j C2-2T SEM, lower magnification(left), higher magnification(right), Nital

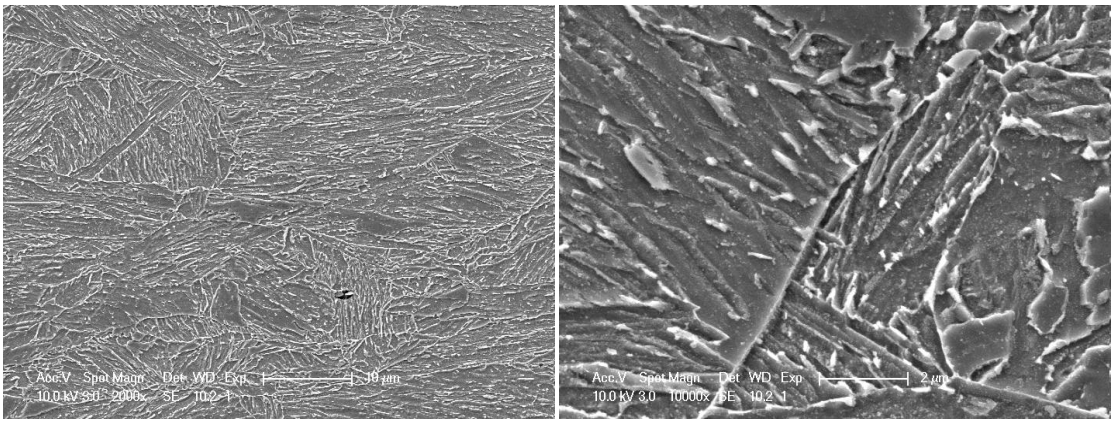

k C2-3T SEM, lower magnification(left), higher magnification(right), Nital

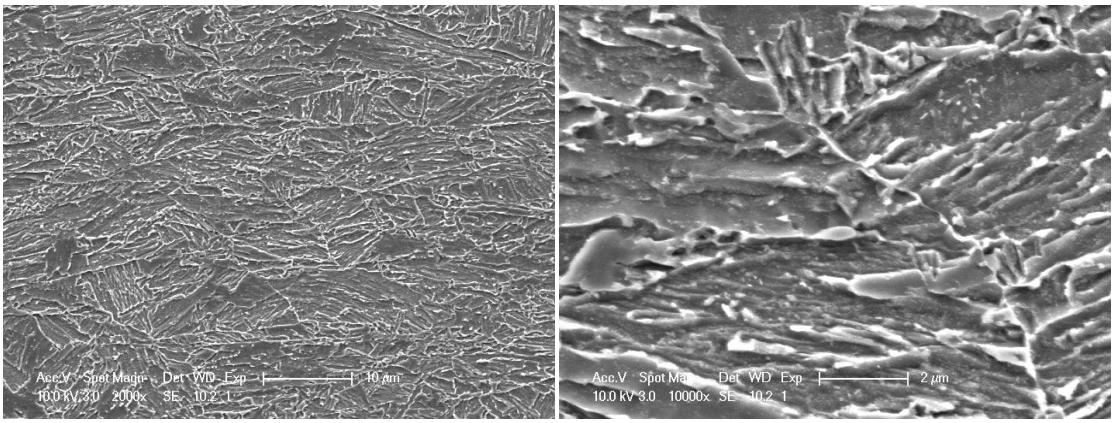

l C2-4T SEM, lower magnification(left), higher magnification(right), Nital

Figure 5.36 SEM micrographs of Steel A, B & C, etched with nital

5.3.2.3 **Mechanical properties**

The tensile results such as YS, UTS, the ratio of YS and UTS, the uniform elongation and total elongation, and Vickers hardness(VHN) are listed in Table 5.10. The large difference between VHN and strength in steel C2-4 is from the different area of plate cooled at different rate due to the non-uniform cooling of the steel plate.

Table 5.10 The tensile properties(Longitudinal direction)

Sample No.	YS, Mpa	UTS, Mpa	YS/TS ratio	VHN (500g)	El%	
					UE	TE
A2-1	648	886	0.73	270	7.8	26.6
A2-2	543	782	0.70	272	9.2	27.1
A2-3*[6]	604	789	0.76	273	8.6	27.7
B2-1	704	864	0.82	268	6.3	25.0
B2-2	691	831	0.83	302	6.6	25.8
B2-3	701	841	0.83	270	7.2	26.2
B2-4	703	841	0.84	269	8.0	27.7
C2-1	964	1161	0.83	377	4.3	19.2
C2-4(**)[7]	724	978	0.74	377	6.7	21.8

[6] The symbol(*) denotes unreliable average caused by a large variation in results from the two tensile tests.

[7] The symbol(**) denotes a lower than expected strength based on the VHN of the CVN impact specimens.

Table 5.11 lists the upper shelf energy (USE) and the impact transition temperatures at 50J, 100J and 150J. As shown in the table, the upper shelf energy and impact transition temperatures are very different for the same composition but with different cooling process.

Table 5.11 Impact transition temperatures (℃) at 50,100 & 150J and the upper shelf energy (T-L)

	50J	**100J**	**150J**	**USE,J**
A2-1T	-77	-66	-58	235
A2-2T	-43	-18	-6	190
A2-3T	-40	-16	4	193
B2-1T	-95[8]	-83	-66	264
B2-2T	-71	-62	-55	263
B2-3T	-44	-17	-7	196
C2-1T	-25	--	--	88
C2-4T	-60	0	--	100

[8] The data indicated in red are obtained by extrapolation.

5.3.3 **The interrupt direct quenching**

During the hot rolling stage, the processes were designed to obtain a fine and uniform austenite during rough rolling and heavy pancaking of austenite during the finishing reduction. Another hot rolling, interrupt direct quenching was used for steel A, B and C. The process is shown in Figure 4.4. Other samples were direct quenched into water to room temperatures immediately after rolling. These steels were labeled A-3, B-3 and C-3.

All three steels A-3, B-3 and C-3 have largely martensitic microstructures, as illustrated in the SEM micrographs, Figure 5.37-Figure 5.39. As shown in high magnification of SEM micrographs, the martensite has different packet sizes in Steel A, B & C. Sample B-3 has the smaller packet size than sample A-3 because of the refinement of austenite grain size by titanium. However, the packet size of martensite in sample C-3 is huge, which can be more than 40μm, as shown in Figure 5.39.

The Vickers hardness data were measured for the direct quenched steels, and the sample C-2 is listed for comparison in Figure 5.40. L and T represent the hardness tested in the longitudinal or transverse direction. The figure illustrates that the hardness of sample A-3 can be a little higher than B-3, even though B has higher alloy contents. This should be because steel A is without titanium, the austenite grain size can be 20μm larger than steel B, as shown in the results in Table 5.1. That may increase the hardenability of steel A. Steel C has the highest hardness values because of its high alloy contents and boron in steel.

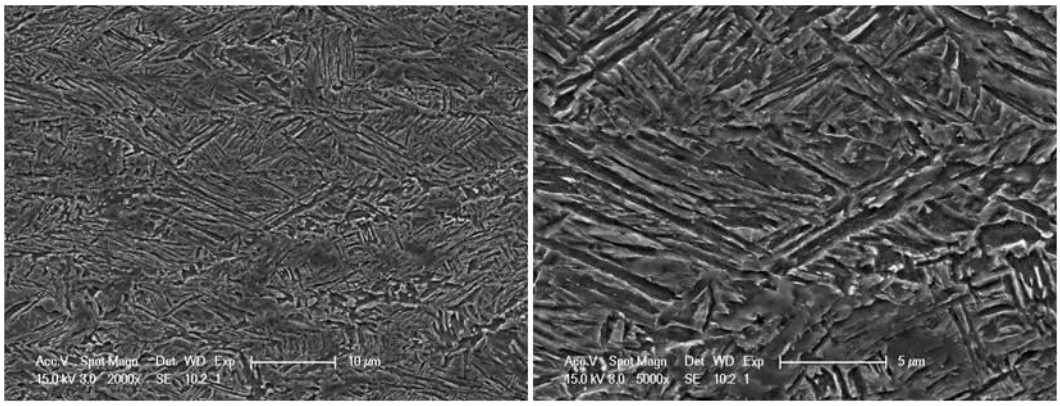

Figure 5.37 SEM micrographs of A-3 (transverse). Left:2000X; Right:5000X

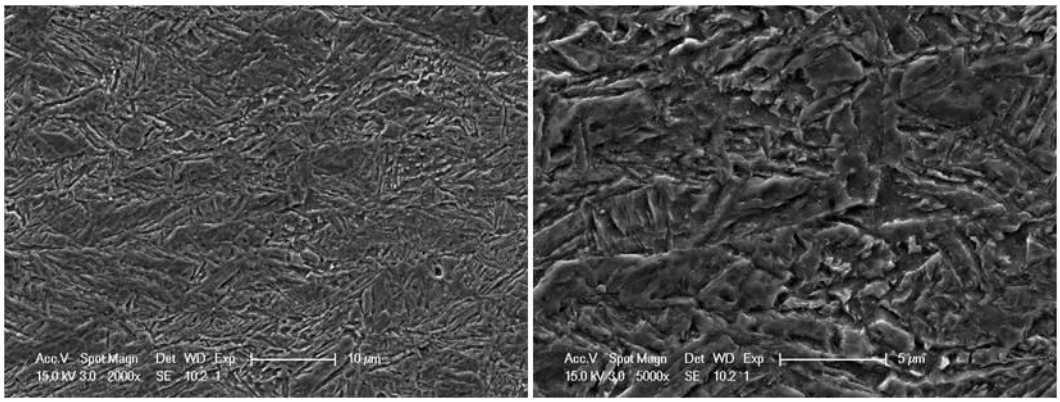

Figure 5.38 SEM micrographs of B-3 (transverse). Left:2000X; Right:5000X

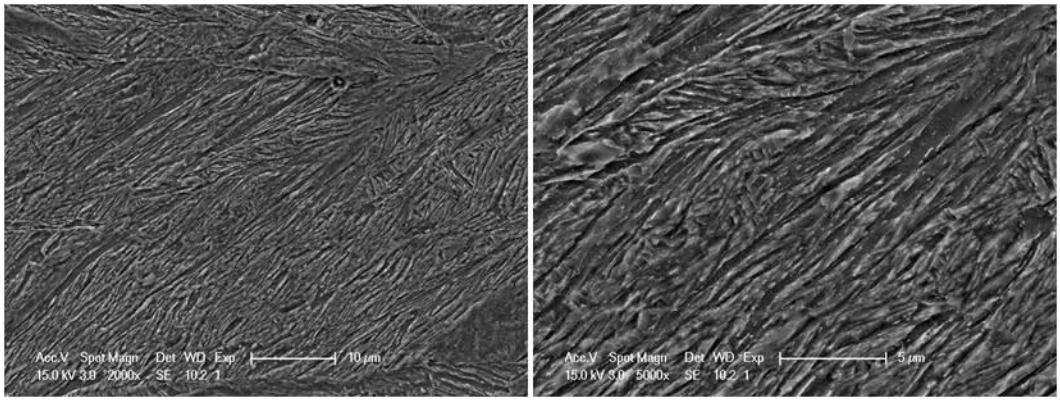

Figure 5.39 SEM micrographs of C-3 (transverse). Left:2000X; Right:5000X

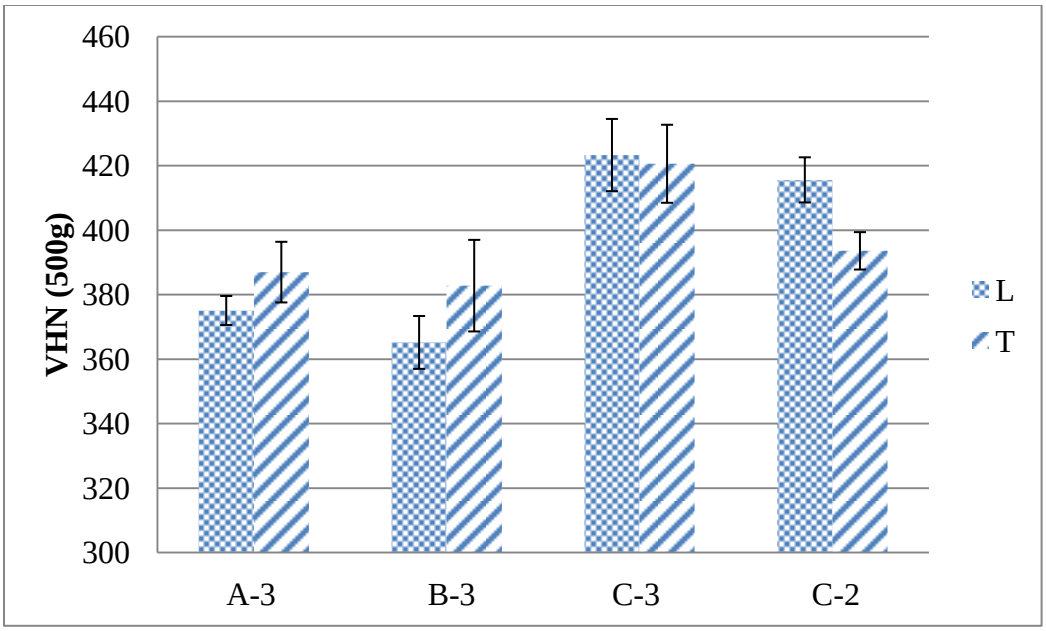

Figure 5.40 Vickers Hardness, L: longitudinal direction; T: transverse direction.

Table 5.12 Tensile data of C-2 and B-3

	Transverse			**Longitudinal**		
	Elongation	UTS, MPa	YS, MPa	Elongation	UTS, MPa	YS, MPa
C-2	19.05%	1164	960	23.5%	1140	932
B-3				19%	1096	882

Table 5.13 The absorbed energy in Charpy impact testing(Unit: Joule)

	A-3		B-3		C-2
	-20 ℃	-40 ℃	-20 ℃	-40 ℃	-20 ℃
Specimen1	119	128	174	170	21
Specimen2	141	150	179	180	15
AVG	130	139	176	175	18

5.3.4 **Characterization of martensite-austenite constituents in hot rolled steels**

Although in the direct quenching steels, the microstructures are mostly martensite. The strength and toughness are mostly dependent on the lath size and the packet size of martensite. However, for the bainitic microstructure, the MA constituent seems to be an important factor that affects the impact toughness of steels. The MA constituents were revealed by LePera etchant for the hot rolled steels in the second experiment. Figure 5.41 a-l revealed the distribution of MA constituents in samples A2-1T to C2-4T. The MA constituents are white after LePera etching. As shown in the Figures, the size and volume fraction of MA vary with steel compositions and cooling patterns.

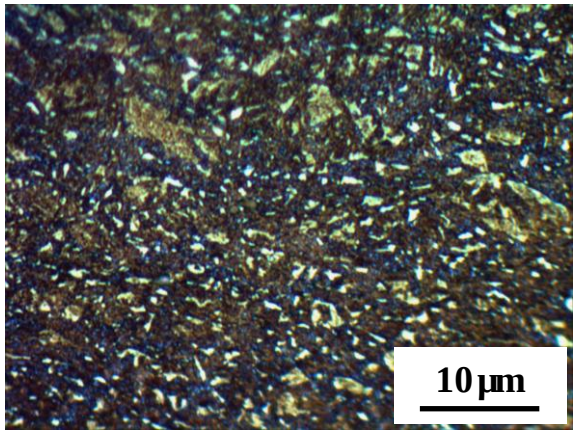

a A2-1T OM + LePera, MA(white area)

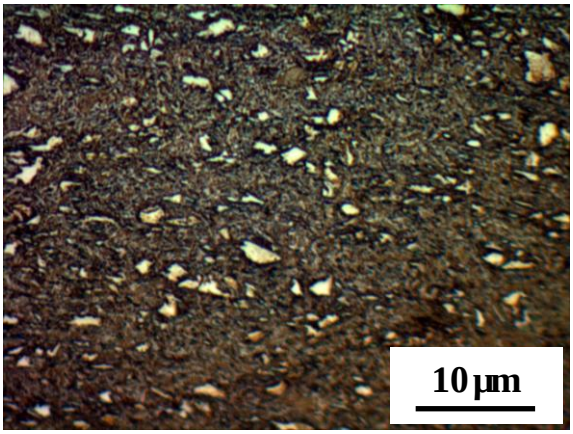

b A2-2T LePera, MA(white area)

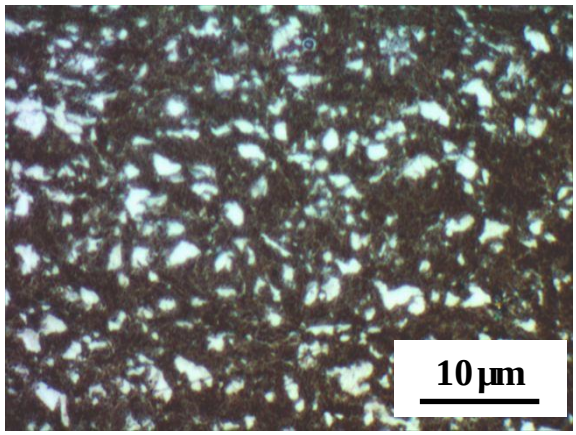

c A2-3T LePera, MA(white)

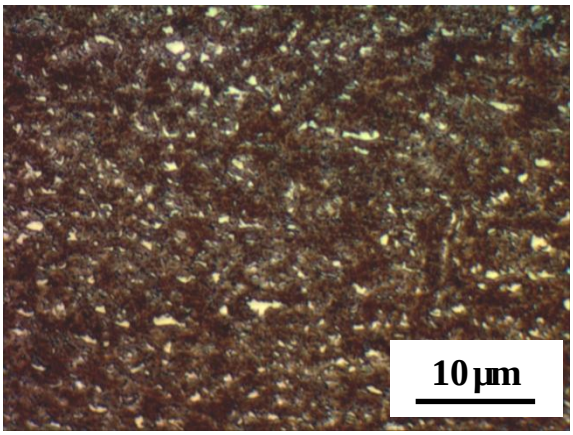

d A2-4T LePera, MA(white)

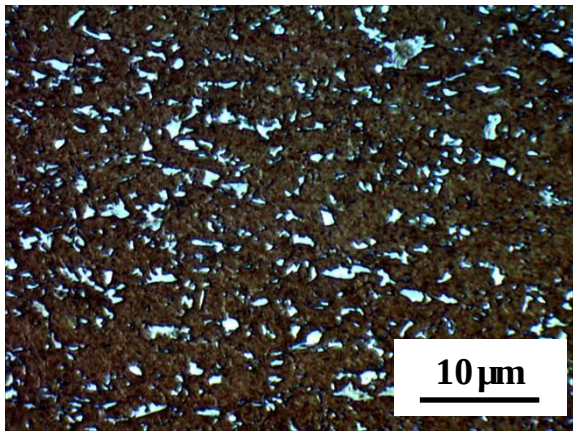

e B2-1T LePera, MA(white)

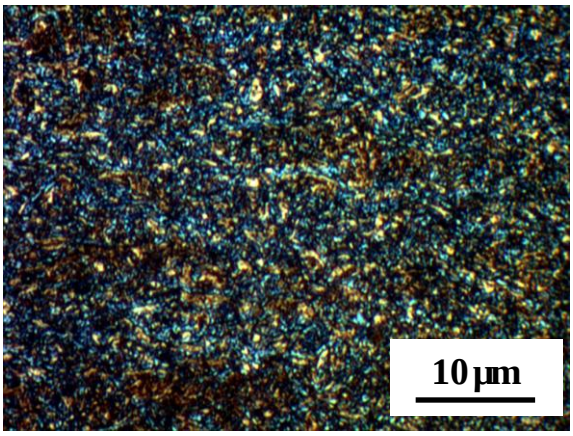

f B2-2T LePera, MA(white)

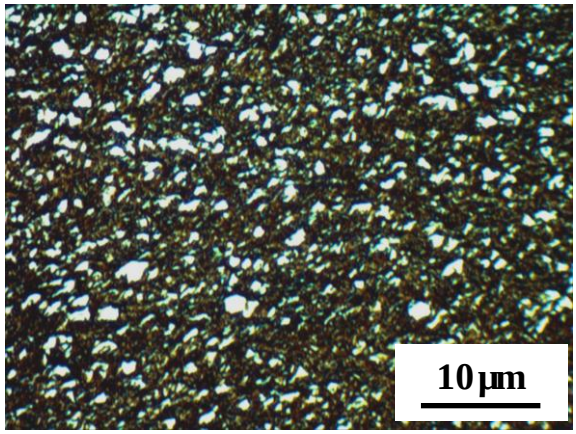

g B2-3T LePera, MA(white)

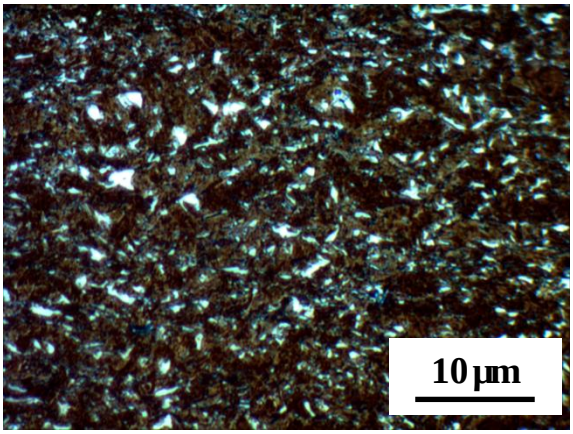

h B2-4T LePera, MA(white)

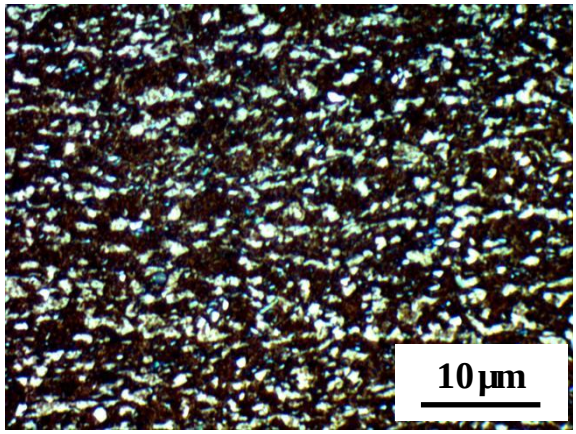

i C2-1T LePera, MA(white)

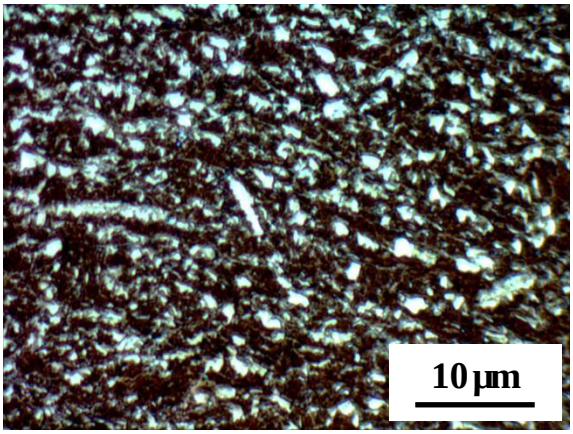

j C2-2T LePera, MA(white)

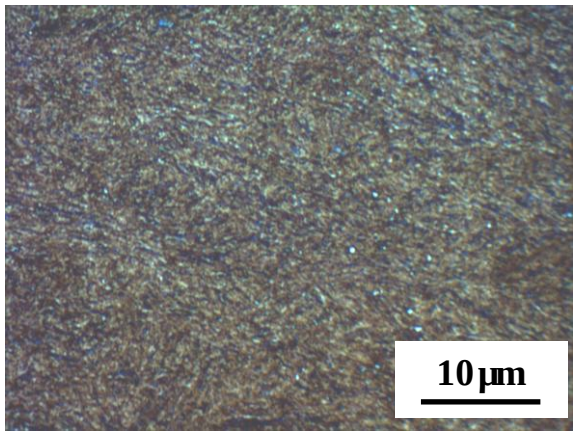

k C2-3T LePera, MA(white)

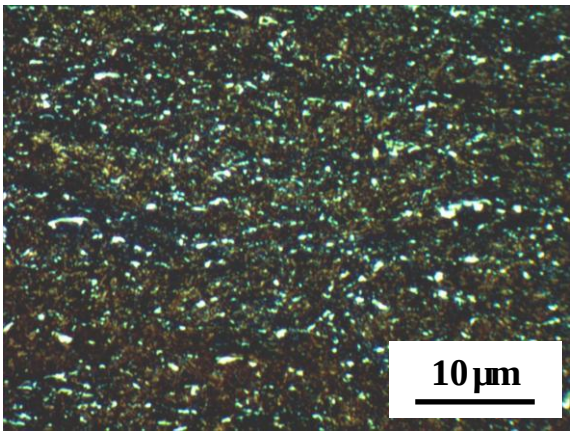

l C2-4T LePera, MA(white)

Figure 5.41 Optical microstructure, etched with LePera; MA(white area)

5.3.5 **Effect of holding time on the formation of bainite**

Figure 5.42 is the schematic diagram for the isothermal heat treatments. The samples in steel 1A were used. Samples were reheated to 1150 ℃ and held for 2 minutes, and then quenched at a fast cooling rate (greater than 30 ℃/s) to 450 ℃ to assure most of austenite decomposes below the bainite start temperature. The different holding time: 1min, 4min, 10min and 40min were investigated at 450 ℃. The optical and SEM microstructures are shown in Figure 5.43 & Figure 5.44. The figures show that microstructures are granular bainite when austenite was cooled down to 450 ℃. Because the austenite is equiaxed without deformation, bainite size looks as big as the size of austenite. With the holding time prolonged, the transformation was changed. After 4 minutes holding, small fractions of martensite or austenite are found along austenite grain boundaries. When the holding time was extended to 10 minutes, increased areas of martensite were seen along the prior austenite grain boundaries. Sample A04, 40 minutes of holding time, contained more and larger segregated microstructures. Some are formed between two adjacent austenite grains. The SEM microstructures and LePera etched microstructures showed more clearly that this kind of massive microstructure is martensite. It may be from the carbon diffusion at 450 ℃. It clearly showed that carbon is easily segregated, firstly to the austenite grain boundaries. During isothermal holding, austenite starts to transform into bainitic ferrite. Because the saturation of carbon is much lower in a ferritic microstructure, the carbon partitions into remaining untransformed austenite. Results also show carbon partitioning does not only take place in a single austenite grain, but carbon segregates into several adjacent austenite grains rather easily, as shown in Figure 5.44 and Figure 5.45(A05). The VHN hardness in Figure 5.46 also showed the second phases (the martensite distributed in the matrix grainular bainite) with

much higher hardness numbers. However, with longer holding time, the hardness of the second phase in A04 is lower than that in A03 due to the existence of more fractions of the second phases and lowering carbon content in martensite with increase of time at 450 ℃.

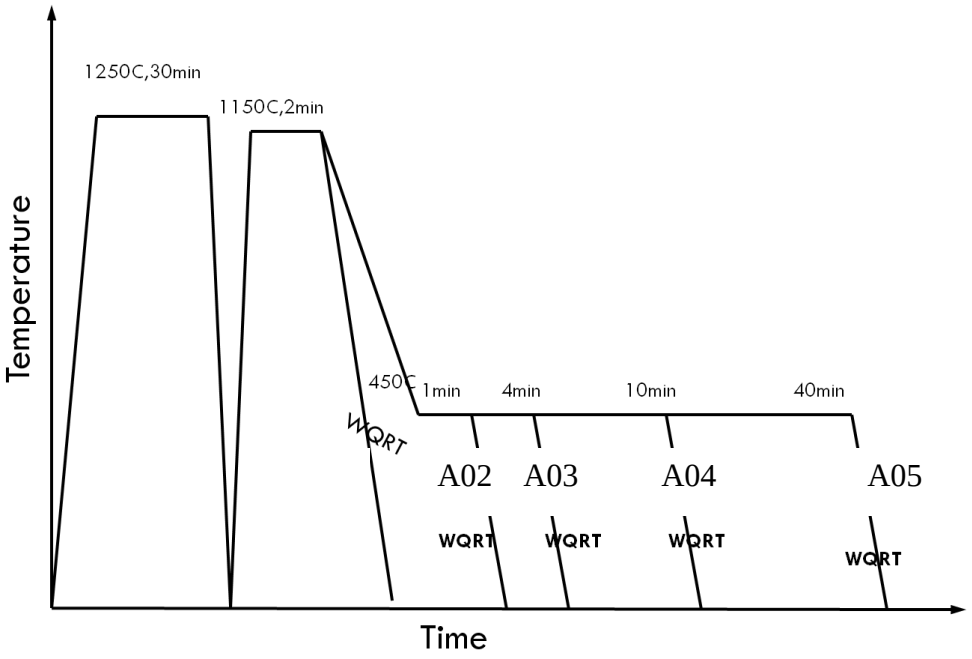

Figure 5.42 Schematic diagram for isothermal heat treatment

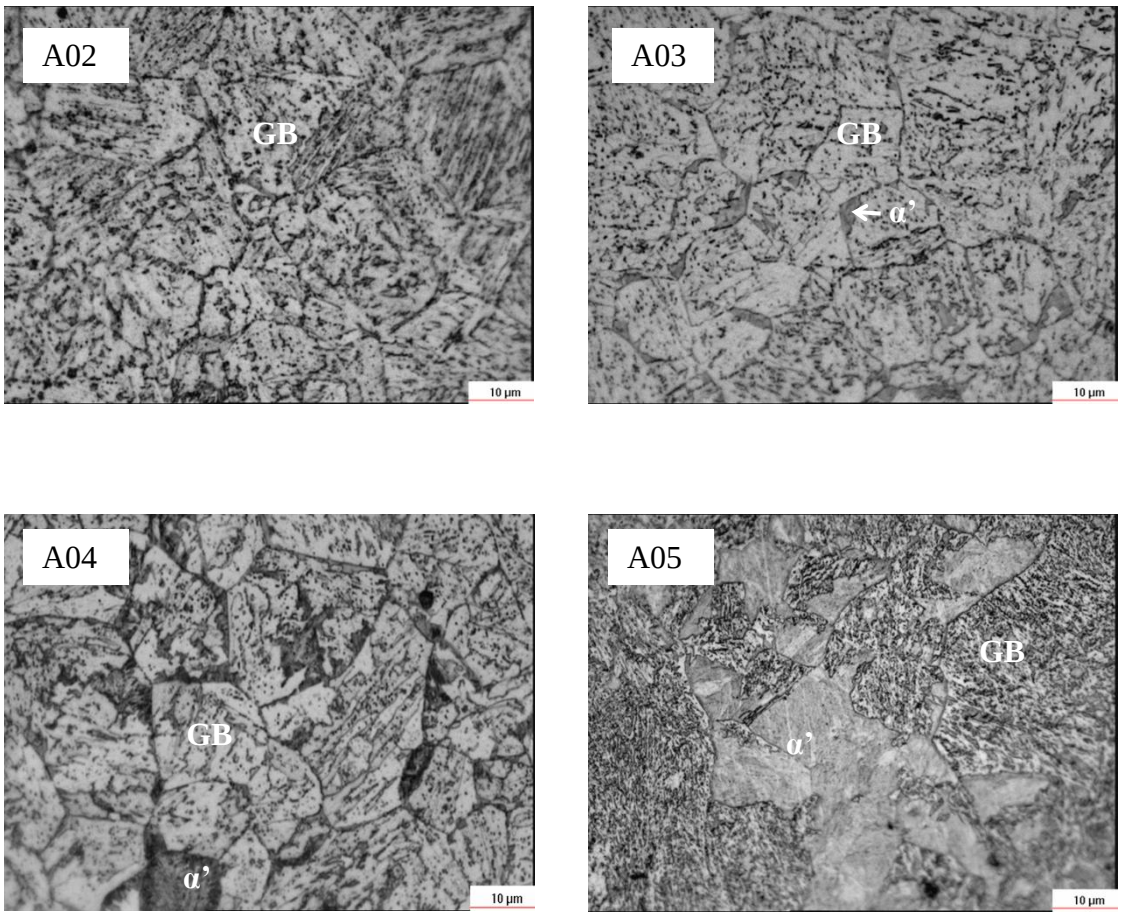

Figure 5.43 The optical microstructures of isothermal treated transformation. Granular bainite(GB), martensite(α'), as indicated. Isothermal treated at 450 ℃, A02: 1min; A03: 4min; A04: 10min; A05: 40min.

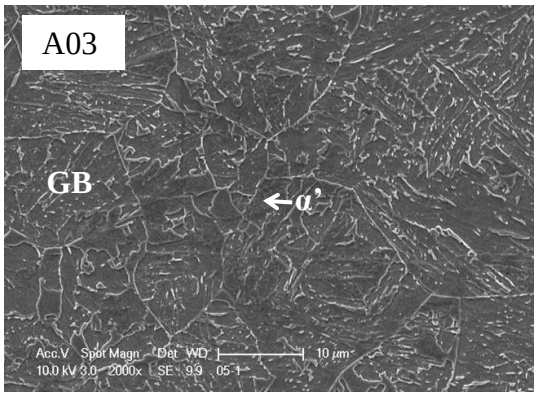

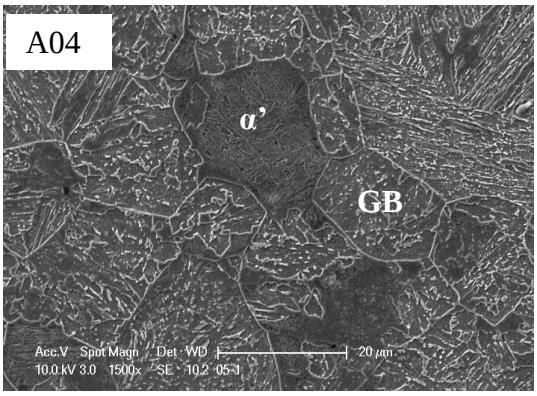

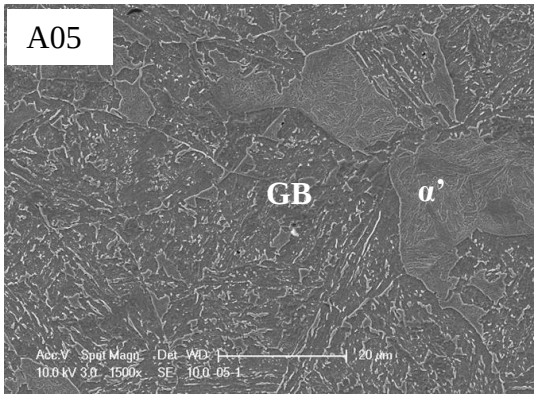

Figure 5.44 The SEM micrographs of isothermal treated transformation. Granular bainite(GB), martensite(α'), as indicated.

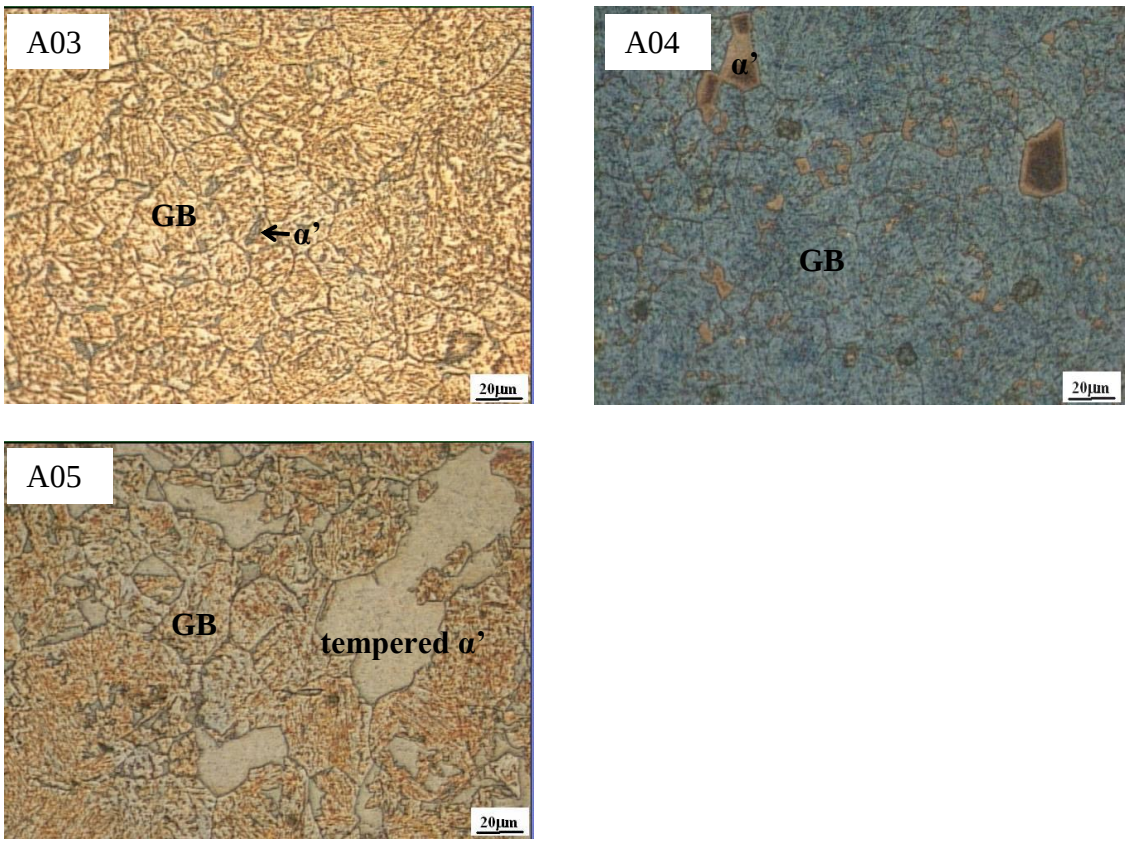

Figure 5.45 The micrographs of LePera etched samples. Granular bainite(GB), martensite(α'), as indicated.

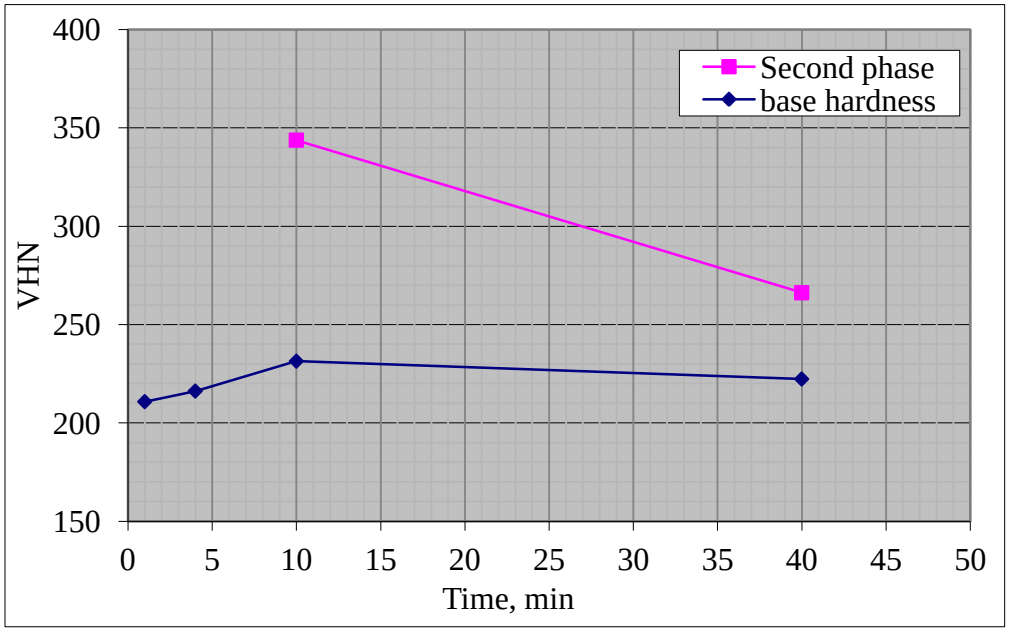

Figure 5.46 The influence of isothermal holding time on Vickers hardness

5.3.6 **Effect of isothermal holding temperatures on the formation of bainite**

Six isothermal temperatures were used for the isothermal transformation study. Steel samples were first reheated to 900 ℃ for 2 minutes, and then quenched in molten sodium nitrate salt at 600 ℃, 550 ℃, 500 ℃, 450 ℃, 400 ℃, and 350 ℃, respectively. The samples were held isothermally in the molten liquid for 3minutes at each designated temperature. The samples were then quenched into water, instantly, to room temperature. The SEM microstructures, etched in 2% nital, are shown in Figure 5.47. At 600 ℃, only ferrite was transformed from austenite and after water quenching; the remaining austenite was transformed into martensite. The hardness number

is highest after quenching, as shown in Figure 5.48. While quenched after 550℃, the microstructure is composed of bainitic ferrite and some martensite. In samples isothermally held at 500℃ and 450℃, granular bainite was obtained. But at 350℃, the microstructures may be tempered martensite since the isothermal temperature is already below the Ms temperature. Figure 5.48 illustrates the influence of isothermal temperatures on the hardness. It can be seen from the graph that the hardness is lowest at 400℃. It shows that lowering isothermal temperatures can decrease the amount of MA and reduce the size of MA.

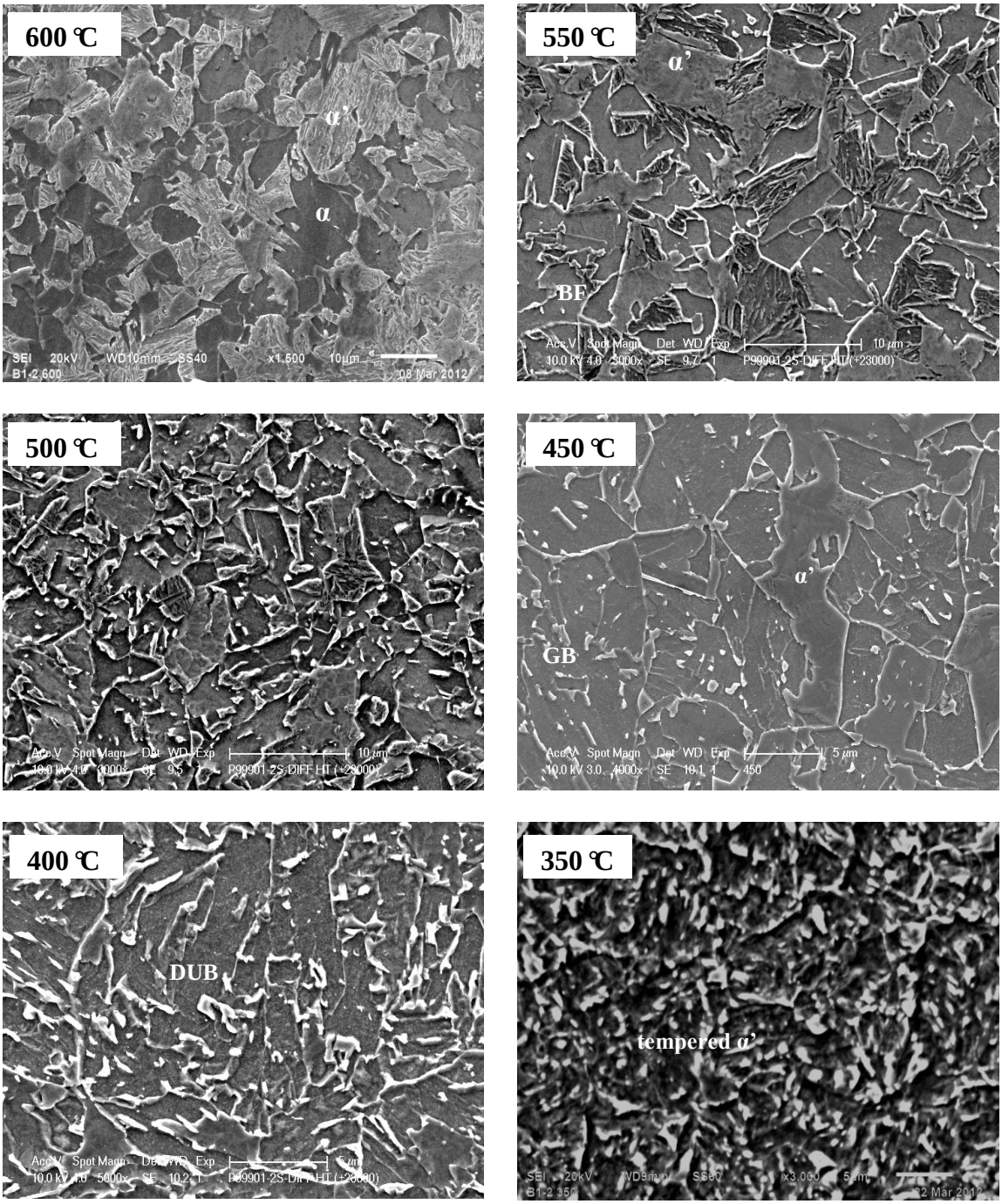

Figure 5.47 The SEM micrographs at different isothermal temperatures. Ferrite: α; martensite: α'; Bainitic ferrite: BF; Granular bainite: GB; degenerate upper bainite: DUB; tempered martensite: tempered α'

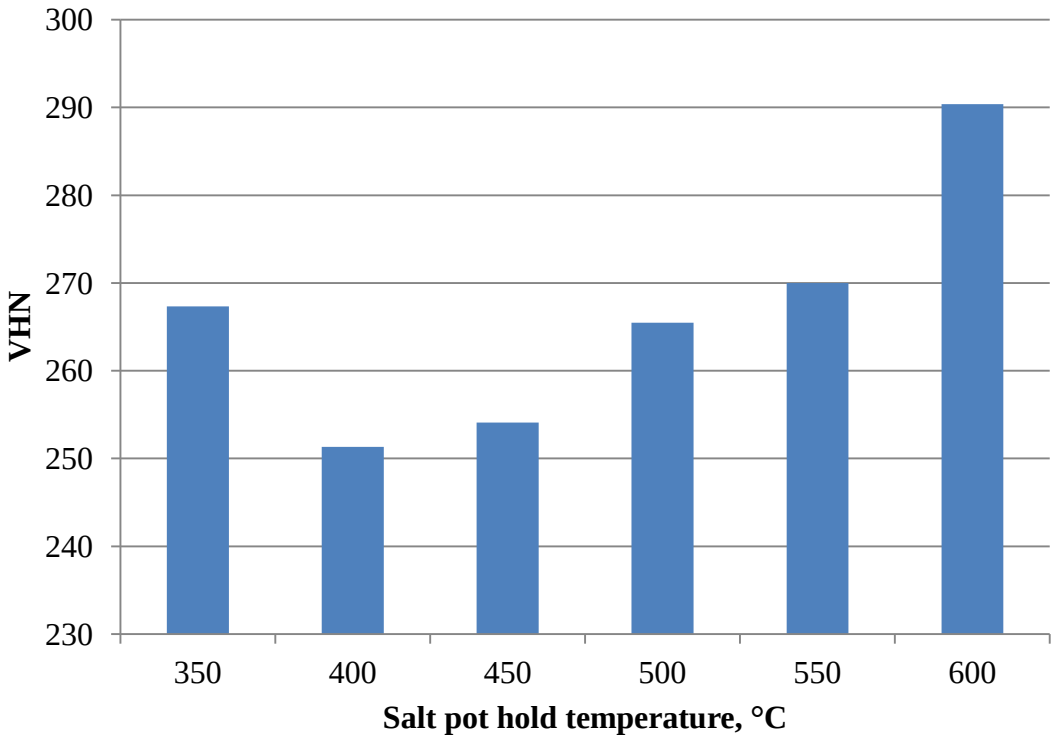

Figure 5.48 Influence of isothermal temperatures on hardness

5.3.7 **Effect of finishing hot rolling temperatures on the MA constituents during bainite transformation**

The isothermal time and isothermal temperatures have been discussed for the transformation of bainite. In this section, the effect of the finishing temperatures on the formation of MA for steel B was investigated. Figure 5.49 shows the schematic diagram of the hot deformation and cooling path used in this experiment. The steel was reheated at 1150℃ for 2 minutes, and three deformation passes were conducted and three finishing temperatures were compared to study the

formation of MA. The MA constituents revealed by LePera etchant are shown in Figure 5.50. The higher finishing temperatures resulted in a higher volume fraction of MA and a larger size of MA.

Figure 5.51 showed the hardness increased with increase of finishing temperatures. The change of volume fraction of MA is shown in Figure 5.52. When the finishing temperature is at 825 ℃ or 900 ℃, the volume fraction of MA is below 2%, however, the volume fraction of MA can reach about 12% when the finishing temperature is 950 ℃.

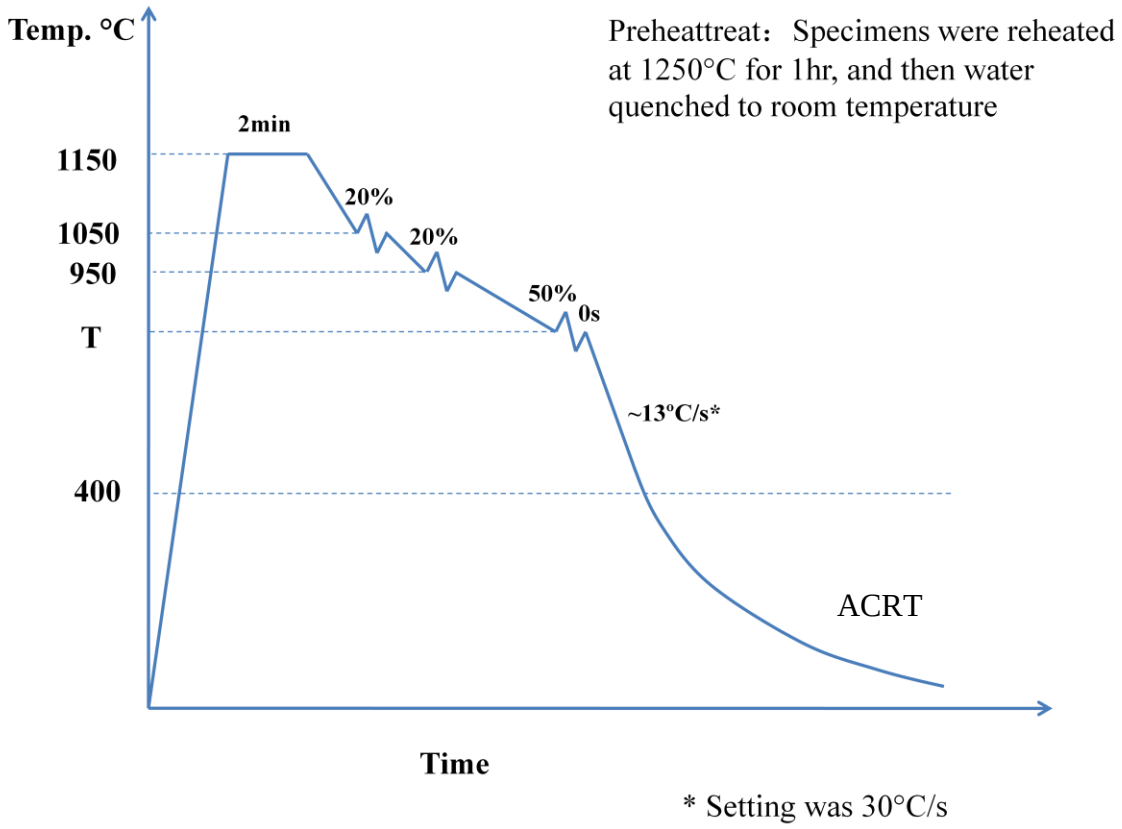

Figure 5.49 Schematic diagram of hot deformation. T is the variable temperature for comparison. T is selected as 950 ℃, 900 ℃ or 825 ℃.

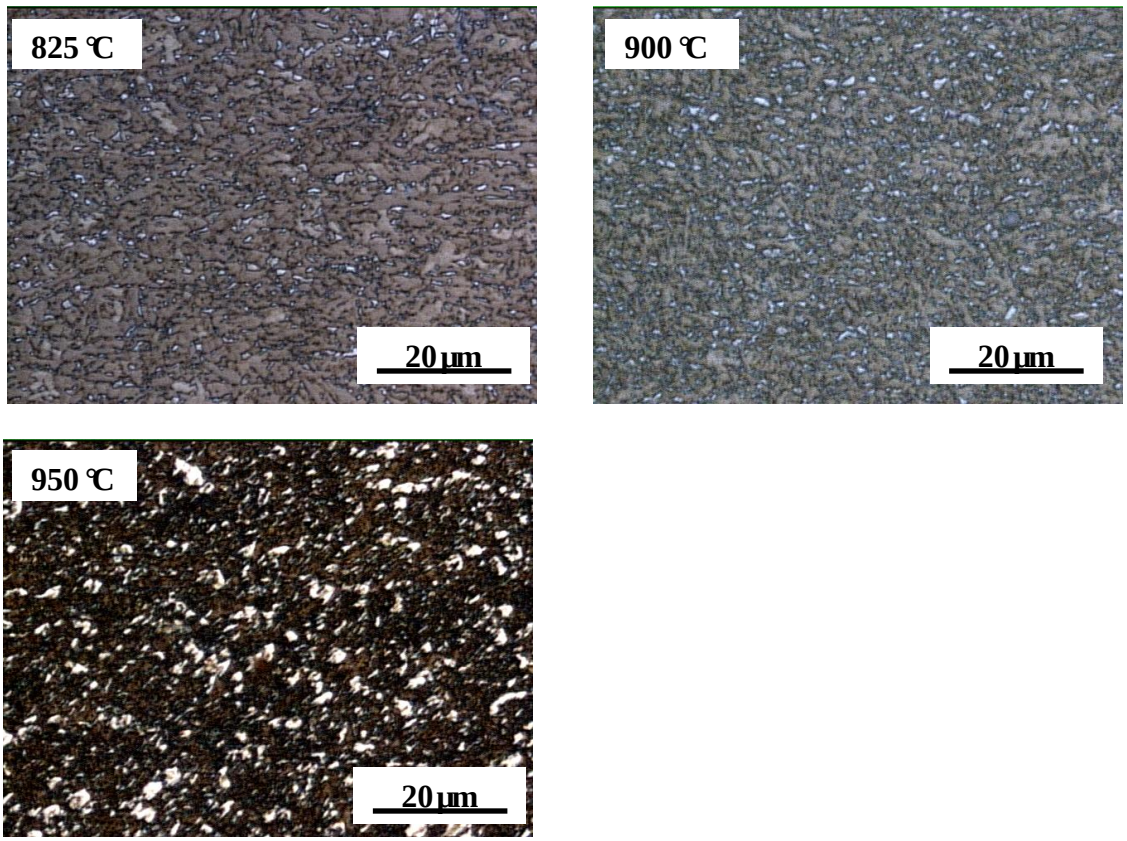

Figure 5.50 Distribution of MA in samples with three finishing temperatures: 825 ℃, 900 ℃ & 950 ℃

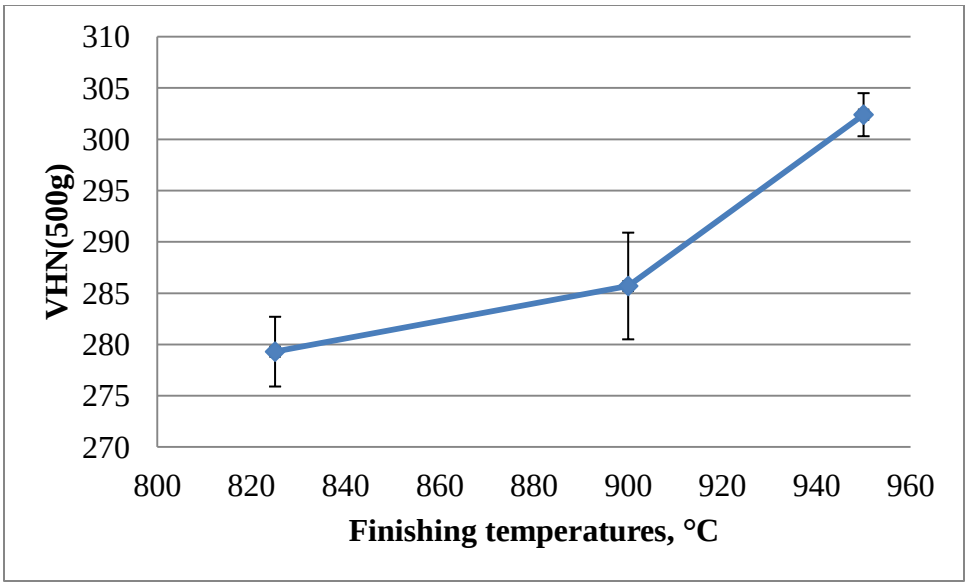

Figure 5.51 The influence of finishing temperatures on Vickers hardness

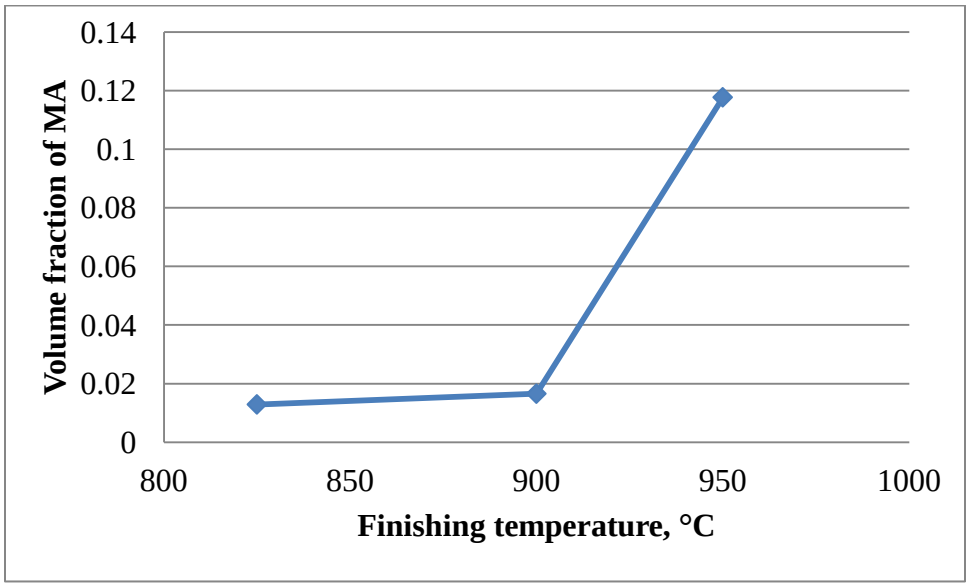

Figure 5.52 The influence of finishing temperatures on the volume fraction of MA

5.4 INFLUENCE OF THERMOMECHANICAL PROCESSING DELAY TIME ON THE MA CONSTITUENTS

For the finishing temperature at 825℃, several different delay times after deformation were investigated on the formation of MA, as illustrated in Figure 5.53. The white areas in Figure 5.54 are MA constituents. Figure 5.55 plots the changes of the volume fraction of MA with delay time. Although it was shown that the low finishing temperature, 825℃, can reduce the amount of MA, once the delay time prolonged, the MA increased. When the delay time increased from 0 second to 400 seconds, the volume fraction of MA increased from 1.3% to 4.8%.However, the hardness in Figure 5.56 does not show a big difference except for the larger deviation after longer delay time.

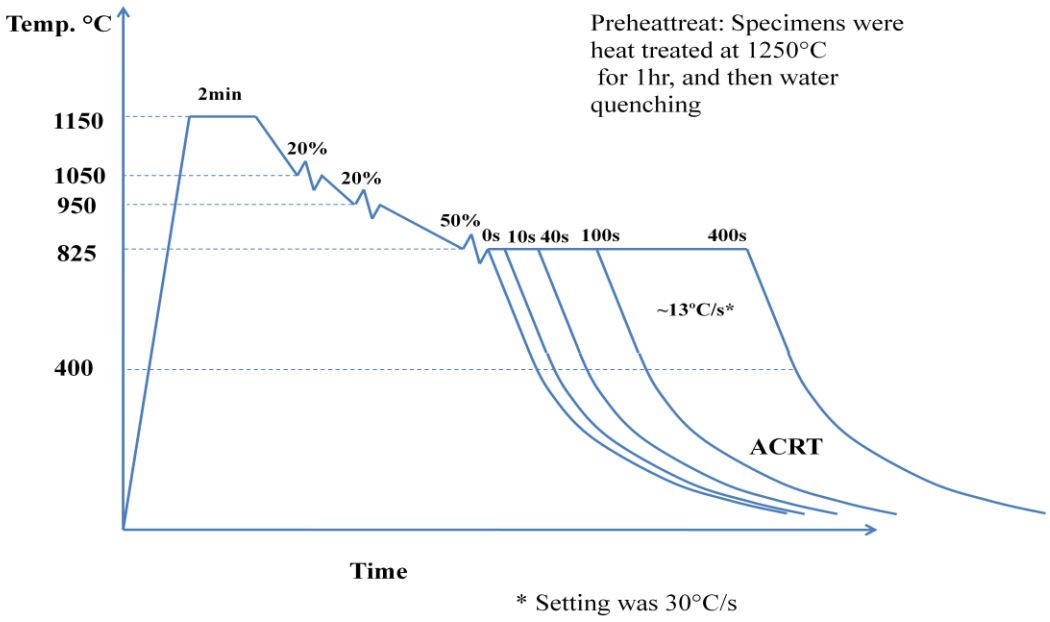

Figure 5.53 The schematical diagram of thermomecanical processing for the study of different delay time

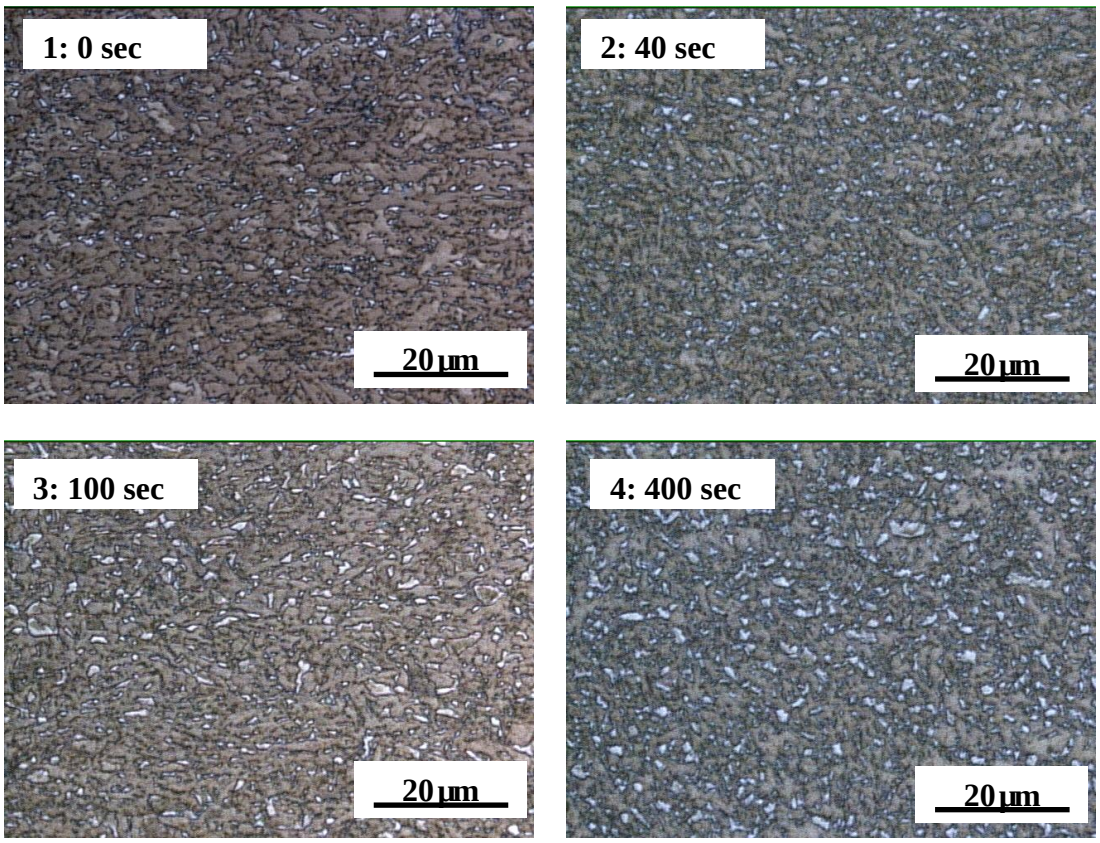

Figure 5.54 The evolution of MA with the different delay time after deformation

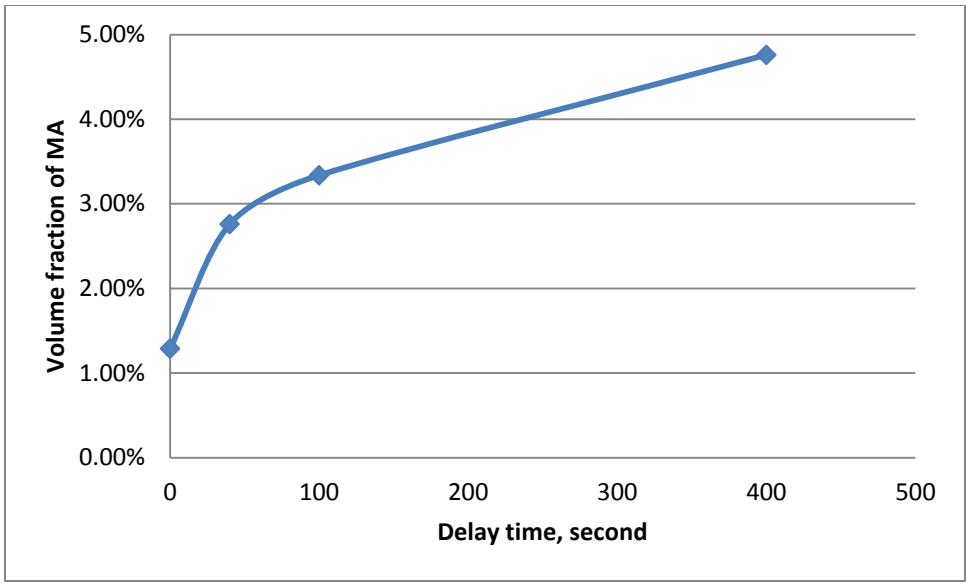

Figure 5.55 The influence of delay time on volume fraction of MA after rolling and holding at 825 ℃

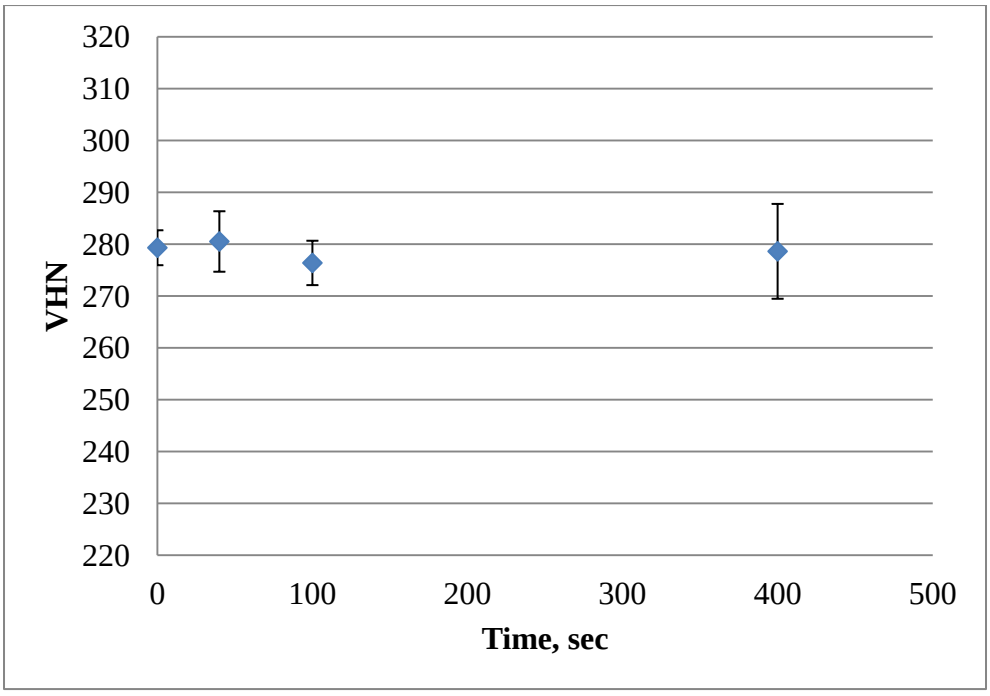

Figure 5.56 Average bulk Vickers hardness for different delay times

5.5 STUDY OF THE CONTINUOUS BAINITE TRANSFORMATION

5.5.1 **Slow cooling rate during bainite transformation**

Figure 5.57 shows the schematic diagram of thermomechanical processing for bainite transformation during a continuously slow cooling rate. The samples were reheated at 1150 ℃ for two minutes, and two passes deformation was at 1000 ℃, and another two passes deformation at 850 ℃ to get pancaked austenite grains. After deformation, a 30 ℃/s cooling rate was used to cool the samples. Sample A was cooled to 700 ℃ and then direct quenched into water. The other samples were fast cooled down to 530 ℃, and then further cooled at about 1 ℃/s to several lower temperatures, from which they were water quenched. As shown in the figure, samples B, C, D and E were cooled to 530 ℃, 520 ℃, 510 ℃ and 470 ℃, respectively. The different microstructures are shown in Figure 5.58 & Figure 5.59.

After quenching from 700 ℃, most all of microstructures are martensite. At 530 ℃, some of the austenite has already been transformed into bainite. For samples C, D and E, the microstructures look similar, as shown in Figure 5.58 and Figure 5.59. Figure 5.60 shows the distribution of MA in the matrix. The corresponding hardness is shown in Figure 5.61.

The figures showed that the change of hardness and volume fractions is very little. Nano indentation was used to measure the hardness of microstructures after transformation. Two samples B and D were prepared to compare the hardness, as shown in Figure 5.62 and Figure 5.63. The load was set at 1000 μN, and the unit of the results is GPa. Nano indentation was used to evaluate the hardness of the bainitic microstructures in samples B and D. The microstructure is composed of bainitic ferrite and martensite or MA constituents. In Figure 5.61, for sample B, the fast cooling rate to 530 ℃, the nano indentation number is about 2GPa to 3.6GPa for bainitic

ferrite. And the number in martensite or MA is about 6GPa. However, after 20 seconds with slow cooling down to 510℃, the hardness number for martensite or MA can be in the range between 5.3 and 10.7 GPa, as indicated in Figure 5.63. This should be evidence that MA becomes harder during slow continuous cooling. The reasonable explanation for the high indentation number could be that the carbon partitioned into remaining austenite from bainitic ferrite increase the final hardness of the MA. The time in slow cooling provided ample time for carbon partitioning.

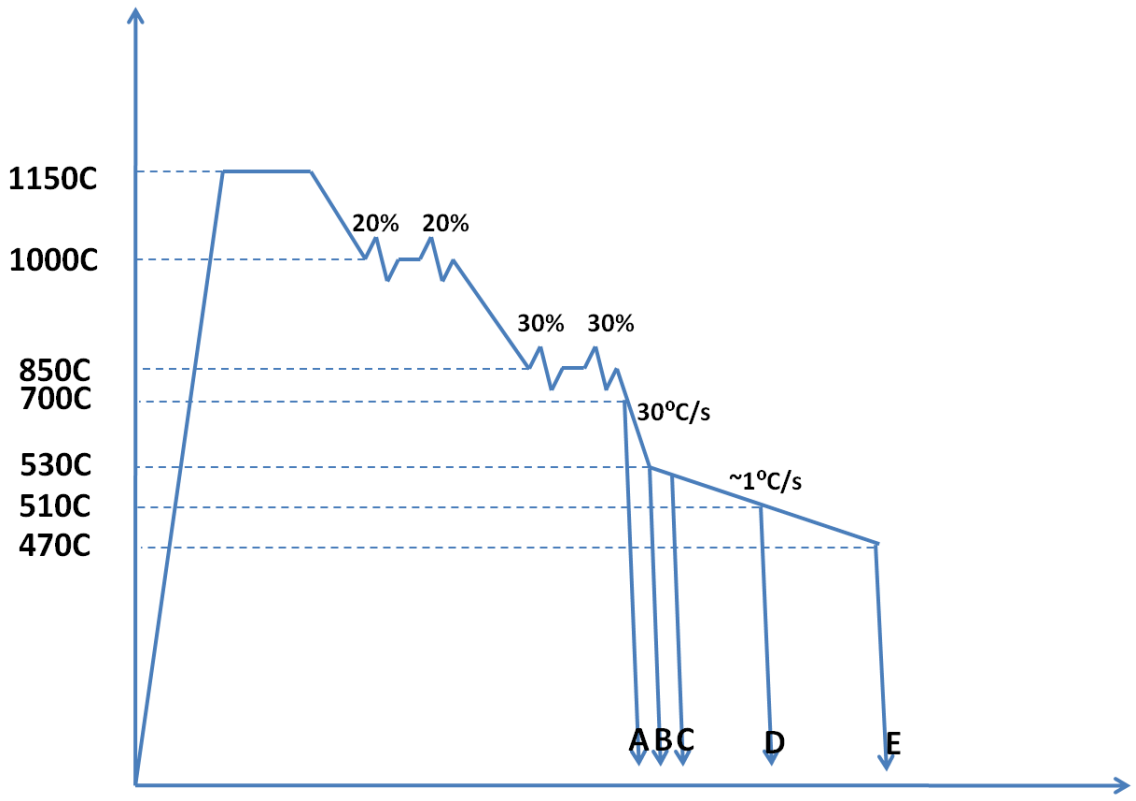

Figure 5.57 The schematic diagram of thermomecanical processing for bainite transformation during a continuously slow cooling rate

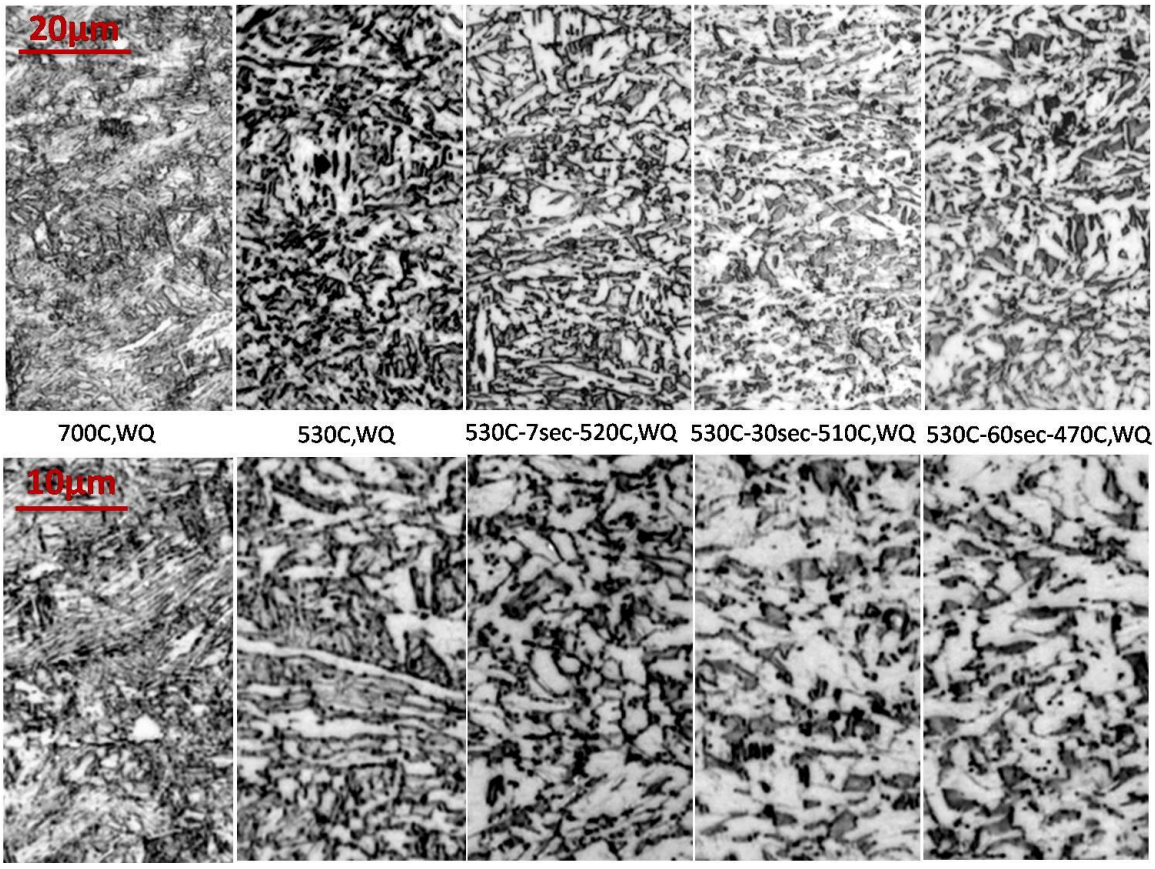

Figure 5.58 The optical micrographs of samples etched in nital, low magnification (above), high magnification (below)

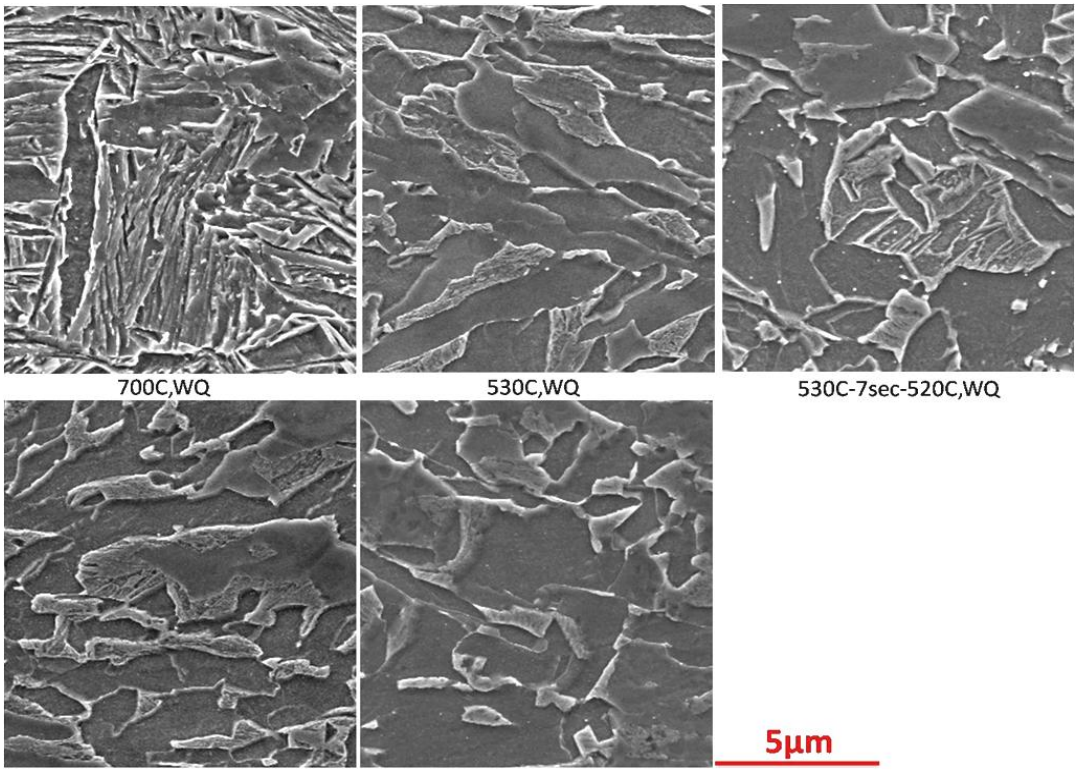

Figure 5.59 The SEM micrographs etched in nital

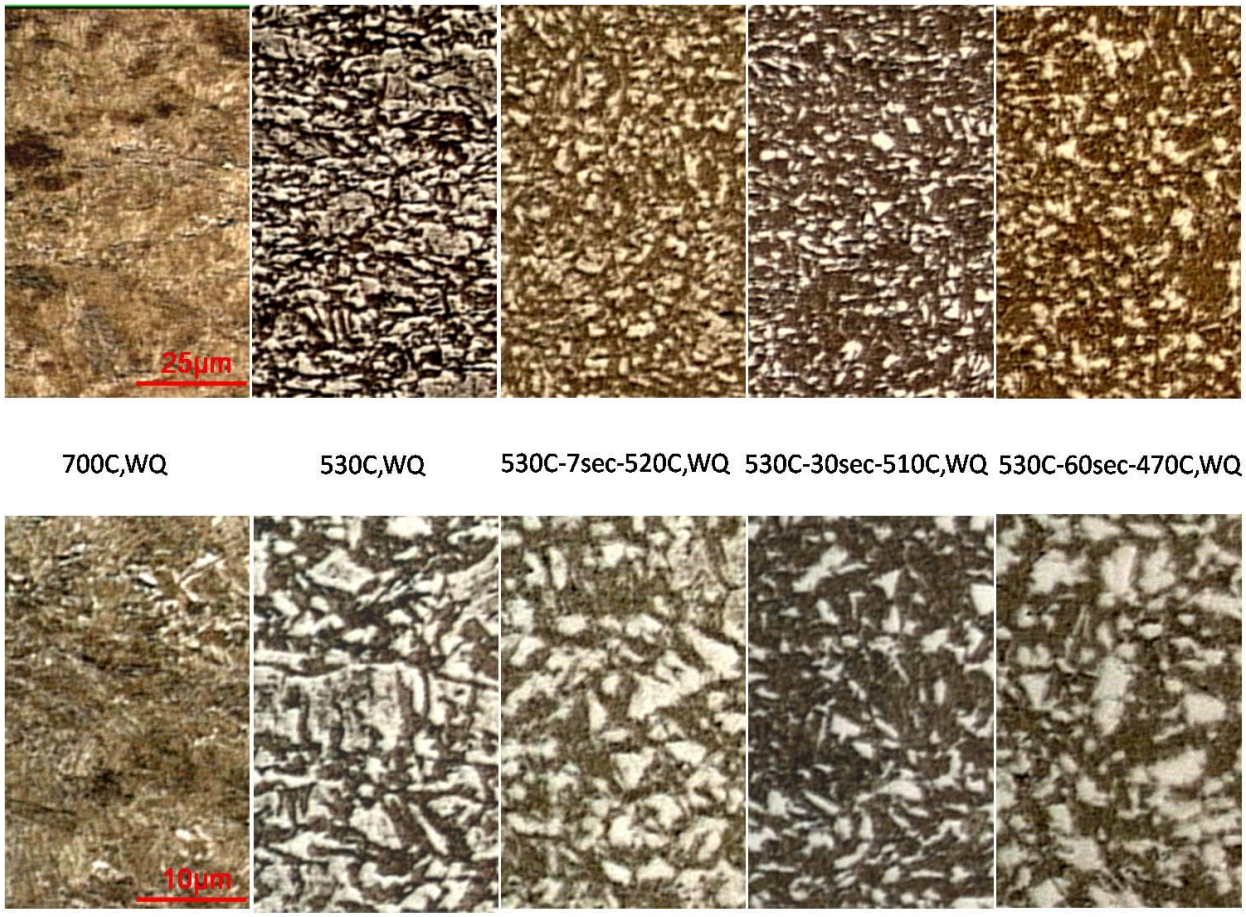

Figure 5.60 The optical micrographs of samples etched in LePera, low magnification (above), high magnification (below)

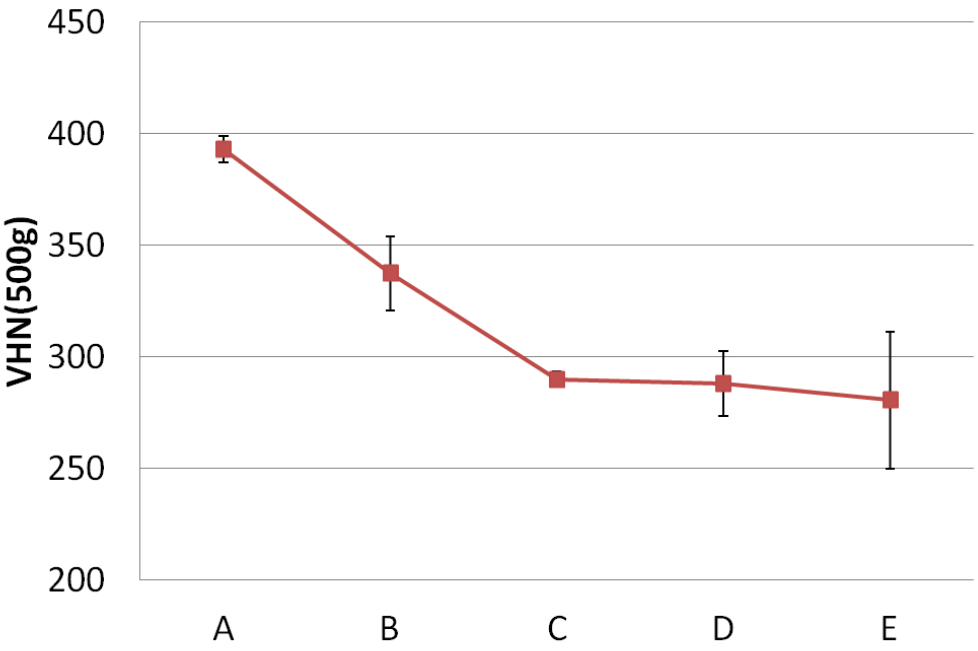

A	B	C	D	E
700C,WQ	530C,WQ	530C-7s-520C,WQ	530C-30s-510C,WQ	530C-60s-470C,WQ

Figure 5.61 Vickers hardness of samples A, B, C, D, E

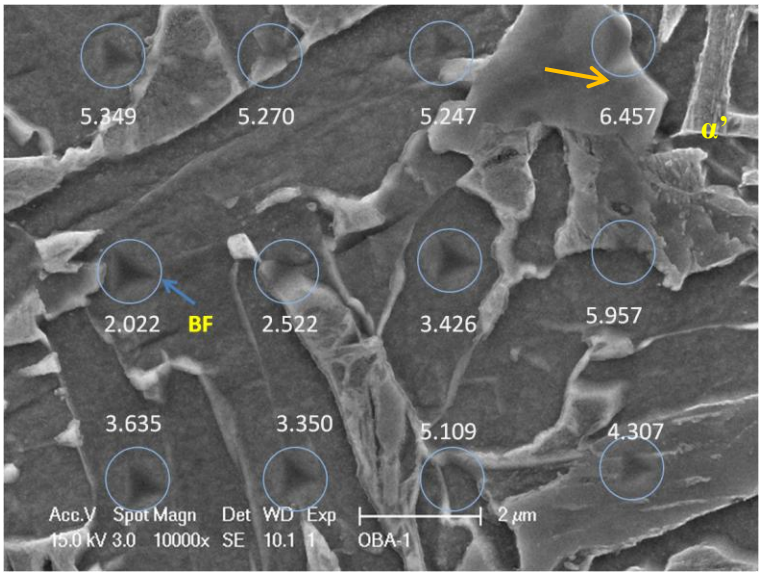

Figure 5.62 Nano indentation in sample B (bainitic ferrite(BF) arrow indicated, Martensite (α') or MA as indicated)

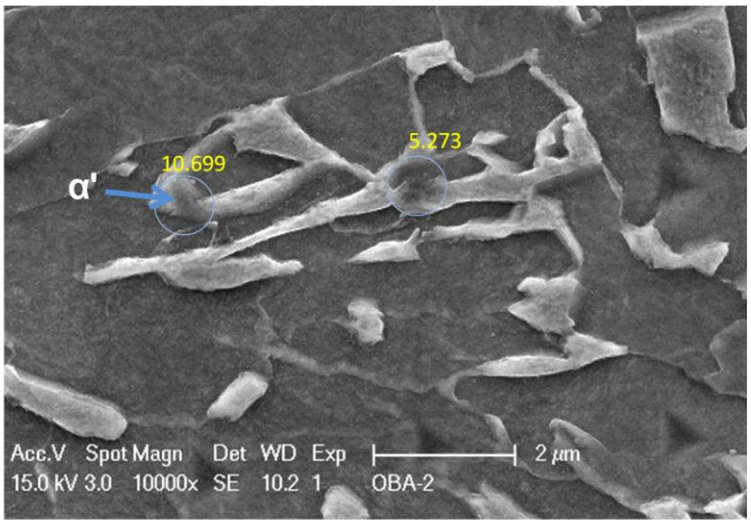

Figure 5.63 Nano indentation in sample D, Martensite (α') or MA as indicated

5.5.2 **Fast cooling rate during bainite transformation**

Figure 5.64 is a schematic diagram of thermomechanical processing for bainite transformation during fast continuous cooling. Samples were fast cooled (about 30 ℃/s) to five different finishing temperatures (or WET), named T1, T2, T3, T4 and T5, respectively. And then the samples were water quenched into room temperature to see the microstructures at those temperatures since water quenching should avoid any transformation except for the remaining austenite that was transformed into martensite. The microstructures etched in nital are shown in Figure 5.65 and Figure 5.66. It showed in sample T2 (570 ℃) that bainite already started to be formed from austenite. However, the volume fraction of bainite is less than 10%. At 530 ℃, it seemed that more than 50% percent of austenite has been transformed into bainite. However, at 510 or 470 ℃, most of austenite has been transformed into bainite. The LePera etching in Figure 5.67 revealed the evolution of martensite or MA during the fast continuous cooling. Most of martensite was found in samples T1 and T2 as shown in Figure 5.67. When the temperatures decreased, the volume fraction of martensite or MA decreased apparently. However, since the cooling rate between finishing temperatures and the water quenching temperatures is fast enough, the diffusion of carbon may be impeded. Thus, the carbon partitioning from bainitic ferrite to MA can be retarded, which can avoid the formation of the very hard, brittle MA in the matrix. The hardness was compared for the samples with the fast cooling rate and slow cooling rate, as shown in Figure 5.68. When the formation of bainite occurred during continuous cooling, the hardness of samples cooled at the fast cooling rate decreased more than that of the slow cooling rate. This is because less austenite was remained when the sample was fast cooled to

470 ℃. While the sample E was slowly cooled to 470 ℃, a higher volume fraction and harder MA was formed.

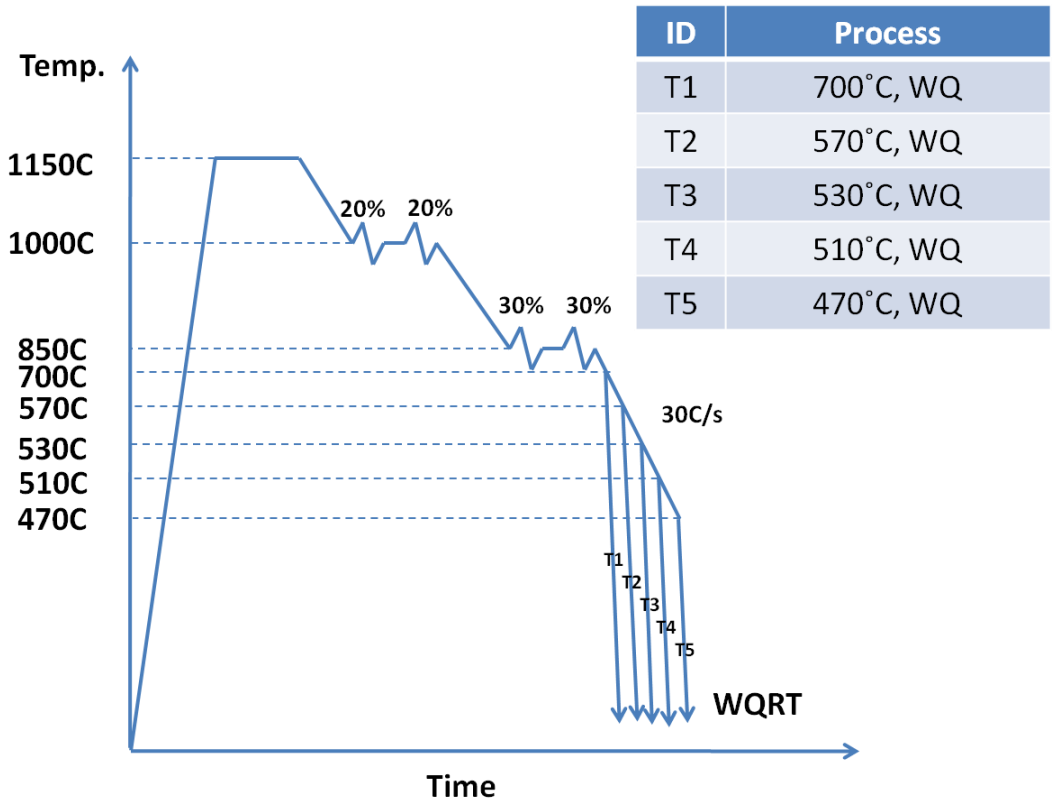

ID	Process
T1	700˚C, WQ
T2	570˚C, WQ
T3	530˚C, WQ
T4	510˚C, WQ
T5	470˚C, WQ

Figure 5.64 The schematic diagram of thermomecanical processing for bainite transformation during fast slow cooling rate

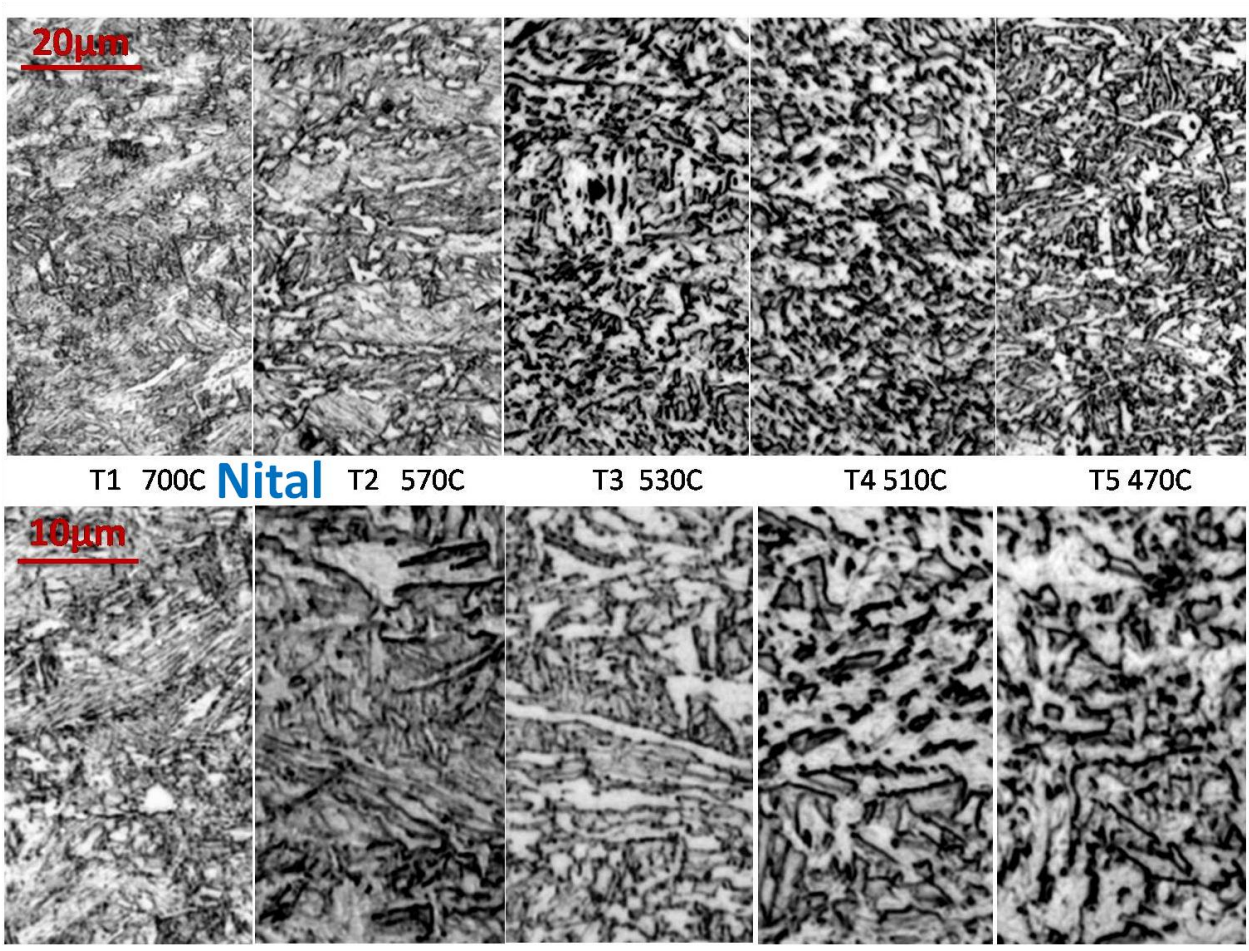

Figure 5.65 The optical micrographs of samples etched by nital, low magnification (above), high magnification (below). T1: mostly martensite; T2: a small fraction of bainite appears; T3: about 50% martensite remained; T4: bainite but with large MA constituents; T5: bainite with small MA constituents.

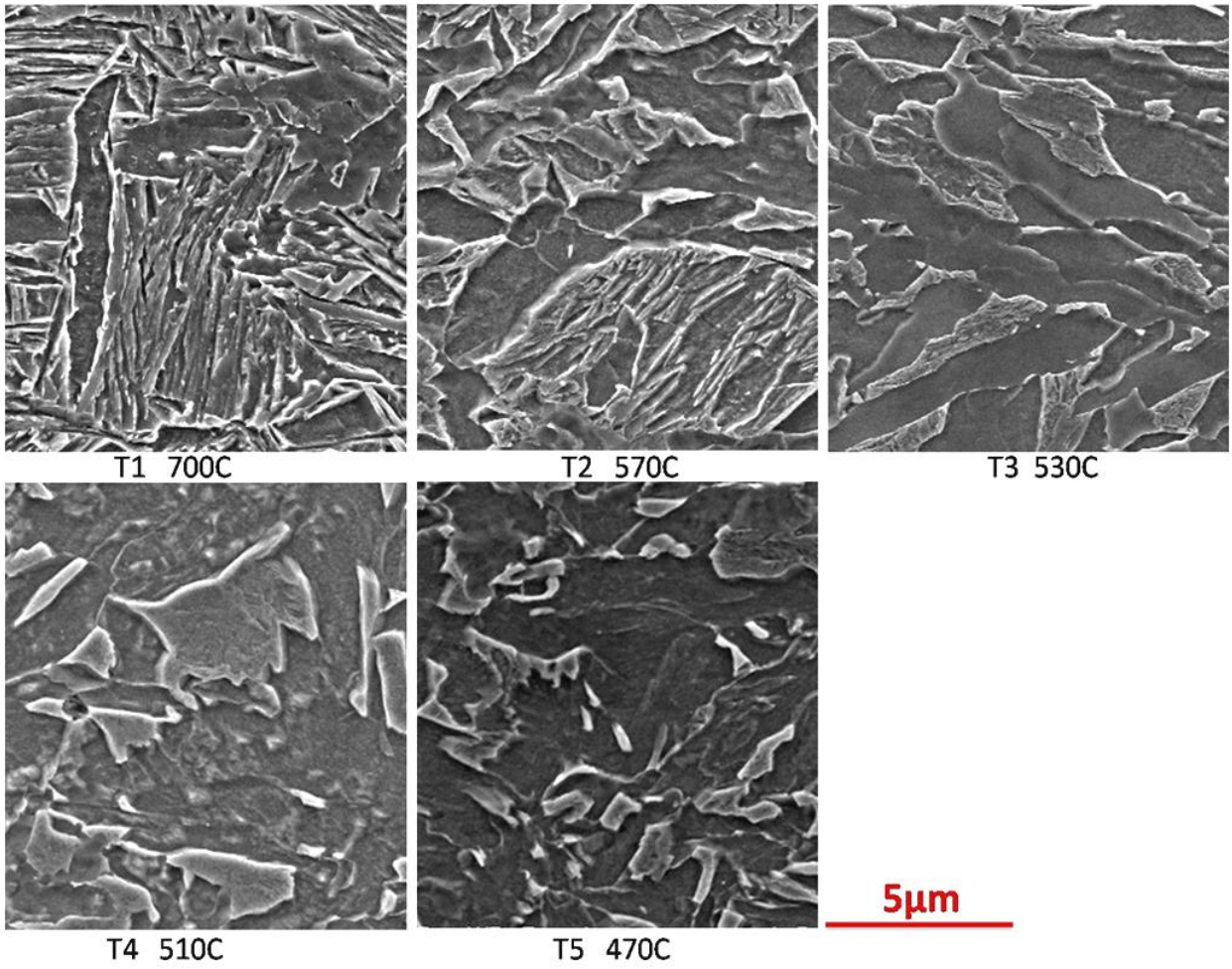

Figure 5.66 The SEM micrographs etched by nital, low magnification (above), high magnification (below)

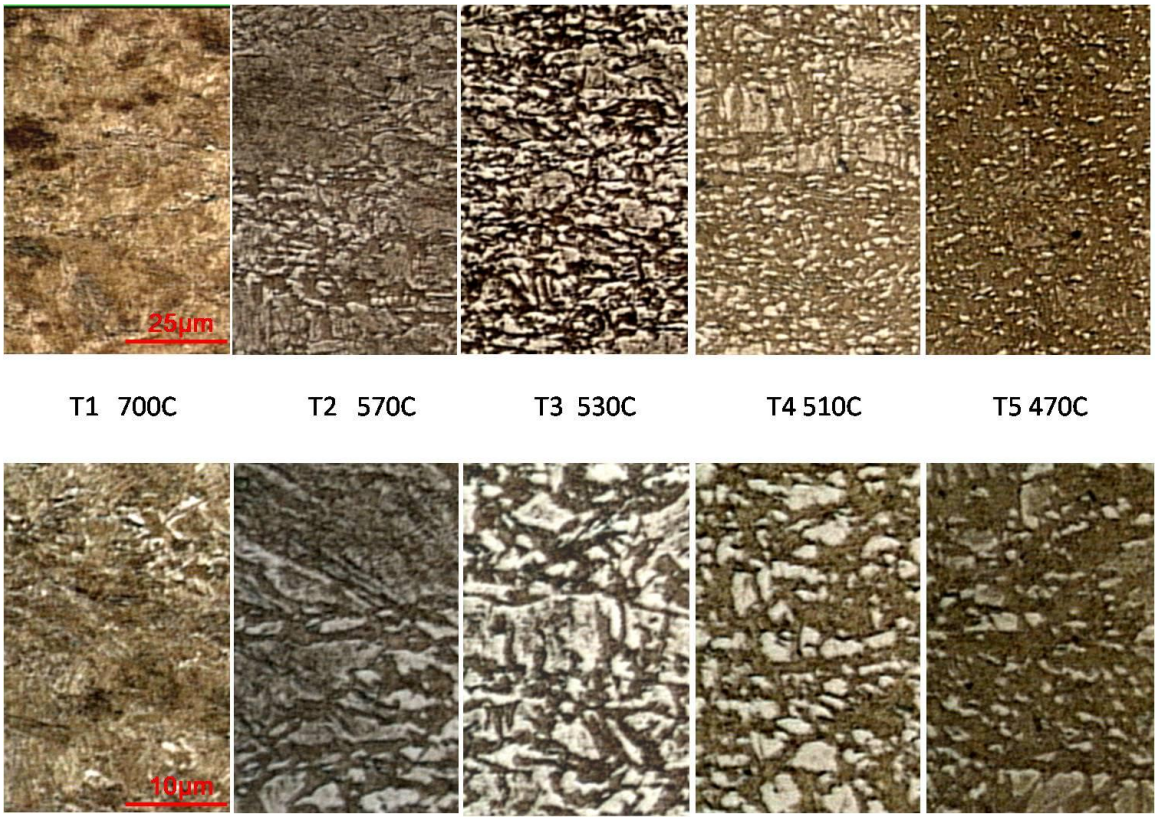

Figure 5.67 The optical micrographs etched by LePera, low magnification (above), high magnification (below)

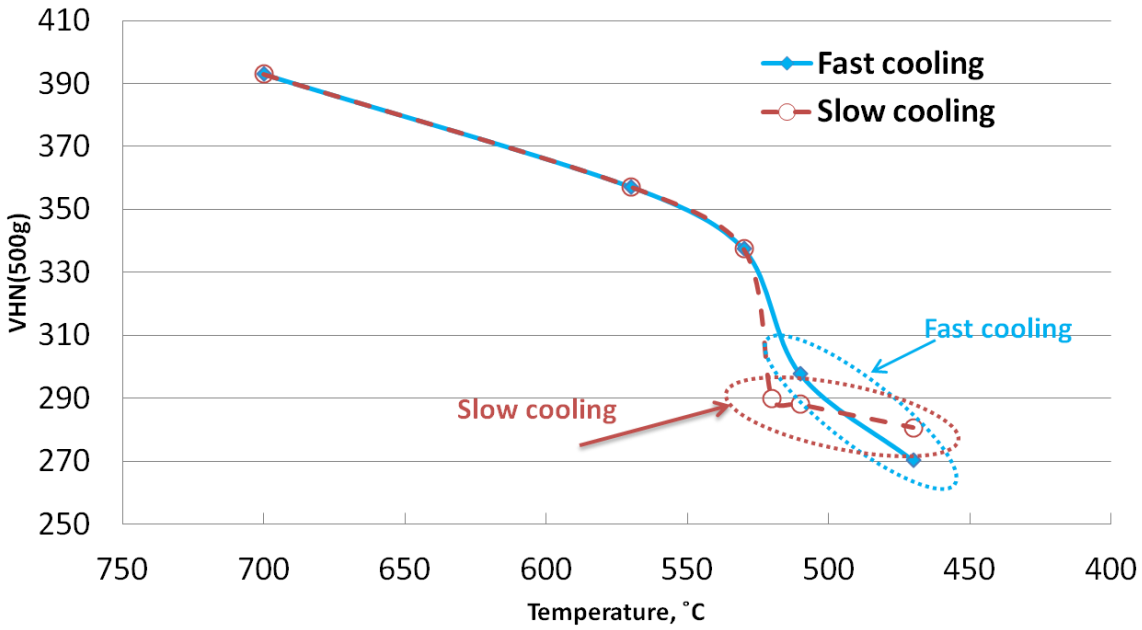

Figure 5.68 The hardness for the samples cooled with fast and slow cooling rates

6.0 DISCUSSION

6.1 TOUGHNESS AND MA ANALYSIS IN HIGH STRENGTH STEELS

In very low carbon high strength steels, bainite, or the mixture of bainite and martensite are required to guarantee sufficiently high strength. Due to the decrease of carbon composition and the increase of alloy elements, the formation of ferrite and pearlite is strongly retarded. However, even at low carbon contents, there is more carbon present than can be dissolved by the bainitic ferrite. Therefore, the formation of MA is inevitable during bainite transformation because carbon is not enough to form M3C carbides. MA has been considered one factor that negatively affects the toughness of HAZ[48, 102] and also the toughness of base steel in the literature[103]. In this section, the size and the volume fraction of MA are discussed with respect to their effect on the toughness of steels.

Eight steel samples were selected to investigate MA and toughness. The MA constituents were revealed by LePera etching, as shown in Figure 5.41. However, no large difference among the microstructures in 5.3.2.2 can be apparently seen. The LePera etching showed the large difference of the distribution of MA in samples. Comparing these figures shown in Figure 5.41, two parameters of MA should be considered in steel: the size of MA and the volume fraction of MA. As shown in Figure 5.41 and Figure 6.1, the steel may have high volume fraction of MA but with small size of MA, such as A2-1T and C2-4T. The steel will also have another possibility that has a big size of MA but smaller fraction of MA, such as A2-2T. Another more common

possibility is with higher volume fractions and large sizes of MA in steel, such as A2-3T, B2-3T and C2-1T.The distribution of MA after image processing is more clearly shown in Figure 6.1.

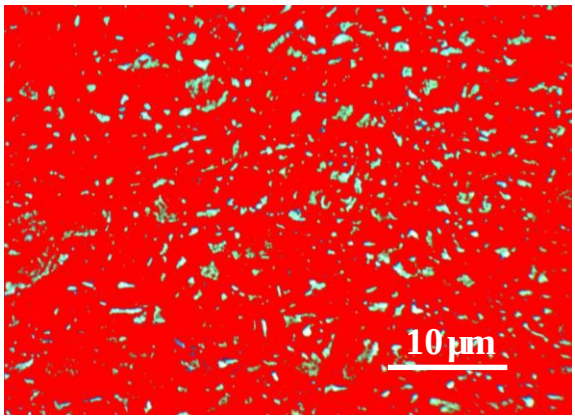

a A2-1T reconstruction of MA(white area)

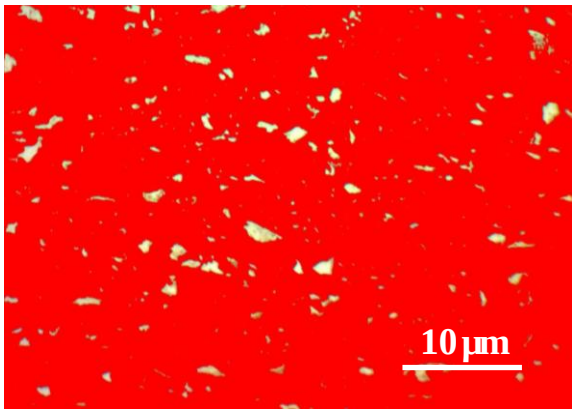

b A2-2T reconstruction of MA (white area)

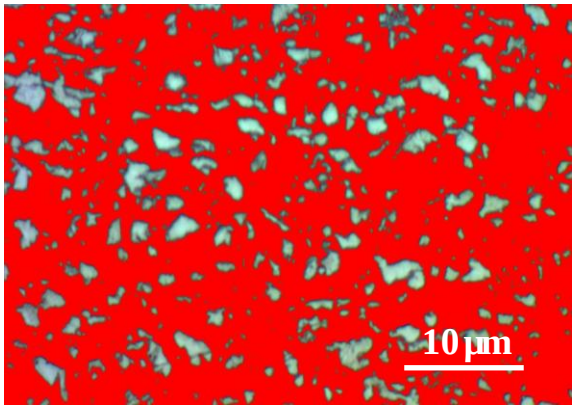

c A2-3T reconstruction of MA (white area)

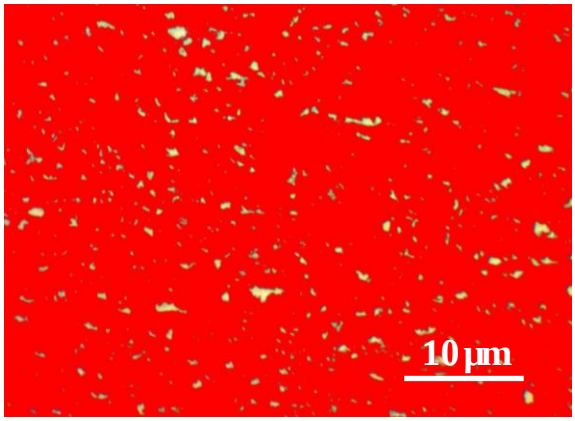

d B2-1T reconstruction of MA (white area)

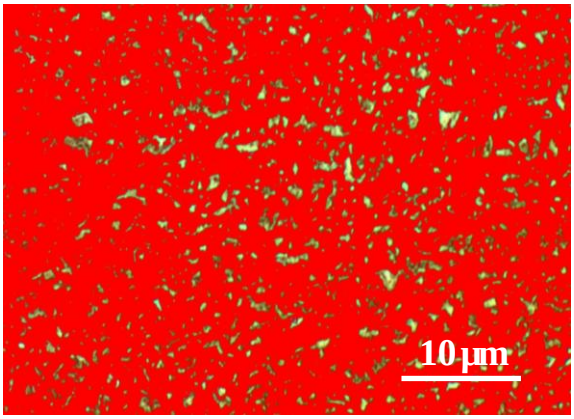

e B2-2T reconstruction of MA (white area)

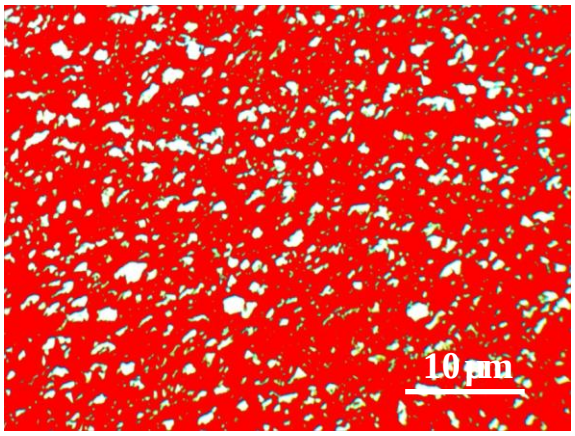

f B2-3T reconstruction of MA (white area)

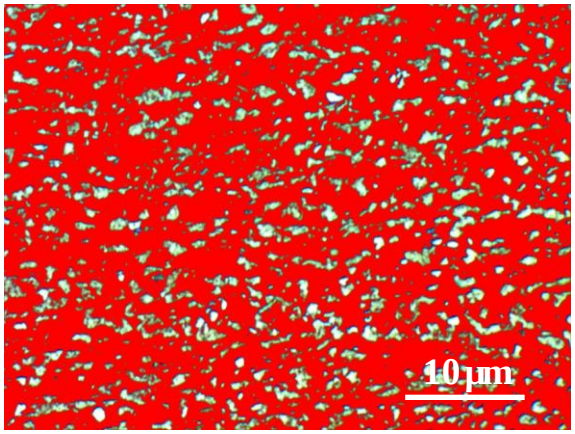

g C2-1T reconstruction of MA (white area)

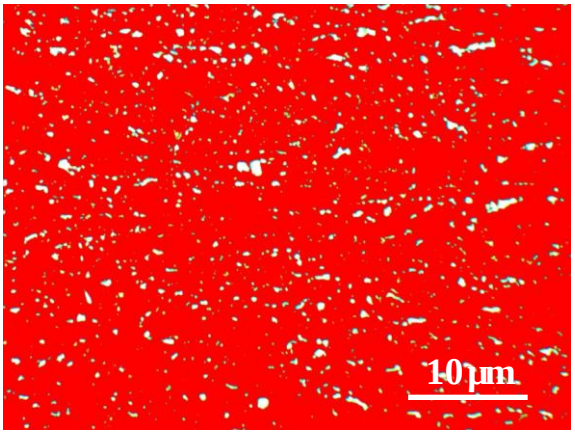

h C2-4T reconstruction of MA (white area)

Figure 6.1 The distribution of MA in eight samples, after image processing. a-c: Steel A2-1~3, d-f: Steel B2-1~3, g-h: Steel C2-1 and C2-4

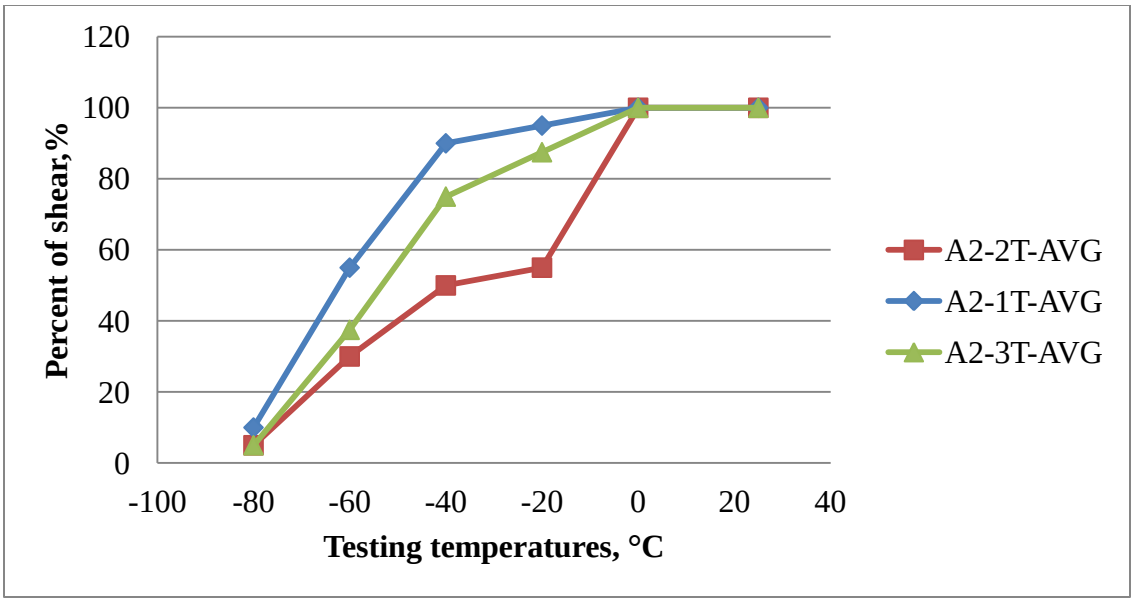

(a) The shear area of specimens vs. testing temperature

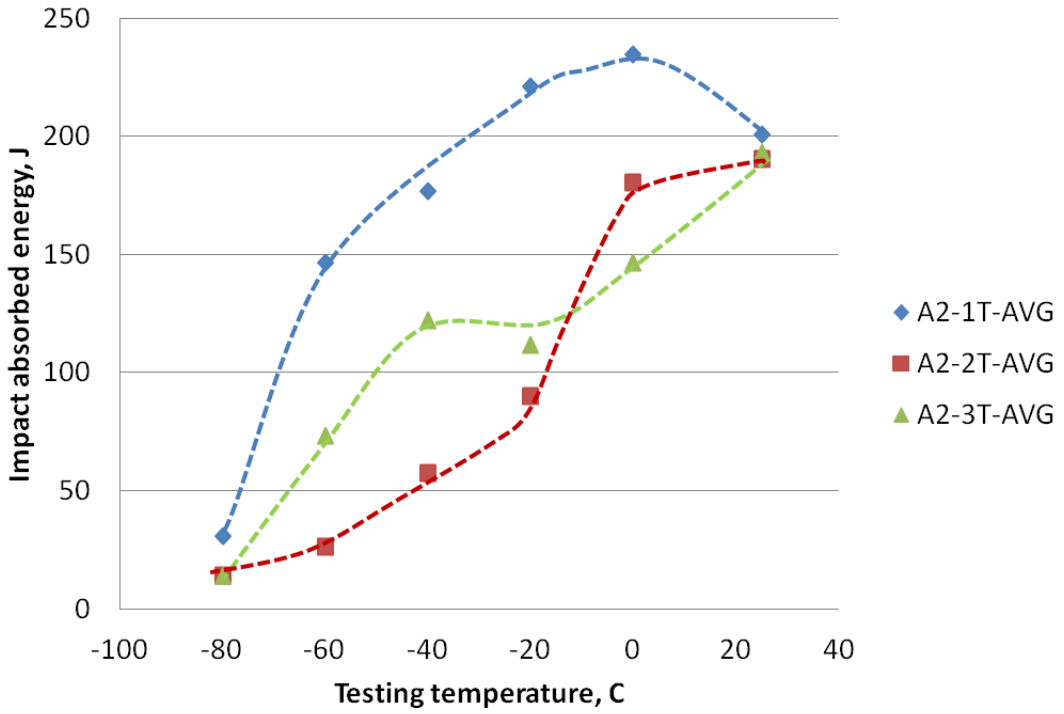

(b) The impact absorbed energy vs. testing temperature

Figure 6.2 The Charpy impact testing results of steel A2

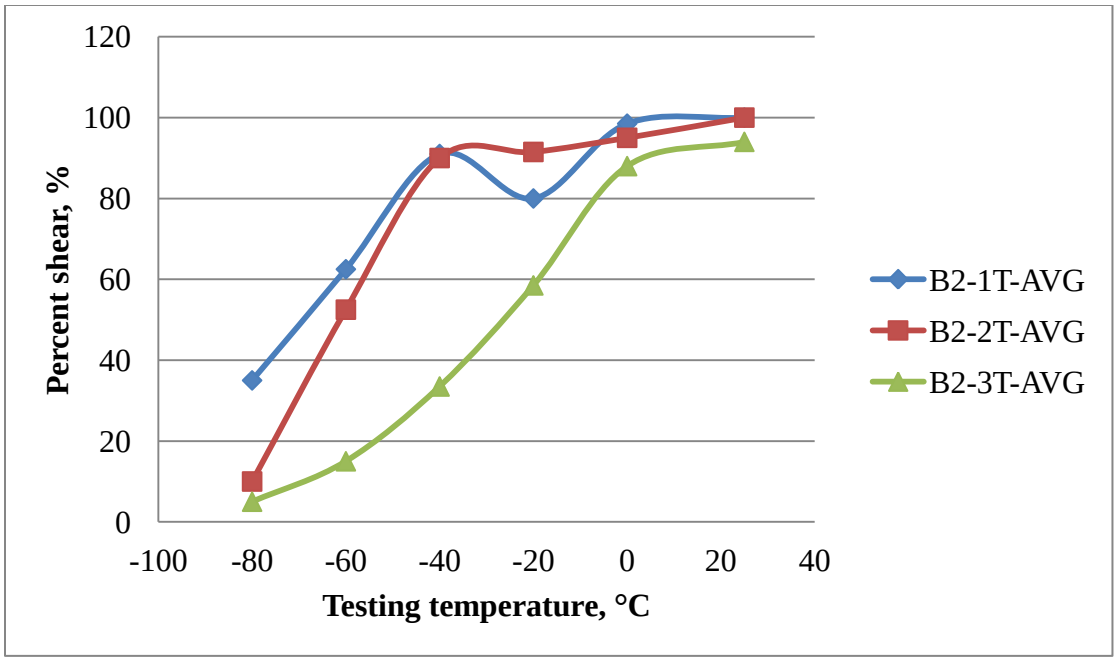

(a) The shear area of specimens vs. testing temperature

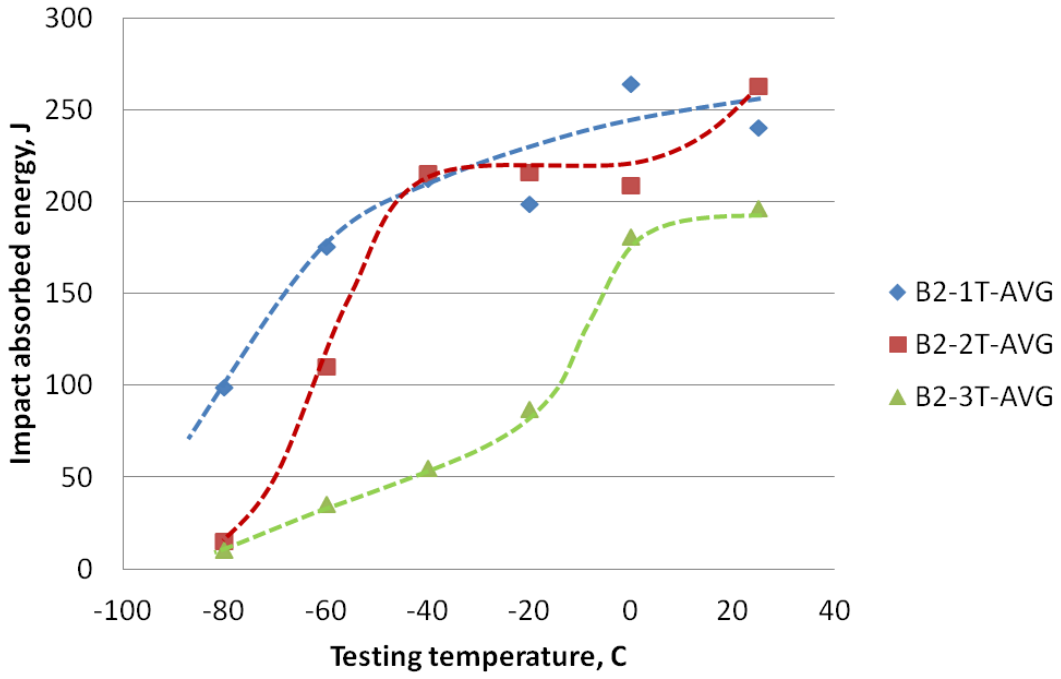

(b) The impact absorbed energy vs. testing temperature

Figure 6.3 The Charpy impact testing results of steel B2

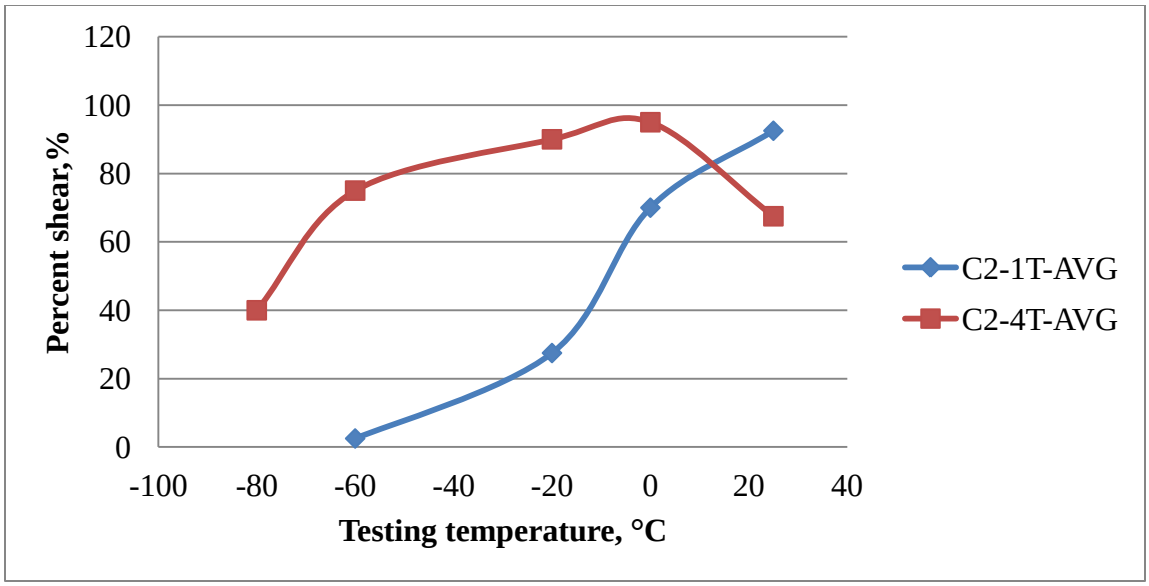

(a) The shear area of specimens vs. testing temperature

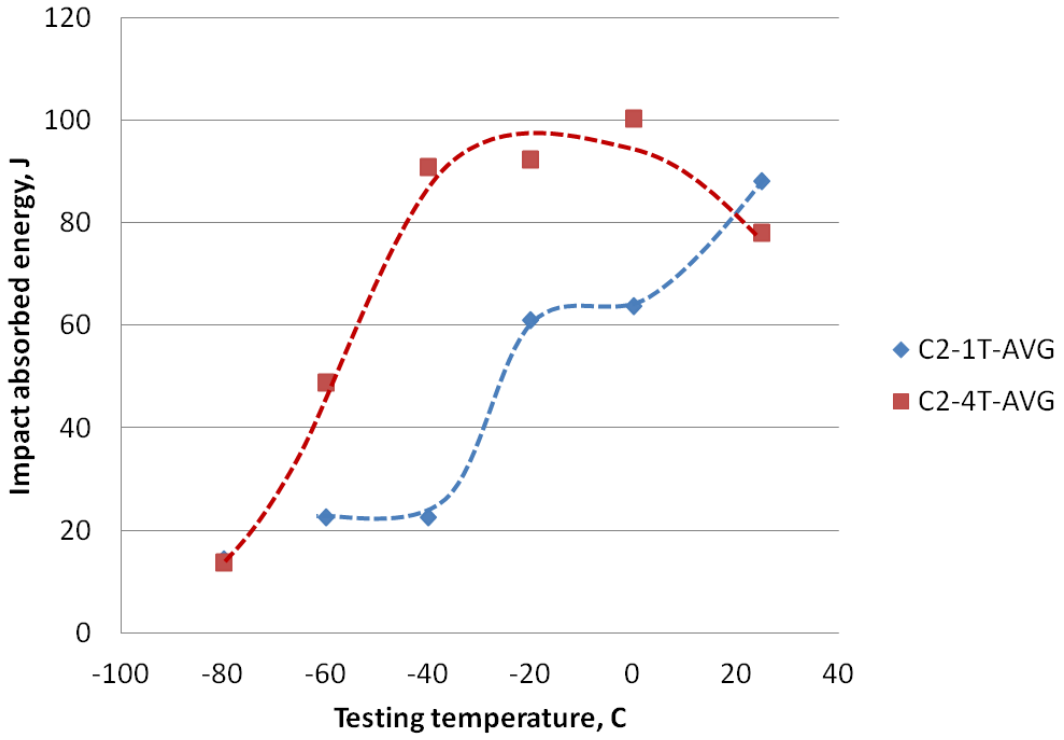

(b) The impact absorbed energy vs. testing temperature

Figure 6.4 The Charpy impact testing results of steel C2

Figure 6.2 to Figure 6.4 show the percentage of shear area and impact absorbed energy of Charpy impact specimens in steel A2, B2 and C2. It was found that the percent of shear area varies with the microstructures greatly even for the same steel composition. In these figures, A2-2T, B2-3T and C2-1T showed higher ductile brittle transition temperatures. However, the toughness is complicated in the high strength steel with complex microstructures. Since MA is not a significant problem in ferrite pearlite steels, MA was studied mainly in HAZ in welding and was found it dramatically deteriorates toughness of weldments. Recently, some researchers studied MA in X70 linepipe steels[77, 78, 104], and some others think that the low angle grain boundary is more important for deteriorating toughness[30]. It is hard to judge which one is more correct than the other, but it can be said they are partially correct, because the toughness in a multi-scale, multi-phase mixture, is not supposed to be determined by one factor but by a combination of factors taken together. Some possible factors related to microstructures and toughness will be discussed in this section.

Since the large size of MA may easily induce the stress concentration between MA and bainitic ferrite, Figure 6.5 and Table 6.1 illustrate the relationship among upper shelf energy, the maximum size of MA and the volume fraction of MA. The definition of the maximum size is a statistical number in this study. It is an average size of the largest 5% of MA constituents in same size microstructure areas. The data of steel B2 illustrate the obvious and rapid decrease of upper shelf energy with the increase of maximum size of MA and the volume fraction of MA. However, the upper shelf energy was observed to be affected by the maximum size of MA more than the volume fraction of MA. In steel A2, the upper shelf energy is 201J for steel A2-1 with 11vol% MA and 1.77 μm of the maximum size of MA. The upper shelf energy is 193J for steel A2-3. However, the volume fraction of MA is only 4%, but the maximum size of MA, 2.15 μm,

is larger. This example shows that a higher volume fraction of MA did not inevitably result in the loss of upper shelf energy. Therefore, the upper shelf energy seems to be related more to the size of MA than volume fraction of MA.

Table 6.1 The sizes and volume fractions of MA and the upper shelf energy

Steel A2	**Max. size of MA, μm**	**Vol. MA**	**Upper Shelf Energy, J**
No.1	1.77	0.11	201
No.2	2.15	0.04	193
No.3	3.45	0.22	190
Steel B2	**Max. size of MA, μm**	**Vol. MA**	**Upper Shelf Energy, J**
No.1	2.02	0.11	240
No.2	1.49	0.07	263
No.3	2.23	0.22	196

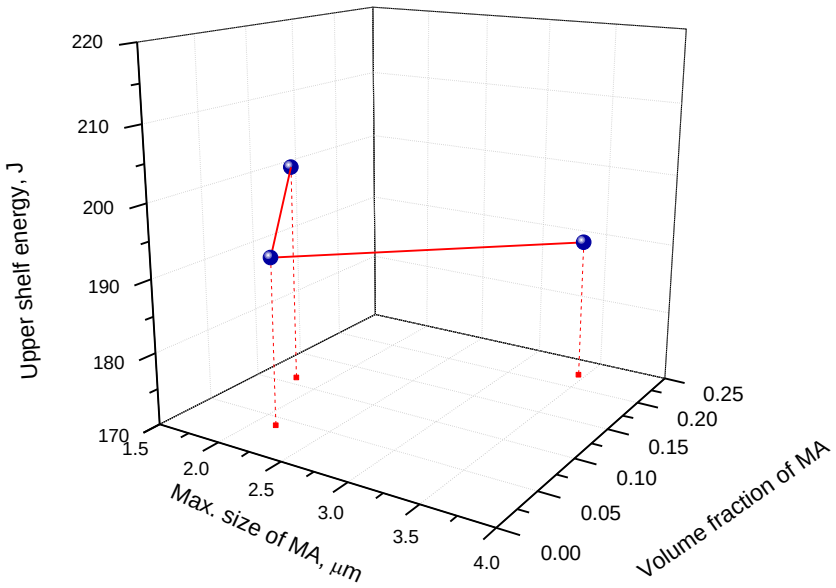

(a) Upper shelf energy vs. max. size & vol. of MA in Steel A2

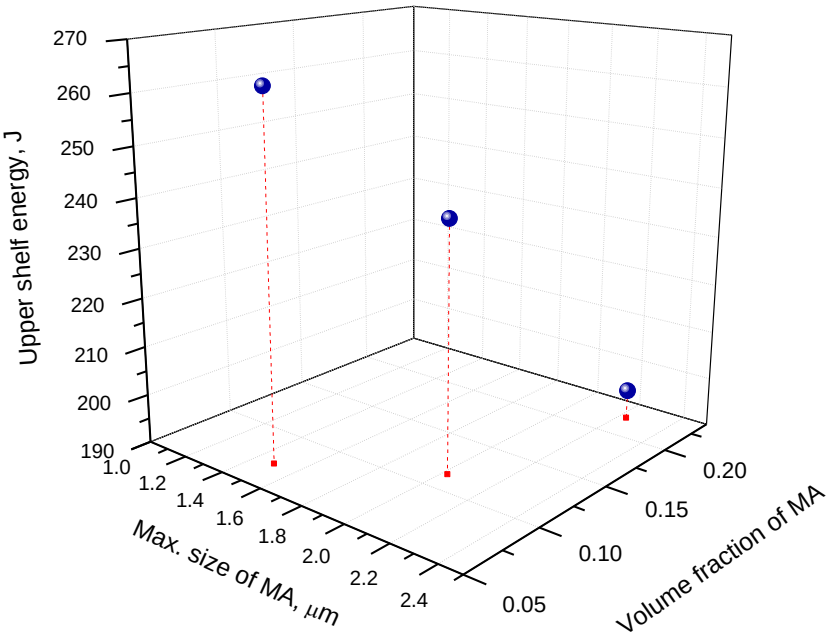

(b) Upper shelf energy vs. max. size & vol. of MA in Steel B2

Figure 6.5 Upper shelf energy vs. Max. size of M-A constituents & Vol. of MA (a) steel A2, (b) steel B2.

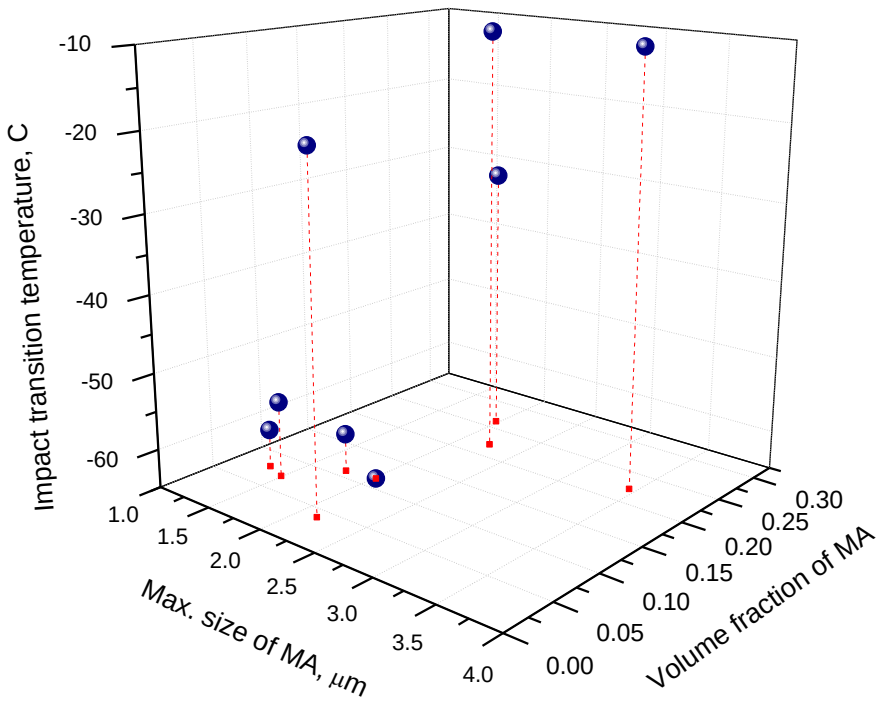

Figure 6.6 DBTT vs. Max. size of M-A & Vol. of MA

The DBTT versus maximum size of MA and volume fraction of MA is shown in a three dimensional graph, Figure 6.6 and the data are listed in Table 6.2. The figure includes all the DBTT data of steel A2, B2 and C2. The figure showed that the DBTT is affected by maximum size and volume fraction of MA. The DBTT can be below -55 ℃ when both the volume fraction of MA is 10% and the maximum size of MA is below 2.0 μm. A sample with 4% MA but the maximum size of MA is 2.15 μm, has a high DBTT. Others points in the figure also showed the DBTT increased with volume fraction of MA when the maximum size of MA is similar.

But, in general, low DBTT were associated with low volume fraction and small size of MA.

Table 6.2 The effect of maximum size and volume fractions of MA on DBTT

Specimens	Max. size of MA, μm	Vol. MA	DBTT, ℃
1	2.02	0.11	-65
2	1.77	0.11	-60
3	1.31	0.08	-60
4	1.49	0.07	-55
5	1.98	0.26	-30
6	2.15	0.04	-20
7	2.23	0.22	-10
8	3.45	0.22	-10

6.2 THE FORMATION OF M-A CONSTITUENTS DURING BAINITE TRANSFORMATION

The formation of MA cannot be eliminated but can be reduced by thermomechanical processing during bainite transformation. According to the results in Chapter 5, the MA can be controlled by thermomechanical processing. The results in 5.4, 5.5 and 5.6 showed the effects of some parameters on the formation of MA, such as finishing temperatures, isothermal holding time, isothermal temperatures, cooling rates and so on. However, all of these parameters can be related to a common factor, the diffusion of carbon in bainitic ferrite during transformation.

There has been a debate if the transformation of bainite is a diffusion controlled transformation or a displacive controlled transformation[105, 106]. Recently, the displacive transformation is more acceptable [40, 45, 107]. Bhadeshia did a wide and deep study for the transformation of bainite in steels. He pointed out that the distinct difference between

Widmanstätten ferrite and bainitic ferrite is the mode of transformation, whether it is diffusion controlled or displacive controlled[28].

However, the displacive transformation mode is absolutely a non-equilibrium transformation. Especially for the transformation of austenite to bainite, the bainite start transformation temperature approximately ranges from about 600 ℃ to about 400 ℃. In this temperature range, the diffusion rates of substitutional elements are very low, not enough driving force energy can be fulfilled. It is very difficult for the substitutional atoms to make a reconstructive movement in a very limited time. However, the diffusion rate of carbon is still very high. It is high enough to diffuse in the grains in seconds to minutes. Thus, the importance of the diffusion of carbon during the bainite transformation was attempted to be explained from thermodynamics and kinetics[108, 109]. Some results of carbon partitioning from martensite to austenite have been interested and discussed in some reports[110-112].

According to the bainite transformation, two scenarios for carbon partitioning should be considered for the formation of MA constituents. The first one is before the bainite transformation and the second below bainite transformation should be considered.

As introduced in 2.6.2, Figure 2.14 is used to explain the bainite transformation and indicates the important temperature T_0 for bainite transformation. From the free energy curves, it can be seen that bainite transformation can take place only when steel is cooled below T_0. When the finishing cooling temperature is higher than T_0, the bainite transformation does not proceed according to thermodynamics. Here, a similar schematic diagram to Figure 2.14 is used to explain the carbon partitioning above T_0 and the formation of MA in the final microstructures, as shown in Figure 6.7. C_0 in the figure is the critical carbon concentration for bainite transformation. At temperature T, if the carbon concentration is lower than C_0, the free energy

curves indicate that bainite transformation can proceed. However, if the carbon concentration is higher than C_0, the transformation from austenite to bainitic ferrite by displacive mode becomes impossible according to the free energy curves. The different delay times after finishing deformation temperature were compared for the effect on the formation of MA constituents in 5.4. Given longer time for carbon partitioning, the more MA constituents are formed observed in the final microstructure at room temperature. It should be explained by carbon partitioning and segregation. After deformation, the stored energy is not uniformly distributed in steel. Some areas, which has high stored energy, such as austenite grain boundaries and some defects(for example, dislocations), are the sites on which carbon atoms preferentially segregate. Thus, the carbon concentration in these local areas gradually increases. Once the carbon concentration exceeds the critical carbon concentration C_0, the bainite transformation cannot proceed completely. The reaction must stop in these local areas when steel is rapidly cooled to temperature T. The remaining untransformed austenite subsequently transform into martensite and a small amount of it is still retained, which is called MA constituent. In summary, considering carbon partitioning above T_0, it should be pointed out that carbon partitioning increase carbon segregation and that impedes completely bainite transformation. The formation of MA is dependent on the extent of carbon segregations above temperature T_0.

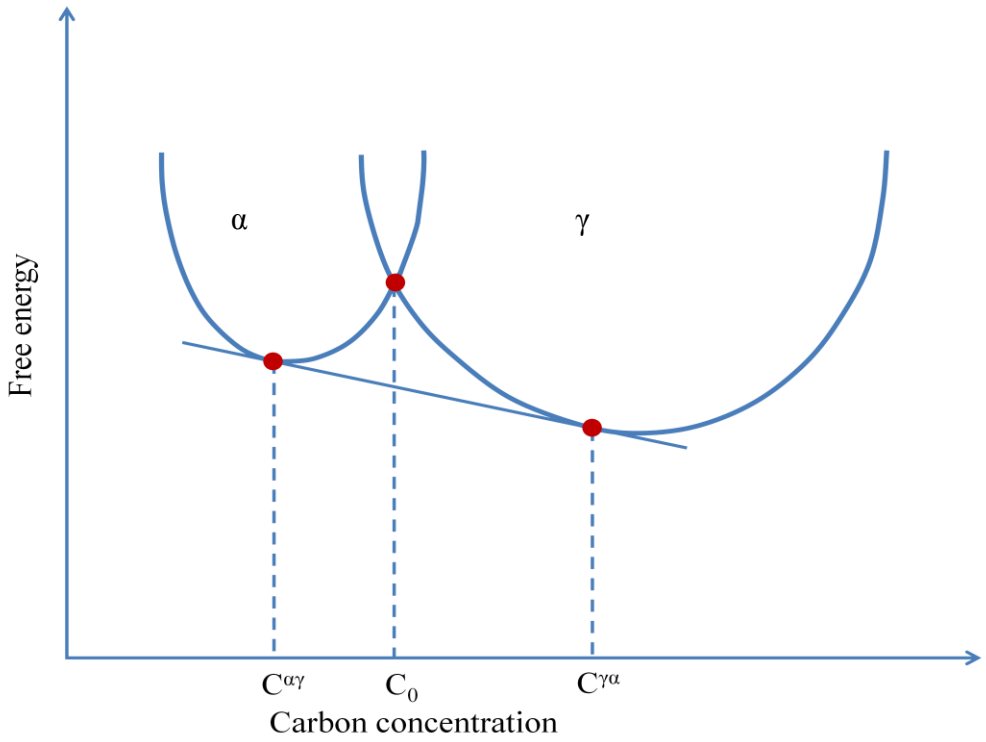

Figure 6.7 Schematic diagram of free energy curves at temperature T

The incomplete bainite transformation can result in the formation of MA constituents as discussed above. However, it is found that even a relative high complete bainite transformation may also contain a large amount of MA constituents. Thus, the formation of MA constituents below T_0 is discussed as follows.

According to the thermodynamics description, Figure 6.8 is tried to explain the mechanism. The schematic austenite and ferrite free energy curves illustrated the supersatuaration of carbon during bainite transformation. Figure 6.8 illustrates the free energy changes at two different temperatures. The blue solid line curves represent the free energy at temperature, T, and the blue dash line curves illustrate the free energy at lower temperature, T'.

The free energy of ferrite, α, is shown in the left curves, and the right two curves illustrate the free energy of austenite, γ.

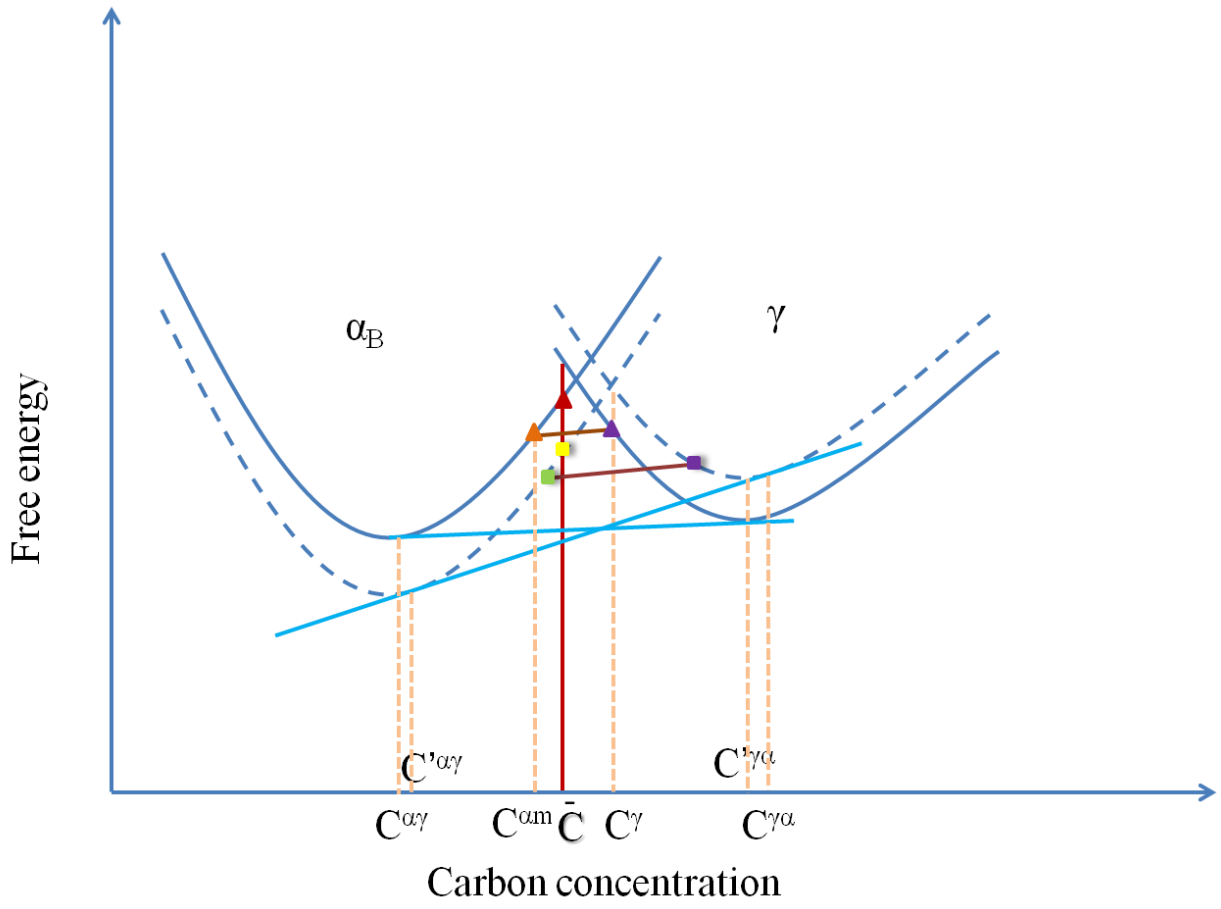

Figure 6.8 Schematic diagram illustrating the chemical free energy changes with regards to average carbon concentration in austenite (solid line curves: at T; dash line curves: at T'.) T'<T

$\bar{C}$ is the composition of the steel. In this figure, At T, $\bar{C}<C_0$, bainite can continue as diffusionless transformation, so does bainite transformation at lower temperature T', as shown in this plot. Let's consider the stability of bainitic ferrite at two different temperatures.

At higher temperature T, bainitic ferrite (the red triangle) contains more energy than that at lower temperature T'(yellow square), so we can see the lower free energy of bainitic ferrite is more stable at T'. One measurement of stored energy of bainitic ferrite in steel may explain it. See Figure 6.9 . The steel transformed at higher temperature has higher stored energy.The stored energy is calculated according to Shi-Hoon Choi's computation[113-115].

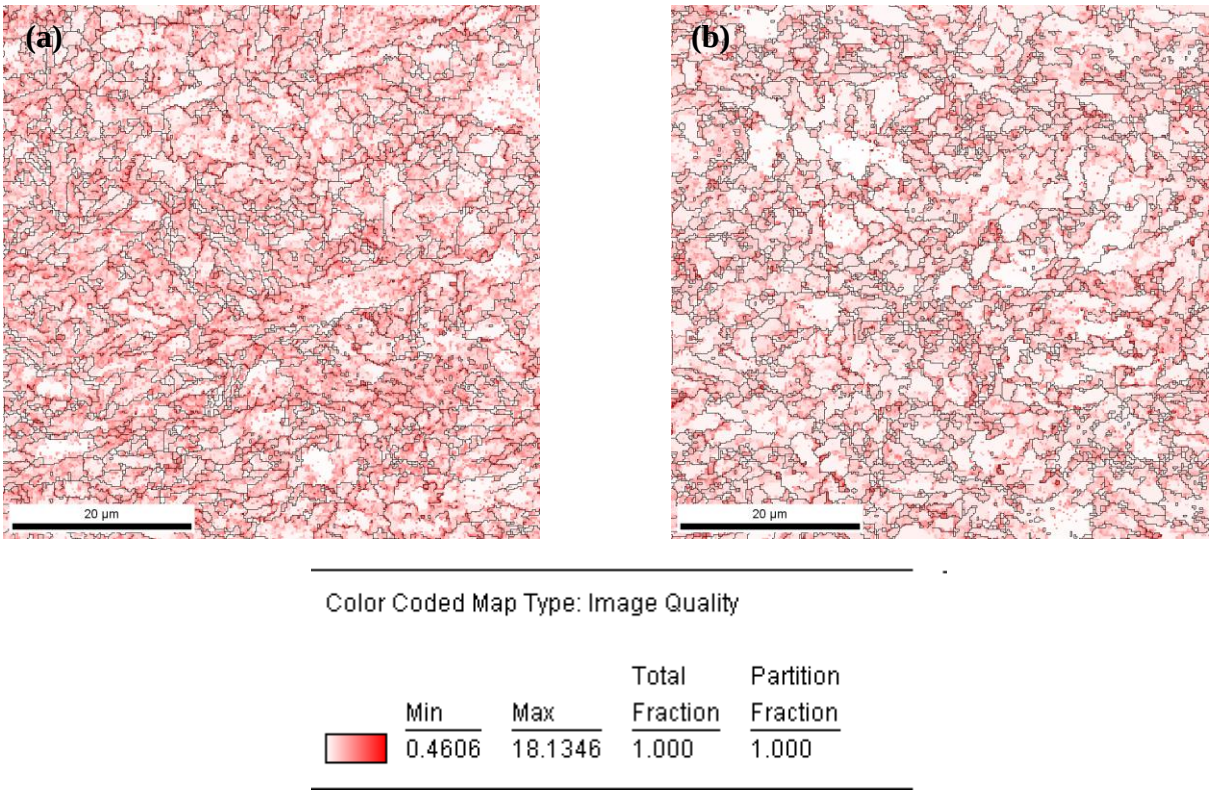

Figure 6.9 The stored energy in bainite with different finishing cooling temperature. (a)Higher WET: 500 ℃. Average stored energy: 4.29J/cm3; (b) Lower WET: 400 ℃. Average stored energy: 3.24J/cm3

Suppose the steel is rapid cooled down to T, and then it is isothermally held for some time. As indicated in Figure 6.8, the composition of bainite indicated by red triangle is not stable, it can decompose into two different phases: γ (assuming time and diffusivity are sufficient, the composition of γ is Cγ) , according to the free energy curves, once the other composition is fixed, the carbon composition of bainite should be also fixed. See the tie line along the yellow square. To achieve the compositions, according to the free energy curves, the decomposition is spontaneous. Because the diffusivity of carbon at T is relatively high, and the concentration of austenite is Cγ, which is a lower concentration when compared to the concentration of austenite at a lower temperature, say T'. From the view point of kinetics, the carbon partitioning is much easier to achieve. Therefore, at T, carbon concentration over $C^{\alpha m}$ is not stable.

Now, let's consider bainite transformed at T'. Upon isothermally held at T', it's impossible to obtain austenite when carbon concentration less than C^{γ} because the free energy of the austenite would be higher than that of bainitic ferrite at T' according to thermodynamics. The supersatuaration of carbon in bainite at lower temperature T' is more stable for two reasons. 1. To reduce the carbon concentration in bainite from $\bar{C}$ to $C^{\alpha m}$ for ferrite, the corresponding of carbon concentration in austenite will be much higher than that at T. See the two points indicated by red line. That means the partitioning of carbon from bainitic ferrite to austenite needs more time and so that decomposition becomes difficult controlled by kinetics. 2. Another reason is that carbon diffusion rate becomes slow at lower temperatures, which slows down the partitioning to a more extent. In other words, the supersatuaration of carbon in bainite at T' is more stable.

Thus, a lower temperature can hinder the partitioning of carbon, so does the formation of austenite. And, after cooling to room temperature, most of this types of austenite can transform into MA. Thus, the volume fraction of MA constituents can be also reduced.

At temperature T, which is below Bs temperature, according to the free energy tangent rule, the carbon at $\bar{C}$ in austenite at the start of the bainitic ferrite reaction will diffuse to $C^{\alpha\gamma}$ in ferrite and $C^{\gamma\alpha}$ in austenite to achieve the equilibrium balance. However, the displacive transformation always takes place in a very short time[116, 117]. Thus, some of the austenite can transform into bainite at the same composition in the displacive mode in a very short time. In this case, the carbon concentration is inhabited in the bainite from the austenite, which is the average concentration of carbon in austenite or a little bit less. However, this initial carbon in bainitic ferrite ($\sim\bar{C}$) is unstable according to the free energy curves in the figure. To simplify the situation, only one austenite grain is considered. At temperature T, if enough time is given, the composition will diffuse to have a tendency to achieve the equilibrium state. The ideal state is that the concentration of carbon in ferrite is $C^{\alpha\gamma}$ and in retained austenite it is $C^{\gamma\alpha}$. The results of isothermal holding time in 5.4.1 conformed to the thermodynamics explanation. Prolonging the holding time at T, the carbon diffuses to some small austenite area. Thus, these small austenite areas grow along grain boundaries or dislocations preferentially (See Figure 5.43). From the point view of thermodynamics, the more carbon is in the austenite, the more stable it is. Thus, more carbon from carbon supersaturated ferrite diffuses into the austenite. The evidence of A04 in Figure 5.43 has shown that holding at 450 ℃ for 10 minutes, more large size of MA was formed with a high hardness number. During the segregation of carbon in the carbon enriched austenite, the free energy of the austenite will be lower than the free energy of adjacent bainitic ferrite; thus some of the neighboring austenite will grow and coalesce. Therefore, in A05, it

appeared that two neighboring austenite grains transformed to martensite after water quenching into room temperature.

Figure 6.10 illustrates a part of Fe-C diagram. Considering the effect of the alloy elements on the Ar3, the Ar3 temperatures will decrease and the three phase equilibrium line will also be lowered to some extent. To simplify the transformation model, a normal Fe-C diagram was illustrated. At equilibrium below the T_E, the austenite (γ) should completely decompose into ferrite (α) and cementite. But austenite does not decompose at a temperature below the equilibrium temperature when the composition, $\bar{C}$, in austenite is rapidly cooled to a low temperature, T (which is supposed to be lower than Bs), it is in a non-equilibrium. The formation of pearlite can be completely hindered. When steel is rapidly cooled down to T, and then isothermally treated at T, the composition tends to move towards equilibrium at that temperature, and this equilibrium is a kind of para-equilibrium because the substitutional atoms can hardly move and only carbon can move and affect the microstructures. According to the inverse level rule, considering the equilibrium of carbon in steel, the volume fraction of austenite at T is:

$$V_A = \frac{\bar{C} - C^{\alpha\gamma}}{C^{\gamma\alpha} - C^{\alpha\gamma}} \times V \tag{6.1}$$

where V_A is the volume fraction of austenite, V_F is the volume fraction of ferrite, and V is total volume fraction of microstructure, $V = V_F + V_A$.

Assuming the volume fraction of austenite, V_A, only transforms into MA, then the volume fraction of MA, V_{MA}, could be equal to or less than V_A. Thus, the volume fraction of MA is dependent on the average carbon concentration and the carbon concentration in ferrite and austenite in equilibrium. Since the maximum solubility of carbon in ferrite increases as the temperature decreases, as shown in Figure 6.10, V_A will be expected to be lower at a lower

bainite transformation temperature, which finally reduces the volume fraction of MA. It has been proved by the results of evolution of the volume fraction of MA in 6.4.2.

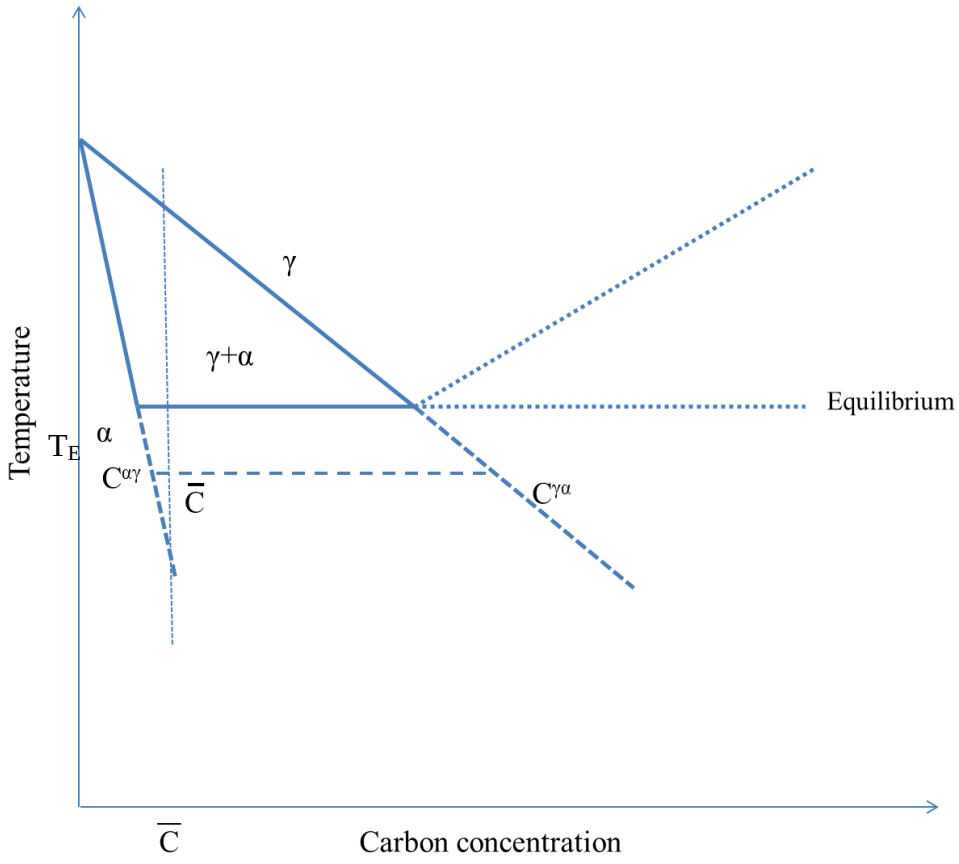

Figure 6.10 Schematic diagram of a corner of the Fe-C diagram

In summary, to avoid the formation of a great amount of MA, some measures can be taken according to the thermodynamics and kinetics view. The first is to reduce carbon composition in steel, for example, in our research steel, the carbon content is supposed to reduce from 0.07 to 0.04, but the disadvantage is, this will lower the yield strength of steels. The second way is to lower the Bs temperature. The third method is to rapidly cool steel to a lower temperature, which can retard the carbon diffusion in the microstructures, as well as reduce the volume fraction of MA "in equilibrium".

6.3 EFFECT OF TRANSFORMATION TEMPERATURES ON THE CRYSTALLOGRAPHIC TEXTURE OF BAINITE

The mechanical properties of bainitic steels could be dependent on the crystallographcic texture of bainite transformed from austenite. The transformation of bainite is a kind of displacive transformation. Greninger and Troiano[118] found the habit plane of bainite is irrational and different from that of martensite in the same steel. And the habit plane indices vary with the transformation temperatures and the carbon concentration of steel.

Figure 6.11 shows the irrational habit plane of bainite and the habit plane of martensite in the same steel. The results showed the habit plane of bainite is different from martensite, and it also varies with transformation temperatures. A similar orientation of the habit plane of bainite was found by Bowles and Kennon in a 0.4wt%C steel[119].

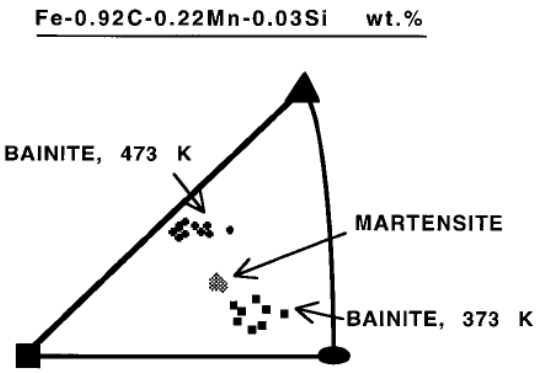

Figure 6.11 An example showing the irrational habit plane of bainite which varied with transformation temperatures[118]

To understand the crystallographic texture of bainite in low carbon bainitic steels, two samples B2-1 and B2-3 after deformation were selected from to compare the orientations of bainite after displacive transformation from austenite. As shown in Chapter 5, the water end temperatures for B2-1 and B2-3 are approximately 400 ℃ and 500 ℃.

The microstructure is compared for B2-1 and B2-3, as shown in Figure 6.12, since the strength of the two specimens are very close, as illustrated in Table 6.3. The Vickers hardness numbers are 268 and 270 for B2-1 and B2-3, respectively, which are almost the same. The data from tensile tests are shown in Table 6.3. The table also shows very similar data for B2-1 and B2-3, and only the difference is that the UTS of B2-1 has about 23 MPa higher of strength than that of B2-3. The microstructure looks similar for the two different processes in SEM. It is one kind of continuous cooling bainitic microstructure, which is composed of bainitic ferrite and some fraction of Martensite-Austenite constituents. It is hard to quantitatively measure the grain

size or effective grain size for bainite in Figure 6.12. Judging from the microstructures, we might say the “grain size” looks a little smaller in Figure 6.12 (b) than that in Figure 6.12 (a).

Table 6.3 Mechanical properties of specimens B2-1 & B2-3

	YS, Mpa	UTS, Mpa	YS/TS ratio	VHN (500g)	El%	
					UE	TE
B2-1	704	864	0.82	268	6.3	25.0
B2-3	701	841	0.83	270	7.2	26.2

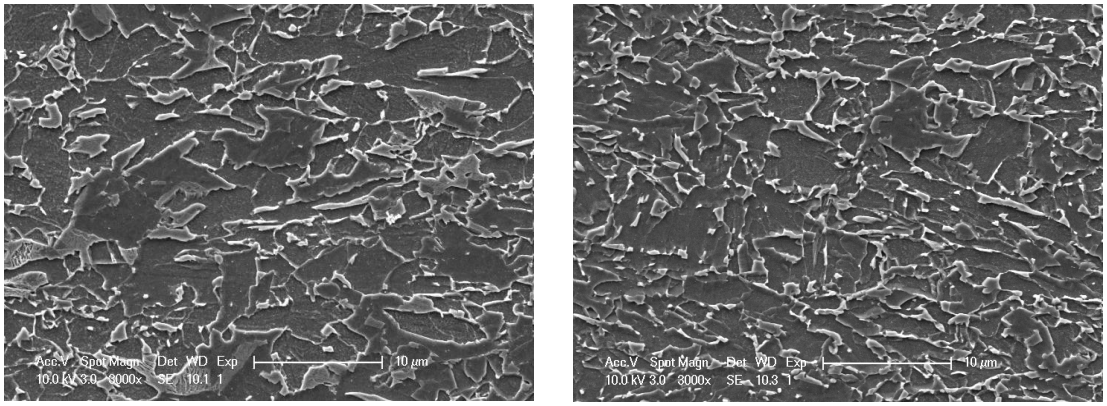

(a) (b)

Figure 6.12 SEM microstructure of (a) sample B2-1; (b) sample B2-3

However, the results of Charpy impact toughness are very different, as shown in Figure 6.3. In the figure, the curves of impact absorbed energy and ductile brittle transition curves of B2-1 and B2-3 were compared. The upper shelf energy of B2-1 is about 250J, and the energy of B2-3 is about 200J. As can be seen from Figure 6.3, DBTT of B2-3, about -20℃, is 40℃ higher than that of B2-1.

As discussed in the above section, toughness is believed to be dependent on volume fraction of MA and the size of MA. Moreover, another factor which is always very important for steel design is grain size, or effective grain size (or packet size) in bainitic steels and martensitic steels. However, in low carbon bainitic steels, the microstructures are complex and neither grain size nor effective grain size is clearly observed. Thus, in the following sections, the texture of bainite, crystallographic packet size and grain boundary character distribution will be discussed with regard to toughness.

6.3.1 **Texture of bainitic transformation**

To understand the evolution of crystallographic texture of bainite in low carbon bainitic steels, the orientation of microstructure was studied by inverse pole figures. Figure 6.13 shows the EBSD image quality maps of B2-1 and B2-3 with the color of inverse pole figure. As represented by the colors, the orientation of B2-1 and B2-3 are apparently different. It can be seen that the orientation of grains in B2-1 is more random than B2-3. And the orientations of the most grains are distributed in the area near <331>), as shown in Figure 6.14(a). However, most of the microstructure in B2-3 shows high density close to <113>, as the pink indicates in Figure 6.14 (b). The results show the evidence that the bainite transformation at different temperatures may cause the very different orientations. In high carbon steels, the habit planes of bainite

formed at 200 ℃(473K) and 100 ℃ (373K) are around <113> and <331>, respectively, as shown in Figure 6.11[118]. Comparing the results in our research with the results in reference[118], for very low carbon steel with continuous cooling, the observed orientation of bainite is very similar to the habit planes in low carbon or high carbon steels. The only difference is that the formation temperatures are much higher in the very low carbon steels. Thus, it can be said that bainite transformation has preferential crystallographic texture orientations with regards to transformation temperatures even for the very low carbon steels. At a higher temperature, the orientation of bainite is close to <113>. And at a low temperature, the orientation is preferentially near <331>. However, it seems that bainite transformation has this crystallographic texture orientation trend but does not have a fixed orientation index. It is controlled by the transformation temperatures and the cooling rates. A rapid cooling rate can hinder the bainite transformation at high temperatures, but a slow cooling rate increases the variety of bainitic crystallographic textures due to the continuous bainite transformation at different temperatures.

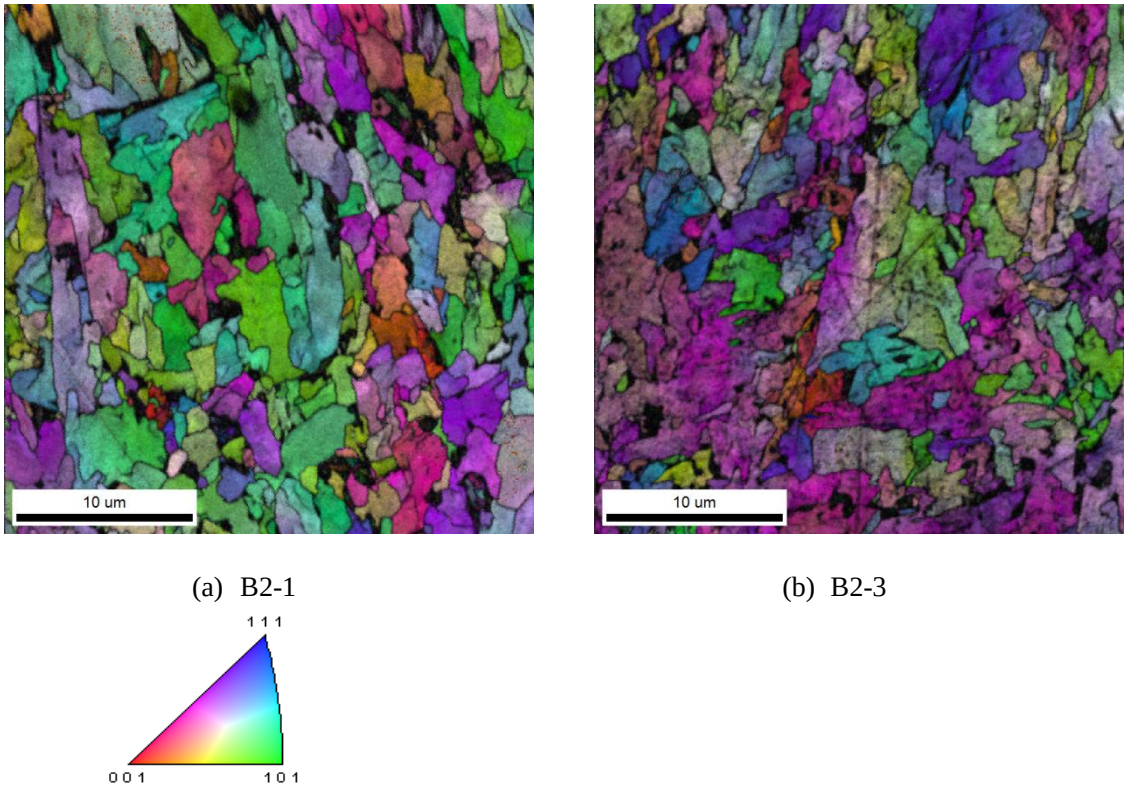

(a) B2-1 (b) B2-3

Figure 6.13 EBSD image quality maps with inverse pole figure (IPF)

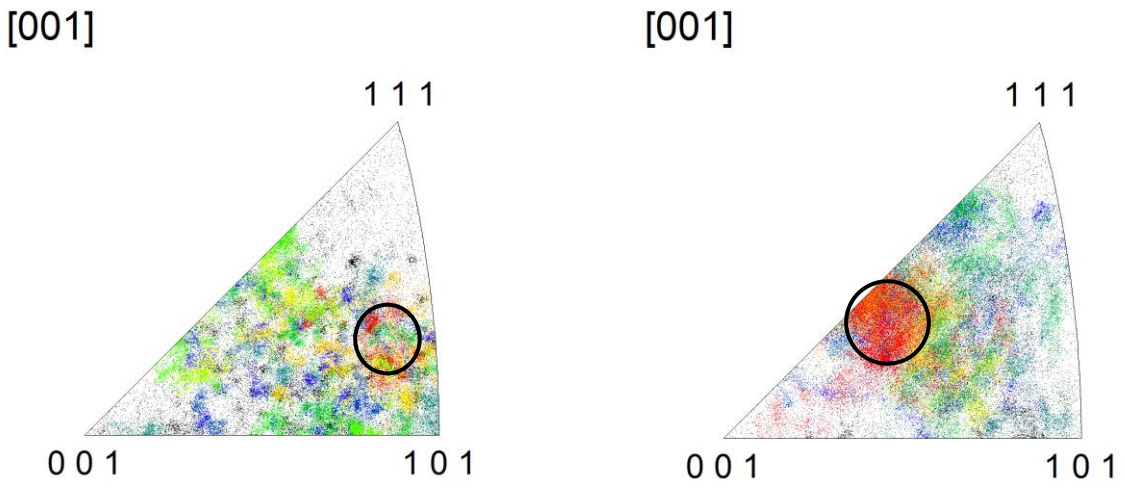

(a) B2-1 (b) B2-3

Figure 6.14 The orientations of bainite with different transformation temperatures (a): ~<331>; (b): ~<113>.

6.3.2 **Grain boundary characterization**

Another factor that should be considered is the grain boundary character distribution. The grain boundary energy is believed to affect the crack propagation in steels. Some papers have proved the special CSL grain boundaries can hinder the crack propagation more than the other high angle grain boundaries in fcc materials[49, 72, 120, 121].

Although microstructures of B2-1 and B2-3 were observed in SEM in high magnification, it is still difficult to recognize the relationship between impact toughness and grain boundaries. Thus, EBSD techniques were used for its accurate orientation measurements[86, 122]. Crystallographic packet size was proposed and determined by EBSD. As determined by OIM analysis, the CSL grain boundaries are compared in Figure 6.15. It shows the frequencies of CSL grain boundaries (low Σ boundaries ($\Sigma \leq 29$)) and random boundaries ($\Sigma > 29$) according to Brrandon's criterion ($\Delta\Theta \leq 15° \ \Sigma^{-1/2}$)[75]. The number fraction of CSL grain boundaries in steel B2-1 is higher than that in B2-3. CSL grain boundaries are low energy boundaries, which have the capability to hinder crack propagation along grain boundaries than random grain boundaries with higher energy. However, Σ1 grain boundary (low angle grain boundaries are called Σ1 in CSL grain boundaries definition) is a disadvantage for improving toughness, although it has lower energy in that kind of grain boundaries. The reason is that the misorientation of low angle grain boundary between two grains is too small, which cannot become a boundary that hinders the cracking. This is consistent with the results shown in reference[123]. The low angle grain boundaries cannot be considered as "real" grain boundaries, even if they are very clear in SEM micrographs. In Figure 6.15, GBCD is compared for the two samples. It is found that B2-1 has a

high fraction of CSL grain boundaries and low fraction of Σ1 grain boundaries while B2-3 has the contrary results.

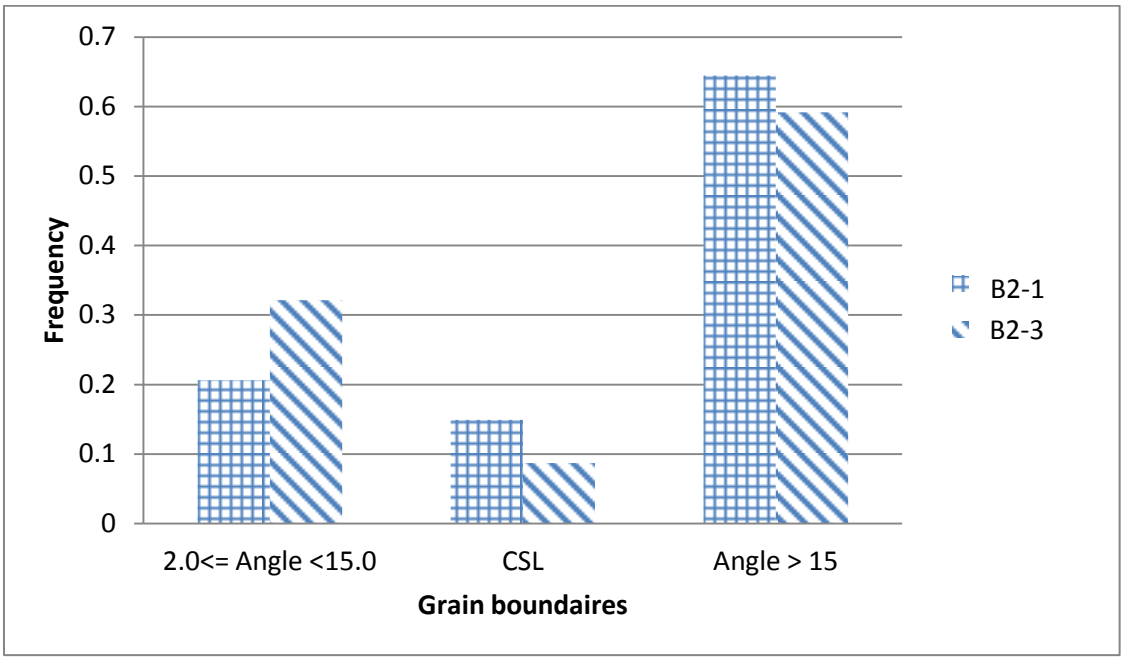

Figure 6.15 The frequency of grain boundary character distribution

The grain boundaries are characterized by EBSD techniques, as shown in Figure 6.16. The figures in the left column illustrate grain boundaries in B2-1, and those in B2-3 are shown in the right column. In the figures, the blue line indicates low angle grain boundary (Σ1), red line indicates CSL grain boundary (Σ3- Σ29) and black represents random grain boundary. Figure 6.16(a) has all the boundaries information in B1 & B3, respectively. When all boundaries are considered, comparing these two figures, it can be seen that the "grain size" of B2-1 is even coarser than that of B2-3, similar to the microstructure in SEM (Figure 6.12). However, if only

random grain boundaries are considered (Figure 6.16 (b)), both of them have big “grain size”, which is more than 10 μm. When the special CSL grain boundaries are considered together with random boundaries, it shows that the grains have been divided into smaller size in B2-1 than B2-3. In recent research work, CSL grain boundaries are found to have better resistance to crack propagation[124, 125].

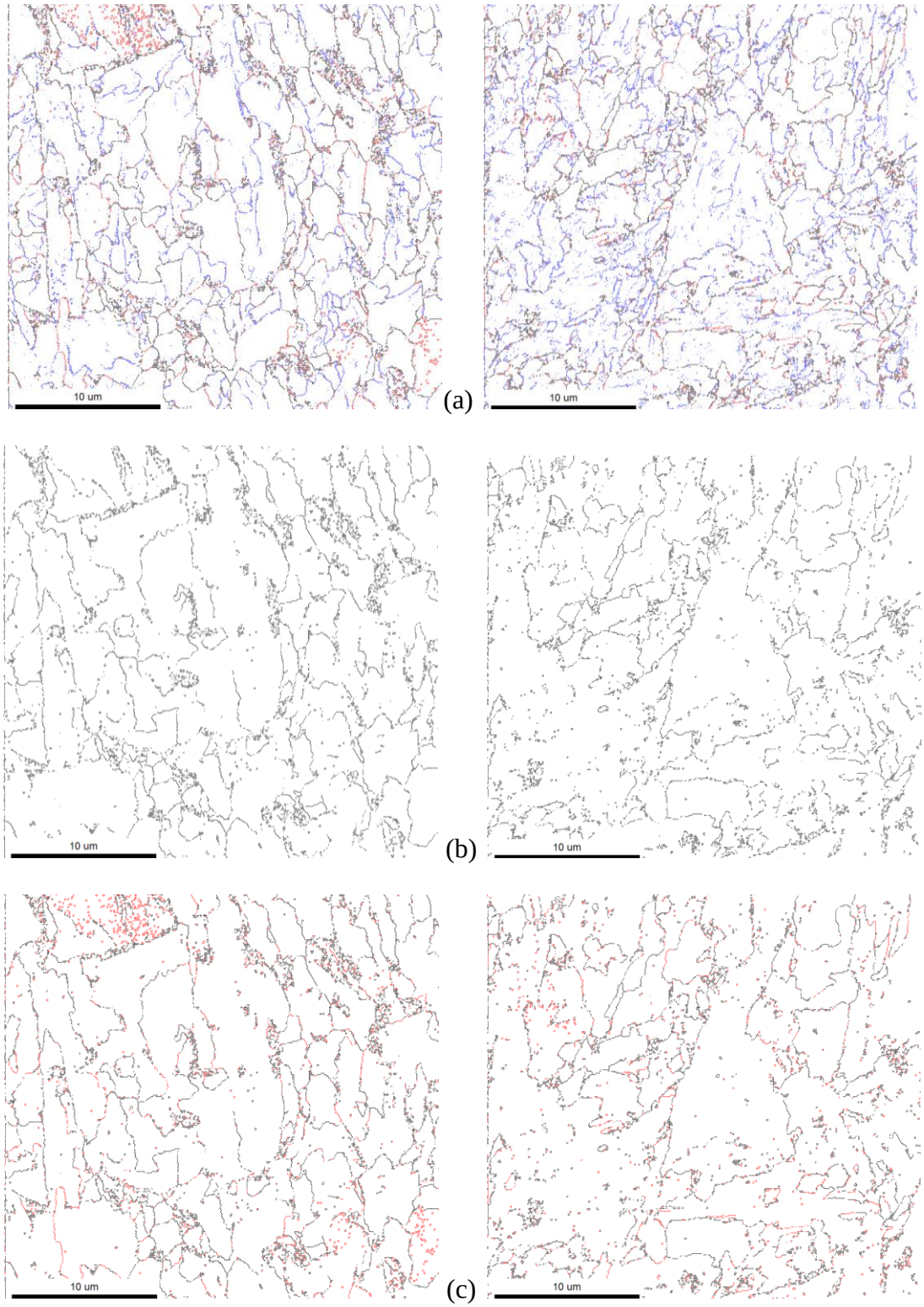

Figure 6.16 The distribution of grain boundaries.(Left: Sample B2-1; Right: Sample B2-3)

6.3.3 **Transformation orientations, GBCD and toughness**

With consideration of random grain boundaries and CSL grain boundaries, the crystallographic packet size instead of bainite packet size is depicted in Figure 6.17. The crystallographic packet is termed according to the common orientations for laths or sub grains in bainite or martensite to distinguish the bainite packet, or morphological packet, which only based on microscopically parallel laths or sub grains[126, 127]. The different colors represent the different crystallographic packet size in the figures. As highlighted in Figure 6.17 (a), the maximum diameter of crystallographic packet size is approximately 9μm. Other secondary large size is about 5-6 μm due to the packets being divided into several parts by random or CSL grain boundaries. However, in Figure 6.17 (b), although this steel also has many grain boundaries, as shown in SEM (Figure 6.12) & EBSD OIM analysis (Figure 6.16(a)), a big fraction of them are Σ1. The misorientation of Σ1 grain boundary is usually measured 5~9 ° in the steel, which is not considered as packet boundary in the EBSD analysis. Therefore, only random and CSL grain boundaries are considered in sample B2-3, and big crystallographic packet size were obtained. The maximum of crystallographic packet size is about 15μm (if we don't consider the limitation of EBSD study area, and the actual crystallographic size should be larger for both samples). As highlighted in Figure 6.17, the largest crystallographic packet size in B2-1 and B2-3 are different. The largest for B2-1 is near the orientation of <331>, however, the largest for B2-3 is close to <113>. The results showed the crystallographic packet size near <113> is larger. The big crystallographic packet size around <113> may be another predominant reason deteriorating the toughness.

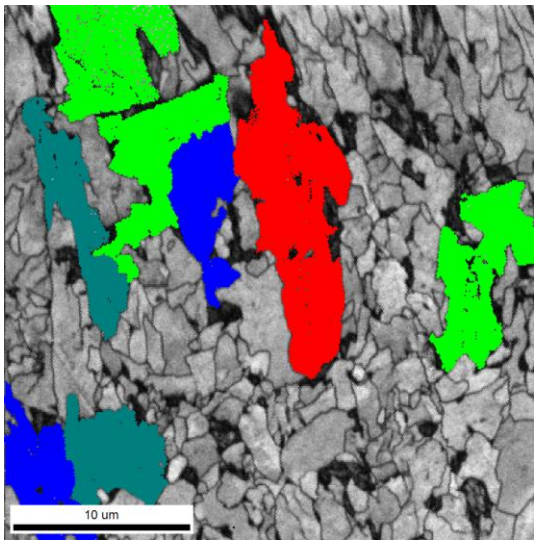

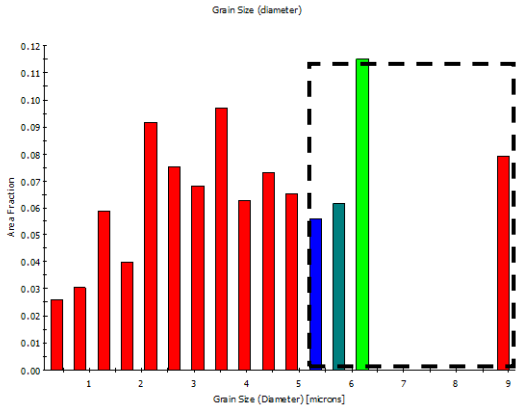

(a) B2-1

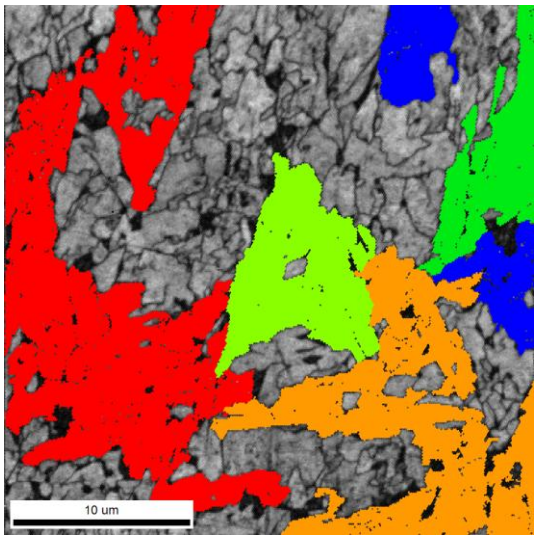

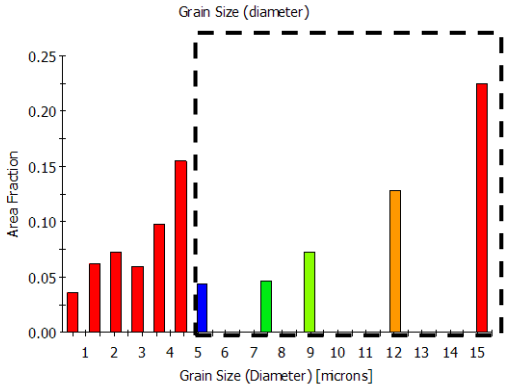

(b) B2-3

Figure 6.17 The crystallographic packet size in (a) B2-1 and (b) B2-3. The colors were highlighted with different packet size corresponding to the right column bars.

6.3.4 **TEM (MA lattice pattern, orientation of bainitic ferrite)**

The results were confirmed by TEM observations. Bright field images in Figure 6.16(a, c) shows different contrast between MA and bainitic ferrite. The black area in Figure 6.18(a) is confirmed to be MA by diffraction. The lighter area is bainitic ferrite. The diffraction pattern (Figure 6.18(d)) from the black area shown in Figure 6.16(c) has two different spot patterns that almost overlap[128, 129]. Careful analysis suggests that one spot pattern is from martensite and the other is from austenite[103, 130]. The two patterns show Nishiyama-Wassermann orientation relationship ($\{111\}\gamma // \{011\}\alpha$; $<110>\gamma // <100>\alpha$)[107]. The diffraction pattern also proves that the black area contains both martensite and retained austenite. A bright field image of an MA grain in B2-3 acquired at higher magnification is shown in Figure 6.18(c). The contrast details illustrate the microstructure in MA is not homogeneous. It is composed of dark areas and grey areas. The dark areas contain many dislocations, which should be martensite because generally martensite has a higher dislocation density. The grey area is retained austenite. The orientation of most ferrite grains in B2-3 is close to <113> zone axis according to the diffraction pattern shown in Figure 6.18(b).

For sample B2-1, which has a lower WET temperature, the TEM microstructures are shown in Figure 6.19 (a) & (b). In the figures, Region A is the MA constituent. Due to fast cooling to a lower temperature, the sample contains more dislocations. The dislocations moved and formed some small low angle grain boundaries. The size of the subgrains is about 0.5~1μm, as shown in Region B in Figure 6.19(a).The dislocations in low angle grain boundaries and sub grain boundaries are indicated by arrows. In a bright field image acquired at a higher magnification, some precipitates are observed at high dislocation-density areas and the grain

boundaries between bainitic ferrite and MA, which could be the niobium carbonitrides. According to the diffraction pattern in Figure 6.19(c), the preferential orientation of bainitic ferrite grains is close to <331>. The TEM results are consistent with EBSD results, further providing evidence that the preferential orientation of bainitic ferrite is close to <113> at a higher temperature, and is changed to <331> at a lower temperature.

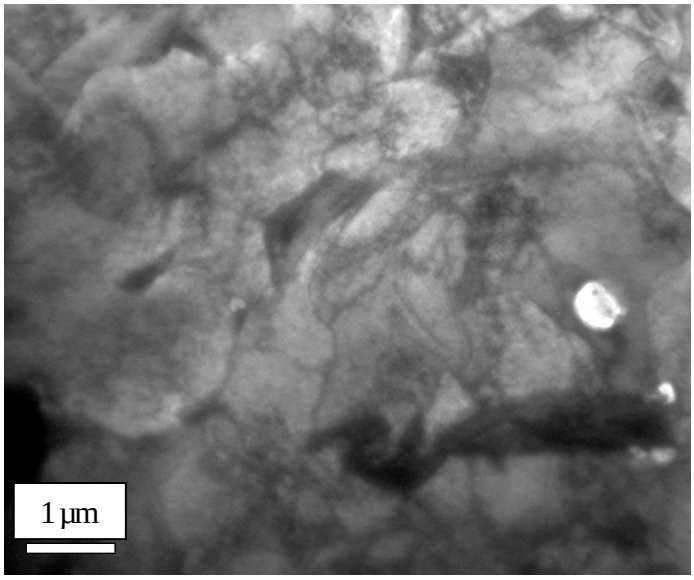

(a) Transmission electron micrograph of B2-3

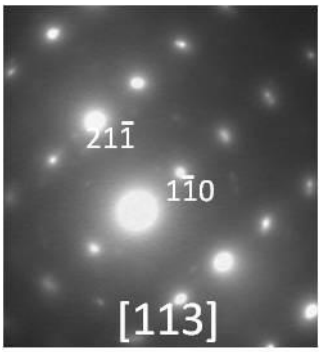

(b) Diffraction pattern of bainitic ferrite

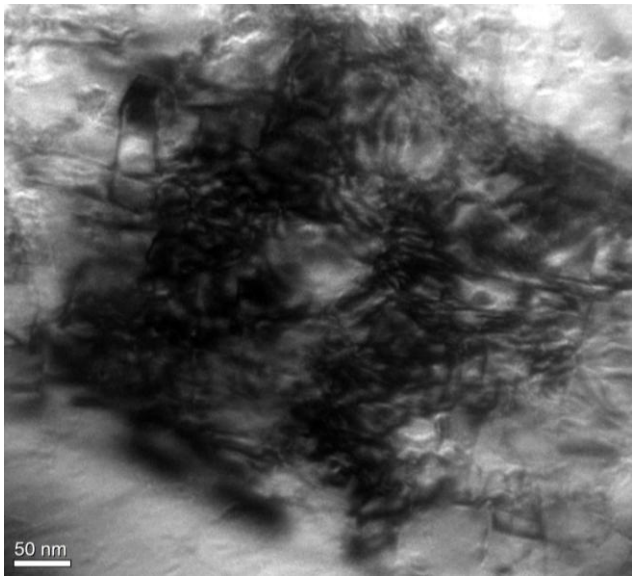

(c) M-A constituents

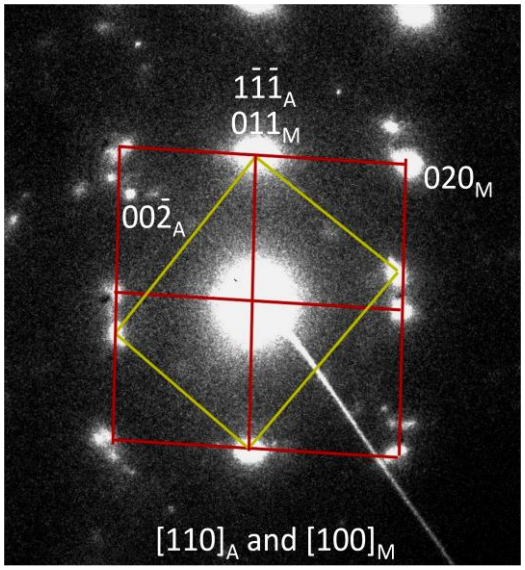

(d) Diffraction pattern of MA

Figure 6.18 Transmission electron micrograph of B 2-3

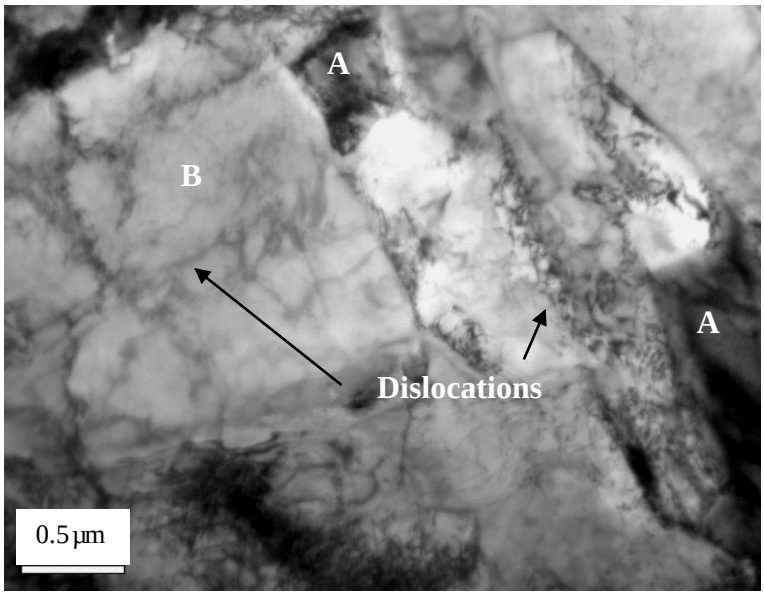

(a) Transmission electron micrograph of B2-1

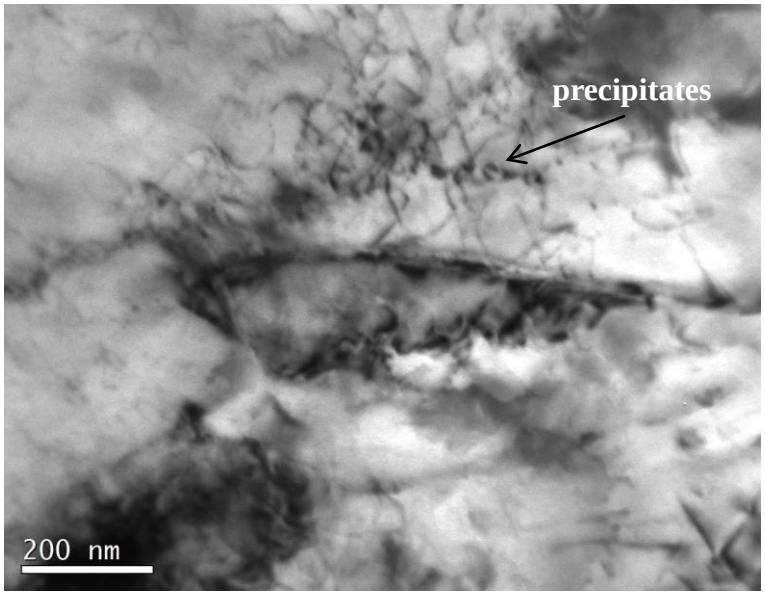

(b) High magnification of B2-1

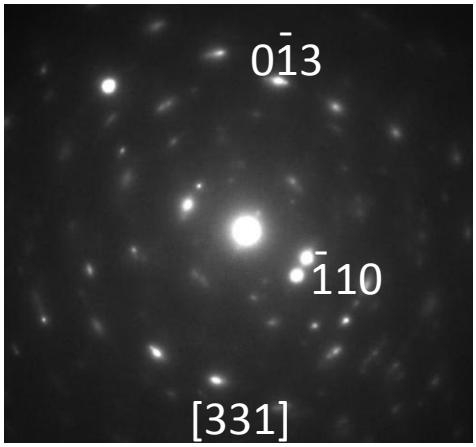

(c) Diffraction pattern of B2-1

Figure 6.19 Transmission electron micrograph of B 2-1

6.4 TOUGHNESS IMPROVEMENT

As discussed in the above sections, the toughness of low carbon high strength bainitic steels is mostly controlled by three factors: martensite-austenite constituents, crystallographic packet size and grain boundary character distribution. The results and discussion have already shown that reducing the volume fraction and size of MA, decreasing the crystallographic packet size and increasing special CSL grain boundaries can improve toughness. It should be noted that each of the factors can improve toughness, but all the three factors should be fulfilled to obtain high toughness in low carbon high strength bainitic steels. Fortunately, the trend of the change of factors seems in the same direction to improve toughness. For instance, the decrease of MA is accompanied by reducing crystallographic packet size and increases CSL grain boundaries. The following will be discussed according to the view point of physical metallurgy and thermodynamics.

6.4.1 **Austenite grain size**

Austenite is the first key factor which will affect both strength and toughness during the thermo mechanical processing. All the subsequent microstructures can be determined by the austenite state to some certain extent. The austenite grain coarsening study mainly talked about the relationship between grain coarsening temperatures and some alloy elements. The mixture of austenite grain size inevitably brings different final microstructures after thermomechanical processing due to the different stored energies and different nucleation sites in grains. To obtain the optimum mechanical properties, the grain coarsening temperature ranges should be avoided to prevent the non-uniform austenite grains. The results in 5.1 showed that the addition of 0.3wt%

chromium can lower the grain coarsening temperatures for about 100 ℃. The titanium can retard the austenite grain boundary migration, thus retarding austenite grain growth. Comparing the results of the four steels in 5.1, it can be seen that the range of grain coarsening temperatures vary from 1000 ℃ to 1220 ℃. Thus, the reheating temperatures should be selected with consideration of some alloying elements in steels.

The pancaked austenite is designed in HSLA steels after hot deformation. Sv is a parameter to describe it. The more pancaked, the higher value Sv is, and the more deformation bands will appear in a pancaked austenite. Due to the increase of nucleation sites, refinement of grains is obtained for the formation of ferrite. And for the reason of heavy deformed pancaked austenite grain, the width of an elongated austenite can be reduced to small number compared to the size of austenite. The deformed bands will further subdivide the austenite, thus resulting in blocking the length of bainitic ferrite or martensite lath. Moreover, for some low carbon bainitic steels, the morphology of bainite is close to acicular ferrite and granular bainite, the boundaries of microstructures are unclear. But the MA seems to be related to the austenite grain size. The results in 5.4.1 showed the isothermal holding increased the amount of MA. The results also indicated the size of MA can easily increase up to the size of austenite, as shown in Figure 5.43 and Figure 5.44. More related results will be discussed about MA in the latter section.

6.4.2 **Crystallographic packet size and carbon diffusion**

6.4.2.1 **Crystallographic packet size**

Ferrite grain refinement definitely improves toughness. Unfortunately, with the development of high strength steels, more complex microstructures are designed in HSLA steels (acicular ferrite, bainite, lath martensite). For these types of microstructures, one common point is that no clear

grain size can be defined. Researchers have tried to describe and obtain a size definition of microstructures. The definitions of facet size, packet size and effective grain size were proposed[33, 131]. Like the Hall-Petch equation for strength, one general form of the dependence of DBTT on grain size in carbon steel can be written as[132]:

$$DBTT = T_0 + kd^{-1/2} \tag{6.3}$$

where T_0 and k are experimentally determined constants and d is the effective grain size.

All the definitions above are according to the observation from OM or SEM micrographs. However, the experimental accuracy of the size cannot be guaranteed since the effective grain size or packet size is sometimes hard to recognize. Owing to the development of EBSD techniques, all the misorientations of grain boundaries and the orientations are recorded, the crystallographic packet size is supposed to be used. In ferrite grains, the crystallographic packet size should be equal to the ferrite grain size. In bainitic steels or martensitic steels, the crystallographic packet size is sometimes equal to bainitic or martensitic packet size, but sometimes it may be greater than the latter if the observed packet has very close orientations.

For samples B2-1 and B2-3, with two different water end temperatures, the crystallographic orientations of planes are different. The orientations of bainite should be inherited from deformed austenite texture. Some results showed the main texture in deformed austenite are Brass [{011}<211>] and Copper [{112}<111>] textures[133]. Three different orientation relationships are frequently cited to explain the transformation textures, namely Kurdjumov-Sachs ($\{111\}_\gamma$ // $\{011\}_\alpha$; $<011>_\gamma$ // $<111>_\alpha$), Nishiyama-Wassermann ($\{111\}_\gamma$ // $\{011\}_\alpha$; $<110>_\gamma$ // $<100>_\alpha$) and Bain ($\{001\}_\gamma$ // $\{001\}_\alpha$; $<110>_\gamma$ // $<100>_\alpha$) [133]. Although the relationships are very different, they differ from each other for about only a few degrees. It has

been found that two main textures {332}<113> and {113}<110> are formed from the austenite transformation. Some parameters such as amounts of Nb or V, austenite grain size and some substitutional solutes were found to affect transformation textures. For example, Nb increases the {113}<110> in steels[133, 134].

Like the two different transformation textures from deformed austenite, two different orientations of bainite can be found in samples B2-1 and B2-3, which are close to <331> and <113>, respectively.. As observed by other researchers, the orientation of bainite planes is irrational[]. The different orientations of bainite can grow in for the different processes and different alloying elements. However, since only one composition was used, it is found in our experiments that the orientation is only related to the transformation temperatures. From the higher temperatures to lower temperatures, the orientation of bainite is from the region around <113> to <331>. It might be due to the driving force for the displacive transformation. At higher temperature, less driving force is provided for atom movements displacively. However, at lower temperature, more driving force is for the coordinated movement of atoms. For bainite transformation, Bs temperature is around or higher than 500 ℃, and it is hard to eliminate all the orientation formed at that high temperature, and niobium may increase the <113> orientation in steel which can be explained by niobium promoting the formation of bainite at higher temperatures.

Evidence shows the orientation <113> of bainite is related to a large crystallographic packet size. After continuous cooling, the orientations distribute more randomly, and the crystallographic packet size becomes smaller. Considering the crystallographic packet size and toughness, one way suggested to improve toughness is that a rapid cooling should be used to a low bainite transformation temperature to avoid the formation of bainite with <113> orientation.

6.4.2.2 **Carbon diffusion and the formation of MA**

As shown in the former discussion, the carbon diffusion is discussed as a key point to control bainite and the formation of MA from thermodynamics and kinetics. One more experiment was designed to control MA according to the explanation in 6.2. The schematic diagram of the heat treatment process is shown in Figure 6.20. The same composition of steel B was selected and samples were cut into 10mm*10mm* 10mm cubes for heat treatment. Samples were reheated to 850℃ and held for 5 minutes. Austenite grain size was expected to be small size in order to minimize the effect of austenite grain size on formation of MA. A 30℃/s cooling rate was used to cool specimens to three different temperatures: 550℃(BH1), 500℃(BH2) or 450℃(BH3). When reaching temperatures, a 60 seconds isothermal treatment was used and then was air cooled to room temperature. The microstructures etched with LePera are shown in Figure 6.21. And the volume fraction of MA was illustrated in a graph versus the bainite transformation temperatures (Figure 6.22). The volume fraction and size of MA decreased with a lower isothermal temperature. The results provided good evidence to the analysis of carbon diffusion and the formation of MA. Therefore, the improvement of toughness as the following: reducing carbon diffusion rate; limiting the holding time; reducing the carbon concentration from 0.07% to below 0.05wt%. The low supersaturated carbon concentration should reduce MA to a small amount.

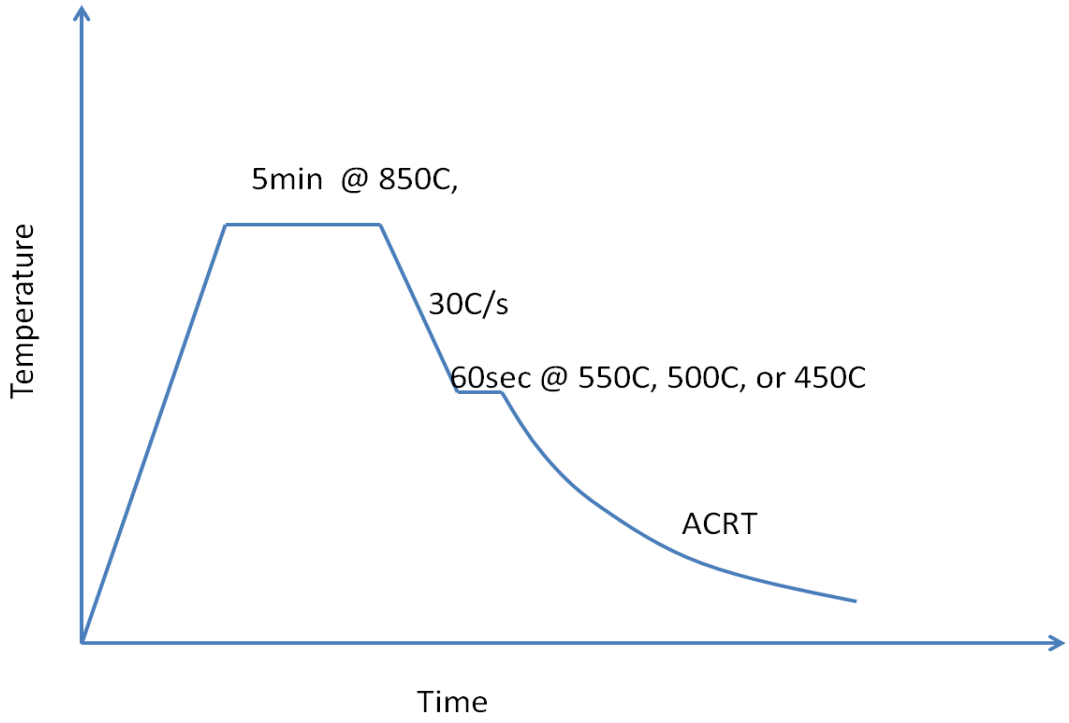

Figure 6.20 Schematic diagram of heat treatment for study of formation of MA. The sample No.: BH1: at 550 ℃; BH2: at 500 ℃; BH3: at 450 ℃.

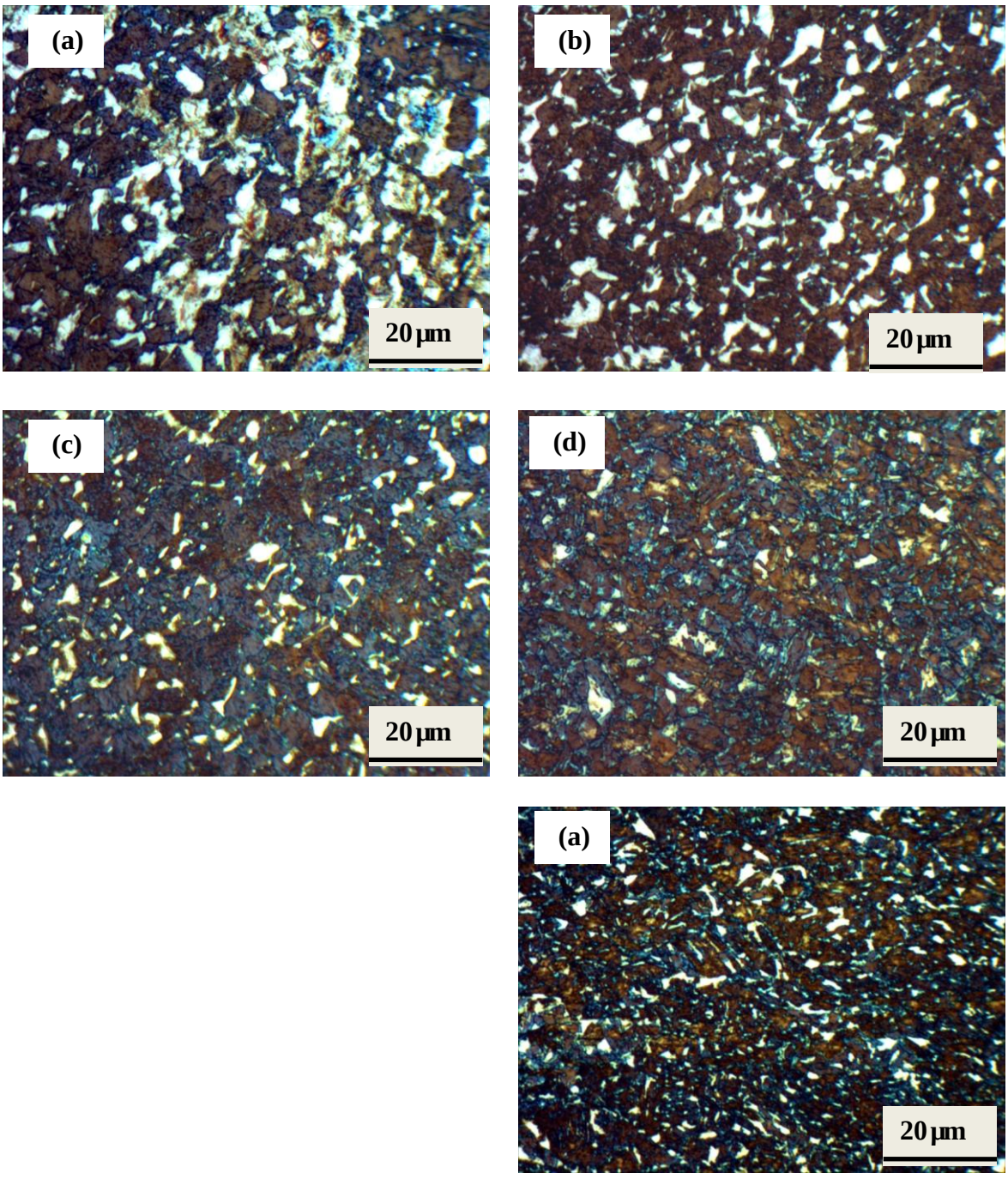

Figure 6.21 The distribution of MA with different heat treatments, etched with LePera. (a) BH1: heat treated at 550 ℃; (b) BH2: heat treated at 500 ℃; heat treated at 450 ℃; (d) BH2S: was heat treated at 850 ℃ and 30 ℃ /s cooled to 500 ℃, and then very slow cooling rate (0.1 ℃/s) was applied until 200 ℃ to compare to sample BH2. (e) BH2D: 40% reduction at 1050 ℃, and 50% reduction at 850 ℃, and then 30 ℃ /s cooled to 500 ℃ to compare to sample BH2.

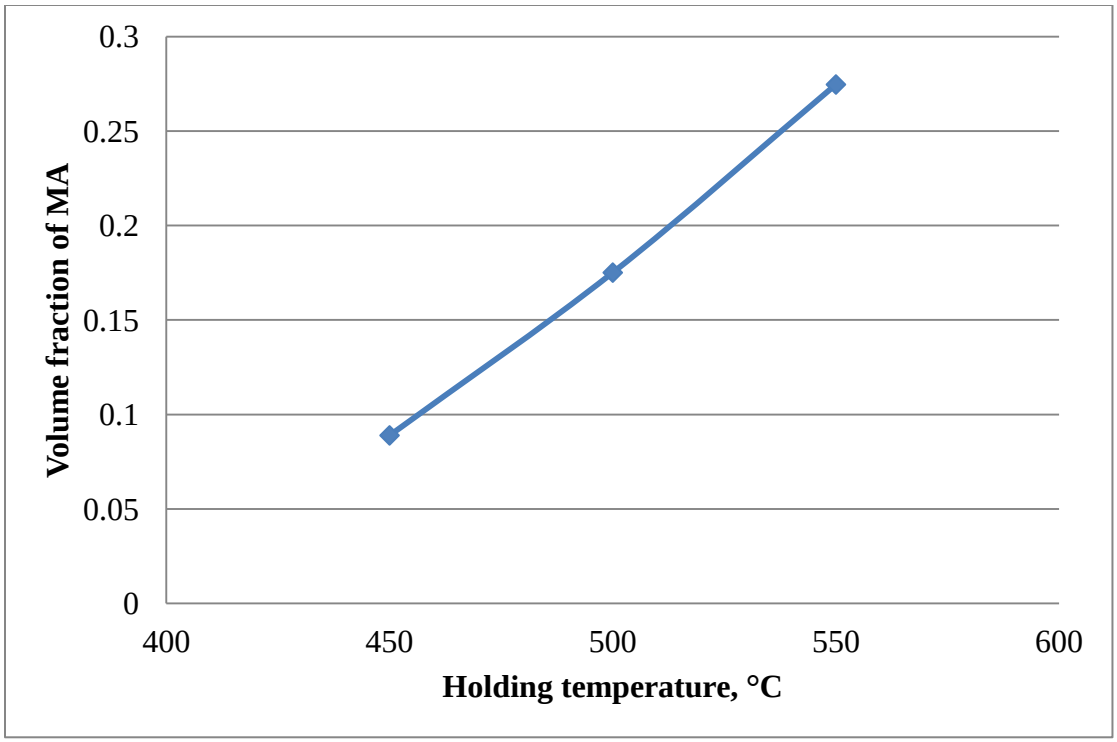

Figure 6.22 Effect of different bainite transformation temperatures on volume fraction of MA

Some other measures were taken to control size and volume fraction of MA. Two experiments were designed to compare the results of BH2. One sample, BH2D, was reheated to 1150 ℃ and isothermally held for 2 minutes, and then at 1050 ℃, 40% deformation was applied for recrystallization. After that, 50% deformation at 850 ℃ was selected to increase Sv and deformation bands in austenite. A temperature of 850 ℃ was selected and then the same cooling process was used to compare to BH2. Another sample, BH2S, was heat treated at 850 ℃ and 30 ℃ /s cooled to 500 ℃, and then very slow cooling rate (0.1 ℃/s) was applied until 200 ℃.

The microstructures are shown in Figure 6.21 (d) & (e). The size of MA in sample BH2D is apparently smaller than BH2 due to the small austenite grain size and subgrain size were designed. The volume fraction of MA can also be reduced by a very slow cooling rate after bainite transformation. This may be because some of MA was tempered during the slow cooling from 500℃ to 200℃. The volume fractions of MA in three different processes are illustrated in Figure 6.23. The deformation can reduce the volume fraction of MA a little. But it can reduce more for the size of MA. The very slow cooling rate can have enough time for martensite to decompose. Thus, the volume fraction of MA in BH2S is reduced from 17% to 5%.

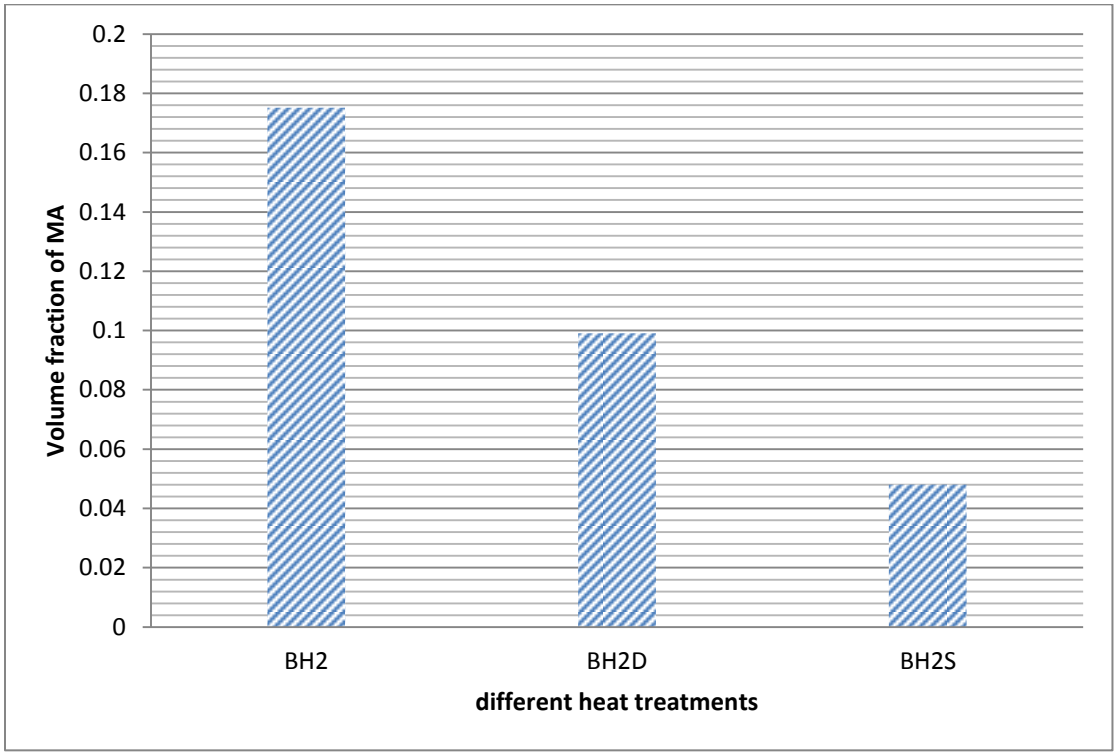

Figure 6.23 Effect of different heat treatments on volume fraction of MA

6.4.3 **Grain boundary character distribution**

CSL grain boundaries seemed to affect toughness recently[72, 124, 125]. In our results, the CSL grain boundaries have already been discussed in steel B2-1and B2-3. Less Σ1 grain boundaries and more CSL grain boundaries seemed to improve toughness of materials. The CSL grain boundaries of five samples were studied. BH2 sample was selected as the base sample. Sample BL2 was heat treated with lower heating temperatures, 800℃, compared to BH2; BH3 is with 450℃ for holding after fast cooing rate, as show in Figure 6.20. BH2S and BH2D has been described in the former paragraphs for samples with deformation, or slow cooling to room temperatures, respectively. The CSL grain boundaries analyzed by EBSD-OIM techniques are shown in Figure 6.24. It shows that lowering the heating temperatures, lowering the finishing cooling temperatures and the deformation increase the fraction of CSL grain boundaries. The sample B2HS with very slow cooling rate does not affect CSL grain boundaries very much as seen from Figure 6.24d.

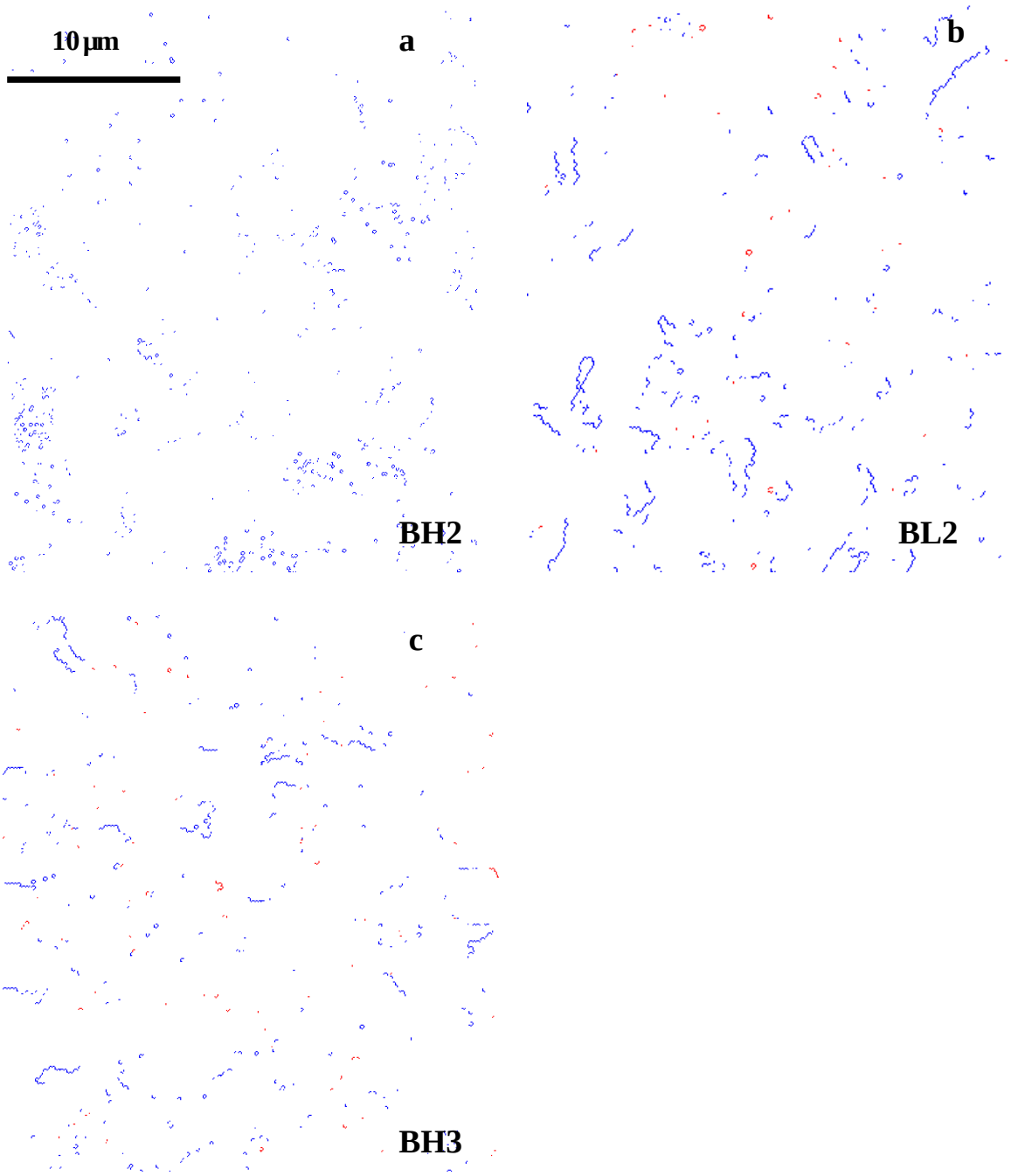
10 µm
a
BH2
b
BL2
c
BH3

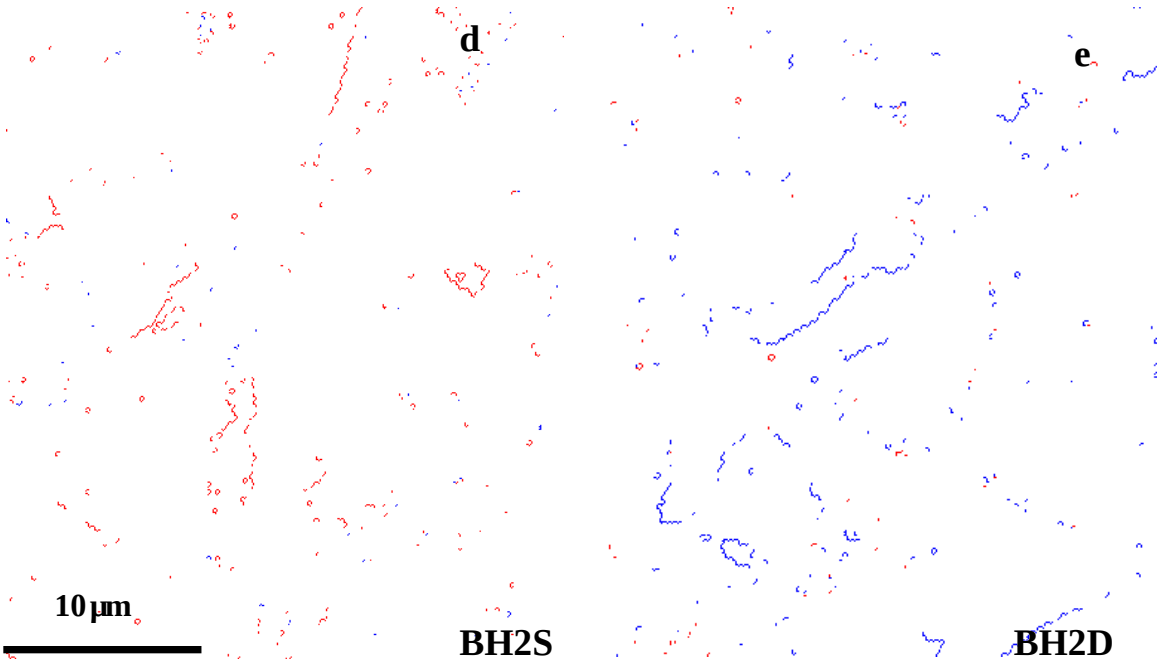

Figure 6.24 Distribution of CSL grain boundaries in different samples. (a) BH2: heat treated at 500 ℃; (b) BL2: (reheated at a lower temperature:800 ℃ and heat treated at 500 ℃;(c) BH3: heat treated at 450 ℃; (d) BH2S: was heat treated at 850 ℃ and 30 ℃ /s cooled to 500 ℃, and then very slow cooling rate (0.1 ℃/s) was applied until 200 ℃ to compare to sample BH2. (e) BH2D: 40% reduction at 1050 ℃, and 50% reduction at 850 ℃, and then 30 ℃ /s cooled to 500 ℃ to compare to sample BH2.

6.4.4 **The cooling rate and toughness improvement**

As discussed in the above results, the three main factors that dominate toughness of steel with a constant pior-austenite grain size are MA, crystallographic packet size and the CSL grain boundaries, which are all related to carbon diffusion, carbon super saturation in steel and bainite transformation temperatures, etc. Thus, the cooling rate is the most important parameters for the toughness improvement since the cooling rate can not only change the diffusion time, but also affect the bainite start transformation temperatures. Figure 6.25 shows the dilation of samples in 7 cooling rates which is from 0.5 ℃/s to 40 ℃/s. The curves in the figure shows the range of

bainite start temperature is from about 580 ℃ to 430 ℃ for the difference of cooling rates. Another group of curves with deformation at 850 ℃ are shown in Figure 6.26. The bainite start transformation temperatures vary much less due to the increase of driving force for the formation from 0.5 ℃/s to 10 ℃/s compared with the curves in Figure 6.26. A temperature between 10 ℃/s and 20 ℃/s should be a critical temperature for bainite start transformation since the cooling rate slower than 10 ℃/s or faster than 20 ℃/s does not change the start transformation very much.

A schematically "special CCT diagram" of the formation of bainite and MA is shown in Figure 6.27. The three dotted lines denote the three cooling rates. The shadow region marks the formation of MA(one assumption here is that the MA does not decompose or is tempered after its formation, that is, at least air cooling or faster cooling rate will be used below the region). Ms in the figure is the martensite start temperature. Bainite transformation is classified into three types as B_I, B_{II} and B_{III} in the low carbon high strength steels studied. This is different from the definition of three types of bainite[135]. It is classified according to carbon diffusion and the crystallographic orientations. B_I is the region with small displacive movement, which usually has big crystallographic packet size. The super saturation of carbon in bainitic ferrite is lower and with many MA constituent particles and islands, usually called granular bainite. B_{II} is the region with higher super saturation of carbon and smaller bainitic ferrite with different orientations. The crystallographic packet size is smaller and the size and volume fraction of MA is also smaller in B_{II}. The B_{III} is the region limiting the carbon diffusion in a very short distance. The morphology may be closer to lath martensite.

For improvement of toughness, the microstructure formed in the lower B_{II} or B_{III} region is suggested.

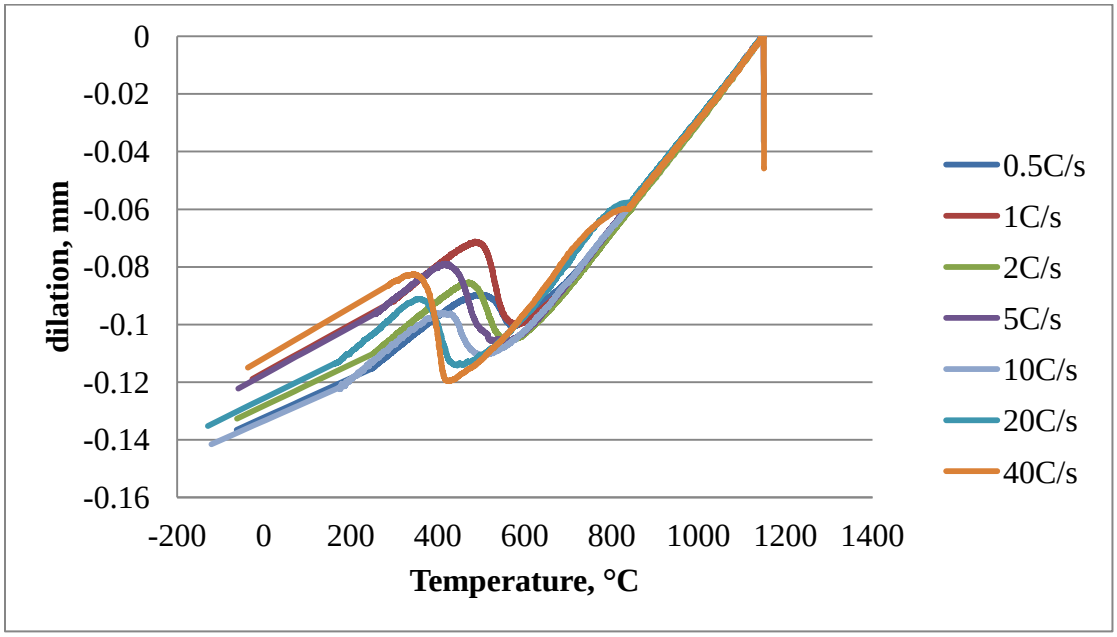

Figure 6.25 The dilation vs. temperature curves in seven different cooling rates, without deformation

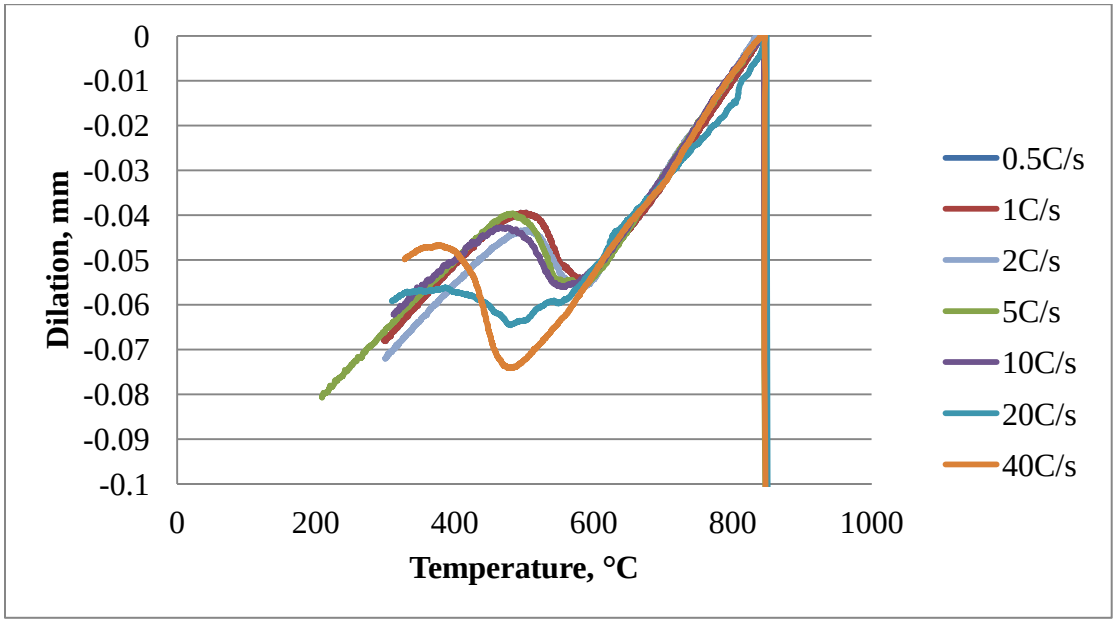

Figure 6.26 The dilation vs. temperature curves in seven different cooling rates, with deformation

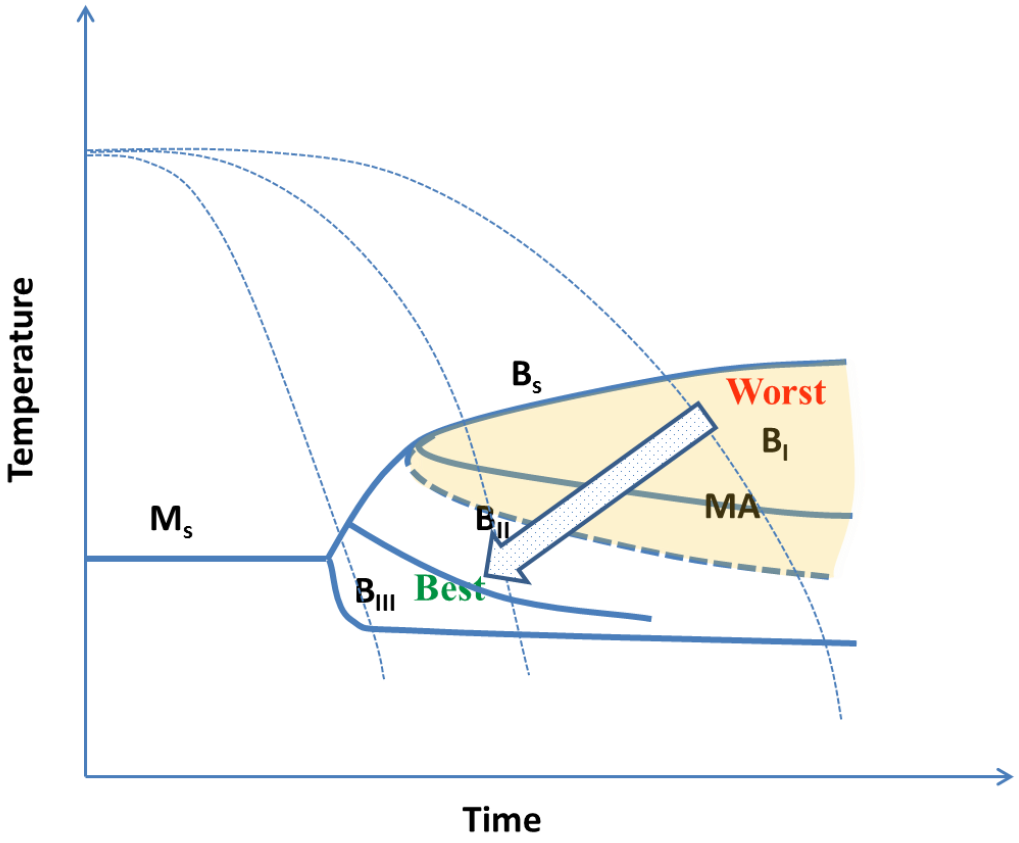

Figure 6.27 A schematically "special CCT diagram" for the formation of the different types of bainite and MA constituents. Worst and best toughness region is indicated.

7.0 CONCLUSIONS

In the study of low carbon high strength steels, the following conclusions can be made regarding the decomposition of austenite, the formation of MA, orientation of bainite, toughness improvement, and so on.

1. Upon reheating, abnormal grain growth was observed in the steels. The addition of 0.3wt% more Cr reduced the temperature for abnormal grain growth by 100℃. The microalloying element, titanium, can form precipitates on the austenite grain boundaries, thus retarding the grain coarsening temperatures. The chromium should be controlled to be appropriate to a reheating temperature that avoids the abnormal grain growth region.

2. The complete recrystallization temperature, T_{95}, and recrystallization stop temperature T_5, were determined. T_{95} is about 1050℃ and T_5 is between 900 and 950℃ in steel 1B with 30% deformation.

3. The bainite start temperature ranged from 400℃ to 580℃, depending on the cooling rates. In the steel without deformation, the effect of cooling rate on the variation of Bs temperature is large. However, with deformation, Bs does not change much when the cooling rates are less than 10℃/s.

4. During the continuous bainitic transformation, the strength of materials does not vary much for the different complicated microstructures. However, the difference of toughness can be very large. It is related to three important factors: a. the size and volume fraction of MA, b. the crystallographic packet size, and c. the CSL grain boundaries. The large size and high volume

fraction of MA deteriorate DBTT and upper shelf energy. The crystallographic packet size was used to evaluate the toughness of bainitic steels. It is found that small crystallographic packet size can also improve toughness. Moreover, more CSL grain boundaries were found in a sample with good toughness.

5. The phase transformation of austenite by rapid continuous cooling represents para-equilibrium or non-equilibrium condition. The formation of MA is dependent on carbon diffusion in steel. According to thermodynamics and kinetics analysis, the stability of carbon supersatuaration is lower and the carbon diffusion rate is also higher at a higher temperature, which causes the formation of more MA. Thus, short holding time is recommended during high temperature bainite transformation.

6. The orientations of bainite are related to transformation temperatures. The deformed austenite has a tendency to transform into bainite with the orientation near <113> at high bainite transformation temperatures while the orientation around <331> of bainite is inclined to be obtained at low temperatures. The crystallographic packet size is related to the orientations of bainite. Results show that the crystallographic size is larger for the orientation near <113> than the size near the orientation of <331>.

7. Bainite start temperatures are dependent on cooling rates according to dilotometric results. The samples without deformation have gradually decreasing bainite start temperatures. However, the samples with deformation show a critical cooling rate for lowering bainite start temperatures. Only a very fast cooling rate, greater than 20℃/s, can avoid the formation of bainite at higher temperatures.

8. The formation of CSL grain boundaries is found to relate to deformation state, finishing cooling temperatures, as well as reheating temperatures.

9. Three types of bainite were classified, based on carbon diffusion and crystallographic orientation in low carbon high strength steels. BI is the region with small displacive movement, which usually has a large crystallographic packet size. The super saturation of carbon in bainitic ferrite is lower and contains many MA constituents, usually called granular bainite. BII is the region with higher super saturation of carbon and smaller bainitic ferrite with different orientations. The crystallographic packet size is smaller and the size and volume fraction of MA is also smaller in BII. BIII is the region in which the carbon diffusion is limited to a very short distance. The morphology may be closer to that of lath martensite.

APPENDIX A

AUSTENITE GRAIN SIZE

A.1 THE AUSTENITE GRAIN SIZE AFTER DEFORMATION(STEEL 1A)

The changes of austenite grain size in steel 1A and steel 1B for study of T95 and T5 are listed in the following tables. The deformation conditions are illustrated in Figure 5.6. Table A. 1 shows the relationship between average austenite grain sizes and six different finishing deformation (deformation: 10%) temperatures. Table A. 2 shows the percent of grains with average aspect ratio $\geqslant 1.6$. The ratio is used to define the critical number for recrystallization and non-recrystallization grains. Similarly, Table A. 3 shows the data with 30% deformation.

Table A. 1 Austenite Grain Size of Steel 1A (10%ε)

Condition	Actual deformation temp., ℃	Average grain size, μm	Standard deviation
1075°C, ε=10% (A1)	**1083**	**22.8**	**8.3**
1050°C, ε=10% (A2)	**1058**	**22.0**	**9.8**
1025°C, ε=10% (A3)	**1025**	**17.7**	**9.5**
950°C, ε=10% (A4)	**942**	**18.3**	**8.1**
900°C, ε=10% (A5)	**900**	**18.0**	**9.9**
860°C, ε=10% (A6)	**859**	**18.3**	**8.9**

Table A. 2 Aspect Ratio of Grains in Steel A, ε=10%

Condition	Number of measurement	Number of grains with aspect ratio≥1.6	Percent of grains with average aspect ratio ≥1.6
1075°C, ε=10% (A1)	**101**	**24**	**23%**
1050°C, ε=10% (A2)	**144**	**60**	**43%**
1025°C, ε=10% (A3)	**166**	**35**	**21%**
950°C, ε=10% (A4)	**123**	**27**	**22%**
900°C, ε=10% (A5)	**121**	**48**	**40%**
860°C, ε=10% (A6)	**130**	**84**	**65%**

Table A. 3 Austenite Grain size of Steel A, ε=30%

Condition	Actual deformation temp., ℃	Average grain size, μm	Standard deviation
1075°C, ε=30%, A1	**1075**	**21.8**	**10.3**
1050°C, ε=30%, A2	**1052**	**15.4**	**9.1**
1025°C, ε=30%, A3	**1025**	**14.1**	**8.8**
950°C, ε=30%, A4	**950**	**13.8**	**9.1**
900°C, ε=30% , A5	**920**	**12.8**	**7.8**
860°C, ε=30%, A6	**859**	**13.4**	**8.2**

A.2 THE AUSTENITE GRAIN SIZE AFTER DEFORMATION(STEEL 1B)

The results of steel 1B with different deformation: 10% and 30%, are shown in Table A. 4, Table A. 5 and Table A. 6, Table A. 7, respectively. All the microstructures are illustrated in Appendix B.

Table A. 4 Austenite Grain size of Steel B, ε=10%

Condition	Actual deformation temp., ℃	Average grain size, μm	Standard deviation
1075°C, ε=10%, B1	**1070**	**23.5**	**9.1**
1050°C, ε=10%, B2	**1055**	**23.4**	**9.4**
1025°C, ε=10%, B3	**1030**	**23.3**	**10.0**
950°C, ε=10%, B4	**940**	**23.4**	**9.3**
900C°C, ε=10%, B5	**920**	**22.4**	**9.8**
860°C, ε=10%, B6	**846**	**21.7**	**9.0**

Table A. 5 Aspect Ratio of Austenite Grains in Steel B, ε=10%

Condition	Number of measurement	Number of grains with aspect ratio≥1.6	Percent of grains with average aspect ratio ≥1.6
1075 ℃, ε=10%, B1	**164**	**24**	**14.6%**
1050°C, ε=10%, B2	**130**	**21**	**16.2%**
1025°C, ε=10%, B3	**130**	**20**	**15.3%**
950°C, ε=10%, B4	**120**	**36**	**30%**
900C°C, ε=10%, B5	**112**	**50**	**46%**
860°C, ε=10%, B6	**128**	**80**	**62%**

Table A. 6 Austenite Grain size of Steel B, ε=30%

Condition	Actual deformation temp., ℃	Average grain size, μm	Standard deviation
1075°C, ε=30%, B1	**1075**	**20.8**	**5.5**
1050°C, ε=30%, B2	**1053**	**21.3**	**6.7**
1025°C, ε=30%, B3	**1025**	**20.9**	**7.0**
950°C, ε=30%, B4	**947**	**22.0**	**10.4**
900°C, ε=30%, B5	**900**	**30.1**	**9.7**
860 ℃, ε=30%, B6	**860**	**30.3**	**11.7**

Table A. 7 Aspect Ratio of Austenite Grains in Steel B, ε=30%

Condition	Number of measurement	Number of grains with aspect ratio≥1.6	Percent of grains with average aspect ratio ≥1.6
1075°C, ε=30%, B1	**118**	**2**	**1.7%**
1050°C, ε=30%, B2	**117**	**2**	**1.7%**
1025°C, ε=30%, B3	**107**	**10**	**9.3%**
950°C, ε=30%, B4	**80**	**36**	**45%**
900°C, ε=30%, B5	**70**	**62**	**89%***
860°C, ε=30%, B6	**70**	**56**	**80%**

APPENDIX B

THE MICROSTRUCTURES OF 1A AND 1B

B.1 MICROSTRUCTURES OF STEEL 1A

The austenite grain boudaries were revealed by saturated piciric acid for steel 1A and 1B to see the evolution of austenite and recrystallization. Each temperature in the corner of figures indicates the size of austenite grains at that temperature after deformation (Figure 5.6).

Figure B. 7-1 and Figure B. 7-2 show the austenite grain size at 1150 ℃ and 1125 ℃ after deformation.

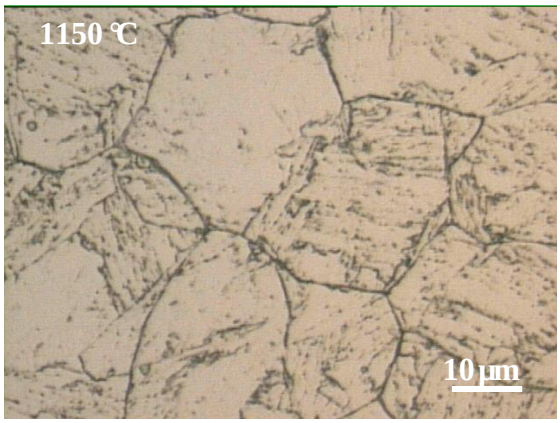

Figure B. 7-1 1150 ℃, WQRT

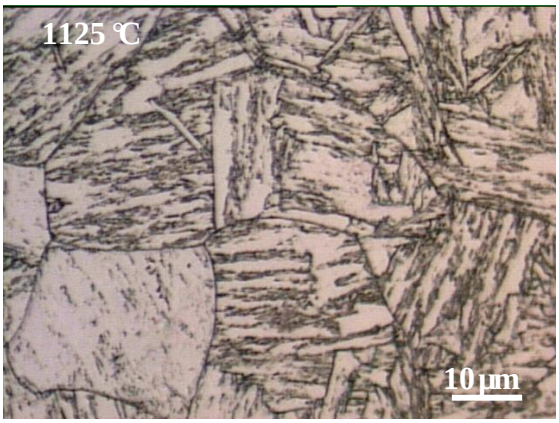

Figure B. 7-2 1125 ℃, WQRT

The following figures (Figure B. 7-3-Figure B. 7-8) are the austenite microstructures after 10% deformation at six different temperatures.

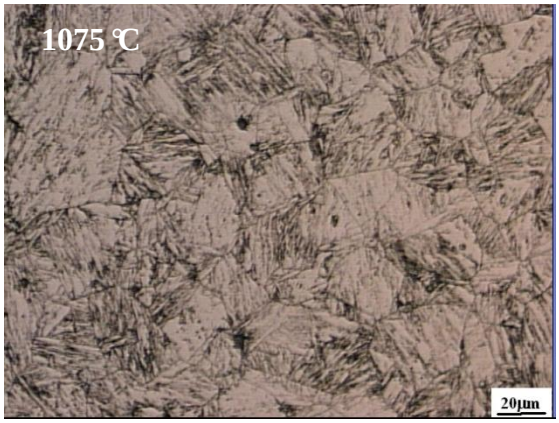

Figure B. 7-3 1075 ℃, WQRT

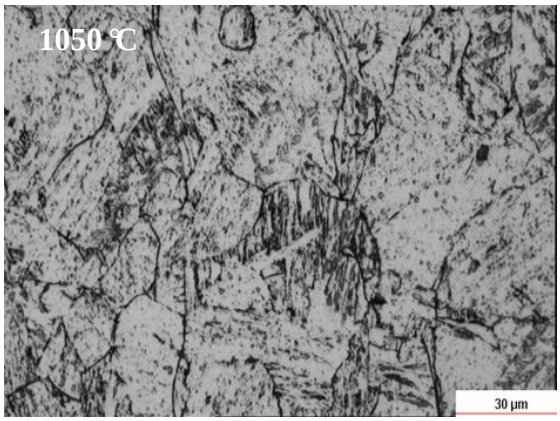

Figure B. 7-4 1050 ℃, WQRT

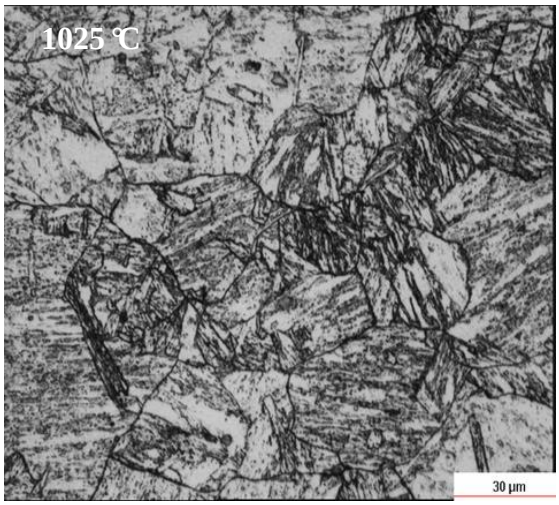

Figure B. 7-5 1025 ℃, WQRT

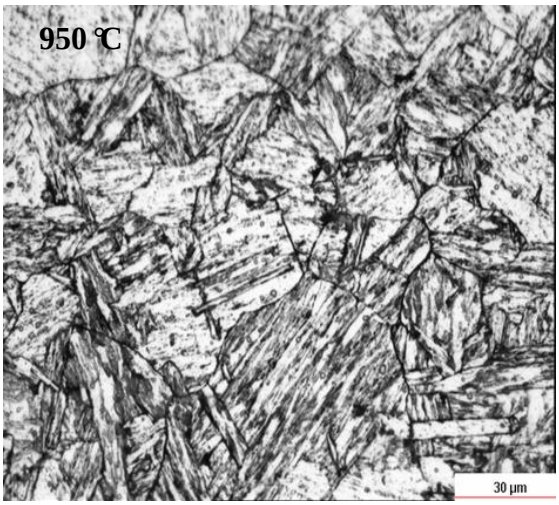

Figure B. 7-6 950 ℃, WQRT

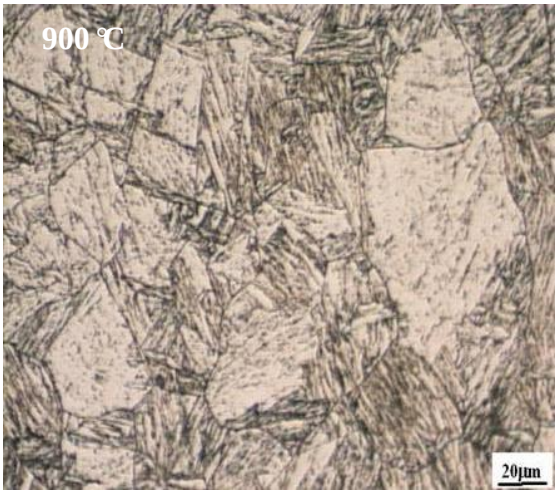

Figure B. 7-7 900 ℃, WQRT

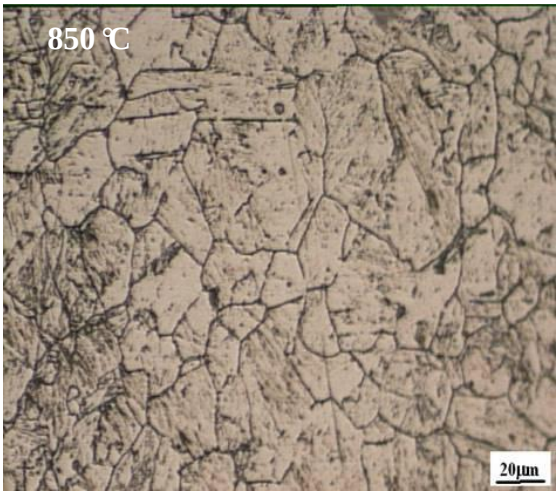

Figure B. 7-8 850 ℃, WQRT

Figure B. 7-9- Figure B. 7-14 are the austenite microstructures after 30% deformation at six different temperatures.

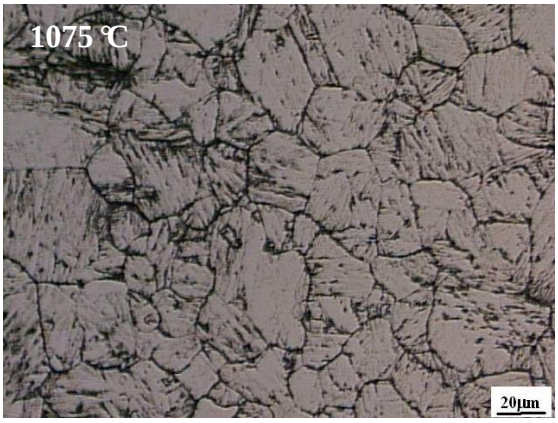

Figure B. 7-9 1075 ℃, WQRT

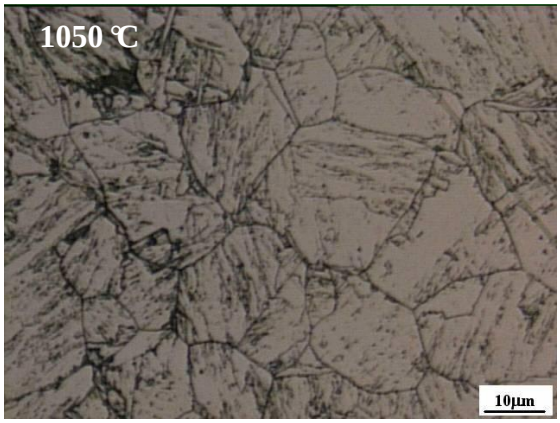

Figure B. 7-10 1050 ℃, WQRT

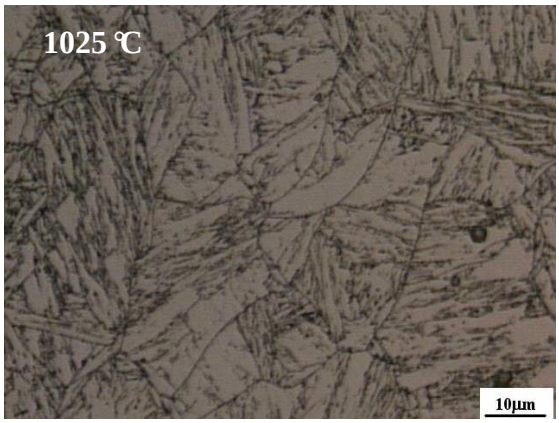

Figure B. 7-11 1025 ℃, WQRT

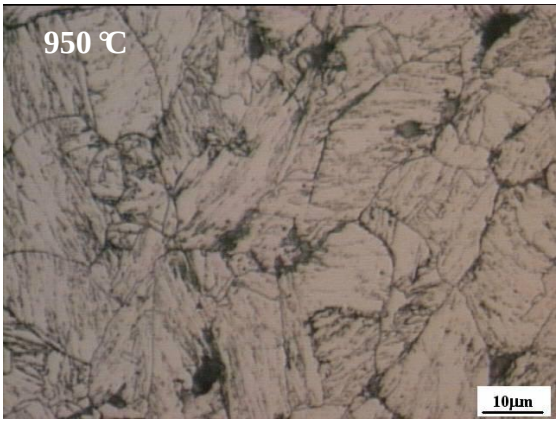

Figure B. 7-12 950 ℃, WQRT

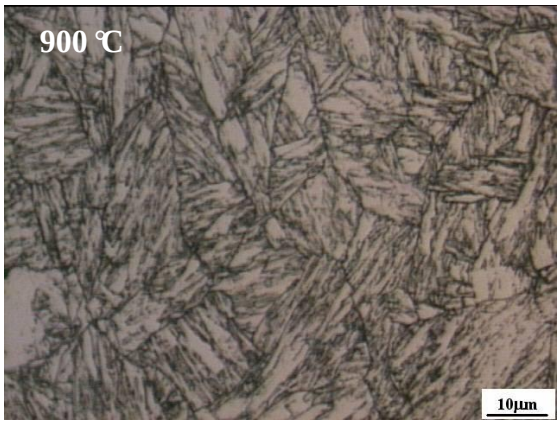

Figure B. 7-13 900 ℃, WQRT

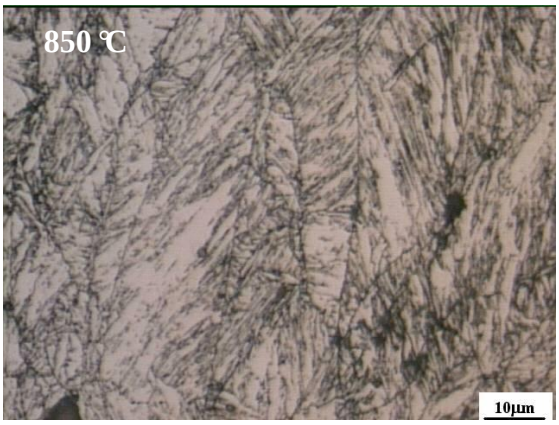

Figure B. 7-14 850 ℃, WQRT

B.2 MICROSTRUCTURES OF STEEL 1B

The austenite grain size of steel 1B were compared after each deformation(Figure 5.6). The temperatures in the figure indicate the deformation temperature for investigation the austenite grain size. The evolution of austenite grains in recrystallization rolling region is shown in Figure B. 7-15 to Figure B. 7-17.

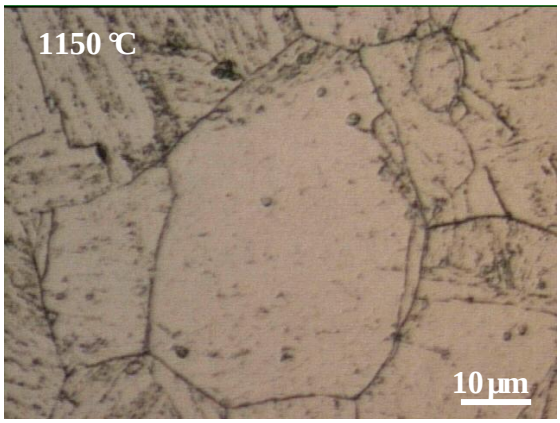

Figure B. 7-15 1150 ℃, WQRT

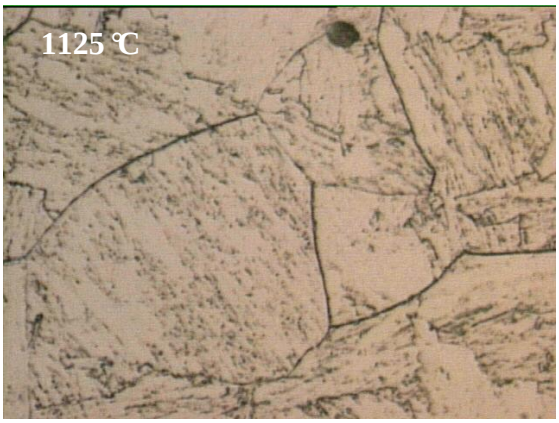

Figure B. 7-16 1125 ℃, WQRT

Figure B. 7-17 1100 ℃, WQRT

The following figures (Figure B. 7-18-Figure B. 7-23) are the austenite microstructures of steel 1B after 10% deformation at six different temperatures.

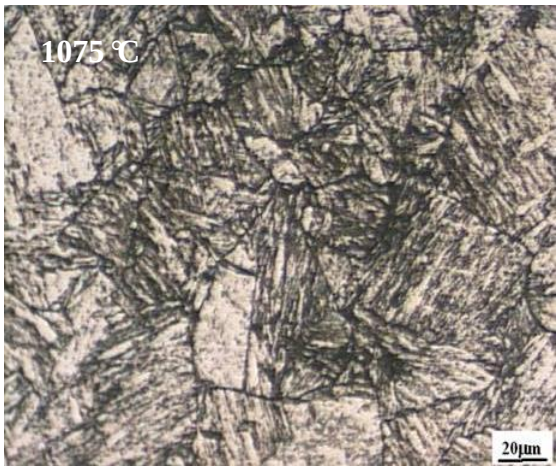

Figure B. 7-18 1075 ℃, WQRT

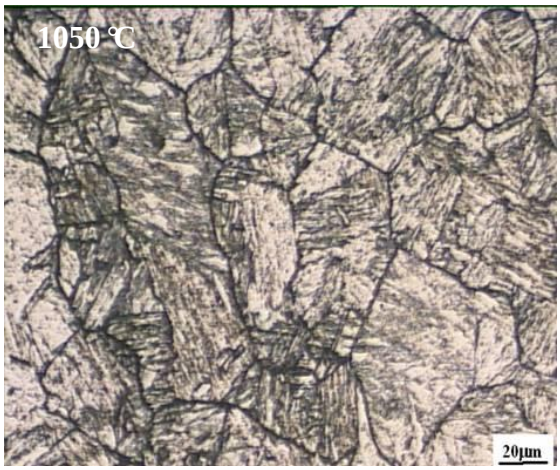

Figure B. 7-19 1050 ℃, WQRT

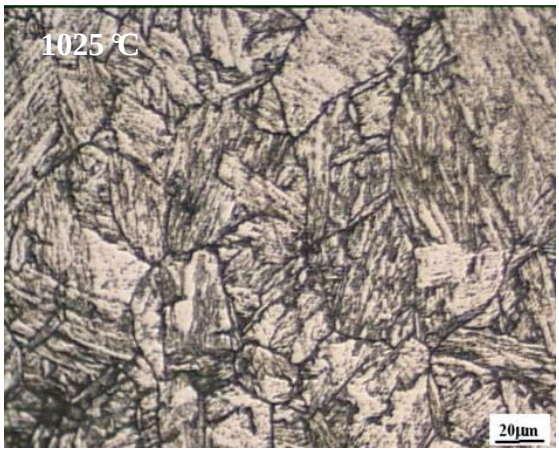

Figure B. 7-20 1025 ℃, WQRT

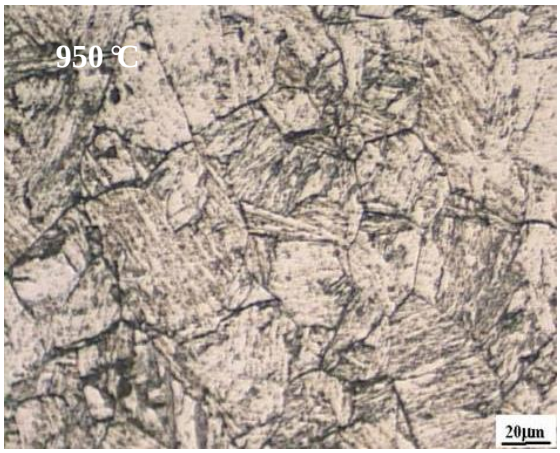

Figure B. 7-21 950 ℃, WQRT

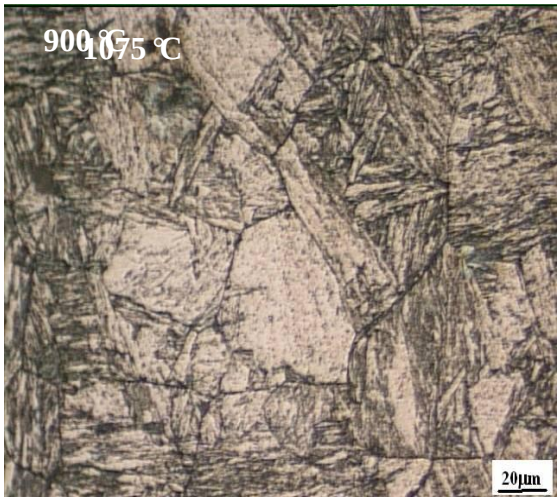

Figure B. 7-22 900 ℃, WQRT

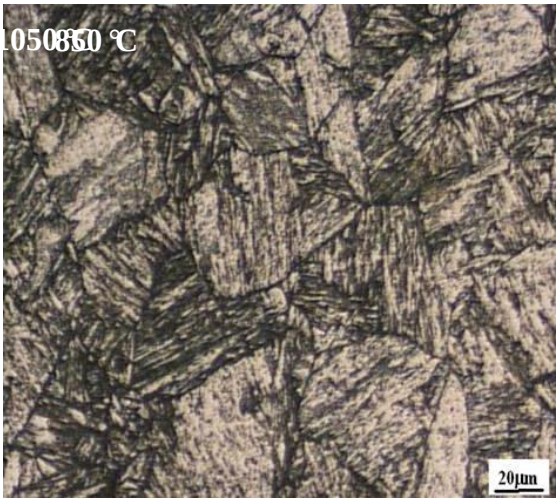

Figure B. 7-23 850 ℃, WQRT

The figures from Figure B. 7-24 to Figure B. 7-29 show the austenite microstructures of steel 1B after 30% deformation at six different temperatures.

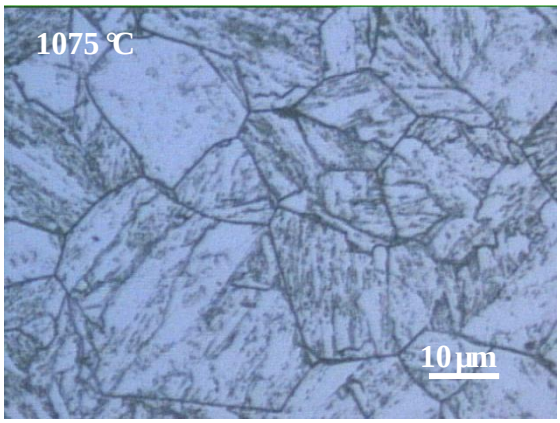

Figure B. 7-24 1075 ℃, WQRT

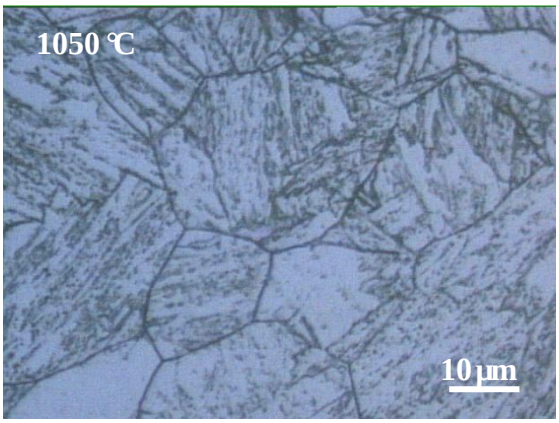

Figure B. 7-25 1050 ℃, WQRT

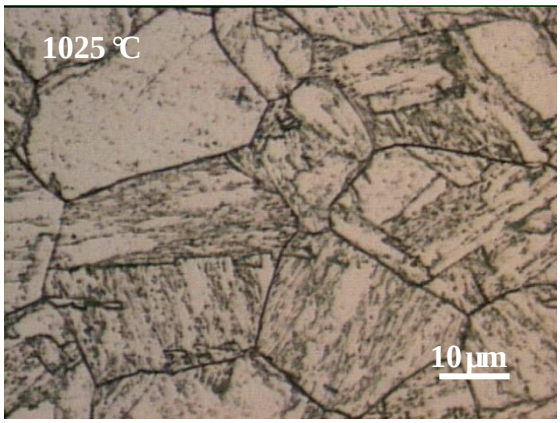

Figure B. 7-26 1025 ℃, WQRT

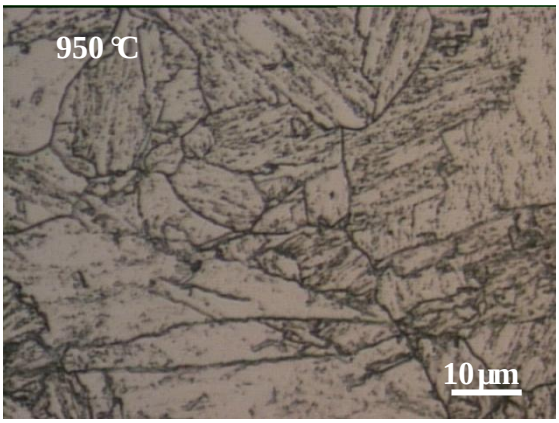

Figure B. 7-27 950 ℃, WQRT

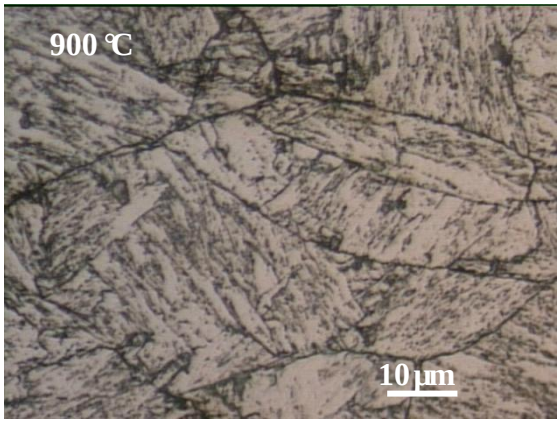

Figure B. 7-28 900 ℃, WQRT

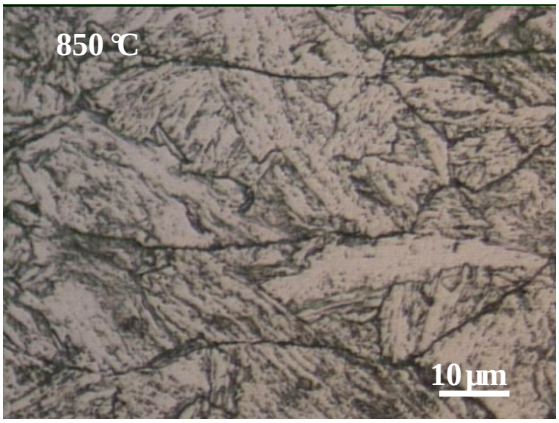

Figure B. 7-29 850 ℃, WQRT

BIBLIOGRAPHY

1. DeArdo, A.J., et al., *On strength of microalloyed steels: an interpretive review.* Materials Science and Technology, 2009. **25**(9): p. 1074-1082.

2. Denys, R., *Pipeline technology : proceedings of the 3rd International Pipeline Technology Conference, Brugge, Belgium, May 21-24, 2000*. 1st ed. 2000, Amsterdam ; New York,: Elsevier.

3. Terada, Y., et al., *Development of API X100 UOE line pipe.* Nippon Steel Technical Report(Japan), 1997. **72**: p. 47-52.

4. Okaguchi, S., et al., *Development and mechanical properties of X120 linepipe.* International Journal of Offshore and Polar Engineering, 2004. **14**(1): p. 29-35.

5. Papka, S.D., et al., *Full-size testing and analysis of X120 linepipe.* International Journal of Offshore and Polar Engineering, 2004. **14**(1): p. 42-51.

6. Dieter, G.E., *Mechanical metallurgy*. 3rd ed. McGraw-Hill series in materials science and engineering. 1986, New York: McGraw-Hill. xxiii, 751 p.

7. Graf, M.K., et al., *High-strength large-diameter pipe for long-distance high-pressure gas pipelines.* International Journal of Offshore and Polar Engineering, 2004. **14**(1): p. 69-74.

8. Shinmiya, T., et al. *Development of high deformability linepipe with resistance to strain-aged hardening by heat treatment on-line process*. 2007.

9. Hillenbrand, H.G., et al. *Development of large-diameter pipe in grade X100*. 2000.

10. Asahi, H., et al., *Development of plate and seam welding technology for X120 linepipe.* International Journal of Offshore and Polar Engineering, 2004. **14**(1): p. 11-17.

11. Yoo, J.Y., et al., *New Development of High Grade X80 to X120 Pipeline Steels.* Materials and Manufacturing Processes, 2011. **26**(1): p. 154-160.

12. Koo, J.Y., et al., *Metallurgical design of ultra high-strength steels for gas pipelines.* International Journal of Offshore and Polar Engineering, 2004. **14**(1): p. 2-10.

13. Gräf, M., H. Hillenbrand, and P. Peters, *Accelerated Cooling of Steel.* TMS, Warrendale (Pa), 1986: p. 165-179.

14. Pickering, F.B., *Physical metallurgy and the design of steels*. Materials science series. 1978, London: Applied Science Publishers. xii, 275 p.

15. Hillenbrand, H.G., et al. *Development of high strength material and pipe production technology for grade X120 line pipe*. 2004.

16. Asahi, H., et al., *Pipe production technology and properties of X120 linepipe.* International Journal of Offshore and Polar Engineering, 2004. **14**(1): p. 36-41.

17. Akasaki, H., *Progress in Pipe and Tube Technology and Its Future Prospect–Application and Manufacturing-*. Nippon Steel Technical Report, 2004. **No.90**: p. 7.

18. Garcia, C.I., et al. *On the Microstructure of Plate Steels for API-5L X120 Applications*. 2012: Trans Tech Publ.

19. Garcia, C., et al., *On the strength of microalloyed steels-An interpretive review*.

20. Mannucci, G., *Fracture properties of API X100 gas pipeline steels*.

21. Graville, B., *Cold cracking in welds in HSLA steels.* Welding of HSLA(Microalloyed) Structural Steels; Rome, 1976: p. 85-101.

22. Dearden, J., *HO'Niell: Trans.* Inst. Weld, 1940. **3**: p. 203.

23. Ito, Y. and K. Bessho, *Cracking parameter of high-strength steels related to heat affected zone cracking (1st report).* J Jpn Weld Soc, 1968. **37**(9): p. 983–991.

24. Bhadeshia, H.K.D.H. and R.W.K. Honeycombe, *Steels : microstructure and properties*. 3rd ed. 2006, Amsterdam ; Boston ; London: Butterworth-Heinemann. xi, 344 p.

25. Hume-Rothery, W., R.E. Smallman, and C.W. Haworth, *The structure of metals and alloys*. 5th ed. Monograph and report series no. 1. 1969, London,: Metals & Metallurgy Trust. viii, 407 p.

26. Pickering, F. and T. Gladman, *Metallurgical developments in carbon steels.* ISI Special Report, 1963. **81**(10).

27. Honeycombe, R. and G. Smith, *Yield Points in Microalloyed Titanium Steels.* Strength of Metals and Alloys, 1982. **1**: p. 407-412.

28. Kelly, A., *Strengthening methods in crystals*. 1971: Elsevier Publishing Company.

29. Gladman, T., *Precipitation hardening in metals.* Materials Science and Technology, 1999. **15**(1): p. 30-36.

30. Gladman, T., D. Dulieu, and I. McIvor. *Structure/Property Relationships in High-Strength Micro-Alloyed Steels*. in *Microalloying 75*. 1977. New York: Union Carbide Corporation.

31. Gladman, T., *The physical metallurgy of microalloyed steels*. Book / the Institute of Materials. 1997, London: Institute of Materials. x, 363 p.

32. Brozzo, P., et al., *Microstructure and cleavage resistance of low-carbon bainitic steels.* Metal Science, 1977. **11**(4): p. 123-130.

33. Naylor, J. and P. Krahe, *The effect of the bainite packet size on toughness.* Metallurgical and Materials Transactions B, 1974. **5**(7): p. 1701-1704.

34. Edmonds, D. and R. Cochrane, *Structure-property relationships in bainitic steels.* Metallurgical and Materials Transactions A, 1990. **21**(6): p. 1527-1540.

35. Morito, S., et al., *The morphology and crystallography of lath martensite in Fe-C alloys.* Acta materialia, 2003. **51**(6): p. 1789-1799.

36. Humphreys, F.J. and M. Hatherly, *Recrystallization and related annealing phenomena*. 2004: Pergamon.

37. Detert, K., *Recrystallization of Metallic Materials.* Recrystallization of Metallic Materials, 1978.

38. Nes, E., N. Ryum, and O. Hunderi, *On the Zener drag.* Acta Metallurgica, 1985. **33**(1): p. 11-22.

39. Palmiere, E.J., *Suppression of recrystallization during the hot deformation of microalloyed austenite*. 1991, University of Pittsburgh. p. xix, 198 leaves.

40. Bhadeshia, H.K.D.H., *Bainite in steels : transformations, microstructure and properties*. Book / Institute of Materials. 1992, London: Institute of Materials. xxii, 451 p.

41. Krauss, G., *Steels : processing, structure, and performance*. 2005, Materials Park, Ohio: ASM International. xix, 613 p.

42. Ohmori, Y., H. Ohtani, and T. Kunitake, *BAINITE IN LOW-CARBON LOW-ALLOY HIGH-STRENGTH STEELS.* TRANS IRON STEEL INST JAP, 1971. **11**(4): p. 250-259.

43. Suikkanen, P., *Development and processing of low carbon bainitic steels*, in *Department of Mechanical Engineering*. 2009, University of Oulu. p. 482.

44. Zener, C., *Kinetics of the Decomposition of Austenite.* Trans. Aime, 1946. **167**: p. 550-595.

45. Bhadeshia, H. and D. Edmonds, *The mechanism of bainite formation in steels.* Acta Metallurgica, 1980. **28**(9): p. 1265-1273.

46. Ali, A. and H. Bhadeshia, *Nucleation of Widmanstätten ferrite.* Materials Science and Technology, 1990. **6**(8): p. 781-784.

47. Matsuda, F., et al., *Effect of M-A constituent on fracture behavior of 780 and 980 MPa class HSLA steels subjected to weld HAZ thermal cycles.* Trans. JWRI(Japan), 1994. **23**(2): p. 231-238.

48. Matsuda, F., et al., *Review of Mechanical and Metallurgical Investigations of MA Constituent in Welded Joint in Japan.* Transactions of the JWRI(Japan Welding Research Institute)(Japan), 1995. **24**(1): p. 1-24.

49. Palumbo, G., et al., *On a more restrictive geometric criterion for" special" CSL grain boundaries.* Scripta materialia, 1998. **38**(11): p. 1685-1690.

50. Kim, Y.M., et al., *Effects of molybdenum and vanadium addition on tensile and charpy impact properties of API X70 linepipe steels.* Metallurgical and Materials Transactions a-Physical Metallurgy and Materials Science, 2007. **38A**(8): p. 1731-1742.

51. Ale, R., J. Rebello, and J. Charlier, *A metallographic technique for detecting martensite-austenite constituents in the weld heat-affected zone of a micro-alloyed steel.* Materials Characterization, 1996. **37**(2-3): p. 89-93.

52. Kawabata, F., et al. *Morphological effect of local hard phase on toughness of local brittle zone*. 1992.

53. Ohkita, S. and Y. Horii, *Recent development in controlling the microstructure and properties of low alloy steel weld metals. Review.* ISIJ International(Japan), 1995. **35**(10): p. 1170-1182.

54. Yakubtsov, I.A. and J.D. Boyd, *Bainite transformation during continuous cooling of low carbon microalloyed steel.* Materials Science and Technology, 2001. **17**(3): p. 296-301.

55. Cota, A.B. and D.B. Santos, *Microstructural characterization of bainitic steel submitted to torsion testing and interrupted accelerated cooling.* Materials Characterization, 2000. **44**(3): p. 291-299.

56. KOZASU, I. *Hot Rolling as a High-Temperature Thermo-Mechanical Process*. in *Microalloying 75*. 1975.

57. Manohar, P.A. and T. Chandra, *Continuous cooling transformation behaviour of high strength microalloyed steels for linepipe applications.* Isij International, 1998. **38**(7): p. 766-774.

58. Dong, H. and X.J. Sun, *Deformation induced ferrite transformation in low carbon steels.* Current Opinion in Solid State & Materials Science, 2005. **9**(6): p. 269-276.

59. Weng, Y.Q., *Microstructure refinement of structural steel in China.* Isij International, 2003. **43**(11): p. 1675-1682.

60. Yang, Z.M. and R.Z. Wang, *Formation of ultra-fine grain structure of plain low carbon steel through deformation induced ferrite transformation.* Isij International, 2003. **43**(5): p. 761-766.

61. Li, C.M., H. Yada, and H. Yamagata, *In situ observation of gamma ->alpha transformation during hot deformation in an Fe-Ni alloy by an X-ray diffraction method.* Scripta Materialia, 1998. **39**(7): p. 963-967.

62. Yada, H., C. Li, and H. Yamagata, *Dynamic Transformation during Hot Deformation in Iron–Nickel–Carbon Alloys.* Isij International, 2000. **40**(2): p. 200-206.

63. Li, C.M., H. Yada, and H. Yamagata, *An in-situ X-ray diffraction study of gamma ->alpha transformation during hot deformation in Fe-6mass%Ni-0.0008 similar to 0.29mass%C alloys.* Isij International, 1999. **39**(2): p. 209-211.

64. Hurley, P.J. and P.D. Hodgson, *Formation of ultra-fine ferrite in hot rolled strip: potential mechanisms for grain refinement.* Materials Science and Engineering a-Structural Materials Properties Microstructure and Processing, 2001. **302**(2): p. 206-214.

65. Qi, J.J., W.Y. Yang, and Z.Q. Sun, *Ultra-fine ferrite formation during deformation of undercooled austenite in a low carbon steel.* Acta Metallurgica Sinica, 2002. **38**(9): p. 897-902.

66. Du, L.X., et al., *Investigation on the conditions of strain-induced ferrite transformation of low carbon steel.* Acta Metallurgica Sinica, 2002. **38**(10): p. 1031-1036.

67. Meyer, L., et al. *Columbium, Titanium, and Vanadium in Normalized, Thermo-Mechanically Treated and Cold-Rolled Steels*. in *Micro Alloying 75*. New York.

68. DeArdo, A.J., *Niobium in modern steels.* International Materials Reviews, 2003. **48**(6): p. 371-402.

69. LIANG, X., et al., *Effect of Cooling Rate on Microstructures and Properties of Directly Quenched Steel.* Materials for Mechanical Engineering, 2007.

70. Watanabe, T., *An approach to grain boundary design for strong and ductile polycrystals.* Res Mechanica, 1984. **11**: p. 47-84.

71. Watanabe, T., et al., *Grain boundaries in rapidly solidified and annealed Fe-6.5 mass% Si polycrystalline ribbons with high ductility.* Acta Metallurgica, 1989. **37**(3): p. 941-952.

72. Lim, L. and T. Watanabe, *Fracture toughness and brittle-ductile transition controlled by grain boundary character distribution (GBCD) in polycrystals.* Acta Metallurgica Et Materialia, 1990. **38**(12): p. 2507-2516.

73. Palumbo, G., E. Lehockey, and P. Lin, *Applications for grain boundary engineered materials.* JOM Journal of the Minerals, Metals and Materials Society, 1998. **50**(2): p. 40-43.

74. Kronberg, M. and F. Wilson, *Secondary recrystallization in copper.* AIME TRANS, 1949. **185**: p. 501-514.

75. Brandon, D., *The structure of high-angle grain boundaries.* Acta Metallurgica, 1966. **14**(11): p. 1479-1484.

76. Hasson, G. and C. Goux, *Interfacial Energies of Tilt Boundaries in Aluminum. Experimental and Theoretical Determinations.* Scr. Metall., 1971. **5**(10): p. 889-894.

77. Shin, S.Y., et al., *Correlation of microstructure and charpy impact properties in API X70 and X80 line-pipe steels.* Materials Science and Engineering: A, 2007. **458**(1-2): p. 281-289.

78. Shin, S.Y., et al., *Analysis of fracture toughness in transition temperature region of APIX70 and X80 linepipe steels.* Journal of the Korean Institute of Metals and Materials, 2007. **45**(8): p. 447-457.

79. Heckmann, C.J., et al., *Development of low carbon Nb-Ti-B microalloyed steels for high strength large diameter linepipe.* Ironmaking & Steelmaking, 2005. **32**(4): p. 337-341.

80. Han, S.Y., et al., *Effect of Mo, Cr, and V on Tensile and Charpy Impact Properties of API X80 Linepipe Steels Rolled in Single Phase Region.* Journal of the Korean Institute of Metals and Materials, 2008. **46**(12): p. 788-799.

81. Hwang, B., C.G. Lee, and T.H. Lee, *Correlation of Microstructure and Mechanical Properties of Thermomechanically Processed Low-Carbon Steels Containing Boron and Copper.* Metallurgical and Materials Transactions a-Physical Metallurgy and Materials Science, 2010. **41A**(1): p. 85-96.

82. Garcia Gonzalez, J.E. and University of Pittsburgh. School of Engineering, *Study of the Effect of Hot Rolling Processing Parameters on the Variability of HSLA Steels*. 2002, University of Pittsburgh: Pittsburgh, PA.

83. R. Herberz, H.W., Stachl Eisen, 1981. **101**: p. 29.

84. Lepera, F.S., *Improved etching technique to emphasize martensite and bainite in high-strength dual-phase steel.* J. Met., 1980. **32**(3): p. 38-39.

85. Wu, J.H., et al., *Image quality analysis: A new method of characterizing microstructures.* Isij International, 2005. **45**(2): p. 254-262.

86. Engler, O. and V. Randle, *Introduction to texture analysis: Macrotexture, microtexture, and orientation mapping*. 2009: CRC.

87. Wilson, A. and G. Spanos, *Application of orientation imaging microscopy to study phase transformations in steels.* Materials characterization, 2001. **46**(5): p. 407-418.

88. Gourgues, A.F., H. Flower, and T. Lindley, *Electron backscattering diffraction study of acicular ferrite, bainite, and martensite steel microstructures.* Materials Science and Technology, 2000. **16**(1): p. 26-40.

89. Bouyne, E., et al., *Use of EBSD technique to examine microstructure and cracking in a bainitic steel.* Scripta materialia, 1998. **39**(3).

90. Ruiz-Aparicio, A. and University of Pittsburgh. School of Engineering, *Evolution of Microstructure in Nb-Bearing Microalloyed Steels Produced by the Compact Strip Production Process*. 2004, University of Pittsburgh: Pittsburgh, PA.

91. Ayache, J., et al., *Sample preparation handbook for transmission electron microscopy: Methodology*. 2010: Springer Verlag.

92. Oliver, W.C. and G.M. Pharr, *Measurement of hardness and elastic modulus by instrumented indentation: Advances in understanding and refinements to methodology.* Journal of Materials Research, 2004. **19**(1): p. 3-20.

93. Oliver, W.C. and G.M. Pharr, *Nanoindentation in materials research: Past, present, and future.* Mrs Bulletin, 2010. **35**(11): p. 897-907.

94. *Nanoindentation*. Available from: http://en.wikipedia.org/wiki/Nanoindentation.

95. Coladas, R., et al., *Austenite grain growth in medium and high-carbon steels microalloyed with niobium.* Metal Science, 1977. **11**(11): p. 509-516.

96. Speich, G., et al., *Formation of ferrite from control-rolled austenite.* Phase transformations in ferrous alloys, 1983: p. 341-389.

97. DeArdo, A.J., G. Ratz, and P. Wray, *Thermomechanical processing of microalloyed austenite: proceedings of the International Conference on the Thermomechanical Processing of Microalloyed Austenite*. 1982: Metallurgical Society of AIME.

98. *JMatPro: practical software for materials properties*.

99. Suikkanen, P., P. Karjalainen, and A.J. DeArdo, *Effect of Carbon Content on the Phase Transformation Characteristics, Microstructure and Properties of 500 Mpa Grade*

Microalloyed Steels with Non-Polygonal Ferrite Microstructures. Metallurgia Italiana, 2009(7-8): p. 41-54.

100. TAKEUCHI, I., et al. *Crack arrestability of high-pressure gas pipelines by X100 or X120*. 2006.

101. Bodnar, R., et al., *Accelerated cooling on Burns Harbor's 160 in. plate mill.* Accelerated Cooling/Direct Quenching of Steels; Indianapolis, Indiana, 1997: p. 3-13.

102. Ikawa, H., H. Oshige, and T. Tanoue, *Effect of martensite-austenite constituent on HAZ toughness of a high strength steel.* Transactions of the Japan Welding Society, 1980. **11**(2): p. 87-96.

103. Wang, C., et al., *Transmission electron microscopy of martensite/austenite islands in pipeline steel X70.* Materials Science and Engineering: A, 2006. **438**: p. 267-271.

104. Shin, S.Y., et al., *Fracture toughness analysis in transition temperature region of API X70 pipeline steels.* Materials Science and Engineering: A, 2006. **429**(1): p. 196-204.

105. Hehemann, R., K. Kinsman, and H. Aaronson, *A debate on the bainite reaction.* Metallurgical and Materials Transactions B, 1972. **3**(5): p. 1077-1094.

106. Bramfitt, B. and J. Speer, *A perspective on the morphology of bainite.* Metallurgical and Materials Transactions A, 1990. **21**(3): p. 817-829.

107. Christian, J., *The Theory of Transformations in Metals and Alloys: Part I+ II*. 2002: Elsevier.

108. Gaskell, D.R., *Introduction to the Thermodynamics of Materials*. 2003: Hemisphere Pub.

109. Porter, D.A. and K.E. Easterling, *Phase transformations in metals and alloys*. 1992: CRC.

110. Speer, J., et al., *Carbon partitioning into austenite after martensite transformation.* Acta materialia, 2003. **51**(9): p. 2611-2622.

111. Clarke, A., et al., *Carbon partitioning to austenite from martensite or bainite during the quench and partition (Q&P) process: A critical assessment.* Acta materialia, 2008. **56**(1): p. 16-22.

112. Edmonds, D., et al., *Quenching and partitioning martensite—A novel steel heat treatment.* Materials Science and Engineering: A, 2006. **438**: p. 25-34.

113. Lee, B.J. and S.H. Choi, *Computation of grain boundary energies.* Modelling and Simulation in Materials Science and Engineering, 2004. **12**: p. 621.

114. Choi, S.H. and Y.S. Jin, *Evaluation of stored energy in cold-rolled steels from EBSD data.* Materials Science and Engineering: A, 2004. **371**(1): p. 149-159.

115. Fang, C. and University of Pittsburgh. School of Engineering, *Annealing and Precipitation Behavior During Batch Annealing of HSLA Steels*. 2011, University of Pittsburgh: Pittsburgh, PA.

116. Bunshah, R. and R. Mehl, *Rate of propagation of martensite.* Trans. Aime, 1953. **197**: p. 1251.

117. Reed-Hill, R.E., *Physical metallurgy principles.*

118. Greninger, A.B. and A. Troiano, *Crystallography of austenite decomposition.* Metals Technology, 1940: p. 1212.

119. Bowles, J., *NF Kennon, J Australian Inst*. 1960, Metals.

120. Pan, Y., et al., *Grain-boundary structure effects on intergranular stress corrosion cracking of alloy X-750.* Acta materialia, 1996. **44**(12): p. 4685-4695.

121. Crawford, D.C. and G.S. Was, *The Role of grain boundary misorientation in intergranular cracking of Ni-16Cr-9Fe in 360° C argon and high-Purity water.* Metallurgical and Materials Transactions A, 1992. **23**(4): p. 1195-1206.

122. Adams, B.L., S.I. Wright, and K. Kunze, *Orientation imaging: the emergence of a new microscopy.* Metallurgical and Materials Transactions A, 1993. **24**(4): p. 819-831.

123. Kim, M.C., Y. Jun Oh, and J. Hwa Hong, *Characterization of boundaries and determination of effective grain size in Mn-Mo-Ni low alloy steel from the view of misorientation.* Scripta materialia, 2000. **43**(3): p. 205-212.

124. Watanabe, T. and S. Tsurekawa, *The control of brittleness and development of desirable mechanical properties in polycrystalline systems by grain boundary engineering.* Acta materialia, 1999. **47**(15-16): p. 4171-4185.

125. Watanabe, T. and S. Tsurekawa, *Toughening of brittle materials by grain boundary engineering.* Materials Science and Engineering: A, 2004. **387**: p. 447-455.

126. Suikkanen, P.P., et al., *Crystallographic Analysis of Martensite in 0.2 C-2.0 Mn-1.5 Si-0.6 Cr Steel using EBSD.* Journal of Materials Science & Technology, 2011. **10**.

127. P.P. Suikkanen, C.C., A.J. DeArdo and L.P. Karjalainen, *Crystallography of Isothermally Transformed Bainite in 0.2C-2.0Mn-1.5Si-0.6Cr steel*. 2010, University of Oulu: Unpublished.

128. De Graef, M., *Introduction to conventional transmission electron microscopy*. 2003: Cambridge Univ Pr.

129. Fultz, B. and J.M. Howe, *Transmission electron microscopy and diffractometry of materials*. 2002: Springer Verlag.

130. Williams, D.B. and C.B. Carter, *The Transmission Electron Microscope.* Transmission Electron Microscopy, 2009: p. 3-22.

131. Hwang, B., et al., *Effective grain size and Charpy impact properties of high-toughness X70 pipeline steels.* Metallurgical and Materials Transactions A, 2005. **36**(8): p. 2107-2114.

132. Díaz-Fuentes, M., A. Iza-Mendia, and I. Gutierrez, *Analysis of different acicular ferrite microstructures in low-carbon steels by electron backscattered diffraction. Study of their toughness behavior.* Metallurgical and Materials Transactions A, 2003. **34**(11): p. 2505-2516.

133. Ray, R. and J. Jonas, *Transformation textures in steels.* International Materials Reviews, 1990. **35**(1): p. 1-36.

134. Davies, G., J. Kallend, and P. Morris, *The Hot Deformation of Austenite.* AIME, New York, 1977. **599**.

135. Ohtani, H., et al., *Morphology and properties of low-carbon bainite.* Metallurgical and Materials Transactions A, 1990. **21**(3): p. 877-888.